

Structure and Dynamics of Self-Healing Polyurethanes

Montano, V.

DOI

[10.4233/uuid:6ad1f5f3-c8b0-4d01-b875-5586a25744bd](https://doi.org/10.4233/uuid:6ad1f5f3-c8b0-4d01-b875-5586a25744bd)

Publication date

2021

Document Version

Final published version

Citation (APA)

Montano, V. (2021). *Structure and Dynamics of Self-Healing Polyurethanes*. [Dissertation (TU Delft), Delft University of Technology]. <https://doi.org/10.4233/uuid:6ad1f5f3-c8b0-4d01-b875-5586a25744bd>

Important note

To cite this publication, please use the final published version (if applicable).
Please check the document version above.

Copyright

Other than for strictly personal use, it is not permitted to download, forward or distribute the text or part of it, without the consent of the author(s) and/or copyright holder(s), unless the work is under an open content license such as Creative Commons.

Takedown policy

Please contact us and provide details if you believe this document breaches copyrights.
We will remove access to the work immediately and investigate your claim.

Structure and Dynamics of Self-Healing Polyurethanes

Structure and Dynamics of Self-Healing Polyurethanes

Proefschrift

ter verkrijging van de graad van doctor
aan de Technische Universiteit Delft,
op gezag van de Rector Magnificus prof. dr. ir. T.H.J.J. van der Hagen,
voorzitter van het College voor Promoties,
in het openbaar te verdedigen op dinsdag 16 Maart 2021 om 12:30 uur

door

Vincenzo Montano

Master of Science in Materials Engineering and Nanotechnology,
Politecnico di Milano, Milan, Italië,
geboren te Acerra, Italië.

The dissertation has been approved by the promotors

Composition of the doctoral committee:

Rector Magnificus	Chairman
Dr. S.J. García Espallargas	Delft University of Technology, promotor
Prof. dr. ir. S. van der Zwaag	Delft University of Technology, promotor

Independent members:

Prof. dr. M. Urban	Clemson University, U.S.A.
Prof. dr. ir. S. Leeuwenburgh	Radboud Universiteit
Prof. dr. S.J. Picken	Delft University of Technology
Dr. A.C.C. Esteves	Eindhoven University of Technology
Dr. A. Smits	Croda Nederland B.V.

Reserve lid:

Prof. C.A. Dransfeld	Delft University of Technology
----------------------	--------------------------------

The research carried out in this thesis was funded by Dutch National Organization for Scientific Research, Domain Applied and Engineering Sciences (NWO-TTW) under the grant number 15010 and Croda Nederland B.V.



CRODA

Keywords: Self-healing, Polyurethanes, Dynamics, Entropy.

Printed by: Proefschriftmaken

Cover: Artistic representation of scratch closure. Design by Giulia Bottino.

Copyright © 2021 by Vincenzo Montano

ISBN 978-94-6384-195-5

An electronic version of this dissertation is available at

<http://repository.tudelft.nl/>.

*Questa va ai ragazzi di periferia
Alla nostra fame
Alle immagini del passato
A quello che costruiremo in futuro*

Contents

1 Introduction	1
1.1 Introduction to self-healing polymers	2
1.2 Dynamics of intrinsic healing: from macroscopic closure to molecular repair	4
1.2.1 Macroscopic closure	4
1.2.2 Molecular treatment of self-healing	5
1.3 Challenges and prospects	7
1.4 Thesis scope and outline	7
References	8
2 Controlling healing and toughness in polyurethanes by branch-mediated tube dilation	15
2.1 Introduction	17
2.2 Experimental Section	18
2.2.1 Materials	18
2.2.2 Synthesis of branched diol monomers	18
2.2.3 Syntheses of the brush polyurethanes	20
2.2.4 Characterisation Methods	21
2.3 Results and discussion	23
2.3.1 Effect of brush length on polyurethane microstructure and dynamics	23
2.3.2 Impact of induced crystallization on the healing behavior	35
2.4 Conclusions	41
2.5 Supporting Information	42
References	62
3 A deconvolution protocol of the mechanical relaxation spectrum to identify and quantify individual polymer feature contributions to self-healing	67
3.1 Introduction	69
3.2 Experimental and Fitting Protocol	71
3.2.1 Polymers Syntheses	71
3.2.2 Rheological Measurements and Tensile Properties	73
3.2.3 Fitting protocol	74
3.3 Results	76
3.4 Discussion	82
3.4.1 Type and distribution of relaxation events	82
3.4.2 Physical meaning of the fitting parameters	83

3.4.3	Relating fitting protocol outcome to self-healing efficiency.	85
3.5	Conclusions.	89
	References.	90
4	Linking interfacial work of deformation from deconvoluted macro-rheological spectrum to early stage healing in selected polyurethanes	95
4.1	Introduction.	97
4.2	Experimental Section.	98
4.2.1	Materials.	98
4.2.2	Synthesis of segmented polyurethanes.	98
4.2.3	Characterisation Methods.	99
4.3	Results and Discussion.	102
4.3.1	Deconvolution protocol to unveil individual relaxations and related work of deformation.	102
4.3.2	Interfacial work of deformation relation to early-stage healing fracture resistance.	108
4.4	Conclusions.	111
4.5	Supporting Information.	112
	References.	122
5	Scratch closure in thermoplastic polyurethanes: an energetic analysis	125
5.1	Introduction.	127
5.2	Experimental Section.	128
5.2.1	Materials.	128
5.2.2	Synthesis of the TPUs and coating preparation.	128
5.2.3	Characterisation methods.	128
5.3	Results and Discussion.	130
5.3.1	Network architecture influence on shape memory VLTs.	130
5.3.2	Relation between macroscopic scratch closure and released entropy.	134
5.3.3	Entropy storage as a strain-induced phenomenon.	136
5.4	Conclusions.	140
5.5	Supporting Information.	140
	References.	147
6	From damage closure to electrolyte barrier restoration in self-healing polyurethane coatings: a function of the soft-to-hard ratio and hydrogen bond state	151
6.1	Introduction.	153
6.2	Experimental Section.	154
6.2.1	Materials.	154
6.2.2	Synthesis segmented polyurethanes and coating preparation.	155
6.2.3	Characterization Methods.	156

6.3 Results and Discussion	158
6.3.1 Effect of soft phase fraction on polymer structure and dynamics.	158
6.3.2 Effect of soft phase fraction on barrier properties of in- tact coatings.	162
6.3.3 Effect of soft phase fraction on scratch closure kinetics .	163
6.3.4 Effect of soft phase fraction on barrier restoration	166
6.3.5 Physical insights to scratch closure and scratch sealing	169
6.4 Conclusions	172
6.5 Supporting Information	172
References	187
Summary	191
Samenvatting	195
Acknowledgements	199
Curriculum Vitæ	201
List of Publications	203
List of Conferences	205

1

Introduction

*In his youth Albert Einstein spent a year loafing aimlessly.
You don't get anywhere by not "wasting" time.
This is something, unfortunately,
that the parents of teenagers tend frequently to forget.*

Carlo Rovelli, in Seven Brief Lessons on Physics

1.1. Introduction to self-healing polymers

Materials are traditionally optimised for a certain application by following the design rules of damage prevention. The material properties (e.g. its mechanical response) have to match the standard operational conditions magnified by a safety factor that takes into consideration any unforeseen unusual/critical loadings and the inevitable property decrease due to material degradation over time. In these systems, if damage occurs, it is permanent and often growing with time resulting, eventually, to the need to repair the construction [1, 2]. Living organisms have a different approach to deal with damage and use an alternative strategy referred to as 'damage management' [3]. Critical damages are considered to be unavoidable, so organisms respond to it by autonomously initiating damage mitigation actions. At the material level this ability is referred to as 'self-healing'. Scientists have tried to transfer this ability to synthetic materials aiming to replicate the resilience that biological systems have against damage. For these reasons, self-healing materials find their application in fields where a long product lifetime is desired. This guaranteed longevity is even more attractive in applications which are damage sensitive but where maintenance or repair is difficult such as in aerospace, automotive, oil and gas [2].

Self-healing is a thermodynamically expensive process which leads towards restoration of organisation (negative entropy) [4]. Plants can stop the ineluctable descent towards thermodynamic chaos thanks to the presence of embryonic stem cells in the growth zones that enable to form new structures till death [3]. Synthetic materials are not capable to gather and direct energy towards self-procreation and healing but scientists have implemented many creative strategies to invert the thermodynamic inevitable processes. Synthetic and natural self-healing approaches found to date seem to share the common requirement of 'local temporary mobility' [5]: the flow of mass (mobility) located at the damage site (local) only for a certain period of time until the property restoration has been realised (temporary).

In polymers the requirement of local temporary mobility is attained exploiting two distinct strategies. **Extrinsic healing polymers** are essentially conventional non-self-healing polymer matrices compounded with microencapsulated systems containing one or multiple healing agents. The strong stress singularity at the tip of the crack propagating through the matrix causes the rupture of the microcapsules, allowing the reflow of the healing agents into the damage zone [6, 7]. In the first proof-of-concept, the microcapsules contained an unreacted monomer, while a solid catalyst had to be dispersed in the polymer matrix to trigger the conversion of the liquid monomer into a well-adhering gel subsequently turned into a crosslinked polymer [8]. In later approaches both phases were microencapsulated together in a single particle [9], or one of two healing agents were phase separated in the matrix [10]. Different chemistries for the liquid healing agent have been used successfully. The most well-established ones are epoxy-amine, endo-dicylopentadiene and thiol/isocyanate [11–15].

The extrinsic self-healing approach based on a liquid healing agent has the ad-

vantage of being a (potentially) autonomous self-healing system as the liquid will flow out without any further human interaction and no other stimuli such as heat, light, electrical field or pressure need to be applied. Nevertheless, all these extrinsic self-healing systems have some common yet crucial limitations: complex manufacturing and processing [16–18], a limited shelf life, limited healing agent delivery (in particular in case of large damages) and most importantly an intrinsic inability to locally heal the damage more than once. The latter is due to the fact that in the healing reaction the activated healing agent permanently loses its fluidic nature.

In **intrinsic healing polymers** the self-healing ability is endowed by the molecular design of the network without the need to add discrete external healing agents. Upon the occurrence of a damage and after inducing (or retaining) partial or complete physical contact between the separated fracture surfaces, the local polymer diffusion and the recombination of the reversible bonds guarantees the reconstruction of the broken interface. Given the right temperature–time combinations long-range macromolecular mobility is responsible for the complete disappearance of the damage. The mechanism promises a virtual infinite number of healing cycles including multiple healing events at the same location, provided no unwanted side reactions and no “scar-tissue”, i.e. a region in which the material does not return to its pristine state, is present at the end of the healing process. The recombination of the reversible bonds can take place at ambient conditions if the molecular mobility is high enough but often requires the application of different stimuli such as heat, UV light, pH change [19–21]. These stimuli unlock the reversible group, decreasing the polymer viscosity and satisfying the requirement of the local temporary mobility. Alternatively, external pressure can facilitate the desired mobility to allow for interfacial contact of the two sides of a damage. The intrinsic healing concept got broad attention at first in the field of soft hydrogels [22], but it has been successfully extended to thermoplastics [23], thermosets [19] and elastomers [24, 25]. In general, the required strength of the stimulus increases with the mechanical rigidity of the polymer at its operational temperature. The intrinsic self-healing polymers are classified on the base of the dynamic chemistry used to design the reversible moiety:

I) **Reversible covalent chemistry** relies on the recombination of strong covalent bonds. Some of the reversible reactions exploited in the field include retro Diels-Alder reactions [26–29], disulphides and polysulfides [30–34], alkoxyamines [35], trithiocarbonate exchange reactions [36], cross-linked poly(dimethylsiloxane) [37] and diarylbenzofuranone [38]. The reversible covalent bonds, while being very stable at room temperature, are labile at high temperature allowing local flow and healing. The stability of reversible bonds accounts for the high mechanical properties of these polymers, but, as stated earlier, elevated temperatures are generally required to start the healing process.

II) **Supramolecular chemistry** relies on the recombination of physical/secondary interactions. Some studied interactions are ionic bonds [11, 39–43], metal-ligand

coordination [44–49], π - π stacking [50, 51], hydrogen bonding, microphase separation [52, 53] and hydrophobic interactions [23, 54]. Among these, the use of microphase separation and multiple Van der Waals interactions has appeared as a clear direction to turn commodity-like systems into self-healing variants without the introduction of severe chemical modifications [55]. The supramolecular bonds show relatively fast association/dissociation kinetics. This feature has enabled the synthesis of polymers showing complete healing at room temperature. On the other hand, the physical interactions present low bond energy connections thus setting a relatively weak transient network which leads to relatively low mechanical properties. To address this latter issue different strategies have been employed. Guan et al. [56] introduced sacrificial noncovalent bonds to increase the mechanical properties of soft self-healing thermosets. Yanagisawa et al. [57] reported polymers readily healable at room temperature and with high mechanical properties by including dense and non-directional thiourea hydrogen bonding units in the main chain. Susa et al. [51] designed a set of self-healing polyimides where the equilibrium between main chain aromatics and side-chain hydrophobic interactions is responsible for high mechanical properties combined with room temperature healing. These systems present very harsh chemical modifications, therefore new strategies involving the modification of polymer architecture must be explored to conjugate easiness of production, room temperature healing and high mechanical properties [5].

1.2. Dynamics of intrinsic healing: from macroscopic closure to molecular repair

The mending process in the intrinsic self-healing polymers is a hierarchical mechanisms involving different processes at different structural scales. Here a brief overview of such physical/chemical phenomena and of the models developed to capture them is presented.

1.2.1. Macroscopic closure

Physical contact between damaged surface is an essential requirement for self-healing to be able to take place. Only after contact, the molecular mechanisms that determine the interface reconstruction can follow.

At the macroscale the closure of the physical gap can occur following two distinct mechanism: entropy-driven elastic closure and interfacial flow [58, 59].

Polymers, when deformed above a thermal transition and then rapidly cooled while keeping the deformation, are able to retain their temporary shape. If the deformations result in conformational changes in the rubbery amorphous regions without chain slippage, upon re-heating above the thermal transition, the original shape will be recovered [60]. The driving force of the process is the recovery of stored entropy, accumulated during polymer deformation. This phenomenon is known as shape memory effect, a unique feature which manifests itself most prominently in shape memory polymers [61, 62], but in principle can take place in any polymer deformed above its glass transition temperature and well below its melting temperature. Chain slippage during damage (deformation) can be prevented by mi-

crophase segregation, main chain entanglements, chemical/physical crosslinking, or by compatible polymer blending [63–68]. The concept has been implemented in self-healing polymers [59, 69] to provide an autonomous mechanism by which a damage can be partially or fully closed, leading to the contact among the damaged planes. The entropy driven shape memory effect can be quantified by a single dynamic mechanical analysis test determining the stored conformational entropy through the analysis of the viscoelastic length of the transition [60]. In this publication a direct correlation between stored conformational entropy and network junction density (i.e. more crosslinking in mildly crosslinked polymers show higher entropy storage) was demonstrated. However, no direct relation has been shown between the amount of stored entropy and the degree or the kinetics of scratch closure.

1.2.2. Molecular treatment of self-healing

Macroscopic crack closure does not necessarily imply self-healing. For self-healing to occur, the damaged surfaces have to be reconstructed at the molecular level. Therefore it is crucial to get the fundamental knowledge of the molecular and collective processes that regulate the reversibility of such supramolecular reorganization within the polymer network. Herein we focus on the models developed for intrinsic healing polymer via non-covalent interactions.

Major conceptual steps could be formulated thanks to the theoretical model developed by Stukalin et al. [70] for un-entangled networks bearing reversible bonds (stickers). The model consists of small chains with one end anchored in space and the other one behaving as a sticky group, able to associate to form reversible bonds. Depending on the bond strength ε the stickers are classified as “weak” (when $\varepsilon \ll k_b T \ln N$, with N being equivalent to the polymer chain length), “intermediate” ($k_b T \ln N < \varepsilon < 2k_b T \ln N$) and strong ($\varepsilon > 2k_b T \ln N$). Using a scaling theory the authors have determined an analytical relation between τ_{eq} (the equilibration time of excess open stickers upon creation of a fresh interface) and ε . If the waiting time (τ_w) before the two fresh interfaces are put in contact meets the boundary condition $\tau_w > \tau_{eq}$, no self-healing is possible, yet some adhesion regime can be observed. The adhesion regime corresponds to a physical picture in which the two surfaces that are put in contact are at or close to equilibrium, therefore the majority of sticky groups has been reassociating with themselves on the same plane [71]. On the other hand, in case $\tau_w < \tau_{eq}$ self-healing can take place. In this regime healing occurs by hopping dynamics.

The difference between self-healing and self-adhesion proposed in the theory has been validated experimentally by Hawker et al. [72], who demonstrated that healing is only possible within a short period of time after formation of the new fresh fracture surfaces. This work also demonstrated the critical effect that humidity exerts on the “de-activation” of open hydrogen bonds at the fractured surface. The effect of the effective bond life time τ_b on healing kinetics has been investigated by Bose et al. [73], who designed a series of ionomers of equal molecular weight but based on different coordination metals present at different concentrations levels, covering a broad range of supramolecular bond lifetime τ_b . The authors showed a

relation between self-healing (probed via scratch closure measurements), polymer mechanical properties and rheology (τ_b). A desirable combination of good healing and strong mechanical properties is obtained for ionomers with $1\text{ s} < \tau_b < 100\text{ s}$ (at room temperature). Weak mechanical properties and viscous flow driven scratch closure are observed for $\tau_b \ll 1\text{ s}$, while strong mechanical properties show a weak tendency to heal at that temperature when $\tau_b \gg 100\text{ s}$.

It is significantly harder to develop a theory for the healing of entangled polymers since main chain entanglements further restrict dynamics. Leibler, Colby and Rubinstein proposed the sticky reptation model [74]. In this model, S sticker units are attached on an entangled polymer network and the temperature dependence of the viscoelastic properties of the system is derived. Figure 1.1 compares the viscoelastic properties of a polymer chain in absence and in presence of the sticker units in a classical time oscillation shear experiment.

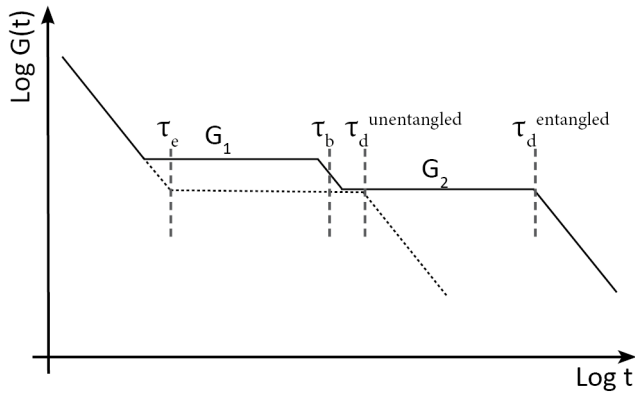


Figure 1.1: Shear modulus time dependency for a linear polymer without supramolecular stickers (dash line) and with a number S of supramolecular stickers, as calculated by Leibler, Colby and Rubinstein [74]

Four regimes are identified: for experimental times $t < \tau_e$ (Rouse time of an entangled strand) the shear modulus $G(t)$ is the same for both the systems. Then two plateaus follows. G_1 is attributed to the mobility restriction operated by the stickers and is proportional to N_e (number density of entanglements) and N_s (the crosslinks between the stickers). G_2 corresponds to the rubbery plateau of a system without stickers, therefore is only proportional to N_e . Ultimately at $t = \tau_d$ terminal chain relaxation occurs. τ_d depends on the fraction of closed stickers p and their lifetime τ_b . The reptation times predicted by the sticky-reptation model are in good agreement with the experimental reptation times obtained by Stadler et al. [75, 76]. Such polymers with a higher number of sticky units are expected to show delayed reptation which translates to a slower healing kinetics, since randomisation of the reforming polymer network at the damage site will take more time. Experimental confirmation was shown by Susa et al. [23]. In that work the authors increased the number of Van der Waals stickers by tuning the stoichiome-

try of a diamine branched monomer and showed progressive delay in the complete recovery of tensile mechanical properties for polymers harnessing higher number of supramolecular stickers.

As argued in Section 1.1. in order to obtain polymers that combine mild temperatures for healing and high mechanical properties at room temperature, there is a tendency to design networks combining multiple reversible blocks of a different chemical nature (e.g. π - π stacking is combined with hydrogen bonding) [51, 56, 57]. However, at present, there is a lack of both experimental and theoretical tools to separate the contributions of the different reversible ligands both to the polymer dynamics and to the healing process. A first attempt was made by Grande et al. for poly(urea-urethane) networks containing both hydrogen bonds and disulphide linkages [77]. Combining fracture mechanics and rheology, the authors were able to separate the contribution of the two reversible ligands to the early stage and long term recovery of the healing polymer fracture properties.

1.3. Challenges and prospects

In the past twenty years research in the field of intrinsic self-healing polymers has mainly focused on novel reversible chemistries to exploit the intrinsic healing property and achieving room temperature healing. Demonstrations of attractive combinations of performance were provided for polymers produced on a lab-scale. However, several questions must be addressed before self-healing polymers can be routinely used on industrial scale. The remaining issues can be divided in two macro groups: scientific issues and application issues.

From a **scientific point of view** the efforts need to focus on the synthesis of healing systems that require minimal chemical modification with respect to the existing non-self-healing variants, as this has the highest chance of industrial applicability and market introduction. Moreover, specific studies need to point at the physical understanding of the polymer structure to self-healing property relation, which appears as the only way to instruct chemists on the optimisation of systems which exploit a number of complex physical-chemical events.

Application-wise, the focus needs to be on applications that can immediately benefit from the use of systems with extended life-time and that do would benefit of minor or no operator maintenance (e.g. ocean-based wind turbines). Moreover, it is fundamental to define industrial international standards to test self-healing ability for the recovery of specific functional properties (e.g. tensile mechanical, fatigue resistance, barrier, aesthetical appearance). While mechanical healing remains a principle asset for many applications, other cases of recovery of the original functionality (such as anti-corrosion in protective organic coatings on metallic substrates) can be of equal importance and need to be determined as well.

1.4. Thesis scope and outline

This thesis aims at the constitution of design rules for the development of self-healing polyurethanes focusing on the understanding of the polymer structure to

self-healing property relation. Moreover, the work focuses on the physical understanding of the dynamic processes of self-healing polymers and their influence both on the early stage and on long term functional property restoration.

Chapter 2 reports the synthesis and characterisation of a series of novel self-healing polyurethanes bearing aliphatic side chains. The length of the aliphatic branch affects the polymer dynamics and the healing behaviour. Moreover, the attention is focused on the branch length and time dependent healing reactions as well as any aging/crystallisation behaviour.

Chapter 3 presents a new and general deconvolution protocol of the mechanical relaxation spectrum of polymers derived from rheology. Using the deconvoluted spectra we discuss how individual molecular features contribute to polymer dynamics and how the energy spent for the various relaxations affects the long term healing behaviour of selected polyamides and polyetherimides.

Chapter 4 focuses on the investigation of early-stage healing of novel self-healing thermoplastic polyurethanes. The polymers are characterised by single edge-notch tensile tests for short healing times at mild temperatures. Using the deconvolution protocol of Chapter 3 we isolate the contribution of hydrogen bonds to the polymer dynamics and investigate the relation between the relaxation energy and the fracture properties of the polymer at early stages of healing.

Chapter 5 addresses quantitatively the relation between elastic scratch closure and stored entropy density measured at the viscoelastic length of transition. To this aim the scratch closure behaviour of a series of thermoplastic polyurethane coatings with controlled architecture is tested by carefully controlling both the damaging and the healing temperature. The stored entropy density near the damage site is calculated using dynamical mechanical analysis tests.

Chapter 6 follows on chapter 5 and presents a series of self-healing thermoplastic polyurethane coatings applied on carbon steel to investigate the effect of soft phase fraction on the gap closure and sealing behaviour and their impact on the restoration of the barrier functionality necessary to protect coated metals against corrosion at damaged locations. The barrier functionality is tested through accelerated electrochemistry and the healing is assessed based on the recovery of the capacitive behaviour after scratch healing.

References

- [1] S. van der Zwaag, *An introduction to material design principles: Damage prevention versus damage management*, in *Self healing materials* (Springer, 2007) pp. 1–18.
- [2] S. van der Zwaag and E. Brinkman, *Self Healing Materials: Pioneering Research in the Netherlands* (IOS Press, 2015).

- [3] O. Speck and T. Speck, *An overview of bioinspired and biomimetic self-repairing materials*, *Biomimetics* **4**, 26 (2019).
- [4] C. E. Diesendruck, N. R. Sottos, J. S. Moore, and S. R. White, *Biomimetic self-healing*, *Angewandte Chemie International Edition* **54**, 10428 (2015).
- [5] S. J. Garcia, *Effect of polymer architecture on the intrinsic self-healing character of polymers*, *European Polymer Journal* **53**, 118 (2014).
- [6] S. R. White, M. M. Caruso, and J. S. Moore, *Autonomic healing of polymers*, *Mrs Bulletin* **33**, 766 (2008).
- [7] W. Post, *Self-Healing Polymer Composites*, Ph.D. thesis, Delft University of Technology, The Netherlands (2017).
- [8] S. R. White, N. R. Sottos, P. H. Geubelle, J. S. Moore, M. R. Kessler, S. Sriram, E. N. Brown, and S. Viswanathan, *Autonomic healing of polymer composites*, *Nature* **409**, 794 (2001).
- [9] S. D. Mookhoek, B. J. Blaiszik, H. R. Fischer, N. R. Sottos, S. R. White, and S. van der Zwaag, *Peripherally decorated binary microcapsules containing two liquids*, *Journal of Materials Chemistry* **18**, 5390 (2008).
- [10] S. H. Cho, H. M. Andersson, S. R. White, N. R. Sottos, and P. V. Braun, *Polydimethylsiloxane-based self-healing materials*, *Advanced Materials* **18**, 997 (2006).
- [11] W. Post, R. K. Bose, S. J. García, and S. van der Zwaag, *Healing of early stage fatigue damage in ionomer/Fe₃O₄ nanoparticle composites*, *Polymers* **8**, 436 (2016).
- [12] D. A. McIlroy, B. J. Blaiszik, M. M. Caruso, S. R. White, J. S. Moore, and N. R. Sottos, *Microencapsulation of a reactive liquid-phase amine for self-healing epoxy composites*, *Macromolecules* **43**, 1855 (2010).
- [13] X. K. Hillewaere, R. F. Teixeira, L.-T. T. Nguyen, J. A. Ramos, H. Rahier, and F. E. Du Prez, *Autonomous self-healing of epoxy thermosets with thiol-isocyanate chemistry*, *Advanced Functional Materials* **24**, 5575 (2014).
- [14] S. Neuser, P. W. Chen, A. R. Studart, and V. Michaud, *Fracture toughness healing in epoxy containing both epoxy and amine loaded capsules*, *Advanced Engineering Materials* **16**, 581 (2014).
- [15] X. K. Hillewaere and F. E. Du Prez, *Fifteen chemistries for autonomous external self-healing polymers and composites*, *Progress in Polymer Science* **49**, 121 (2015).
- [16] K. S. Toohey, N. R. Sottos, J. A. Lewis, J. S. Moore, and S. R. White, *Self-healing materials with microvascular networks*, *Nature materials* **6**, 581 (2007).

- [17] M. Kessler, N. R. Sottos, and S. R. White, *Self-healing structural composite materials*, Composites Part A: applied science and manufacturing **34**, 743 (2003).
- [18] K. S. Toohey, C. J. Hansen, J. A. Lewis, S. R. White, and N. R. Sottos, *Delivery of two-part self-healing chemistry via microvascular networks*, Advanced Functional Materials **19**, 1399 (2009).
- [19] M. AbdollahZadeh, A. C. C. Esteves, S. van der Zwaag, and S. J. Garcia, *Healable dual organic–inorganic crosslinked sol–gel based polymers: crosslinking density and tetrasulfide content effect*, Journal of Polymer Science Part A: Polymer Chemistry **52**, 1953 (2014).
- [20] Z. Hu, D. Zhang, F. Lu, W. Yuan, X. Xu, Q. Zhang, H. Liu, Q. Shao, Z. Guo, and Y. Huang, *Multistimuli-responsive intrinsic self-healing epoxy resin constructed by host–guest interactions*, Macromolecules **51**, 5294 (2018).
- [21] N. Holten-Andersen, M. J. Harrington, H. Birkedal, B. P. Lee, P. B. Messersmith, K. Y. C. Lee, and J. H. Waite, *ph-induced metal-ligand cross-links inspired by mussel yield self-healing polymer networks with near-covalent elastic moduli*, Proceedings of the National Academy of Sciences **108**, 2651 (2011).
- [22] M. Nakahata, Y. Takashima, H. Yamaguchi, and A. Harada, *Redox-responsive self-healing materials formed from host–guest polymers*, Nature communications **2**, 1 (2011).
- [23] A. Susa, R. Bose, A. Grande, S. van der Zwaag, and S. J. Garcia, *Effect of the dianhydride/branched diamine ratio on the architecture and room temperature healing behavior of polyetherimides*, ACS applied materials & interfaces **8**, 34068 (2016).
- [24] L. Zhang, Z. Liu, X. Wu, Q. Guan, S. Chen, L. Sun, Y. Guo, S. Wang, J. Song, E. M. Jeffries, *et al.*, *A highly efficient self-healing elastomer with unprecedented mechanical properties*, Advanced Materials **31**, 1901402 (2019).
- [25] M. Hernández, A. M. Grande, W. Dierkes, J. Bijleveld, S. van der Zwaag, and S. J. García, *Turning vulcanized natural rubber into a self-healing polymer: Effect of the disulfide/polysulfide ratio*, ACS sustainable chemistry & engineering **4**, 5776 (2016).
- [26] X. Chen, M. A. Dam, K. Ono, A. Mal, H. Shen, S. R. Nutt, K. Sheran, and F. Wudl, *A thermally re-mendable cross-linked polymeric material*, Science **295**, 1698 (2002).
- [27] E. B. Murphy, E. Bolanos, C. Schaffner-Hamann, F. Wudl, S. R. Nutt, and M. L. Auad, *Synthesis and characterization of a single-component thermally remendable polymer network: Staudinger and stille revisited*, Macromolecules **41**, 5203 (2008).

- [28] S. Billiet, W. Van Camp, X. K. Hillewaere, H. Rahier, and F. E. Du Prez, *Development of optimized autonomous self-healing systems for epoxy materials based on maleimide chemistry*, *Polymer* **53**, 2320 (2012).
- [29] K. Urdl, S. Weiss, P. Christöfl, A. Kandelbauer, U. Müller, and W. Kern, *Diels-alder modified self-healing melamine resin*, *European Polymer Journal*, 109601 (2020).
- [30] J. Canadell, H. Goossens, and B. Klumperman, *Self-healing materials based on disulfide links*, *Macromolecules* **44**, 2536 (2011).
- [31] H. Otsuka, S. Nagano, Y. Kobashi, T. Maeda, and A. Takahara, *A dynamic covalent polymer driven by disulfide metathesis under photoirradiation*, *Chemical communications* **46**, 1150 (2010).
- [32] U. Lafont, H. Van Zeijl, and S. van der Zwaag, *Influence of cross-linkers on the cohesive and adhesive self-healing ability of polysulfide-based thermosets*, *ACS applied materials & interfaces* **4**, 6280 (2012).
- [33] S. Nevejans, N. Ballard, M. Fernández, B. Reck, S. J. García, and J. M. Asua, *The challenges of obtaining mechanical strength in self-healing polymers containing dynamic covalent bonds*, *Polymer* **179**, 121670 (2019).
- [34] M. Abdolah Zadeh, A. M. Grande, S. van der Zwaag, and S. J. Garcia, *Effect of curing on the mechanical and healing behaviour of a hybrid dual network: a time resolved evaluation*, *RSC advances* **6**, 91806 (2016).
- [35] M. Z. Rong, M. Q. Zhang, *et al.*, *Self-healing polyurethane elastomer with thermally reversible alkoxyamines as crosslinkages*, *Polymer* **55**, 1782 (2014).
- [36] Y. Amamoto, J. Kamada, H. Otsuka, A. Takahara, and K. Matyjaszewski, *Repeatable photoinduced self-healing of covalently cross-linked polymers through reshuffling of trithiocarbonate units*, *Angewandte Chemie* **123**, 1698 (2011).
- [37] P. Zheng and T. J. McCarthy, *A surprise from 1954: siloxane equilibration is a simple, robust, and obvious polymer self-healing mechanism*, *Journal of the American Chemical Society* **134**, 2024 (2012).
- [38] K. Imato, M. Nishihara, T. Kanehara, Y. Amamoto, A. Takahara, and H. Otsuka, *Self-healing of chemical gels cross-linked by diarylbibenzofuranone-based trigger-free dynamic covalent bonds at room temperature*, *Angewandte Chemie* **124**, 1164 (2012).
- [39] R. J. Varley and S. van der Zwaag, *Towards an understanding of thermally activated self-healing of an ionomer system during ballistic penetration*, *Acta Materialia* **56**, 5737 (2008).
- [40] R. J. Varley, S. Shen, and S. van der Zwaag, *The effect of cluster plasticisation on the self healing behaviour of ionomers*, *Polymer* **51**, 679 (2010).

- [41] S. J. Kalista, J. R. Pflug, and R. J. Varley, *Effect of ionic content on ballistic self-healing in EMAA copolymers and ionomers*, *Polymer Chemistry* **4**, 4910 (2013).
- [42] A. Reisch, E. Roger, T. Phoeng, C. Antheaume, C. Orthlieb, F. Boulmedais, P. Lavalle, J. B. Schlenoff, B. Frisch, and P. Schaaf, *On the benefits of rubbing salt in the cut: Self-healing of saloplastic PAA/PAH compact polyelectrolyte complexes*, *Advanced Materials* **26**, 2547 (2014).
- [43] Y. Huang, P. G. Lawrence, and Y. Lapitsky, *Self-assembly of stiff, adhesive and self-healing gels from common polyelectrolytes*, *Langmuir* **30**, 7771 (2014).
- [44] K. A. Williams, A. J. Boydston, and C. W. Bielawski, *Towards electrically conductive, self-healing materials*, *Journal of the royal society interface* **4**, 359 (2007).
- [45] M. Burnworth, L. Tang, J. R. Kumpfer, A. J. Duncan, F. L. Beyer, G. L. Fiore, S. J. Rowan, and C. Weder, *Optically healable supramolecular polymers*, *Nature* **472**, 334 (2011).
- [46] S. Bode, L. Zedler, F. H. Schacher, B. Dietzek, M. Schmitt, J. Popp, M. D. Hager, and U. S. Schubert, *Self-healing polymer coatings based on crosslinked metallosupramolecular copolymers*, *Advanced Materials* **25**, 1634 (2013).
- [47] Z. Wang and M. W. Urban, *Facile uv-healable polyethylenimine-copper (C_2H_5N-Cu) supramolecular polymer networks*, *Polymer Chemistry* **4**, 4897 (2013).
- [48] R. K. Bose, M. Enke, A. M. Grande, S. Zechel, F. H. Schacher, M. D. Hager, S. J. Garcia, U. S. Schubert, and S. van der Zwaag, *Contributions of hard and soft blocks in the self-healing of metal-ligand-containing block copolymers*, *European Polymer Journal* **93**, 417 (2017).
- [49] S. Burattini, H. M. Colquhoun, J. D. Fox, D. Friedmann, B. W. Greenland, P. J. Harris, W. Hayes, M. E. Mackay, and S. J. Rowan, *A self-repairing, supramolecular polymer system: healability as a consequence of donor-acceptor $\pi-\pi$ stacking interactions*, *Chemical communications*, 6717 (2009).
- [50] S. Burattini, B. W. Greenland, D. H. Merino, W. Weng, J. Seppala, H. M. Colquhoun, W. Hayes, M. E. Mackay, I. W. Hamley, and S. J. Rowan, *A healable supramolecular polymer blend based on aromatic $\pi-\pi$ stacking and hydrogen-bonding interactions*, *Journal of the American Chemical Society* **132**, 12051 (2010).
- [51] A. Susa, J. Bijleveld, M. Hernandez Santana, and S. J. Garcia, *Understanding the effect of the dianhydride structure on the properties of semiaromatic polyimides containing a biobased fatty diamine*, *ACS sustainable chemistry & engineering* **6**, 668 (2018).

- [52] Y. Chen, A. M. Kushner, G. A. Williams, and Z. Guan, *Multiphase design of autonomic self-healing thermoplastic elastomers*, *Nature chemistry* **4**, 467 (2012).
- [53] Y. Yang, D. Davydovich, C. C. Hornat, X. Liu, and M. W. Urban, *Leaf-inspired self-healing polymers*, *Chem* **4**, 1928 (2018).
- [54] M. W. Urban, D. Davydovich, Y. Yang, T. Demir, Y. Zhang, and L. Casabianca, *Key-and-lock commodity self-healing copolymers*, *Science* **362**, 220 (2018).
- [55] Y. Yang and M. W. Urban, *Self-healing of polymers via supramolecular chemistry*, *Advanced Materials Interfaces* **5**, 1800384 (2018).
- [56] J. A. Neal, D. Mozhdghi, and Z. Guan, *Enhancing mechanical performance of a covalent self-healing material by sacrificial noncovalent bonds*, *Journal of the American Chemical Society* **137**, 4846 (2015).
- [57] Y. Yanagisawa, Y. Nan, K. Okuro, and T. Aida, *Mechanically robust, readily repairable polymers via tailored noncovalent cross-linking*, *Science* **359**, 72 (2018).
- [58] Y. Yang, X. Ding, and M. W. Urban, *Chemical and physical aspects of self-healing materials*, *Progress in Polymer Science* **49**, 34 (2015).
- [59] C. C. Hornat and M. W. Urban, *Entropy and interfacial energy driven self-healable polymers*, *Nature communications* **11**, 1 (2020).
- [60] C. C. Hornat, Y. Yang, and M. W. Urban, *Quantitative predictions of shape-memory effects in polymers*, *Advanced Materials* **29**, 1603334 (2017).
- [61] A. Lendlein and S. Kelch, *Shape-memory polymers*, *Angewandte Chemie International Edition* **41**, 2034 (2002).
- [62] I. A. Rousseau and P. T. Mather, *Shape memory effect exhibited by smectic-c liquid crystalline elastomers*, *Journal of the American Chemical Society* **125**, 15300 (2003).
- [63] B. T. Michal, C. A. Jaye, E. J. Spencer, and S. J. Rowan, *Inherently photohealable and thermal shape-memory polydisulfide networks*, *ACS Macro Letters* **2**, 694 (2013).
- [64] Y. Yang and M. W. Urban, *Self-repairable polyurethane networks by atmospheric carbon dioxide and water*, *Angewandte Chemie* **126**, 12338 (2014).
- [65] L. Lu, J. Fan, and G. Li, *Intrinsic healable and recyclable thermoset epoxy based on shape memory effect and transesterification reaction*, *Polymer* **105**, 10 (2016).
- [66] G. Rivero, L.-T. T. Nguyen, X. K. Hillewaere, and F. E. Du Prez, *One-pot thermoremendable shape memory polyurethanes*, *Macromolecules* **47**, 2010 (2014).

- [67] E. D. Rodriguez, X. Luo, and P. T. Mather, *Linear/network poly (ϵ -caprolactone) blends exhibiting shape memory assisted self-healing (smash)*, ACS applied materials & interfaces **3**, 152 (2011).
- [68] X. Luo and P. T. Mather, *Shape memory assisted self-healing coating*, ACS Macro Letters **2**, 152 (2013).
- [69] N. García-Huete, W. Post, J. M. Laza, J. L. Vilas, L. M. León, and S. J. García, *Effect of the blend ratio on the shape memory and self-healing behaviour of ionomer-polycyclooctene crosslinked polymer blends*, European Polymer Journal **98**, 154 (2018).
- [70] E. B. Stukalin, L.-H. Cai, N. A. Kumar, L. Leibler, and M. Rubinstein, *Self-healing of unentangled polymer networks with reversible bonds*, Macromolecules **46**, 7525 (2013).
- [71] A. Campanella, D. Döhler, and W. H. Binder, *Self-healing in supramolecular polymers*, Macromolecular Rapid Communications **39**, 1700739 (2018).
- [72] A. Faghijnejad, K. E. Feldman, J. Yu, M. V. Tirrell, J. N. Israelachvili, C. J. Hawker, E. J. Kramer, and H. Zeng, *Adhesion and surface interactions of a self-healing polymer with multiple hydrogen-bonding groups*, Advanced Functional Materials **24**, 2322 (2014).
- [73] R. K. Bose, N. Hohlbein, S. J. Garcia, A. M. Schmidt, and S. van der Zwaag, *Connecting supramolecular bond lifetime and network mobility for scratch healing in poly (butyl acrylate) ionomers containing sodium, zinc and cobalt*, Physical Chemistry Chemical Physics **17**, 1697 (2015).
- [74] L. Leibler, M. Rubinstein, and R. H. Colby, *Dynamics of reversible networks*, Macromolecules **24**, 4701 (1991).
- [75] M. Müller, A. Dardin, U. Seidel, V. Balsamo, B. Iván, H. W. Spiess, and R. Stadler, *Junction dynamics in telechelic hydrogen bonded polyisobutylene networks*, Macromolecules **29**, 2577 (1996).
- [76] L. L. De Lucca Freitas and R. Stadler, *Thermoplastic elastomers by hydrogen bonding. 3. interrelations between molecular parameters and rheological properties*, Macromolecules **20**, 2478 (1987).
- [77] A. Grande, J. Bijleveld, S. J. Garcia, and S. van Der Zwaag, *A combined fracture mechanical–rheological study to separate the contributions of hydrogen bonds and disulphide linkages to the healing of poly (urea-urethane) networks*, Polymer **96**, 26 (2016).

2

Controlling healing and toughness in polyurethanes by branch-mediated tube dilation

Only critics can eradicate materialism, fatalism, atheism, fanaticism and superstition which constitute a threat for all.

Immanuel Kant

This chapter has been published as is

V. Montano, M.M.B. Wempe, S.M.H. Does, J.B. Bijleveld, S. van der Zwaag, S.J. Garcia, *Macromolecules* **52**, 21 (2019)

Abstract

In this work we propose the use of regular branching of polyurethanes as a way to regulate chain dynamics and govern crystallization in highly dense hydrogen bonded systems. As a result, robust and healable polyurethanes can be obtained. To this end we synthesized a range of aliphatic propane diol derivatives with alkyl branches ranging from butyl ($C = 4$) to octadecanyl ($C = 18$). The series of brush polyurethanes was synthesized by polyaddition of the diols and hexamethylene diisocyanate. Polyurethanes with very short ($C < 4$) and very long ($C = 18$) brush lengths did not lead to any significant healing due to crystallization. An intermediate amorphous regime appears for polymers with middle branch lengths ($C = 4$ to $C = 8$) showing a fine control of material toughness. For these systems the side chain length regulates tube dilation and significant macroscopic healing of cut samples was observed and studied in detail using melt rheology and tensile testing. Despite the high healing degrees observed immediately after repair it was found that samples with medium to long length brushes lost their interfacial strength at the healed site after being exposed to the healing temperature for some time after the optimal time to reach full healing. Dedicated testing suggests that annealed samples, while keeping initial tackiness, are not able to completely heal the cut surface. Such a behavior can be attributed to annealing-induced interfacial crystallization promoted by the aliphatic branches in the polymer bulk. Interestingly, no such loss of healing due to annealing was observed for samples synthesized with $C = 4$ and $C = 7$ diols, which is identified as the optimal healing regime. These results point at the positive effect of branching on healing, provided a critical chain length is not surpassed, as well as the need to study healing behavior long after the optimal healing times.

2.1. Introduction

Intrinsic healable polymers, similarly to biological systems, are able to sustain multiple healing events caused by physical damages even at the same location. For this reason these systems are an attractive alternative to the damage prevention approach as a solution to obtain structures with extended lifetime while addressing the critical concerns related to raw material overconsumption and high maintenance costs [1–3].

The macromolecular design of intrinsic healable polymers relies on the presence of both permanent and dynamic bonds. The permanent bonds control the mechanical properties while the dynamic bonds enable the reconstruction of crack interfaces brought in intimate contact and recovery of mechanical integrity. Crosslinking by dynamic covalent bonds [4–8] or the use of hybrid dual networks [9] have been reported as efficient ways to produce healable polymers with engineering-relevant mechanical properties. However heating to relatively high temperatures ($> 70\text{ }^{\circ}\text{C}$) is required to trigger local mobility [10–12]. On the other hand many systems showing near room temperature healing have been created by embedding non-covalent dynamic blocks (e.g. hydrogen bonds [13, 14], host-guest interactions [15, 16], multiple Van der Waals interactions [17, 18]) in low molecular weight polymers. However, these healable polymers and hydrogels are relatively soft with undesirably low toughness and ultimate tensile strength values, strongly limiting their applicability range in engineering applications. One strategy to increase mechanical properties is the increase of the main chain molecular weight leading to entanglements that determine high material robustness. Yet, at near room temperature, chain interdiffusion that leads to randomization at crack site is too sluggish to occur on a reasonable timescale and a poor healing efficiency is obtained [19]. Alternatively when a polymer is designed with a high density of non-covalent dynamic units very brittle and oriented materials are obtained [20]. While this approach has been shown to be successful for the production of new generation liquid crystals [21] and micro-segregated materials [22], these systems do not show any healing ability since annealing-induced crystallization and clustering hinder chain interdiffusion at mild temperature. Sufficiently fast and sufficiently complete self-healing of cracks and scratches at temperatures close to room temperature and high mechanical properties seem mutually exclusive and new strategies involving modification of polymer architectures must be explored [23].

To address this issue different strategies were employed. Guan et al. [24] introduced sacrificial noncovalent bonds to increase the mechanical properties of self-healing thermosets. Yanigisawa et al. [25] reported polymers readily healable at room temperature and with high mechanical properties by including dense and non-directional thiourea hydrogen bonding units in the main chain. Soon thereafter we reported the synthesis of strong and room-temperature healing polyimides based on primary and secondary non-covalent interactions and the fundamental role of short ($C=8$) fully aliphatic branches in regulating chain dynamics [26]. Inspired by this finding, in the present study we investigate the role of the branch length on the relaxation dynamics and crystallization kinetics of polyurethanes with a high density of hydrogen bonding. To this end we synthesized a range of branched

polyurethanes with variable dangling aliphatic chain lengths from C=4 to C=18 on a short repeating unit, leading to high density of urethane units and branches. The series of brush polyurethanes was synthesized by polyaddition of branched diols with varying branch length and hexamethylene diisocyanate. A detailed calorimetry, XRD and rheology study clarified the effect of brush length on the aggregation state and relaxation dynamics, showing that physical properties can be finely adjusted by extending or reducing the lateral branches by few carbon units. Tensile testing was used to assess mechanical behavior and intrinsic self-healing properties. The control of polymer architecture by regular branching in highly hydrogen bonded systems results in a combination of decent mechanical properties (typical for polymers with a high spatial density of hydrogen bonds) and fast self-healing kinetics at near-room temperature. This is attributed to the plasticization effect of side branching and its hindering of H-bond induced crystallization. Moreover, we argue how critical annealing-induced crystallization upon long term exposure to ambient or near- T_g temperatures can be fatal for the healing of this polymer class when branch lengths are higher than C=7, an issue that has been un-addressed in previous studies on comparable systems [25].

2.2. Experimental Section

2.2.1. Materials

1-Bromobutane (99%), 1-bromooctane (99%), 1-bromononane (98%), 1-bromododecane (97%), 1-bromooctadecane (>97%), lithium aluminium hydride (LiAlH₃, pellets, 95%), sodium hydride (NaH, dispersion in mineral oil, 60%), diethyl malonate (99%), dibutyltin dilaurate (DBTL, 95%), dimethylformamide (DMF, anhydrous, 99.8%) were purchased from Sigma-Aldrich. Ethyl acetate (99%, technical), methanol (≥99.5%, technical) and chloroform (≥98%, technical), deuterated chloroform (D-Chloroform, 0.03% TMS) and deuterated dimethylsulfoxide (D-DMSO) were purchased from VWR Chemicals. Hexamethylene diisocyanate (HDI, ≥98%), 1,4-butanediol (BDO, ≥99%) were purchased from TCI Europe. Hydrochloric acid (37%) was purchased from Honeywell. Magnesium sulfate (dried, contains ca 1-2 mol water of hydration, ≥98%) was purchased from Alfa Aesar. All commercial chemicals were used as received. All reactions were carried out under nitrogen atmosphere. The synthesis of the diols and polymers showed high reproducibility.

2.2.2. Synthesis of branched diol monomers

Following the two-step synthesis process shown below for the case of the 2,2-dibutylpropane-1,3-diol (C4DA) six branched short-length diols with different dangling chain lengths were synthesized: 2,2-dibutylpropane-1,3-diol (C4DA), 2,2-diheptylpropane-1,3-diol (C7DA), 2,2-dioctylpropane-1,3-diol (C8DA), 2,2-dinonylpropane-1,3-diol (C9DA), 2,2-didodecylpropane-1,3-diol (C12DA), 2,2-dioctadecylpropane-1,3-diol (C18DA). As a non-branched reference commercial 1,4-butanediol (BDO) was used (HDI_BDO). The molecular structure of the synthesized diols is represented in **Figure 2.1** while **Table 2.1** shows their melting points and the nomenclature used along the text. ¹H-NMR and ¹³C-NMR spectra of all the

synthesized diols are available in Figure S1. Details about synthesis of all diols are available in the Supplementary Information.

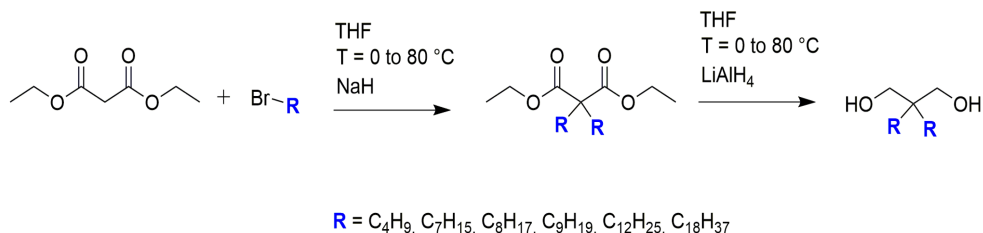


Figure 2.1: **Molecular structure of the synthesized branched diols.**

Step 1: Diethyl 2,2-dibutylmalonate (C4DE)

1-Bromobutane (59.7 g, 0.44 mol) was added to an ice-cooled and vigorously stirred suspension of sodium hydride (17.8 g, 0.45 mol) in anhydrous THF (400 ml). Subsequently, diethyl malonate (23.5 g, 0.15 mol) was added dropwise. The flask was heated to 80 °C and the reaction mixture was refluxed overnight. The solution was then quenched using demineralized water and 10% hydrochloric acid. The salt was then dissolved in excess of aqueous hydrochloric acid and the reaction mixture was extracted using diethyl ether and water. The resulting organic phase was washed three times in 150 mL demineralized water while the aqueous fraction was extracted twice in 100 mL of diethyl ether. The remaining organic layers were combined and dried over magnesium sulphate. The product was further dried at 60°C under vacuum overnight. The resulting crude diethyl 2,2-dibutylmalonate (C4DE) appeared as a yellowish oil (52.5 g, 0.19 mol, 66%) and was used without further purification.

Step 2: 2,2-Dibutylpropane-1,3-diol (C4DA)

52.5 g (0.19 mol) of the crude C4DE was added to a stirred and ice-cooled suspension of lithium aluminum hydride (12.4 g, 0.33 mol) in anhydrous THF (400 mL). The system was subsequently heated to 80 °C and left under vigorous stirring overnight. The resulting suspension was cooled using an acetone / liquid nitrogen bath and quenched with water. The salts were then dissolved in aqueous hydrochloric acid and the reaction mixture was extracted with diethyl ether and water. The organic phase was washed three times in 150 mL of demineralized water and the aqueous fraction was extracted twice using 100 mL of diethyl ether. The resulting organic layers were dried over magnesium sulphate and the solvents were evaporated in vacuo. The product was purified by column chromatography (silica gel 450 g, hexane and ethyl acetate). Pure C4DA was obtained as a white solid (24.3 g, 88%). The synthesis completion was checked with 1H -NMR ($CDCl_3$, 400 MHz)

Table 2.1: **Diols synthesized in this work.** The table includes the specific dangling chain length and melting point as measured by DSC.

Diol	Dangling chains length (# of carbons)	Melting point (°C)
BDO	0	n. a.
C4DA	4	43
C7DA	7	38
C8DA	8	29
C9DA	9	36
C12DA	12	44
C18DA	18	73

by the presence of the most relevant peaks: $^1\text{H-NMR}$ (CDCl_3 , 400 MHz) δ : 3.56 (s, 4H); 2.32 (s, 2H); 1.23 (m, 12H); 0.90 (t, 6H). $^{13}\text{C-NMR}$ (CDCl_3 , 400 MHz) δ : 69.50; 40.88; 30.50; 25.06; 23.60; 14.06.

2.2.3. Syntheses of the brush polyurethanes

Seven brush polyurethanes (**Figure 2.1**) were synthesized using a single-step polymerization process by reacting hexamethylene diisocyanate (HDI) with the seven diols C4DA, C7DA, C8DA, C9DA, C12DA, C18DA, BDO discussed in Section 2.2. The list and overall polymer properties of the resulting brush polymers is shown in **Table 2.2**.

As a mode of example, the synthesis of polymer HDI_C4DA is shown while details of the other synthesis are given in the SI. A solution of HDI (5.382 g, 32 mmol) in anhydrous THF (9 mL, 1/3 vol.) was added to a solution of C4DA (6.019 g, 32 mmol) in anhydrous THF (18 mL, 2/3 vol.) under vigorous stirring. Subsequently DBTL (2.02 g, 3.2 mmol) was injected in the system dropwise. The temperature was increased to 70 °C and the reaction proceeded for 24 hours. The solution was precipitated in methanol (200 mL) resulting in the separation of a viscous white solid. The solution was filtered, and the extracted precipitate was dissolved in 20 mL of chloroform and re-precipitated in methanol. The resulting viscous polymer was dried overnight at 60 °C in vacuo (7.38 g, 65%). The completion of the polyurethane synthesis was monitored by FT-IR analysis through the characteristic carbonyl stretching absorption peak at about 1170 cm^{-1} and the disappearance of isocyanate absorption peak at about 2270 cm^{-1} . $^1\text{H-NMR}$ confirmed the successful polyurethane synthesis through the presence of a singlet at about 5 ppm associated to amide bond protons.

$^1\text{H-NMR}$ (CDCl_3 , 400 MHz) δ : 4.9 (s, 2H); 3.85 (s, 4H); 3.10 (s, 4H); 1.46 (s, 8H), 1.22 (m, 12H), 0.86 (t, 6H).

$^{13}\text{C-NMR}$ (CDCl_3 , 400 MHz) δ : 156.69; 66.58; 40.76; 39.58; 30.89; 29.81; 29.21; 26.26; 24.75; 23.42; 14.04.

The FTIR and $^1\text{H-NMR}$ spectra of all the synthesized polymers can be found in Figure S2.

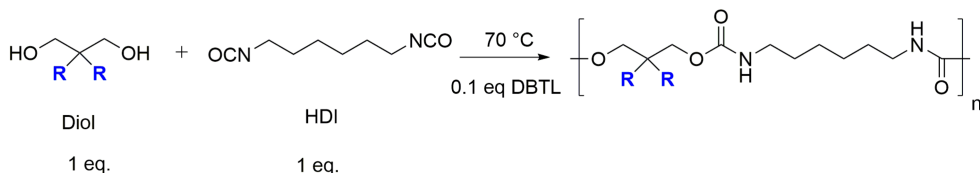


Figure 2.2: **Synthesis route followed for the preparation of the brush polyurethanes.**

2.2.4. Characterisation Methods

Infrared Spectroscopy

Attenuated total reflectance Fourier transform infrared spectroscopy was employed in order to follow reaction completion. Each infrared spectrum was recorded as an average of 8 scans in the wavenumber range $4000 - 500 \text{ cm}^{-1}$.

Proton and carbon nuclear magnetic resonance

$^1\text{H-NMR}$ and $^{13}\text{C-NMR}$ spectra were recorded using a Bruker WM-400 at 25°C using CDCl_3 and DMSO-d_6 as solvents.

Gel permeation chromatography

Molecular weight distributions of synthesized polymers were determined by gel permeation chromatography (GPC) equipped with refractive index detector and using polystyrene standards. The solvent used was tetrahydrofuran (THF) with a polymer concentration of 1 mg/mL .

Thermal Analysis

Thermal properties were determined by thermogravimetric analysis (TGA) and differential scanning calorimetry (DSC). TGA analyses were performed from room temperature to 400°C , under nitrogen atmosphere at 10°C/min heating rate using a Perkin Elmer TGA 4000. DSC measurements were performed under nitrogen at 10 and 20°C/min heating and cooling rates in the temperature range -50°C to 180°C using a Perkin Elmer Pyris Sapphire DSC. The glass transition temperature (T_g) was determined using the inflection point method.

Mechanical properties by tensile testing

Mechanical properties were assessed using an INSTRON Universal Testing machine. Dog-bone specimens were tested according to the ASTM D1708 standard, at a

cross-head speed of 80 mm/min. The average thickness of the specimens was $t=1.3\pm 0.1$ mm. The recovery of the mechanical properties after damage (healing) was determined by healing razor-blade cut dog-bone specimens. After cutting the dog-bone specimens into two parts at room temperature with a razor blade these were immediately brought back in contact under gentle hand-pressure for 10 seconds until they were able to withstand their own weights. Subsequently they were left to heal pressure-less at their individually selected healing temperatures in a circulating air furnace. The healing temperature was selected based on the rheological study and was established at 36 °C in order to maximize network mobility for all the systems in accordance to preliminary temperature sweep analyses. Healing was stopped when there was complete visual disappearance of the macroscopic damage (scar) this being observed after four days (for HDI_C4DA) and 3 hours (for HDI_C7DA and HDI_C8DA) of healing treatment. After healing, the samples were allowed to equilibrate at room temperature (near 20 °C) for 30 minutes prior to tensile testing. The pristine undamaged samples were tested after high temperature shape moulding (at $T = 110$ °C) followed by 30 minutes equilibration at room temperature. At least three samples were tested for each one of the polymers studied (HDI_C4DA, HDI_C7DA, HDI_C8DA) in their pristine and healed states.

Melt rheology

Oscillatory shear experiments were carried out on a strain-controlled Physica MCR 102 (Anton Paar GmbH) rheometer using a parallel plate geometry. The diameter of the plate was 8 mm and the sample thickness was set to 1 ± 0.2 mm. Temperature sweep analyses were carried out in the temperature range -20 °C to 100 °C using a heating rate of 2.8 °C/min. Isothermal frequency sweeps were performed in the range between $0.1 \leq f \leq 10$ Hz. Both temperature sweeps and isothermal frequency sweeps were performed within the linear viscoelastic regime of the tested polymers. Frequency mastercurves were shifted to the reference temperature $T_0 = 20$ °C. The shift factor a_T for the construction of the master curves follows with good approximation the William-Landel-Ferry (WLF) law [27] for HDI_C4DA, HDI_C7DA, HDI_C8DA, indicating rather simple thermo-rheological behaviour. For HDI_BDO, HDI_C9DA, HDI_C12DA, HDI_C18DA the shift factor severely deviated from WLF law, therefore no frequency mastercurve could be constructed.

X-Ray diffraction analysis

X-ray diffraction (XRD) spectra were recorded using a Rigaku MiniFlex 600 diffractometer depositing the materials on aluminum holders. The angle spans between $2\theta = 1^\circ$ to 60° with 0.1° increments, at room temperature. The samples were rotated during the measurement in an evacuated vacuum chamber.

2.3. Results and discussion

2.3.1. Effect of brush length on polyurethane microstructure and dynamics

The completion of the polyurethane reaction is confirmed by FTIR and NMR (**Figure 2.3** and Figure S2). The incorporation of two well-defined aliphatic brushes is confirmed by integrating the strong multiplet peak located at $\delta = 1.25$ ppm in the $^1\text{H-NMR}$ spectrum. The molecular weight distribution of the polymers is reported in **Table 2.2**. The average number (M_n) molecular weight values are in the range of 20 kDa, suggesting that these linear systems behave as non-entangled or lightly entangled linear polymers [27]. The molecular weight distribution for HDI_BDO and HDI_C18DA could not be determined since these polymers were insoluble in THF or NMP. M_n and M_w were found to increase with the brush length. Nevertheless, the result is most likely an artefact of GPC analysis which is based on size exclusion. In this case it is more appropriate to use as internal standard the number average degree of polymerization $X_n = M_n/M_0$, where M_0 is the molecular weight of the repeating unit [28, 29]. Following this criteria it appears that the degree of polymerization is just marginally affected by the brush length. Although the presence of side reactions leading to cyclisation and reduction of polydispersity cannot be fully excluded, we attribute the narrow polydispersity ($\mathcal{D} < 2$) to the suspension of low-molecular weight oligomers in the precipitation solvent (methanol). This was confirmed by analyzing with GPC the solid residue left after centrifugation of the methanol suspensions.

Figure 2.4 relates the optically detectable aggregation state of the synthesized polyurethanes (before and after processing at 110 °C for 1 hour) to their DSC thermograms (second heating scan) as function of increasing brush length. All glass- and melt transition temperatures are reported in Table 2.2. Two distinct behaviors can be observed. While the two extremes (no brushes or very long brushes) show one clear crystalline peak, all other polymers appear as amorphous thermoplastics. A total absence of brushes (HDI_BDO) yields a very fine white powder with a high degree of crystallinity explained by the presence of a high density of hydrogen bonding in the main polyurethane chain. The DSC thermogram shows a high temperature melting peak (at 165 °C) preceded by an endotherm shoulder. As reported elsewhere for linear polyurethanes derived from α,ω -diols [30], the two melting transitions can be attributed to the melting of folded chains and the melting of the extended main chain crystals given by directional hydrogen bonds among urethane linkages respectively. On the other extreme of the figure (highest branch length), sample HDI_C18DA appears as a fine powder that could be thermally processed into a brittle film. Similarly to HDI_BDO, the DSC shows the appearance of a melting peak, yet at lower temperatures (45 °C). This peak can be attributed to aliphatic side chain (brushes) crystallisation as reported for aliphatic polymer chains [31, 32] and in alkyl side chains in comb-like polymers [33, 34]. Such strong interactions between the long 18-carbon aliphatic branches seems to

Table 2.2: **Physical properties of the synthesized polymers.** Effect of aliphatic dangling chain length on molecular weight distribution, glass transition and melting temperature measured by DSC and thermal stability measured by TGA.

Polymer	Brush length (# of C)	M_n kDa	M_w kDa	\bar{D} (-)	X_n (-)	DSC- T_g 10 - 20 °C min ⁻¹ (°C)	DSC- T_m 10 °C min ⁻¹ (°C)	TGA 2%w.l. (°C)
HDI_BDO	0	n.a.*	n.a.*	n.a.*	n.a.*	40 - 43	165	281
HDI_C4DA	4	14.6	20.0	1.3	41	29 - 31	n.a. \$\$	243
HDI_C7DA	7	21.6	29.0	1.3	49	23 - 26	n.a. \$\$	280
HDI_C8DA	8	24.5	30.1	1.2	52	24 - 27	n.a. \$\$	300
HDI_C9DA	9	15.6	21.3	1.3	32	19 - 27	n.a. \$\$	298
HDI_C12DA	12	20.5	34.0	1.6	35	30-n.a. ++	46	312
HDI_C18DA	18	n.a.*	n.a.*	n.a.*	n.a.*	n.a. ++	45	305

*HDI_BDO and HDI_C18DA were not soluble in the available GPC solvents.

\$\$HDI_C4DA, HDI_C7DA, HDI_C9DA, HDI_C9DA did not present melting peaks.

++HDI_C12DA and HDI_C18DA glass transitions overlapped to melting transitions.

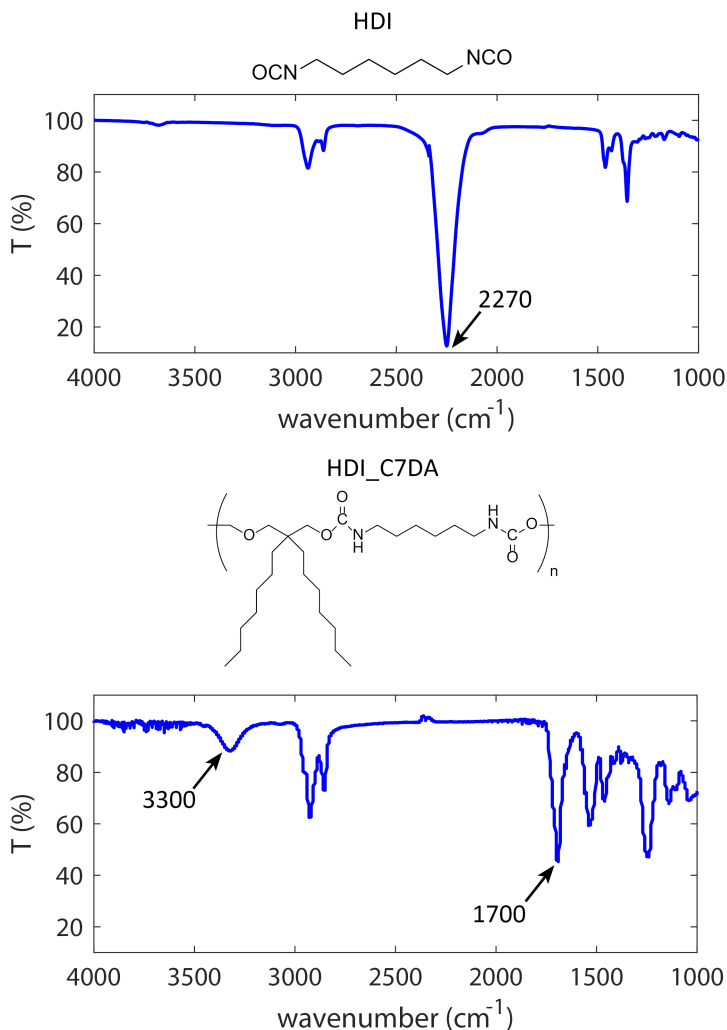


Figure 2.3: **IR spectra of diisocyanate monomer (HDI) and brush polyurethane (HDI_C7DA).** The figure highlights the monomer conversion through the disappearance of the characteristic isocyanate band at 2270 cm^{-1} , and the appearance of amide and carbonyl bands at 3300 cm^{-1} and 1700 cm^{-1} respectively.

prevent the formation of short range H-bonding between the urethane linkages as well as microphase segregation otherwise typical in segmented polyurethanes [35]. The presence of well-defined crystalline phases in HDI_BDO and HDI_C18DA is further supported by XRD spectra (Figure S3). The other four compositions leading to amorphous polymers (C=4, C=7, C=8, C=9) show a slight decrease of the glass transition temperature with the chain length increase (from about $30\text{ }^\circ\text{C}$ for C=4 to $24\pm 1\text{ }^\circ\text{C}$ for C=7 and C=9). In agreement with previous studies on comb poly-

mers with variable branch length, such a decrease in T_g can be attributed to a local plasticization effect until long branches promote local crystallization (detectable already for HDI_C12DA) [36, 37]. Interestingly, these findings are in opposition to those reported by Gerstl et al. [38] who showed the absence of internal plasticization for a series of Poly(alkylene Oxide)s (PAOs) with different side chain lengths. Considering the similarities in terms of side chain length between our PUs and the reported PAOs, the differences in side chain induced plasticization behavior can be attributed to profound differences in main backbone chemical structure (e.g. absence of urethane groups and presence of ether groups in the case of PAOs), and a higher branch spacing and branches per branch point in the case of our PUs. HDI_C12DA shows re-crystallization at cooling rate of 10 °C/min with a melt endotherm at about 45 °C. By increasing the cooling rate to 20 °C/min re-crystallization is partially avoided and a glass transition onset is observed just before a small endotherm peak at about 55 °C in the second heating step. We argue that, when slow cooling is applied (10 °C/min), the flexibility of the fully aliphatic main backbone combined to the plasticization effect due to the long brushes allows macromolecular reorganization towards the most favorable thermodynamic microstructure: a semicrystalline phase of stacked aliphatic side chains. Relevantly, the measured T_m of HDI_C12DA (46 °C) coincides with the melt temperature observed for HDI_C18DA (45 °C) as an additional confirmation that in this system crystallisation is due to side chain stacking. Table 2.2 shows the onset degradation temperature at 2% weight loss. All the polymers show a high temperature stability and a degradation onset between 200 and 300 °C, in agreement with previous reports on linear polyurethanes obtained by polymerisation of linear diols and linear diisocyanates [30, 39]. Thermal stability increases with the brush length. This trend is attributed to the higher thermal screening that long and dense side chains offer to thermally sensitive urethane linkages [40]. In this sense the higher thermal stability of HDI_BDO when compared to HDI_C4DA seems to be an exception. We argue that the improved thermal stability of HDI_BDO is due to the very high degree of hydrogen bonding and main chain crystallinity, favored by absence of lateral brushes. Minimal weight loss (< 0.5 wt%) is observed at temperature lower than 200 °C for all the polymers, indicating that no solvents (DMF, methanol) or unreacted monomers are entrapped at the end of the polymerisation procedure.

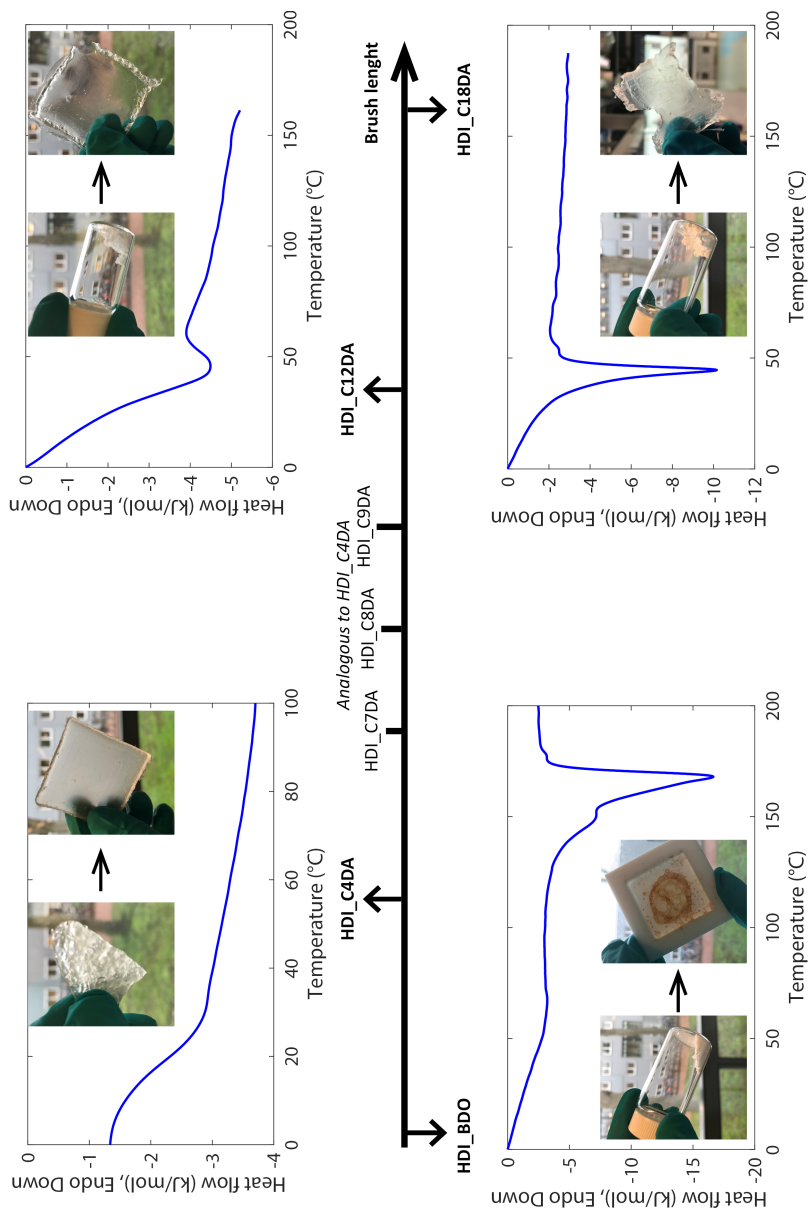


Figure 2.4: **Effect of brush length on the aggregation state and melt/glass transition temperature as analyzed using DSC (second heating scan was used).** In order to obtain homogenous films the polymers were processed at 110 °C. The camera snaps captured the polymer before and after processing. In absence and for very long brush lengths (BDO and C18DA) semicrystalline and brittle polymers were synthesized and no homogeneous films could be obtained. Intermediate brush lengths (C4DA, C7DA, C8DA, C9DA) led to amorphous and ductile polymers that could be processed as homogeneous films for mechanical testing. Long brushes (C12DA) also led to a semicrystalline polymer that could be processed into an homogeneous but brittle film.

Exemplary stress-strain curves of the amorphous and semi-crystalline brush PUs are reported in **Figure 2.5**. HDI_BDO and HDI_C18DA could not be processed and tested due to their high crystallinity and brittleness. Young's modulus (E), yield stress (σ_y), ultimate tensile strength (σ_{UTS}) and strain at break (ε_{break}) values are reported in Table S1. When comparing HDI_C4DA, HDI_C7DA, HDI_C8DA and HDI_C9DA, it can be seen that longer brush lengths lead to a decreasing E and an increasing ε_{break} , in analogy to what has been reported for segmented polyurethanes with decreasing hard segment content [41]. The abrupt increase of ε_{break} and reduction of σ_{UTS} observed in HDI_C9DA is highly reproducible. HDI_C12DA does not follow the same trend and shows the highest E and σ_y among the analysed polymers. We attribute this exceptional mechanical behavior to its crystallinity formed during cooling as previously discussed.

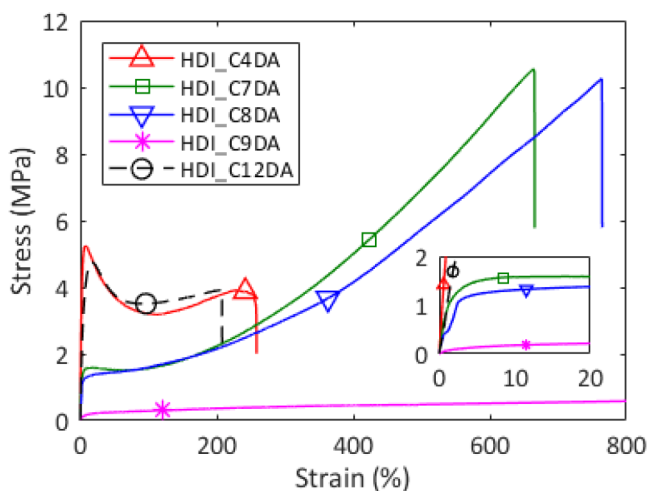


Figure 2.5: **Stress-strain curves at 80 mm/min and 21 °C of HDI_C4DA, HDI_C7DA and HDI_C8DA.** The tests were performed after high temperature shape moulding (at $T = 110$ °C) followed by 30 minutes equilibration at room temperature. The plot shows the effect of brush length on general tensile mechanical performances of amorphous brush polyurethanes. The inset highlights the difference in E and σ_y between HDI_C7DA and HDI_C8DA.

To better understand the role of regular branching on the dynamics of the polyurethanes their macromolecular dynamics was probed in the melt over a broad range of temperatures and frequencies using the well-known time-temperature superposition (TTS) principle. Although the applicability of the TTS principle is generally limited to fluids showing a thermorheologically simple behavior, its applicability and validity to polymers with a complex architecture and intermolecular interactions as self-healing polymers has recently been discussed in depth and applied to various polymeric systems [42–44].

The linear viscoelastic mastercurve of HDI_C8DA is shown in Figure 2.6A. Frequency isotherms are shifted to the reference temperature $T_0 = 20$ °C. The data are presented as elastic modulus (G') and viscous modulus (G'') as function of the angular frequency (ω). Moreover viscoelastic data are reported in the form of the tangent of

the phase angle ($\tan \delta = G''/G'$) which has been reported as being potentially more sensitive in distinguishing features of the relaxation modes associated to aliphatic branches [45–47]. By following the trend of $\tan \delta$ it can be easily inferred that the spectrum resembles the one of lightly entangled polymers where the partial restriction of mobility at $\omega_{cr} < \omega < \omega_\beta$ is attributed to the existence of varying physical interactions. Frequency mastercurves of HDI_C4DA and HDI_C7DA were constructed shifting the data at $T_0 = 20^\circ\text{C}$ showing analogous features (Figure S4). For HDI_C4DA, HDI_C7DA and HDI_C8DA polymers the trend of shift factor is well fitted by William-Landel-Ferry (WLF) law. Frequency mastercurves of HDI_BDO, HDI_C9DA, HDI_C12DA and HDI_C18DA are not presented since the shift factor trend severely diverged from WLF fit. This can be indication of multiple dynamic phenomena occurring in the same frequency range, as it will be discussed in detail further on.

The analysis of the values of the molecular weight between entanglements $M_e = (\rho RT_0)/G_N$ (as calculated for rubber elasticity where ρ is polymer density (assumed 1 kg/L for all the systems), R is the universal gas constant, T_0 is the shifting temperature and G_N is the plateau modulus as obtained from the van Gurp-Palmen plot [48, 49]) clarifies the origin of the physical interactions causing the partial restriction of dynamics at $\omega_{cr} < \omega < \omega_\beta$. For HDI_C4DA, HDI_C7DA and HDI_C8DA $M_e \cong 10.000$ g/mol (Figure 2.6B). For all these polymers the length of the brushes is lower than M_e (brush length ≈ 150 g/mol), therefore the brushes cannot entangle and cannot justify the high mobility restriction at intermediate frequency (in the region $\omega_{cr} < \omega < \omega_\beta$), in a similar fashion to what has been observed elsewhere for comb-polymers with short branches [44,45]. Moreover, the rather low molecular weight of these systems ($M_n \cong 20 \div 34$ kDa, Table 2.2) cannot lead to mobility restrictions at intermediate frequencies due to main chain entanglements as discussed by Doi and Edwards who showed that plateau modulus due to main chain entanglements sets for $M_w > 4 \cdot M_e$ and becomes pronounced for $M_w > 8 \cdot M_e$ [26] (represented as a dashed blue line in Figure 2.6B). Considering the absence of brush and main chain entanglements we attribute the temporary restriction of dynamics in the region $\omega_{cr} < \omega < \omega_\beta$ to the presence of a physical network consisting of hydrogen bond among urethane linkages, in line with the design of densely branched systems bearing effective supramolecular stickers. An additional prove of the presence of effective supramolecular interactions comes from the measure of G' and G'' slopes in the terminal relaxation region (for HDI_C8DA in Figure 2.6A, slope $G' = 1.5$, slope $G'' = 0.8$), which severely deviate from slopes of ideal Rousian dynamics (2 and 1) as previously reported in comparable branched healing polymers [26].

In Figure 2.6B we compare the frequency shift associated to the temporary mobility restriction ($\omega = \omega_{cr}$) of HDI_C4DA, HDI_C7DA and HDI_C8DA following the approach proposed by Kapnistos [45] for comb-like polymers bearing short aliphatic branches. ω_{cr} shift to higher frequencies for higher brush length. Since ω_{cr} determines the access to terminal relaxation, we can conclude that the higher the brush length the easier for the main chain to access terminal relaxation. The most likely explanation is that the aliphatic brushes act as solvent for the main chain (tube dilation), speeding up the main chain relaxation. The dilution effect is magnified

for higher brush length, as observed elsewhere for comb- polymers [45, 46]. Moreover, Figure 2.6B (triangle markers) shows that M_e appears unaffected by the brush length. This confirms the presence of a physical network between urethane linkages. The physical crosslinking distance is unchanged by increasing brush length since it is controlled by the length of the repeating unit (thereby the distance among urethane linkages).

In Figure 2.6B we highlight two regions in which time-temperature superposition was not applicable because the shift factor dependence on temperature severely deviated from the WLF law. For HDI_BDO (not containing any side chains) we argue that the dynamics are governed by main chain crystallisation driven by hydrogen bond among urethane units. For branch lengths higher than 8 (HDI_C9DA, HDI_C12DA, HDI_C18DA) the inapplicability of TTS is attributed to the existence of a concurrent dynamic process due to side chain interactions and stacking.

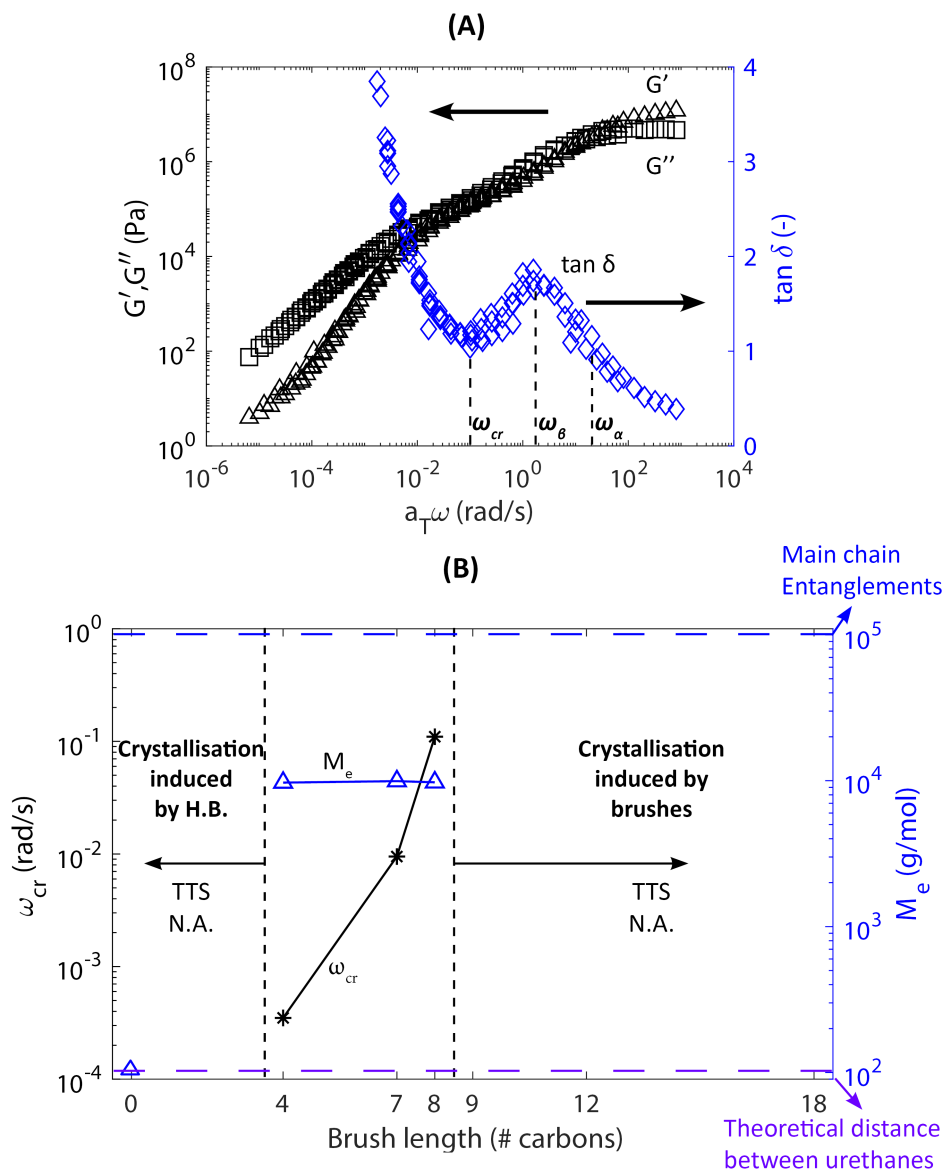


Figure 2.6: **Melt rheology of branched PU.** **(A)** Frequency sweep mastercurve shifted at $T_0 = 20$ °C of HDI_C8DA. **(B)** Effect of brush length on the critical angular frequency (ω_{cr}) corresponding to the minimum of $\tan \delta$ in the apparent plateau region (star markers). Effect of brush length on the molecular weight between entanglements (M_e) calculated by rubber elasticity theory (triangle markers). As effect of enhanced tube dilution ω_{cr} shifts to higher frequency increasing brush length while M_e is unchanged since the distance among urethane linkages is unvaried for all the polymers analysed. For brush length higher than 8, time-temperature superposition (TTS) principle was not applicable. In absence of brushes (HDI_BDO) TTS was not applicable. In both cases the dependence of the shift factor on temperature severely deviated from WLF law. Dashed lines points out the theoretical molecular weight between contiguous urethane units (dash purple line) and the theoretical main chain molecular weight corresponding to the occurrence of main chain entanglements (dash blue line).

Three idealized polymer architecture sketches are shown in **Figure 2.7**: a non-brushed highly crystalline PU (HDI_BDO), an amorphous brushed PU with effective hydrogen bonding among urethane blocks (HDI_C8DA), a densely brushed highly crystalline PU with stacked side aliphatic chains.

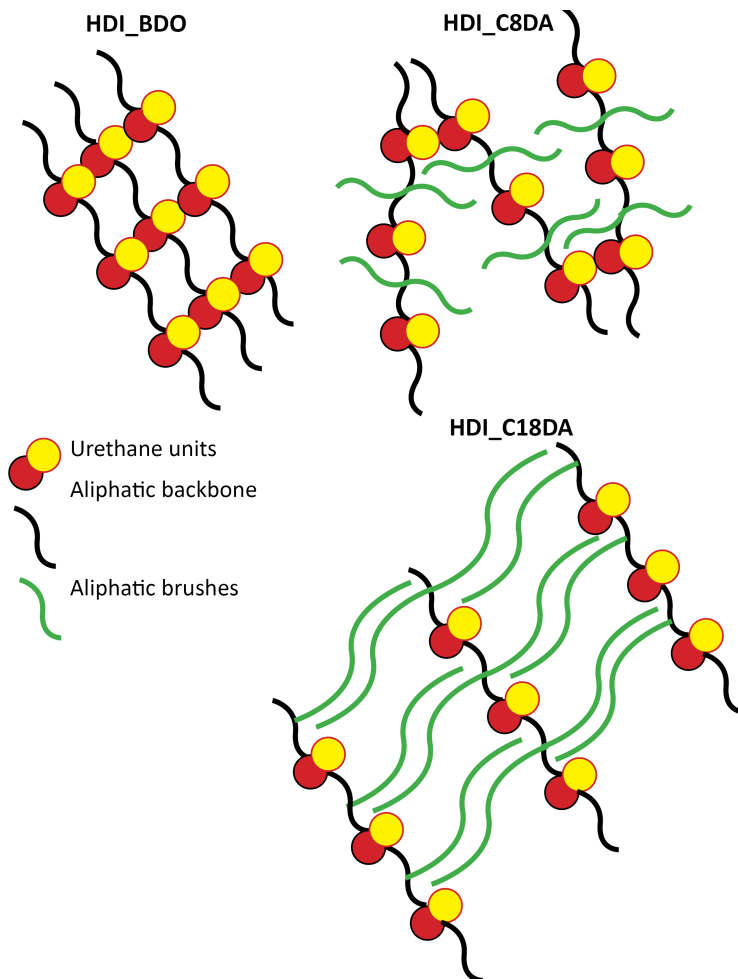
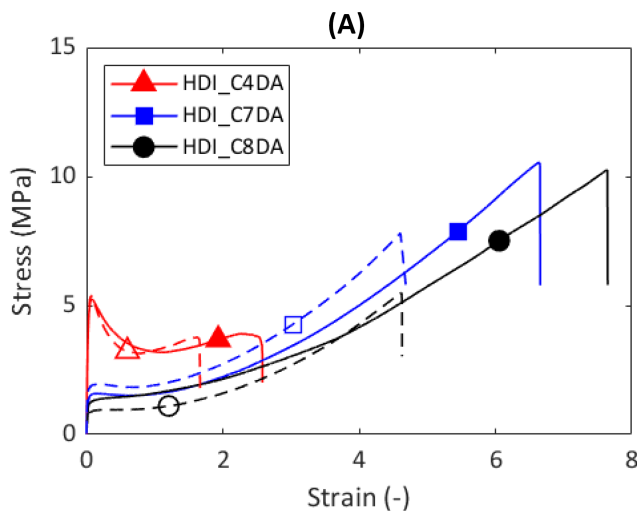


Figure 2.7: **Idealized sketches of macromolecular architecture of various brush polyurethane with different brush length.** In the figure we highlight the formation of well-defined crystalline phases in absence of aliphatic brushes and for very long brushes (C=18). For medium brush length (C=8) a glassy phase is formed with presence of a physical network among urethane linkages.

Melt rheology confirmed the presence of hydrogen bonding interactions among urethane units and the dilution effect operated by aliphatic side chain in amorphous brush polyurethanes. Consequently, we investigated the intrinsic self-healing property by tensile testing for all the systems for which a frequency mastercurve was correctly constructed.

Figure 2.8 shows the healing results of HDI_C4DA, HDI_C7DA and HDI_C8DA. The healing was performed at 36 °C, corresponding to $T_{healing} = T_{\max \tan \delta} + 5$ °C of HDI_C4DA, in order to maximize network mobility for all the systems investigated. Figure 2.8B effectively shows the complete recovery of the strength of the cracked interface at the end of the healing treatment for HDI_C4DA. From Figure 2.8A it is evident that both E and σ_y are fully recovered for all optimally healed systems. Final fracture took place elsewhere in the sample than at the healed original fracture plane.

By connecting macrorheology to tensile testing, the healing mechanism is identified as a three stage process in a similar fashion to what Susa et al. observed for a set of self-healing polyimides [18]. The first stage is governed by short range interactions such as interfacial multiple reforming hydrogen bonding interactions among urethane units at the fractured plane. The dynamics of the reversible bond is consistent with the intermediate range of bond lifetime previously reported for functional (and self-healing) supramolecular polymers [44, 50] (reversible bond lifetime $10 \text{ s} < \tau_{bond} < 100 \text{ s}$) as shown in Section 2.3.1. The second and third stage of healing ("interdiffusion" and "randomization") are then governed by sticky-Rouse reptation occurring at low frequency, at the ultimate crossover between storage and loss moduli (see Figure 2.6).



(B)

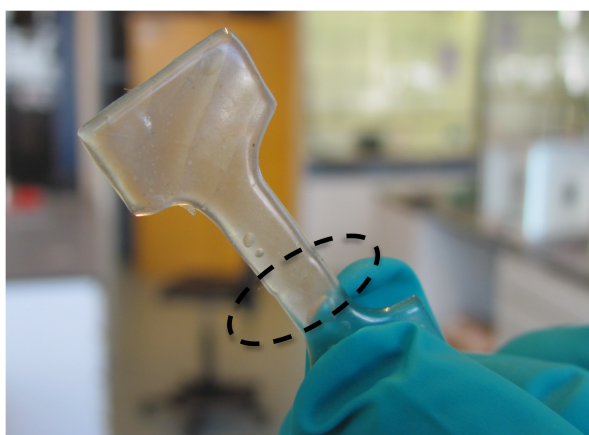


Figure 2.8: **Healing results of branched polyurethanes.** (A) Stress-strain curves of various healing brush polyurethanes tested at 80 mm/min and 21 °C. Pristine samples are reported as continuous lines, healed samples are reported as dash lines. HDI_C4DA was healed for 100 hours at 36 °C. HDI_C8DA and HDI_C7DA were healed for 3 hours at 36 °C. The plot shows recovery of Young's modulus and yield stress. (B) Photo capture of HDI_C4DA after healing for 100 hours days at 36 °C. The black circle highlights the position of the original fracture plane.

The effect of the brush length on the healing kinetics is readily observed by comparing the mechanical characteristic of HDI_C4DA to HDI_C7DA and HDI_C8DA in Figure 2.8A and are summarized in Table 2.3 where healing efficiency (H.E.) is quantified as $H.E. = \frac{\varepsilon_{break\ healed}}{\varepsilon_{break\ pristine}} * 100$. At equal healing temperature ($T_{healing} = 36$ °C) HDI_C8DA and HDI_C7DA show comparable healing efficiency to HDI_C4DA (from 60 to 70 % recovery of pristine strain at break), yet in much shorter time (3 hours versus 100 hours). All samples showed fracture far from the original fracture plane. The result is in line with observations drawn in the macro-rheology study that

Table 2.3: **Macroscopic intrinsic self-healing data of amorphous brush polyurethane systems.** Healing process was stopped when healed interface was not visible.

Polymer	Healing time at $T_{healing} = 36\text{ }^{\circ}\text{C}$ (hours)	H.E.* (%)	Broke in a different spot compared to original fracture plane
HDI_C4DA	100	64	Yes
HDI_C7DA	3	69	Yes
HDI_C8DA	3	61	Yes

*Healing efficiency was quantified as $\text{H.E.} = \frac{\epsilon_{break\ healed}}{\epsilon_{break\ pristine}} * 100$

pointed at an acceleration of the dynamics of the main chain (ω_{cr} shifts towards higher frequencies) with increasing brush length, justifying rapid randomization at crack site.

The amorphous brush polyurethanes showed high mechanical properties and rapid healing at near room temperature. However the novel polymer architecture endowed of short yet dense aliphatic branches may highly influence the kinetics of crystallization with consequences on the intrinsic healing of these brushed polyurethanes. We investigated these effects and discuss the outcomes in the next section.

2.3.2. Impact of induced crystallization on the healing behavior

(Annealing-induced) crystallization is a potential threat for intrinsic healing polymers not commonly studied. Clustering and crystallisation hinder chain interdiffusion and cause interfacial embrittlement preventing randomization at crack site thereby affecting the healing process. The issue becomes particularly crucial for systems with a high density of non-covalent interactions since they are more prone to form ordered phases. It has been reported that polyurethanes undergo morphology reorganisation and phase transition when subjected to long term annealing [51–53]. Nevertheless, no report has shown this potential threat to the healing process in self-healing polymers and polyurethanes in particular. In order to explore the possible impact of annealing-induced crystallization in our healable branched polymers we performed a detailed annealing-crystallization analysis with a special focus on the polymers that appear amorphous when cooling from the melt state.

Figure 2.9 shows the effect of long term annealing at T_g on the mechanical properties of HDI_C7DA and HDI_C8DA. The analysis of *traces a-d* shows that, upon annealing for 170 hours at T_g ($= 27\text{ }^{\circ}\text{C}$), no substantial differences in the pristine mechanical properties and in healing efficiency are observed for HDI_C7DA. We argue that, in the observed timescale, annealing does not lead to any microstructural evolution for HDI_C7DA.

On the other hand, the evolution of the mechanical properties of HDI_C8DA reflects

its dynamic character at T_g . *Traces e and f* show the pristine and healed mechanical properties of fresh (moulded and equilibrated) samples. From these we infer that optimal healing is obtained when healing fresh HDI_C8DA at $T = 36^\circ\text{C}$ for 3 hours. *Trace h* shows that, in contrast to what was observed for HDI_C7DA, the pristine mechanical property of HDI_C8DA are highly affected by annealing procedure at T_g (170 hours at 21°C). Toughness and strength increased while strain at break was reduced indicating annealing induced crystallisation. DSC analysis performed on a sample having received this 170 hours annealing procedure confirmed the transition from a purely amorphous network ($T_g = 21^\circ\text{C}$ before annealing) to a semicrystalline network ($T_m = 49^\circ\text{C}$). The newly found melting temperature nicely matches the melting temperature probed for HDI_C18DA ($T_m = 45^\circ\text{C}$). Therefore we attributed the induced crystallinity to the stacking of the aliphatic brushes.

The semicrystalline HDI_C8DA was healed at $T = 36^\circ\text{C}$ (well below the newly found T_m) to study the potential effect of crystallinity on intrinsic healing. The mechanical results upon healing are reported as *trace j* in Figure 2.9, while **Figure 2.10** shows snapshots of the crack evolution at different healing times and corresponding DSC traces. The resulting mechanical healing efficiency dropped drastically (H.E. $\approx 30\%$) when compared to that of a fresh specimen, but interestingly the broken sample still showed tackiness and 2D interface recovery, even at a healing temperature that was well below the bulk melting temperature. This behavior can be attributed to local plasticization at the newly created free surface, which allows local network mobility well-below bulk melting temperature [54, 55]. On the other hand, the complete suppression of long range dynamics (due to bulk crystallisation) explains the persistence of the original damage scar and the low healing efficiency even when an extended healing time of 120 hours was used.

Trace k addresses the effect of induced crystallisation if the sample is annealed further once optimal healing of a fresh sample is completed. To this purpose a fresh sample was cut, healed for 3 hours at $T = 36^\circ\text{C}$ and then annealed at T_g for 170 hours and tensile tested. The mechanical properties resemble the one of the semicrystalline sample (*trace h*) and good healing efficiency in terms of strain recovery (H.E. = 70 %). In this case both short and long range dynamics were accessed prior to bulk crystallisation justifying the high degree of healing in terms of strain. On the other hand, differently from fresh and healed samples (*traces e and f*), *trace k* samples broke at the original damage site and showed a significant reduction of yield stress compared to pristine sample. These effects are attributed to the loss of interfacial strength at healed site induced by crystallisation.

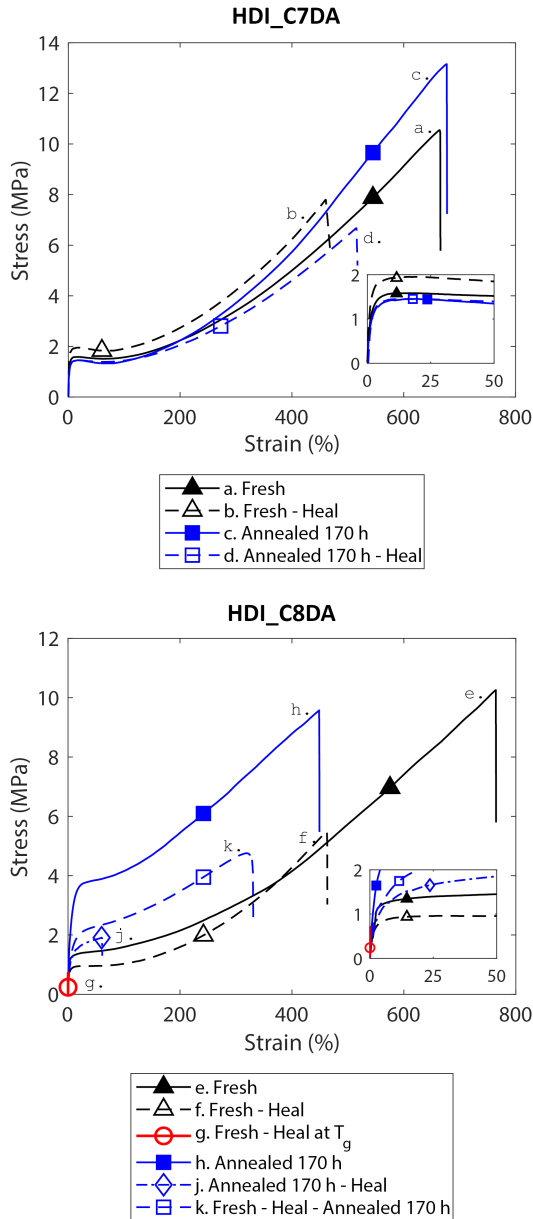


Figure 2.9: **Effect of induced crystallisation on mechanical and healing properties.** (a-d) HDI_C7DA mechanical tensile properties. No differences were observed in healing efficiency and mechanical properties upon long term (170 h) annealing at T_g . (e-k) HDI_C8DA mechanical tensile properties. Good healing efficiency was observed when healing fresh samples at $T = 36^\circ\text{C}$ (traces e, f). No recovery was observed when healing fresh samples at T_g (trace g), as effect of induced crystallisation. Increase of strength and drastic reduction of healing efficiency were observed upon long term (170 h) annealing at T_g and subsequent healing at $T = 36^\circ\text{C}$, as effect of induced crystallisation (traces h, j). Increase of strength and good healing efficiency were observed when subjecting fresh and healed samples to long term (170 h) annealing at T_g (trace k).

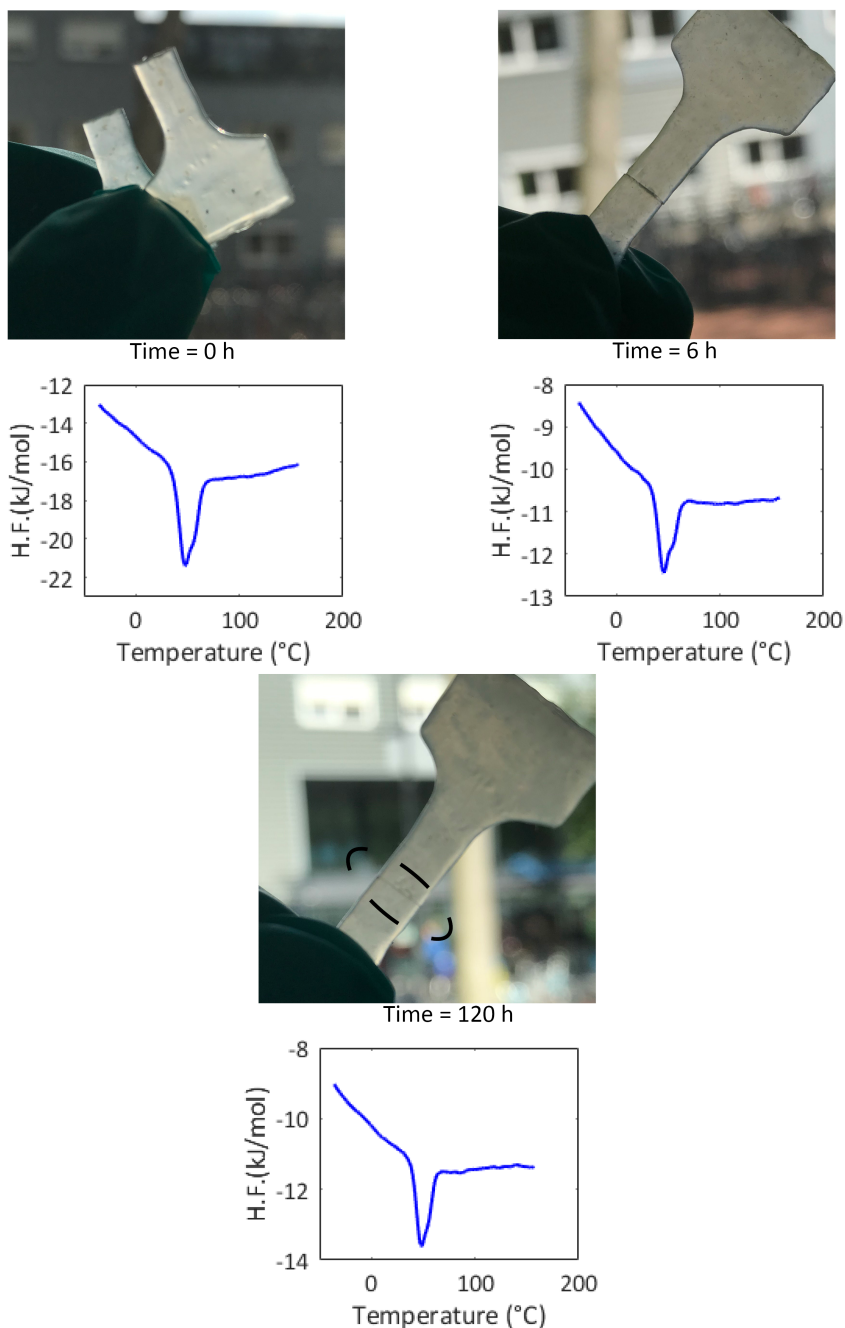
Semicrystalline HDI_C8DA healing at $T = 36\text{ }^{\circ}\text{C}$ 

Figure 2.10: **Healing of a semicrystalline polymer grade.** The photo captures show the progressive scar disappearance in semicrystalline HDI_C8DA when subjected to healing at $T = T_m - 10\text{ }^{\circ}\text{C} = 36\text{ }^{\circ}\text{C}$. The mechanical tensile property of the healed specimen corresponds to *trace j* of Figure 2.9. Time-resolved DSC analysis shows the persistence of crystalline phase throughout the healing process.

Since many healing systems report healing at close T_g one question was still open: what would happen if a fresh sample HDI_C8DA was healed for a long time at T_g ? The results of this healing test are reported as *trace g* in Figure 2.9. While showing tackiness (typical of initial network mobility), at the end of the healing procedure (170 hours at T_g) the healed sample suffered of embrittlement and immediately failed at the original damage site when tensile tested. This demonstrates that no healing is possible in such dynamic system where phase transition (from purely amorphous to semicrystalline) occurs at T_g .

Healing "reactivation" for semicrystalline HDI_C8DA was qualitatively proved by subjecting an annealed sample (170 hours at T_g) to healing temperature above melting ($T = T_m + 10\text{ }^\circ\text{C} = 60\text{ }^\circ\text{C}$). The results are reported in **Figure 2.11A**. The snapshots show that original damage was completely restored in very short timescale (healing time = 10 minutes). DSC analysis shows that amorphous state was restored upon exposure to $60\text{ }^\circ\text{C}$, indicating the reactivation of long range dynamics. An HDI_C18DA sample was healed in a similar fashion above melting ($T = T_m + 10\text{ }^\circ\text{C} = 55\text{ }^\circ\text{C}$). Even in this case rapid scar disappearance was observed (Figure 2.11B), but DSC analysis at the end of the healing procedure confirm that in this case bulk crystallinity is restored immediately after equilibration at room temperature.

The study evidenced the critical effect of annealing induced crystallisation on healing of HDI_C8DA as well as the apparent absence of crystallinity for HDI_C7DA in the observed timescale. Therefore we performed a dedicated study on the effect of brush length on the kinetics of crystallisation. To this purpose, DSC analyses were performed every 24 hours while keeping the polyurethanes at their individual annealing temperatures $T_{ann} = T_{\max \tan \delta} + 5\text{ }^\circ\text{C}$ chosen as such in order to maximize network mobility. Initially HDI_C4DA, HDI_C7DA, HDI_C8DA, HDI_C9DA did not show the presence of any melting peak. With increasing residence time at T_{ann} some systems progressively underwent phase transition and crystallisation, as evidenced by clear melting peaks in the DSC thermograms. **Table 2.4** reports the used annealing temperature (T_{ann}), the time corresponding to the end of the crystallisation process (t_{crys}), and the melting temperature of the crystalline phase (T_m). Analysing t_{crys} we note that the decrease of brush length from 12 to 4 carbons corresponds to a progressive delay of crystallisation kinetics. Crystallisation seems to be absent for the short brush length (HDI_C7DA and HDI_C4DA) since no melt peak was observed on a short timescale (170 hours) nor on a very long annealing timescales (1500 hours). Interestingly, all brush polyurethanes showing crystallisation upon annealing (HDI_C8DA, HDI_C9DA, HDI_C12DA) report melting temperatures in a common range, from 45 to $50\text{ }^\circ\text{C}$. These temperatures match well with the melting temperature of HDI_C18DA which was attributed to side chain stacking. Therefore we argue that crystallisation with annealing in fully aliphatic brush polyurethanes occurs by side chain stacking until a limiting side chain length ($C = 8$) below which brushes are too short to stack and nucleate crystals while they accelerate healing kinetics. This results highlight the crucial role of polymer architecture in the design of efficient and thermally stable healing systems with high density of reversible bonds.

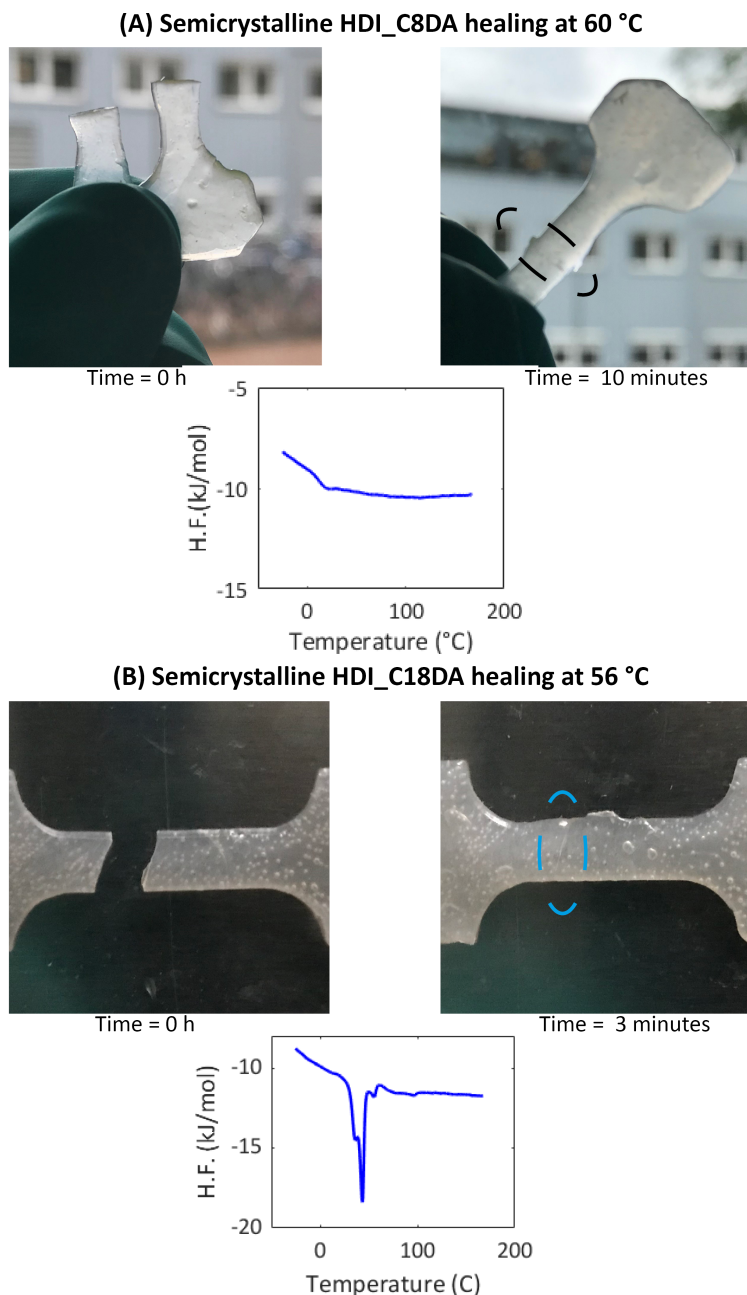


Figure 2.11: **Healing "reactivation" of a semicrystalline polymer grade.** **(A)** Photo captures showing fast scar disappearance and optimal healing for semi-crystalline HDI_C8DA upon healing at $T = T_m + 10\text{ °C} = 60\text{ °C}$. DSC trace shows the absence of any crystalline phase upon healing. **(B)** Photo captures showing fast scar disappearance and optimal healing for semi-crystalline HDI_C18DA when healed at $T = T_m + 10\text{ °C} = 56\text{ °C}$. DSC trace shows the reformation of a crystalline phase upon healing.

Table 2.4: **Crystallisation time of brush polyurethanes.** Note that kinetics slowed down when reducing the length of the brush. The crystallisation kinetics was eventually suppressed for HDI_C4DA and HDI_C7DA.

Polymer	Annealing temperature (°C)	Time for complete crystallisation [t_{crys}] (hours)	Melting temperature [T_m] (°C)
HDI_BDO	n.a.*	n.a.*	165
HDI_C4DA	36	n.a.**	n.a.**
HDI_C7DA	27	n.a.**	n.a.**
HDI_C8DA	21	170	49
HDI_C9DA	21	72	45
HDI_C12DA	21	24	46
HDI_C18DA	n.a.*	n.a.*	45

*HDI_BDO and HDI_C18DA are semicrystalline when cooling from the melt state.

**No crystallisation was observed for HDI_C4DA and HDI_C7DA when annealing for 1500 hours.

2.4. Conclusions

Regular branching is investigated in polyurethanes with high density of reversible bonds as the design strategy to exploit near room temperature intrinsic healing property in robust linear polymers. To this end we synthesized a series of brush polyurethanes by facile polymerisation of diols bearing branches with controlled length from C=4 to C=18 and a commercial di-isocyanate (HDI).

The length of the side aliphatic brush exerts a crucial role in regulating chain dynamics. By using melt rheology we verified effective hydrogen bonding interaction among urethane blocks results in a physical network. In the intermediate branch length regime the brushes, in analogy to comb- polymers with short side chains, act as a solvent, dilating the tube therefore speeding up main chain interdiffusion mediating macroscopic self-healing kinetics. At a critical brush length (C=9), and for all the higher brush lengths, the macromolecular glassy dynamics is totally suppressed by the occurrence of a crystalline phase of stacked side chains.

A detailed calorimetry study clarified the effect of brush length on annealing induced crystallisation. To this end, the polymer systems were subjected to long term annealing at the corresponding glass transition/healing temperature. A higher brush length speeds up the crystallisation kinetics. No crystallisation was observed for the brush polymers synthesized with a side chain length in the range between C=4 and C=7. The result highlights that this range of brush length is the most promising in order to obtain intrinsic healable polymers with a high extent of reversible bond interactions and hence mechanical robustness, yet avoiding side chain crystallization which would block the healing process. Interestingly, the polymers showing interfacial healing were the ones that met the WLF law leading to nicely overlapping segments in the final frequency master curve.

Relevantly we observed that, for crystallised samples, a local reactivation of mobility is still accessible at mild temperatures, below $T_{melting}$. This local mobility allows partial recovery of mechanical damage in reasonable timescale. Ultimately, total (bulk) reactivation of dynamics is observed upon healing for a very short time at temperatures above the melting temperature.

In conclusion we demonstrated that polymer architecture control involving regular branching and high density of reversible physical bonds can be an effective strategy to obtain near room temperature healable polymers with good mechanical properties, provided the side brush length is in the correct range. The approach leaves room for further optimization of both mechanical and healing properties through the control of the number of branching point per macromolecule and the use of multi-dentate reversible bond groups (e.g. urea groups).

2.5. Supporting Information

Synthesis of malonate molecules

Diethyl 2,2-diheptylmalonate (C7DE) The synthesis was performed using the same procedure described in Section 2.1. of the main manuscript. The following materials and quantities were used: 400 mL of anhydrous THF, 23.20 g (0.15 mol) of diethyl malonate, 79.80 g (0.45 mol) of 1-bromoheptane and 18.20 g of sodium hydride (0.46 mol, 60 wt% in mineral oil). The crude product (72.40 g) was used without further purification.

Diethyl 2,2-dioctylmalonate (C8DE) The synthesis was performed using the same procedure described in Section 2.1. of the main manuscript. The following materials and quantities were used: 400 mL of anhydrous THF, 16.04 g (0.10 mol) of diethyl malonate, 57.93 g (0.30 mol) of 1-bromooctane and 12.0 g of sodium hydride (0.30 mol, 60 wt% in mineral oil). The crude product (53.42 g) was used without further purification.

Diethyl 2,2-dinonylmalonate (C9DE) The synthesis was performed using the same procedure described in Section 2.1. of the main manuscript. The following materials and quantities were used: 400 mL of anhydrous THF, 16.88 g (0.11 mol) of diethyl malonate, 61.79 g (0.30 mol) of 1-bromononane and 12.0 g of sodium hydride (0.30 mol, 60 wt% in mineral oil). The crude product (45.04 g) was used without further purification.

Diethyl 2,2-didodecylmalonate (C12DE) The synthesis was performed using the same procedure described in Section 2.1. of the main manuscript. The following materials and quantities were used: 400 mL of anhydrous THF, 12.87 g (0.08 mol) of diethyl malonate, 62.28 g (0.25 mol) of 1-bromododecane and 9.86 g of sodium hydride (0.25 mol, 60 wt% in mineral oil). The crude product (50.4 g) was used without further purification.

Diethyl 2,2-dioctadecylmalonate (C18DE) The synthesis was performed using the same procedure described in Section 2.1. of the main manuscript. The following materials and quantities were used: 400 mL of anhydrous THF, 9.62 g (0.06 mol) of diethyl malonate, 62.46 g (0.19 mol) of 1-bromononane and 7.42 g of sodium

hydride (0.19 mol, 60 wt% in mineral oil). The crude product (45.04 g) was used without further purification.

Syntheses of diol monomers

2,2-Dioctylpropane-1,3-diol (C7DA) The synthesis was performed following the same procedure described in Section 2.2. of the main manuscript. The following materials and quantities were used: 400 mL of anhydrous THF, 49.50 g of crude C8DE and 16.30 g (0.26 mol) lithium aluminium hydride. Preliminary purification was carried out by column chromatography using 450 g of silica and pure hexane. The product final product was eluted by increasing the polarity of the eluent by mixing hexane and ethyl acetate (hexane:ethyl acetate, 7:3(v/v)). Yield = 74%.

$^1\text{H-NMR}$ (CDCl_3 , 400 MHz) δ : 3.50 (s, 4H); 3.20-3.13 (m, 2H); 1.31-1.15 (m, 24H), 0.89-0.82 (t, 6H). $^{13}\text{C-NMR}$ (CDCl_3 , 400 MHz) δ : 69.06; 40.89; 31.87; 30.67; 30.53; 29.25; 22.80; 14.05.

2,2-Dioctylpropane-1,3-diol (C8DA) The synthesis was performed following the same procedure described in Section 2.2. of the main manuscript. The following materials and quantities were used: 400 mL of anhydrous THF, 53.13 g of crude C8DE and 9.93 g (0.26 mol) lithium aluminium hydride. Preliminary purification was carried out by column chromatography using 450 g of silica and pure hexane. The product final product was eluted by increasing the polarity of the eluent by mixing hexane and ethyl acetate (hexane:ethyl acetate, 7:3(v/v)). Yield = 84%.

$^1\text{H-NMR}$ (CDCl_3 , 400 MHz) δ : 3.55 (s, 4H); 2.28 (s, 2H); 1.25 (m, 28H), 0.86 (t, 6H). $^{13}\text{C-NMR}$ (CDCl_3 , 400 MHz) δ : 69.41; 40.95; 31.86; 30.74; 30.65; 29.53; 22.82; 14.07.

2,2-Dinonylpropane-1,3-diol (C9DA) The synthesis was performed following the same procedure described in Section 2.2. of the main manuscript. The following materials and quantities were used: 400 mL of anhydrous THF, 39.10 g of crude C9DE and 11.96 g (0.32 mol) lithium aluminium hydride. Preliminary purification was carried out by column chromatography using 450 g of silica and pure hexane. The product final product was eluted by increasing the polarity of the eluent by mixing hexane and ethyl acetate (hexane:ethyl acetate, 9:1(v/v)). Yield = 75%.

$^1\text{H-NMR}$ (CDCl_3 , 400 MHz) δ : 3.55 (s, 4H); 2.25 (s, 2H); 1.25 (m, 32H), 0.87 (t, 6H). $^{13}\text{C-NMR}$ (CDCl_3 , 400 MHz) δ : 69.48; 40.98; 31.87; 29.60; 29.30; 22.83; 14.07.

2,2-Didodecylpropane-1,3-diol (C12DA) The synthesis was performed following the same procedure described in Section 2.2. of the main manuscript. The following materials and quantities were used: 400 mL of anhydrous THF, 43.67 g of crude C12DE and 11.84 g (0.32 mol) lithium aluminium hydride. Preliminary purification was carried out by column chromatography using 450 g of silica and pure hexane. The product final product was eluted by increasing the polarity of the eluent by mixing hexane and ethyl acetate (hexane:ethyl acetate, 9:1(v/v)). Yield = 77%.

$^1\text{H-NMR}$ (CDCl_3 , 400 MHz) δ : 3.53 (s, 4H); 2.70 (s, 2H); 1.24 (m, 44H), 0.86 (t, 6H). $^{13}\text{C-NMR}$ (CDCl_3 , 400 MHz) δ : 69.33; 40.93; 31.90; 29.68; 29.67; 22.82; 14.08.

2,2-Dioctadecylpropane-1,3-diol (C18DA) The synthesis was performed following the same procedure described in Section 2.2. of the main manuscript. The following materials and quantities were used: 400 mL of anhydrous THF, 47.77 g of crude C18DE and 11.62 g (0.31 mol) lithium aluminium hydride. Preliminary purification was carried out by column chromatography using 450 g of silica and pure hexane. The product final product was eluted by increasing the polarity of the eluent by mixing hexane and ethyl acetate (hexane:ethyl acetate, 9:1(v/v)). Yield = 91%. $^1\text{H-NMR}$ (CDCl_3 , 400 MHz) δ : 3.56 (s, 4H); 2.08 (s, 2H); 1.24 (m, 68H), 0.87 (t, 6H).

Syntheses of brush polyurethanes

HDI_C7DA The compound was synthesized following the procedure described in Section 2.3. The following materials and quantities were used in the synthesis: C7DA (6.0 g, 22.0 mmol) hexamethylene diisocyanate (3.70 g, 22.0 mmol), dibutyltin dilaurate (0.10 mL) and N,N-Dimethylformamide (36 mL). The compound appears as a transparent glassy polymer (yield = 9.7 g, 62%).

$^1\text{H-NMR}$ (CDCl_3 , 400 MHz) δ : 4.83 (s, 2H); 3.86 (m, 4H); 3.11 (m, 4H); 1.47 (m, 8H); 1.23 (m, 24H); 0.86 (t, 6H).

HDI_C8DA The compound was synthesized following the procedure described in Section 2.3. The following materials and quantities were used in the synthesis: C8DA (12.0 g, 40 mmol) hexamethylene diisocyanate (6.72 g, 40 mmol), dibutyltin dilaurate (0.15 mL) and N,N-Dimethylformamide (67 mL). The compound appears as a transparent glassy polymer (yield = 12.47 g, 65%).

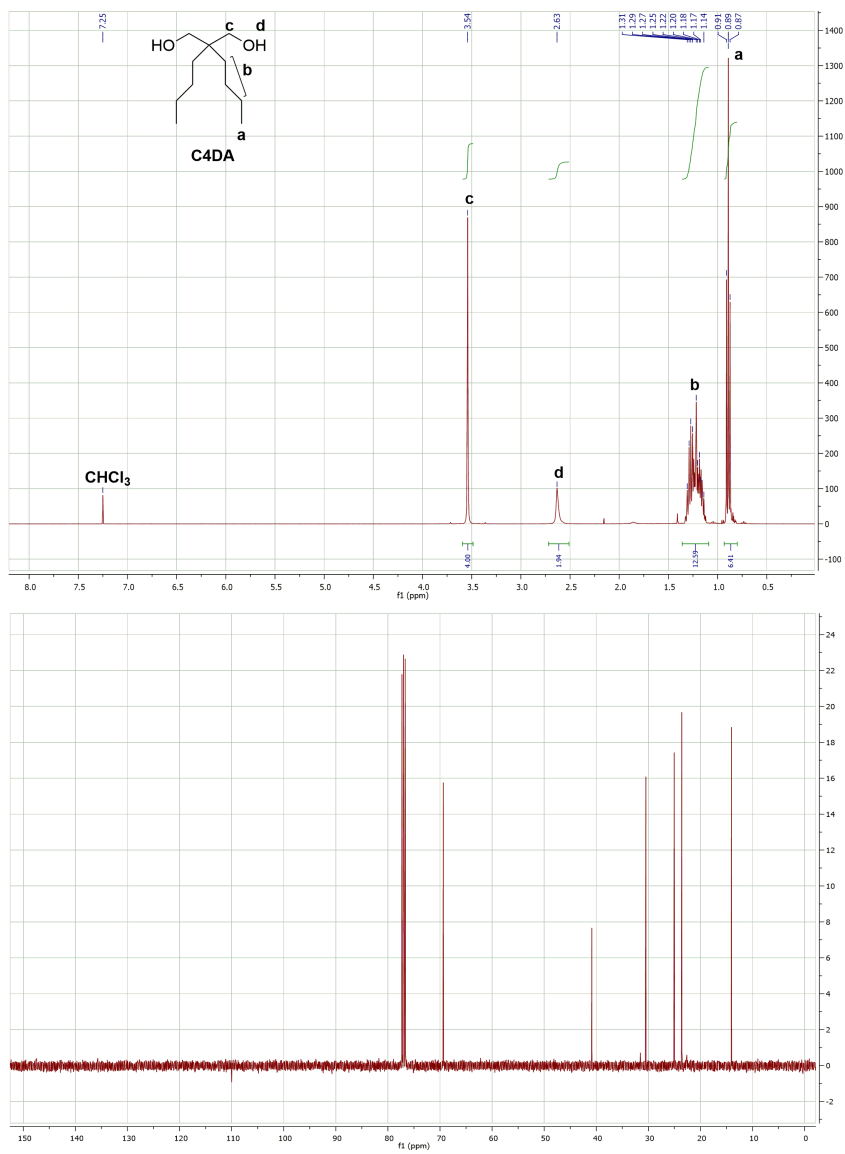
$^1\text{H-NMR}$ (CDCl_3 , 400 MHz) δ : 5.99-4.80 (s, 2H); 3.92-3.81 (m, 4H); 3.16-3.03 (m, 4H); 1.52-1.40 (m, 4H); 1.34-1.14 (m, 32H); 0.89-0.81 (t, 6H).

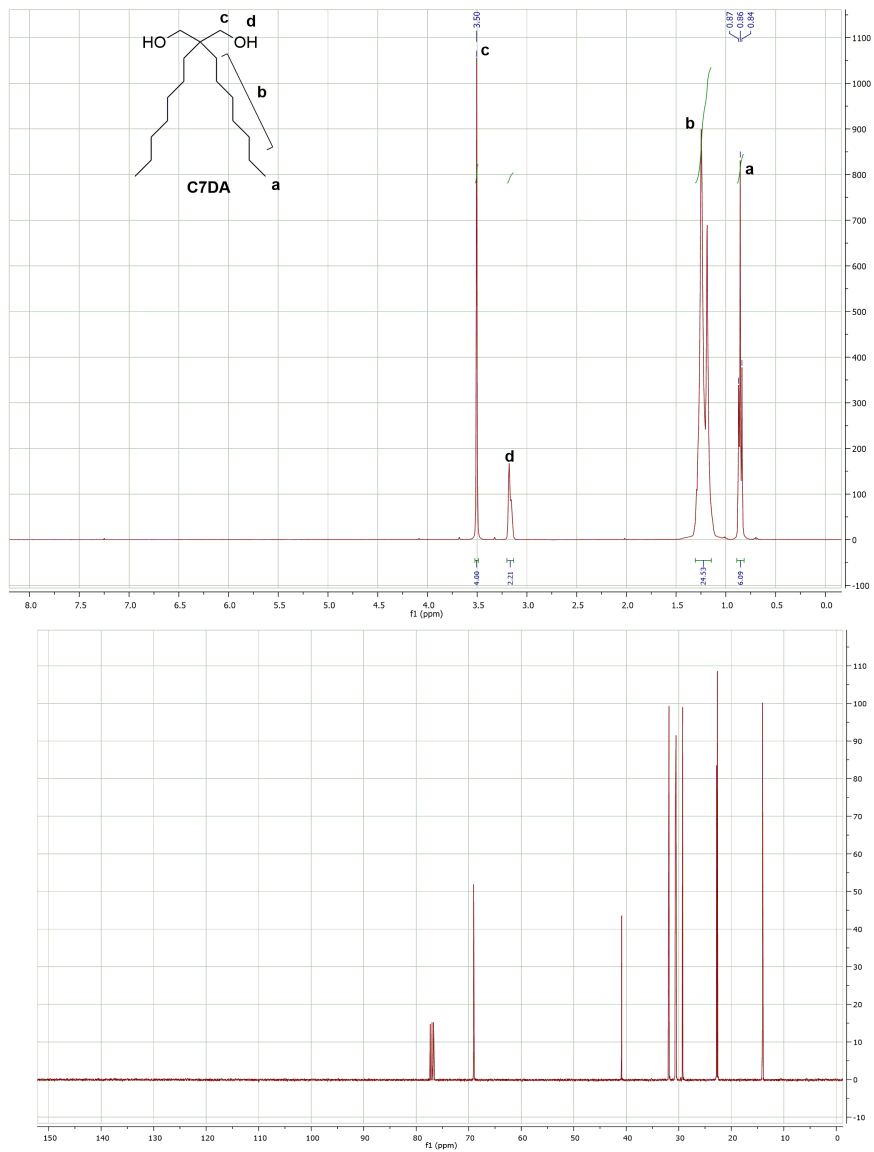
HDI_C12DA The compound was synthesized following the procedure described in Section 2.3. The following materials and quantities were used in the synthesis: C12DA (3.71 g, 9.02 mmol) hexamethylene diisocyanate (1.51 g, 9.02 mmol), dibutyltin dilaurate (0.15 mL) and N,N-Dimethylformamide (10.5 mL). The compound appears as a transparent glassy polymer (yield = 3.32 g, 63%).

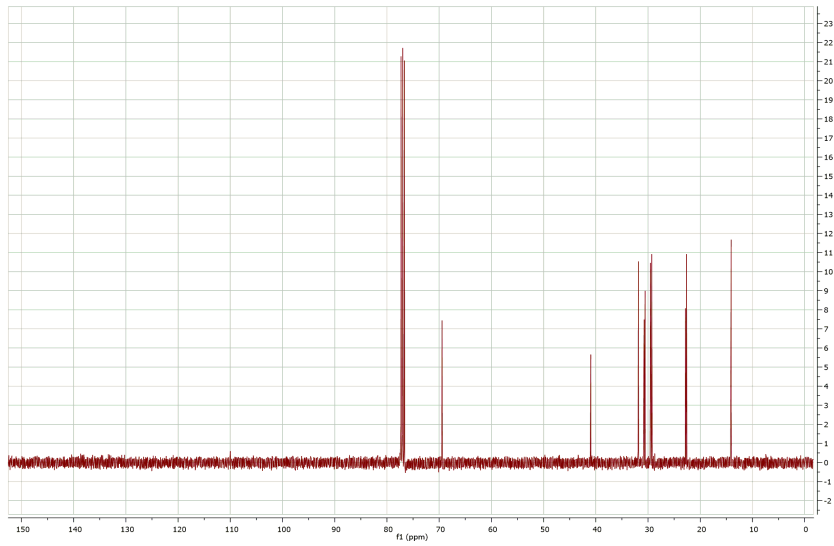
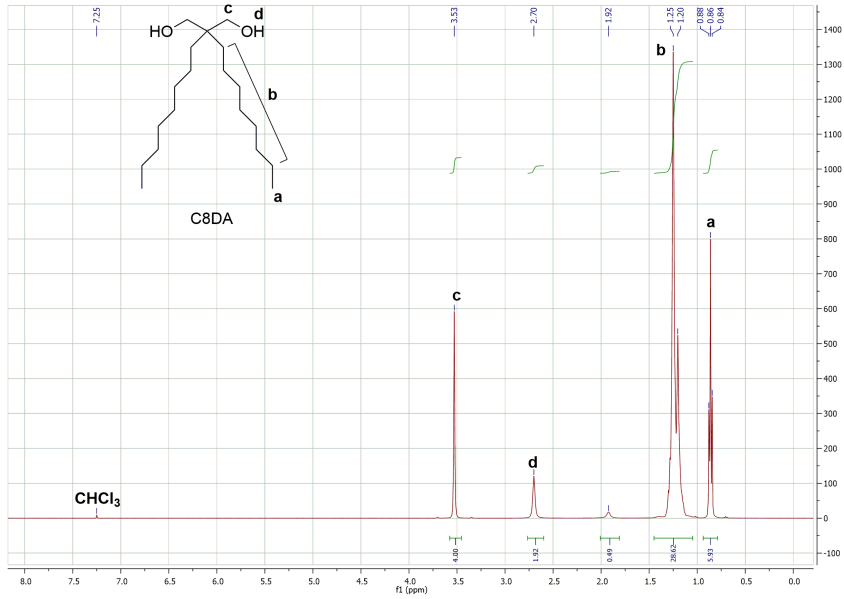
$^1\text{H-NMR}$ (CDCl_3 , 400 MHz) δ : 4.78 (s, 2H); 3.85 (m, 4H); 3.10 (m, 4H); 1.46 (m, 4H); 1.23 (m, 32H); 0.85 (t, 6H).

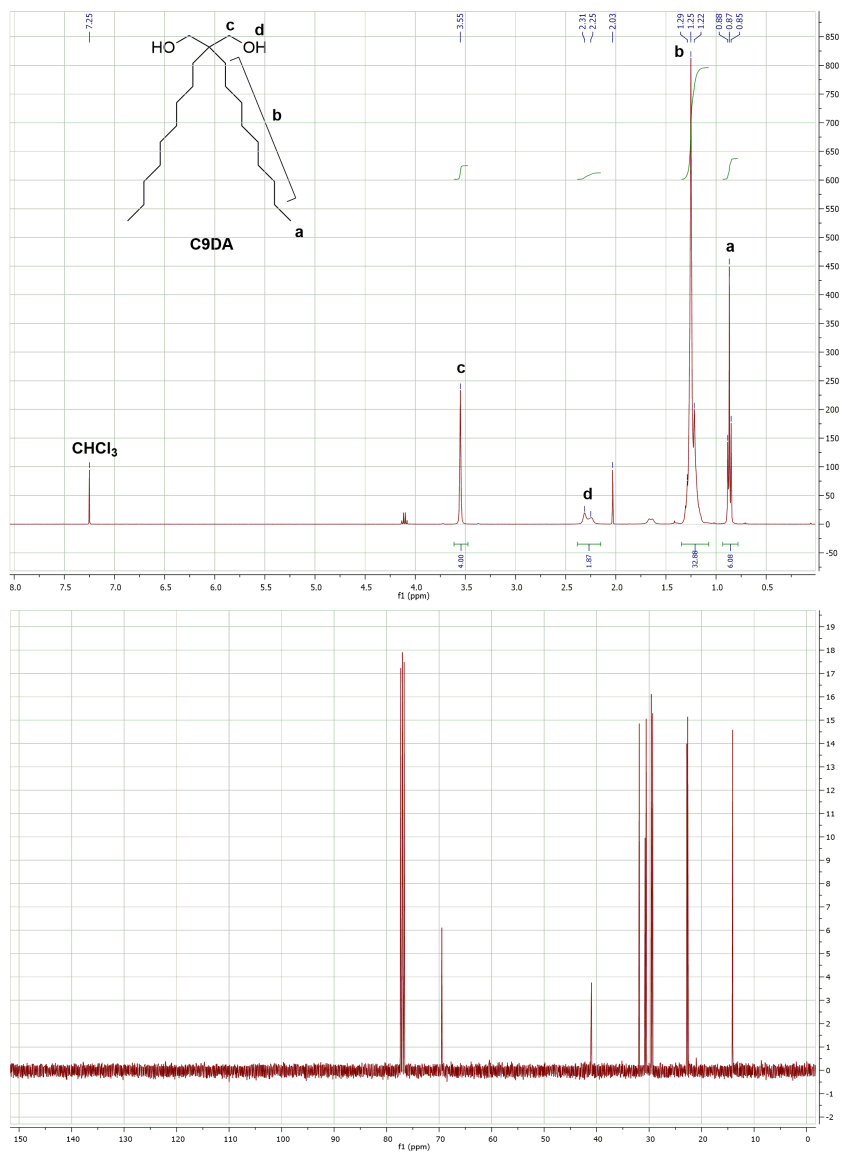
HDI_C18DA The compound was synthesized following the procedure described in Section 2.3. The following materials and quantities were used in the synthesis: C18DA (3.0 g, 5.17 mmol) hexamethylene diisocyanate (0.87 g, 5.17 mmol), dibutyltin dilaurate (0.12 mL) and N,N-Dimethylformamide (10.0 mL). The compound appears as a fine white powder (yield = 3.23 g, 83%).

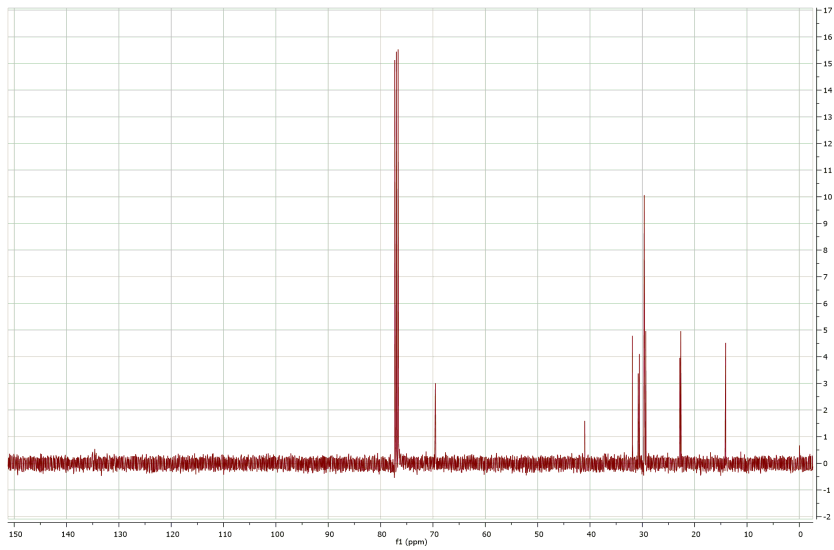
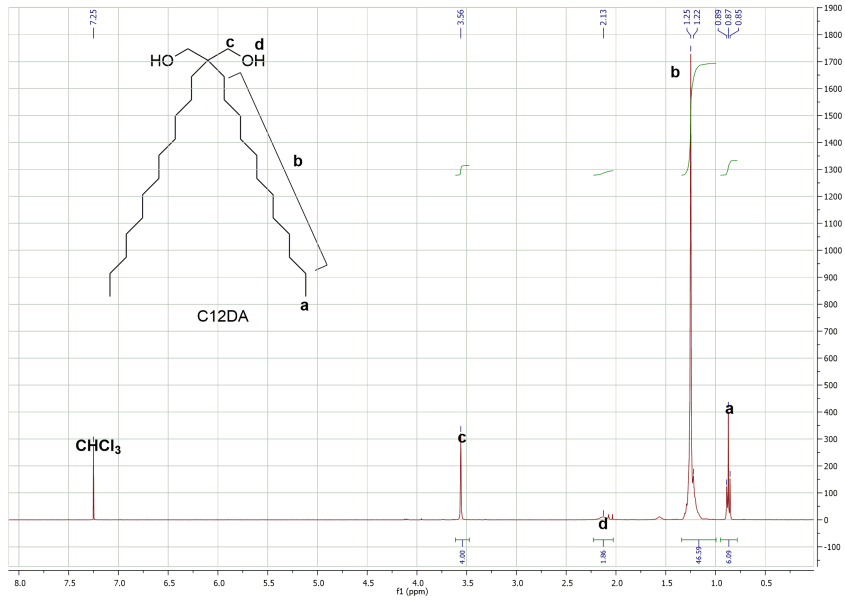
$^1\text{H-NMR}$ (CDCl_3 , 400 MHz) δ : 4.76 (s, 2H); 3.86 (m, 4H); 3.12 (m, 4H); 1.72 (m, 4H); 1.24 (t, 72H); 0.86 (t, 6H).

Figure S1. $^1\text{H-NMR}$ and $^{12}\text{C-NMR}$ spectra of synthesized diols









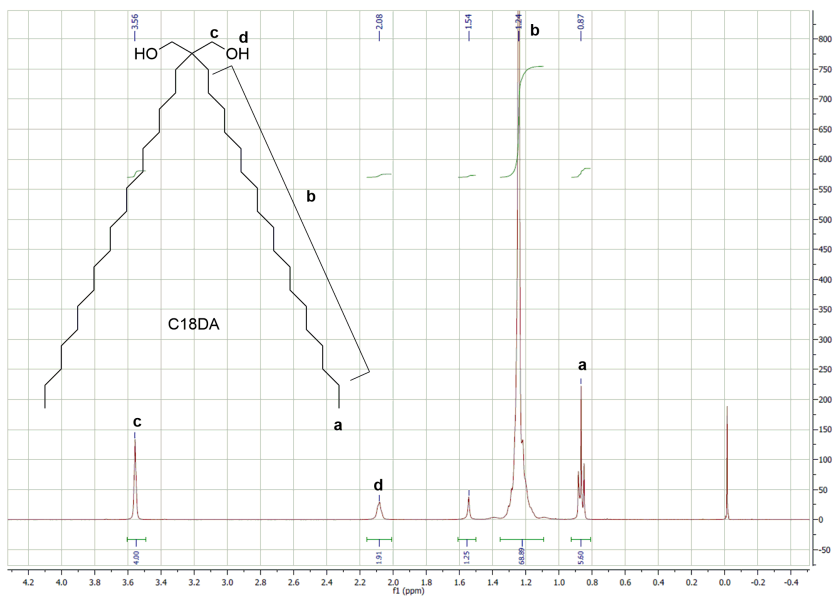
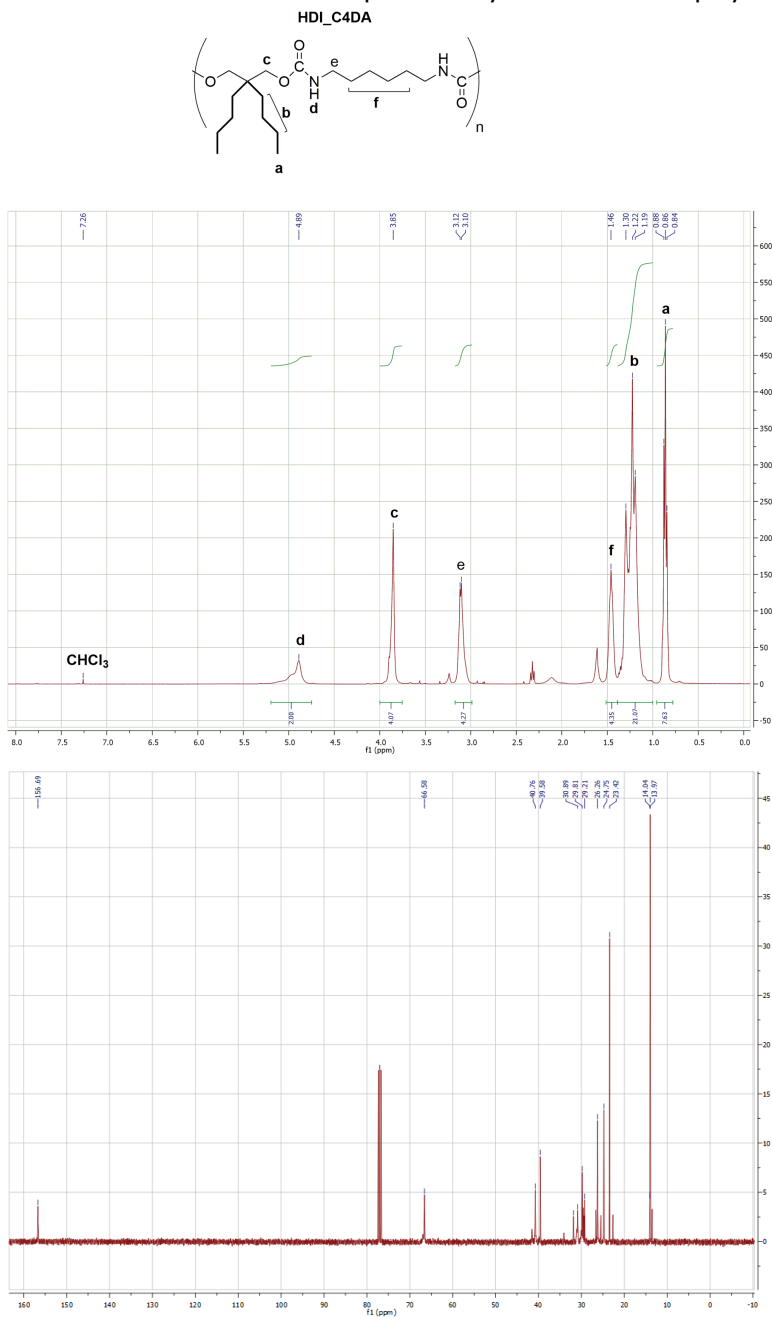
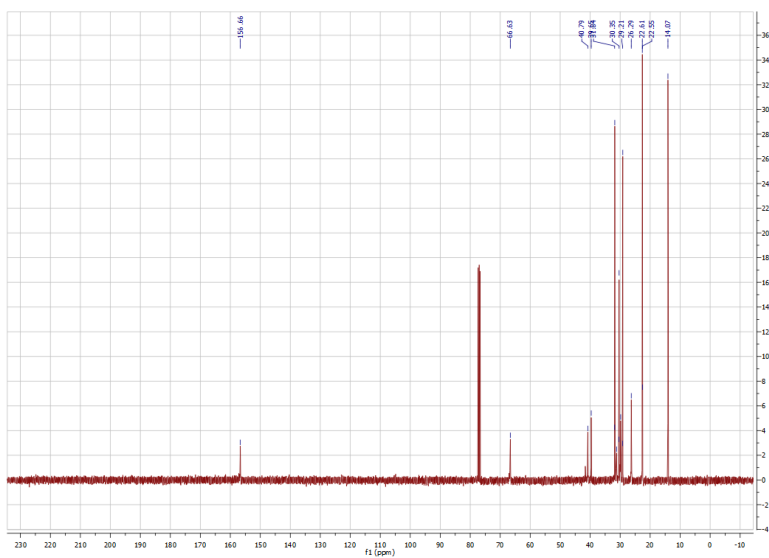
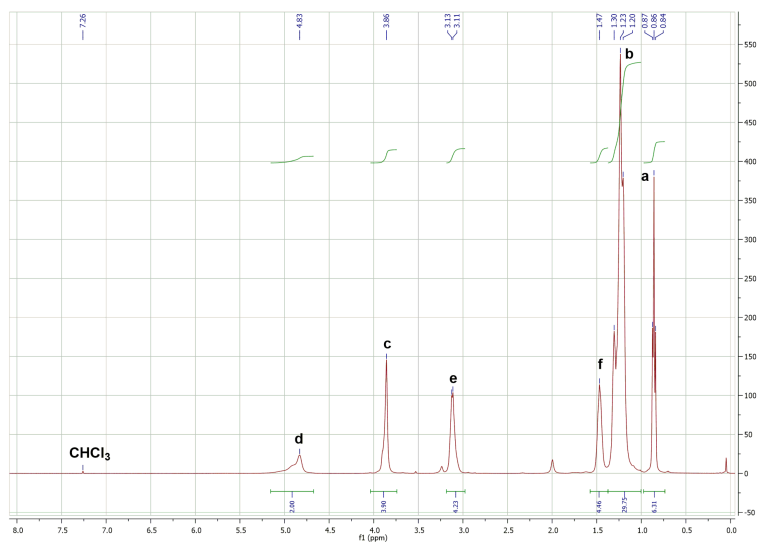
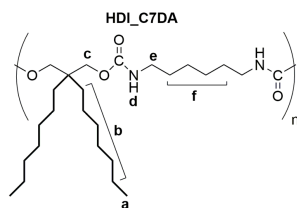
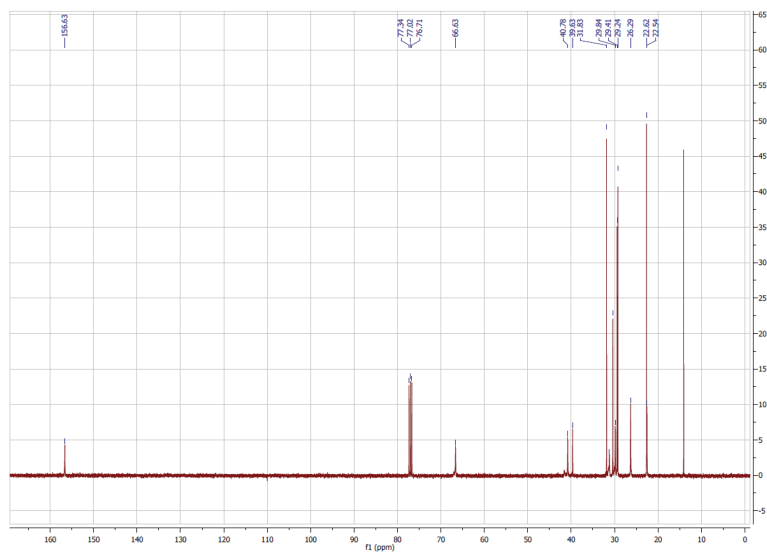
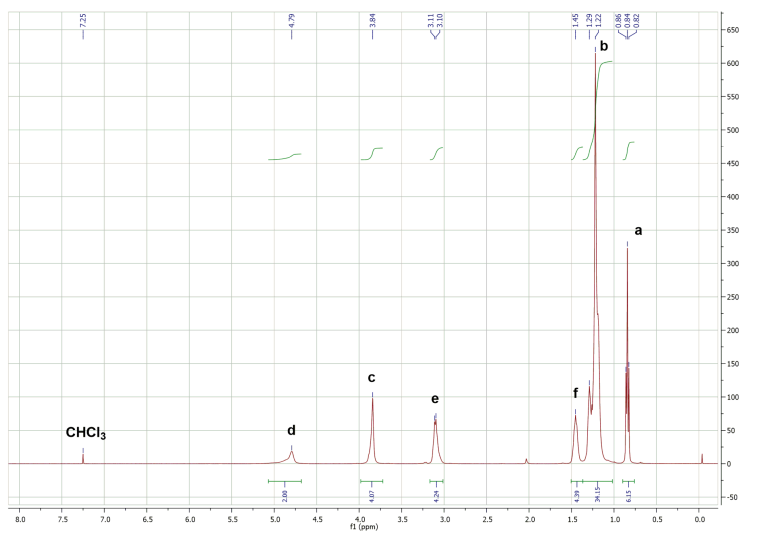
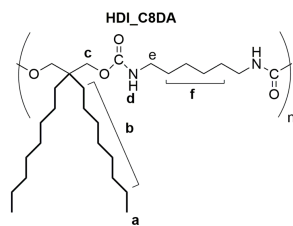
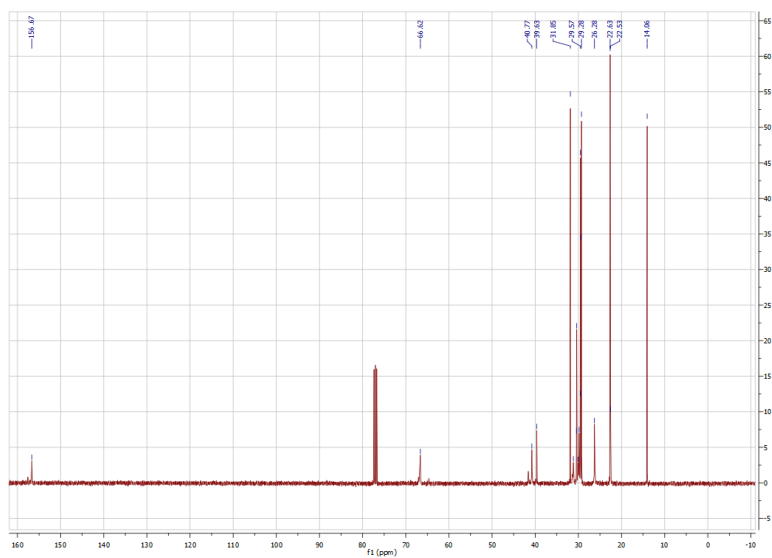
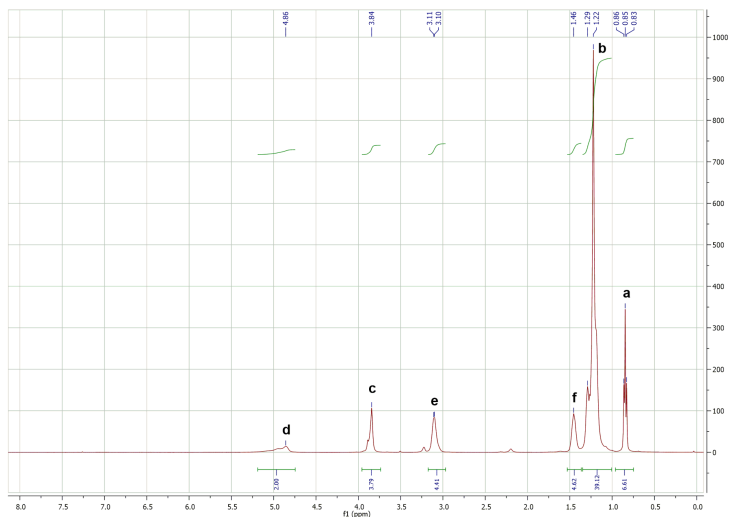
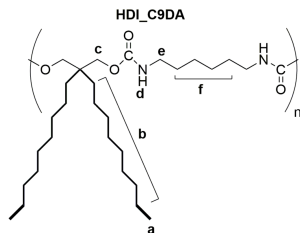


Figure S2. $^1\text{H-NMR}$ and $^{12}\text{C-NMR}$ spectra of synthesized brush polyurethanes







2

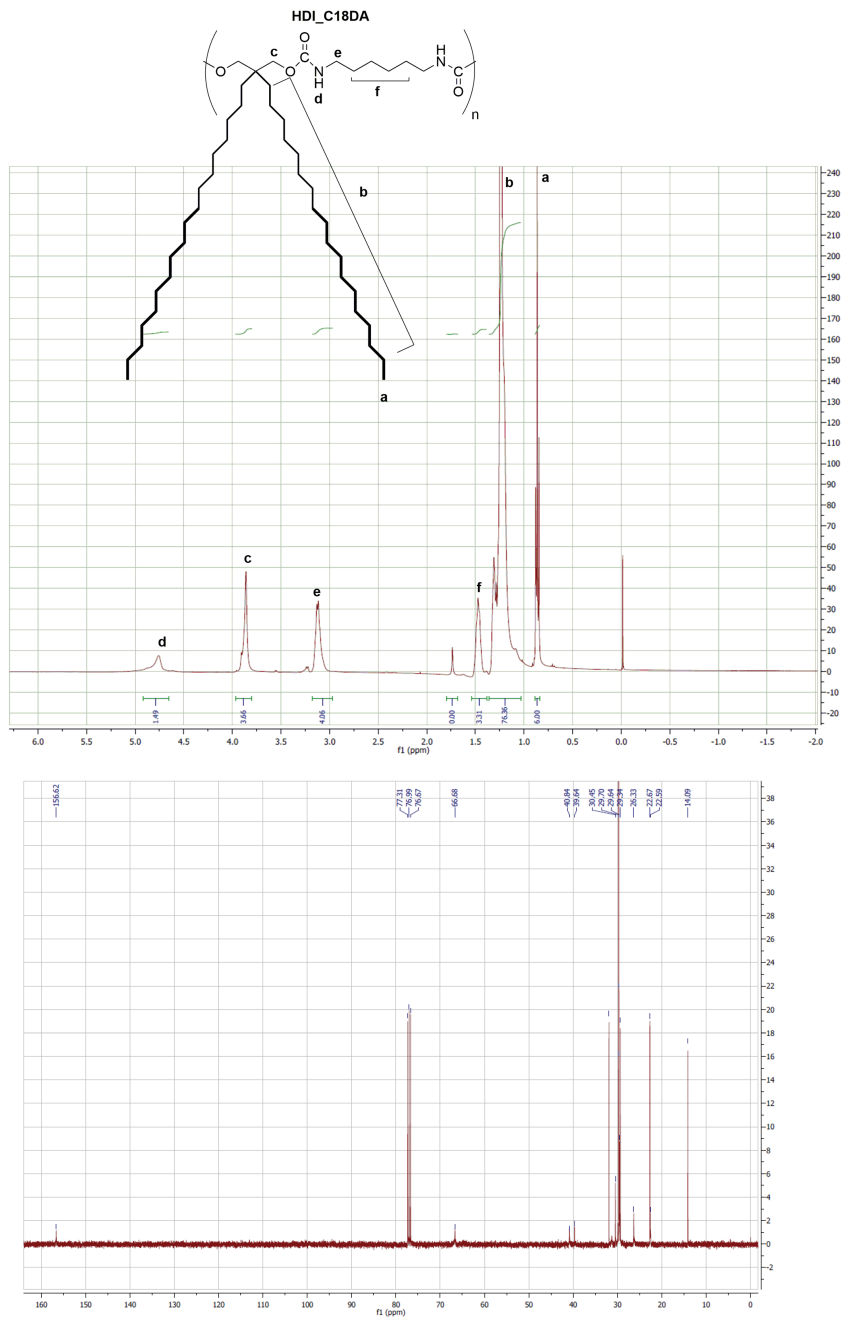


Figure S3. XRD spectra of HDI_BDO and HDI_C18DA.

HDI_BDO and HDI_C18DA are semicrystalline polymers when cooling from the melt. XRD spectra support the formation of high crystalline phase.

A. XRD Spectrum of HDI_BDO

B. XRD Spectrum of HDI_C18DA

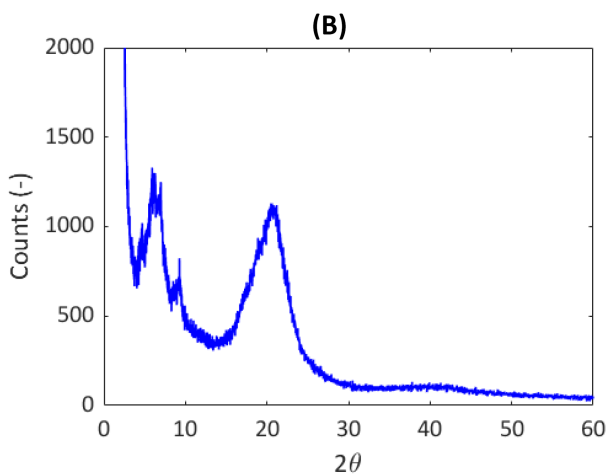
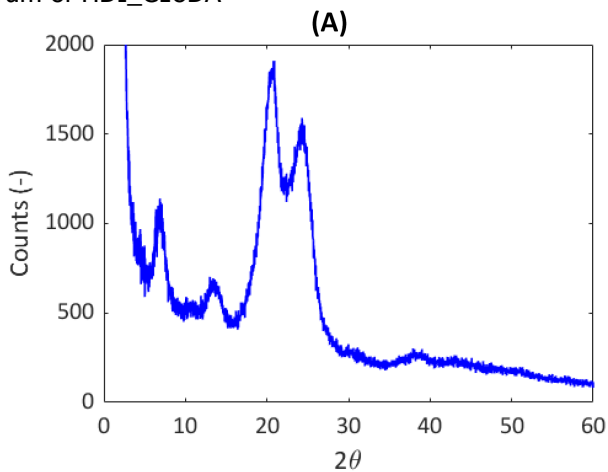


Figure S4. Frequency master-curves of HDI_C4DA (A) and HDI_C7DA (B) shifted at $T_0 = 20$ °C.

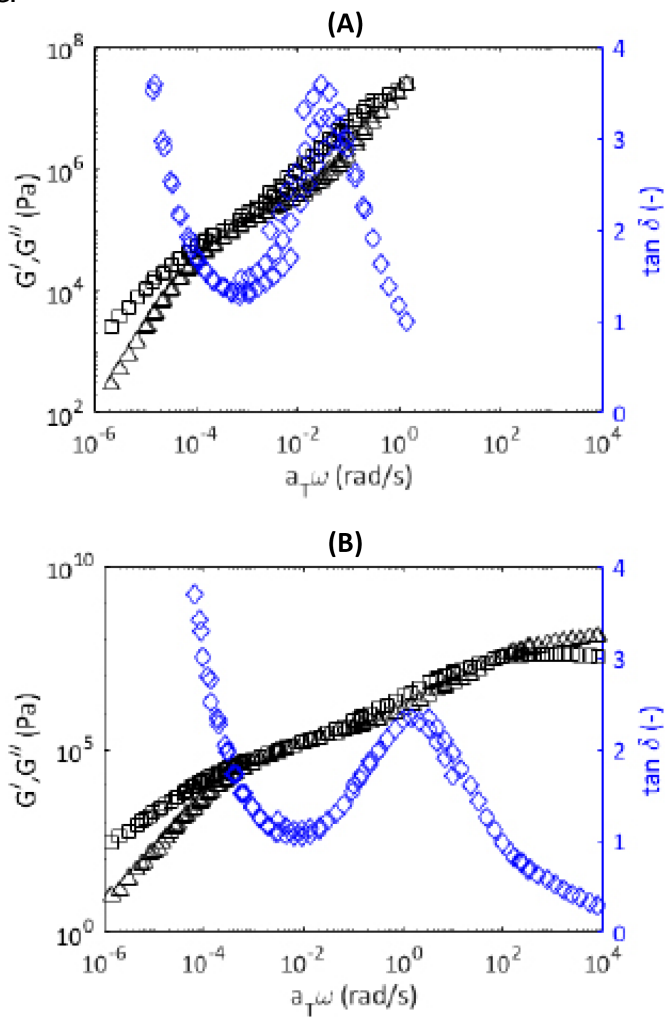


Figure S5. Frequency mastercurve of low molecular weight HDI_C8DA.

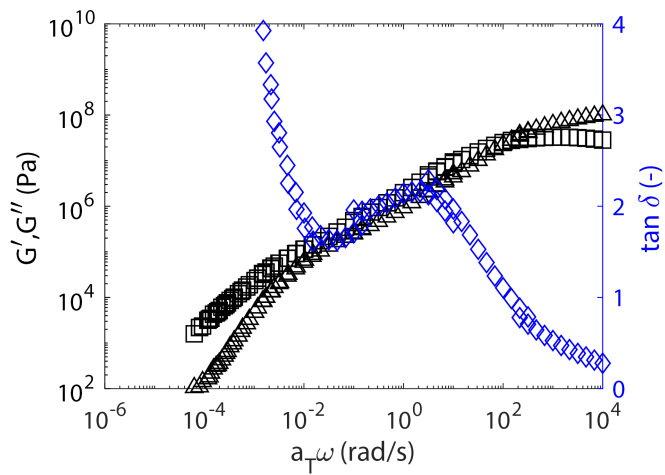


Figure S6. Temperature sweep analyses of amorphous and semicrystalline brush polyurethanes.

(A) Temperature sweep analyses of HDI_C4DA, HDI_C7DA, HDI_C8DA, HDI_C9DA. **(B)** Effect of brush length on maximum damping temperature ($T_{\max \tan \delta}$) and terminal relaxation temperature (T_{terminal}). Note that increasing dangling chain length determines a shift to lower temperature of $T_{\max \tan \delta}$ and T_{terminal} . **(C)** Effect of brush length on maximum absolute value of damping ($\tan \delta_{\max}$). Note that increasing brush length determines a decrease of mechanical damping. **(D)** Temperature sweep analyses of HDI_C8DA, HDI_C9DA, HDI_C12DA. Note that for HDI_C9DA and HDI_C12DA no clear restriction of dynamics was observed. For these polymers the change of slope in $\tan \delta$ was attributed to a competitive crystallisation behaviour from side chain stacking.

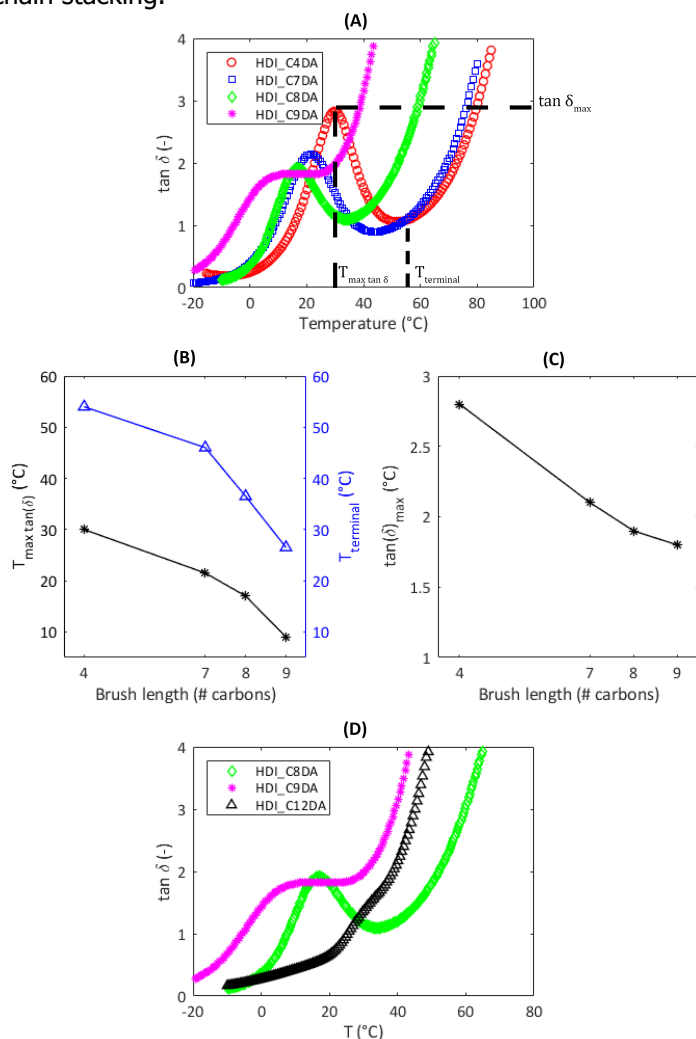


Figure S7. XRD spectra of HDI_C8DA at different annealing times.

The figure shows the evolution of the x-ray diffraction patterns with long-term annealing. After 7 days at 21 °C, HDI_C8DA shows some degree of long range order.

A XRD spectrum immediately after high temperature processing.

B XRD spectrum recorded after annealing for 7 days at 21 °C.

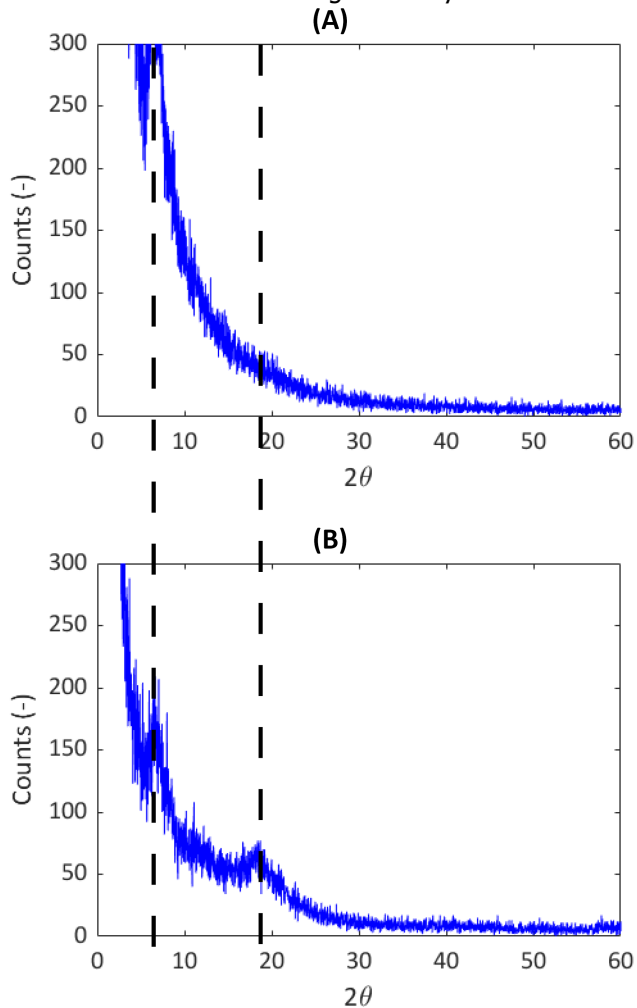


Table S1. Young's modulus (E), yield stress (σ_y), ultimate tensile strength (σ_{UTS}) and strain at break (ε_{break}) of selected brush polyurethanes.

Polymer	E (MPa)	σ_y (MPa)	σ_{UTS} (MPa)	ε_{break} (MPa)
HDI_C4DA	150	5.3	3.9	260
HDI_C7DA	60	1.5	10.5	660
HDI_C8DA	34	1.3	10.2	764
HDI_C9DA	4	0.2	0.6	862
HDI_C12DA	68	4.7	3.9	200

References

- [1] M. D. Hager, P. Greil, C. Leyens, S. van der Zwaag, and U. S. Schubert, *Self-healing materials*, *Advanced Materials* **22**, 5424 (2010).
- [2] R. P. Wool, *Self-healing materials: a review*, *Soft Matter* **4**, 400 (2008).
- [3] C. E. Diesendruck, N. R. Sottos, J. S. Moore, and S. R. White, *Biomimetic self-healing*, *Angewandte Chemie International Edition* **54**, 10428 (2015).
- [4] Y.-L. Liu and T.-W. Chuo, *Self-healing polymers based on thermally reversible diels-alder chemistry*, *Polymer Chemistry* **4**, 2194 (2013).
- [5] S. Nevejans, N. Ballard, J. I. Miranda, B. Reck, and J. M. Asua, *The underlying mechanisms for self-healing of poly (disulfide)s*, *Physical Chemistry Chemical Physics* **18**, 27577 (2016).
- [6] H. Ying, Y. Zhang, and J. Cheng, *Dynamic urea bond for the design of reversible and self-healing polymers*, *Nature communications* **5**, 1 (2014).
- [7] P. Zheng and T. J. McCarthy, *A surprise from 1954: siloxane equilibration is a simple, robust, and obvious polymer self-healing mechanism*, *Journal of the American Chemical Society* **134**, 2024 (2012).
- [8] M. Capelot, D. Montarnal, F. Tournilhac, and L. Leibler, *Metal-catalyzed transesterification for healing and assembling of thermosets*, *Journal of the American chemical society* **134**, 7664 (2012).
- [9] M. AbdolahZadeh, A. C. C. Esteves, S. van der Zwaag, and S. J. Garcia, *Healable dual organic-inorganic crosslinked sol-gel based polymers: crosslinking density and tetrasulfide content effect*, *Journal of Polymer Science Part A: Polymer Chemistry* **52**, 1953 (2014).
- [10] W. Post, A. Cohades, V. Michaud, S. van der Zwaag, and S. J. Garcia, *Healing of a glass fibre reinforced composite with a disulphide containing organic-inorganic epoxy matrix*, *Composites Science and Technology* **152**, 85 (2017).
- [11] X. Chen, M. A. Dam, K. Ono, A. Mal, H. Shen, S. R. Nutt, K. Sheran, and F. Wudl, *A thermally re-mendable cross-linked polymeric material*, *Science* **295**, 1698 (2002).

- [12] J. P. Brutman, P. A. Delgado, and M. A. Hillmyer, *Poly lactide vitrimers*, *ACS Macro Letters* **3**, 607 (2014).
- [13] P. Cordier, F. Tournilhac, C. Soulié-Ziakovic, and L. Leibler, *Self-healing and thermoreversible rubber from supramolecular assembly*, *Nature* **451**, 977 (2008).
- [14] A. Phadke, C. Zhang, B. Arman, C.-C. Hsu, R. A. Mashelkar, A. K. Lele, M. J. Tauber, G. Arya, and S. Varghese, *Rapid self-healing hydrogels*, *Proceedings of the National Academy of Sciences* **109**, 4383 (2012).
- [15] S. Burattini, B. W. Greenland, D. H. Merino, W. Weng, J. Seppala, H. M. Colquhoun, W. Hayes, M. E. Mackay, I. W. Hamley, and S. J. Rowan, *A healable supramolecular polymer blend based on aromatic π - π stacking and hydrogen-bonding interactions*, *Journal of the American Chemical Society* **132**, 12051 (2010).
- [16] M. Nakahata, Y. Takashima, H. Yamaguchi, and A. Harada, *Redox-responsive self-healing materials formed from host-guest polymers*, *Nature communications* **2**, 1 (2011).
- [17] M. W. Urban, D. Davydovich, Y. Yang, T. Demir, Y. Zhang, and L. Casabianca, *Key-and-lock commodity self-healing copolymers*, *Science* **362**, 220 (2018).
- [18] A. Susa, R. Bose, A. Grande, S. van der Zwaag, and S. J. Garcia, *Effect of the dianhydride/branched diamine ratio on the architecture and room temperature healing behavior of polyetherimides*, *ACS applied materials & interfaces* **8**, 34068 (2016).
- [19] D. Adolf, M. Tirrell, and S. Prager, *Molecular weight dependence of healing and brittle fracture in amorphous polymers above the entanglement molecular weight*, *Journal of Polymer Science: Polymer Physics Edition* **23**, 413 (1985).
- [20] O. Lebel, T. Maris, M.-È. Perron, E. Demers, and J. D. Wuest, *The dark side of crystal engineering: creating glasses from small symmetric molecules that form multiple hydrogen bonds*, *Journal of the American Chemical Society* **128**, 10372 (2006).
- [21] S. I. Stupp, V. LeBonheur, K. Walker, L.-S. Li, K. E. Huggins, M. Keser, and A. Amstutz, *Supramolecular materials: self-organized nanostructures*, *Science* **276**, 384 (1997).
- [22] L. M. Leung and J. T. Koberstein, *DSC annealing study of microphase separation and multiple endothermic behavior in polyether-based polyurethane block copolymers*, *Macromolecules* **19**, 706 (1986).
- [23] S. J. Garcia, *Effect of polymer architecture on the intrinsic self-healing character of polymers*, *European Polymer Journal* **53**, 118 (2014).

- [24] J. A. Neal, D. Mozhdghi, and Z. Guan, *Enhancing mechanical performance of a covalent self-healing material by sacrificial noncovalent bonds*, *Journal of the American Chemical Society* **137**, 4846 (2015).
- [25] Y. Yanagisawa, Y. Nan, K. Okuro, and T. Aida, *Mechanically robust, readily repairable polymers via tailored noncovalent cross-linking*, *Science* **359**, 72 (2018).
- [26] A. Susa, A. Mordvinkin, K. Saalwächter, S. van der Zwaag, and S. J. Garcia, *Identifying the role of primary and secondary interactions on the mechanical properties and healing of densely branched polyimides*, *Macromolecules* **51**, 8333 (2018).
- [27] J. D. Ferry, *Viscoelastic properties of polymers* (John Wiley & Sons, 1980).
- [28] K. Vizárová, S. Kirschnerová, F. Kačík, A. Briškárová, Š. Šutý, and S. Katuščák, *Relationship between the decrease of degree of polymerisation of cellulose and the loss of groundwood pulp paper mechanical properties during accelerated ageing*, *Chemical Papers* **66**, 1124 (2012).
- [29] O. Chiantore, M. L. Di Cortemiglia, and M. Guaita, *Changes of degree of polymerisation in the thermal degradation of poly (methyl methacrylate)*, *Polymer degradation and stability* **24**, 113 (1989).
- [30] R. L. McKiernan, S. P. Gido, and J. Penelle, *Synthesis and characterization of polyethylene-like polyurethanes derived from long-chain, aliphatic α , ω -diols*, *Polymer* **43**, 3007 (2002).
- [31] H. Kaufman, A. Sacher, T. Alfrey, and I. Fankuchen, *Side-chain crystallization in alkyl polyacrylates*, *Journal of the American Chemical Society* **70**, 3147 (1948).
- [32] S. A. Greenberg and T. Alfrey, *Side chain crystallization of n-alkyl polymethacrylates and polyacrylates*, *Journal of the American Chemical Society* **76**, 6280 (1954).
- [33] T. Hirabayashi, T. Kikuta, K. Kasabou, and K. Yokota, *Main-chain flexibility and side-chain crystallization of widely spaced comb-like polymers*, *Polymer journal* **20**, 693 (1988).
- [34] H. Shi, Y. Zhao, X. Dong, Y. Zhou, and D. Wang, *Frustrated crystallisation and hierarchical self-assembly behaviour of comb-like polymers*, *Chemical Society Reviews* **42**, 2075 (2013).
- [35] Y. He, D. Xie, and X. Zhang, *The structure, microphase-separated morphology, and property of polyurethanes and polyureas*, *Journal of materials science* **49**, 7339 (2014).
- [36] Y.-L. Lee, P.-H. Sung, H.-T. Liu, L.-C. Chou, and W.-H. Ku, *Dangling polymer networks: glass transition of pu elastomers*, *Journal of applied polymer science* **49**, 1013 (1993).

- [37] W. Yu, M. Du, D. Zhang, Y. Lin, and Q. Zheng, *Influence of dangling chains on molecular dynamics of polyurethanes*, *Macromolecules* **46**, 7341 (2013).
- [38] C. Gerstl, G. J. Schneider, W. Pyckhout-Hintzen, J. Allgaier, D. Richter, A. Alegría, and J. Colmenero, *Segmental and normal mode relaxation of poly (alkylene oxide) s studied by dielectric spectroscopy and rheology*, *Macromolecules* **43**, 4968 (2010).
- [39] R. Vieweg and A. Hochtler, *plastic handbuck*, Volume VII, Polyurethane , 37 (1966).
- [40] D. K. Chattopadhyay and D. C. Webster, *Thermal stability and flame retardancy of polyurethanes*, *Progress in Polymer Science* **34**, 1068 (2009).
- [41] J. W. Van Bogart, P. E. Gibson, and S. L. Cooper, *Structure-property relationships in polycaprolactone-polyurethanes*, *Journal of Polymer Science: Polymer Physics Edition* **21**, 65 (1983).
- [42] M. Müller, U. Seidel, and R. Stadler, *Influence of hydrogen bonding on the viscoelastic properties of thermoreversible networks: analysis of the local complex dynamics*, *Polymer* **36**, 3143 (1995).
- [43] S. Seiffert and J. Sprakel, *Physical chemistry of supramolecular polymer networks*, *Chemical Society Reviews* **41**, 909 (2012).
- [44] R. K. Bose, N. Hohlbein, S. J. Garcia, A. M. Schmidt, and S. van der Zwaag, *Connecting supramolecular bond lifetime and network mobility for scratch healing in poly (butyl acrylate) ionomers containing sodium, zinc and cobalt*, *Physical Chemistry Chemical Physics* **17**, 1697 (2015).
- [45] M. Kapnistos, D. Vlassopoulos, J. Roovers, and L. Leal, *Linear rheology of architecturally complex macromolecules: Comb polymers with linear backbones*, *Macromolecules* **38**, 7852 (2005).
- [46] K. M. Kirkwood, L. G. Leal, D. Vlassopoulos, P. Driva, and N. Hadjichristidis, *Stress relaxation of comb polymers with short branches*, *Macromolecules* **42**, 9592 (2009).
- [47] M. Kempf, D. Ahirwal, M. Cziep, and M. Wilhelm, *Synthesis and linear and nonlinear melt rheology of well-defined comb architectures of PS and PPMS with a low and controlled degree of long-chain branching*, *Macromolecules* **46**, 4978 (2013).
- [48] S. Trinkle and C. Friedrich, *Van Gorp-Palmen-plot: a way to characterize polydispersity of linear polymers*, *Rheologica Acta* **40**, 322 (2001).
- [49] S. Trinkle, P. Walter, and C. Friedrich, *Van Gorp-Palmen plot ii-classification of long chain branched polymers by their topology*, *Rheologica Acta* **41**, 103 (2002).

- [50] T. Aida, E. Meijer, and S. Stupp, *Functional supramolecular polymers*, *Science* **335**, 813 (2012).
- [51] Y. K. Godovsky and G. Slonimsky, *Kinetics of polymer crystallization from the melt (calorimetric approach)*, *Journal of Polymer Science: Polymer Physics Edition* **12**, 1053 (1974).
- [52] D. Nichetti and N. Grizzuti, *Determination of the phase transition behavior of thermoplastic polyurethanes from coupled rheology/DSC measurements*, *Polymer Engineering & Science* **44**, 1514 (2004).
- [53] B. Fernández-d'Arlas, R. P. Baumann, E. Pöselt, and A. J. Müller, *Influence of composition on the isothermal crystallisation of segmented thermoplastic polyurethanes*, *CrystEngComm* **19**, 4720 (2017).
- [54] K. F. Mansfield and D. N. Theodorou, *Molecular dynamics simulation of a glassy polymer surface*, *Macromolecules* **24**, 6283 (1991).
- [55] J. Baschnagel and K. Binder, *On the influence of hard walls on structural properties in polymer glass simulation*, *Macromolecules* **28**, 6808 (1995).

3

A deconvolution protocol of the mechanical relaxation spectrum to identify and quantify individual polymer feature contributions to self-healing

*There are no nations! There is only humanity.
And if we don't come to understand that right soon, there will be no nations,
because there will be no humanity.*

Isaac Asimov

This chapter has been published as is

V. Montano, S.J. Picken, S. van der Zwaag, S.J. Garcia, *Physical Chemistry Chemical Physics* **21**, 10171-10184 (2019)

Abstract

Starting from experimental macro-rheological data we develop a fitting protocol that succeed in the separation of the overlapping relaxation phenomena in the dissipative regime for a set of intrinsic healing polymers, which heal most effectively near their glass transition temperature T_g . To allow for a proper deconvolution the rheological master curves are converted to a relaxation spectrum $H(\tau)$ and this is fitted using an optimized mechanical model, e.g. the Maxwell-Weichert model. The deconvolution of overlapping segmental mobility and reversible interactions is successfully demonstrated for a set polyimide and polyamide polymers containing none, one and two reversible dynamic features near- T_g . Through the fitting parameters, the relaxation timescale of each feature and their apparent process enthalpies is obtained. The quantitative data obtained from the fitting protocol are then compared to macroscopic healing results. As a result, a clear correspondence between the energy stored by the system to accomplish reversible (e.g. H-bonds, π - π) and chain interdiffusion relaxation transitions and the healing efficiency of such polymers is obtained. The implementation of this protocol allows for a clearer identification of the relevant mechanisms in self-healing polymers and paves the way for the development of more efficiently healable polymeric systems.

3.1. Introduction

Intrinsic self-healing polymers can undergo multiple healing events, even at the same location, as the macromolecular design of these systems yields non-permanently consumed reversible chemical or physical bonds leading to the de-construction of crack interfaces brought in intimate contact [1].

Supramolecular chemistry has been particularly beneficial for the development of intrinsic self-healing polymers, particularly at near room temperature [2, 3]. Initial tack and short range interactions followed by time-dependent long range chain interdiffusion and bond reformation, allows partial or full but in any case repeatable restoration of the original material properties [4], albeit mechanical [5], barrier [6], aesthetics or electrical [7]. Many methods developed to identify the underlying physical molecular processes in polymer rheology in general and in self healing in particular have been described in literature [8–12]. Of the available methods, the analysis of frequency domain master curves used to probe polymer dynamics [9,10] should be regarded as a necessary first-order approximation to identify the polymer healing and kinetics [11]. The experimental tool that probes polymer dynamics over wide range of frequencies is the well-known time-temperature superposition (TTS) [13, 14]. Originally TTS has been developed for thermo-rheologically simple fluids but is being used increasingly to analyse the behaviour of more complex and branched polymers [15, 16]. Although self-healing polymers do not behave as simple fluids, the use of the TTS in self-healing polymers has revealed, amongst others, the existence of a clear correlation between terminal relaxation and the degree of substantial macroscopic healing [12]. Nevertheless, when multiple relaxations occur in a restricted timescale range (i.e. overlapping phenomena), it is hard to precisely delineate the dissipation dynamics of the system with the approaches now in use. As a result it is hard to identify the existence of concurrent and overlapping phenomena. This problem becomes relevant when analysing the frequency dependent viscoelastic domain of more advanced self-healing supramolecular polymers. In these systems the dynamic nature of the network stickers often results in the dynamics of the transient network relaxation to overlap with dynamic phenomena occurring in the main chain (i.e. segmental mobility).

In the literature many reports demonstrate optimal intrinsic healing at temperatures close to T_g (glass transition) where the enhanced conformational mobility allows dynamic bond exchange and possibly macromolecular flow [6, 17–19] without a substantial loss of mechanical properties. For such systems the relaxation dynamics related to the presence of supramolecular stickers often overlaps with the main chain segmental mobility, resulting in misleading correlations between kinetics of macroscopic healing and the differences in the timescale of the relaxation processes as well as disagreements with the physics theories developed to theoretically explain intrinsic self-healing in polymers [18, 20, 21]. In that case the macro-rheology does not show a clear separation between the two above-mentioned relaxation mechanisms or, in other terms, it is not possible to clearly distinguish a double plateau of the elastic component of the shear modulus $G'(\omega)$ in the analysed spectrum of frequency [22].

The effective overlap between molecular complexation/de-complexation of reversible

network and main chain segmental mobility is generally analysed by comparing macro-rheological data to molecular rheology predictions such as proposed by Leibler, Rubinstein and Colby [23]. For systems showing overlap between main chain segmental mobility and reversible chain association, the analysis of particular features of the master curve, such as the slope of G' and G'' in the plateau region and the phenomenon of terminal relaxation, are used to prove compliance to the sticky reptation model and so to prove the existence of reversible bonds [18, 20, 24, 25]. More recently, new theories based on slip-link and double reptation models aim to elucidate the reason for the absence of the classical double 'Leibler' plateau in entangled systems bearing sticky units [26, 27].

Despite the elegance of the molecular rheology theories, the problem of defining the individual timescales of the overlapping relaxation phenomena related to stickers and segmental mobility remains unsolved and is addressed in this paper.

In a recent publication Ankiewicz et al. [28] proposed the use of a continuous relaxation spectrum $H(\tau)$ to identify overlapping phenomena in complex polymers. For a series of model H-polymers, the relaxation spectrum $H(\tau)$ revealed relaxation peaks and timescales that could not be directly inferred from the frequency master curves. Following this work, Yesilyurt and co-workers [29], applied an analogue mechanical model (the Maxwell-Weichert model) to determine the correct dissipation dynamics of five reversibly crosslinked hydrogels. The networks were formed from mixtures of two different phenylboronic acid derivatives with two unique diol complexation rates. In their work, the authors showed how the application of the mechanical model to the relaxation spectra $H(\tau)$ allowed deconvolution of the relevant processes and separation of the contributions of the two complexation processes. Inspired by these two works we introduce here a high resolution fitting protocol that enables the deconvolution of the overlapping dissipation dynamics attributed to main chain segmental mobility and reversible junction disengagement of reversible bonds through the use of mechanical analogous model fits, issuing a fundamental problem of near- T_g self-healing polymers where classical representation/analysis of linear viscous data does not provide the distinction of multiple relaxation process. The protocol yields a finite number of parameters that semi-quantitatively capture the different relaxation phenomena, providing an indirect measure of energy stored by each polymer feature during the single relaxation transition. To prove the concept we used two unentangled polyamides and four near- T_g self-healing unentangled polyimides containing short aliphatic branches and aromatics responsible for π - π interactions [18, 20]. The protocol presented here makes it possible to identify the individual contributions to healing showing a clear correspondence between the energy stored by the system to accomplish reversible (e.g. H-bonds, π - π stacking) and chain interdiffusion relaxation transitions and the healing efficiency of such polymers. The results of the study makes it clear that it is important to have a certain temperature distance between T_g and the temperature for sticker relaxations to obtain the desired combination of significant mechanical healing and high mechanical properties. This quantified temperature distance can be used as a new design criterion for the synthesis of stronger yet efficient self-healing polymers.

3.2. Experimental and Fitting Protocol

3.2.1. Polymers Syntheses

To evaluate the potential and validity of the protocol a set of healable polyimide and polyamide polymers with controlled polymer architecture, comparable molecular weights yet a different number of physical reversible groups (H-bonding and π - π interactions) were synthesized. A related non-healing linear polyamide was also synthesized.

Four self-healing polyimides (SH-PIs) were synthesized using the procedures described elsewhere [18, 19]. The monomers used were three different aromatic dianhydrides 4,4'-(4,4'-isopropylidenediphenoxy)bis(phthalic anhydride) (BPADA), 4,4'-oxidiphthalic anhydride (ODPA), 4,4'-(Hexafluoroisopropylidene)diphthalic anhydride (6FDA) and a fatty dimer diamine derived from vegetable oil (Priamine 1075) (provided by Croda Nederland B.V.). The polyimides were divided in two Control Groups (**Figure 3.1**). Control Group 1 consists of two polyimides obtained by polymerisation of Priamine and ODPA. The two polyimides differ in the stoichiometric molar feed Priamine/ODPA: **ODPA-p0.9** (with 10% mol excess of ODPA), **ODPA-p1.0** (at the theoretical stoichiometric ratio). Control Group 2 consists of three polyimides obtained by polymerisation of Priamine and three distinct aromatic dianhydrides. The three polyimides differ in the degrees of rotational freedom (DRF) of the anhydride rigid segment: **BPADA-p1.0** (DRF = 2), **ODPA-p1.0** (DRF = 1), **6FDA-p1.0** (DRF = 0). DRF is related to the flexibility of the dianhydride moiety and in particular to the degree of rotational freedom around central linker (e.g. oxygen atom for ODPA-p1.0). A lower DRF implies higher energy penalty to be paid to explore rotational states, as verified for this set of anhydrides both experimentally and through computations by Susa et al. [20].

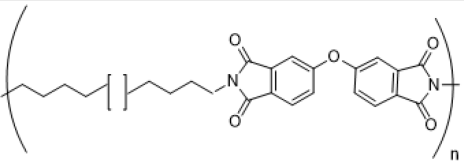
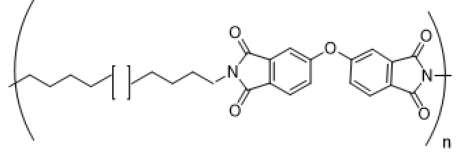
A self-healing polyamide **C9PA** was synthesized using a one-step polymerisation process as described here on. The monomers used were Isophthaloyl chloride (IPC) (Sigma-Aldrich, purum, $\geq 98\%$) and Priamine 1075. The synthesis was conducted in 1-Methyl-2-pyrrolidinone (NMP, Sigma-Aldrich, anhydrous, $\geq 99.5\%$) with monomer molar concentration of 1 mmol/mL, using triethylamine (NET3, Sigma-Aldrich, $\geq 99.5\%$) as acid scavenger in molar concentration of 1.2 mmol/mL. The molar monomer feed was set at theoretical stoichiometric ratio.

IPC was recrystallized by sublimation as described elsewhere [30] and stored under nitrogen. Priamine was weighted directly into a three necks round bottom flask. 2/3 (vol.) of the solvent (NMP) was added to the system. The mixture was magnetically stirred at 200 rpm to favour Priamine dissolution and purged under nitrogen atmosphere. The solution was subsequently cooled to 0 °C using an ice bath in order to avoid unwanted side reactions between the diamine monomer (Priamine) and the acid scavenger (NET3). NET3 was then injected in the system using a syringe. IPC was weighted and dissolved in a separate flask in 1/3 (vol.) of reaction solvent (NMP). This solution was then injected in the main reactor using a syringe, keeping the system under vigorous magnetic stirring. The mixture was kept for 30 minutes at 0°C. Ultimately the temperature was increased to 55 °C for 3 hours. At the end of the reaction the solution was left to cool down to room temperature. The viscous mixture was precipitated in excess of demineralized water and washed

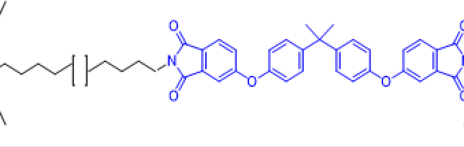
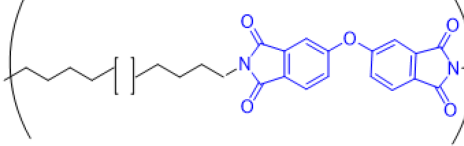
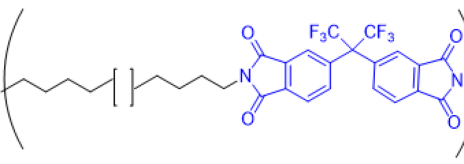
three times. To favour the washing step, the precipitation was performed in a metal blade blender. The precipitate was sheared at 15 krpm for 1 minute. The polymer was separated from the mixture by using a vacuum conical flask and subsequently dried under vacuum at 65 °C overnight.

A non-healing polyamide **Linear-PA** was synthesized following an analogous procedure. The monomer used were IPC and 1,12-Diaminodecane (Sigma-Aldrich, ≥98%). The synthesis was conducted in NMP with monomer molar concentration of 1 mmol/mL, using N₂Et₃ as acid scavenger in molar concentration of 1.2 mmol/mL. The molar monomer feed was set at the theoretical stoichiometric ratio.

SH-PIs, Control Group 1 – Priamine/ODPA molar ratio

Label	Repetitive unit	Feature
ODPA-p1.0		Priamine/ODPA = 1
ODPA-p0.9		Priamine/ODPA = 0.9

SH-PIs, Control Group 2 – Dianhydride type and DRF

Label	Repetitive unit	Feature
BPADA-p1.0		DRF = 2
ODPA-p1.0		DRF = 1
6FDA-p1.0		DRF = 0

Label	Repetitive unit	Feature
C9PA		Two supramolecular units
Linear PA		Non Healing

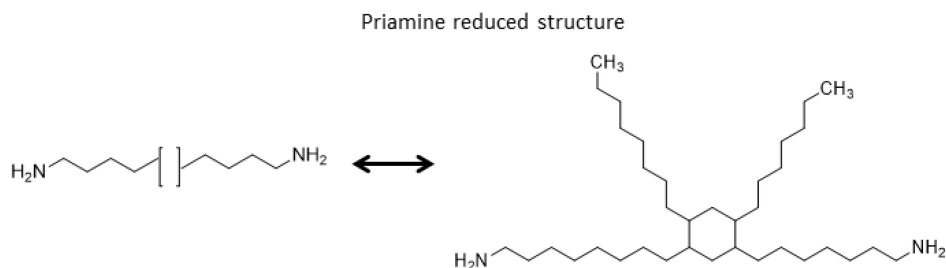


Figure 3.1: **Polymer classes investigated through the application of Maxwell-Weichert mechanical analogue model.** (*Priamine/ODPA*) is the molar ratio between diamine monomer (Priamine 1075) and rigid aromatic dianhydride (ODPA). DRF is degrees of rotational freedom of the aromatic dianhydride block. At the bottom of this figure we present the extended molecular structure of the Priamine monomer incorporated in ODPA-p1.0, ODPA-p1.0, 6FDA-p1.0, BPADA-p1.0, C9PA polymers.

3.2.2. Rheological Measurements and Tensile Properties

Temperature sweep and frequency rheology tests were performed for all polymers to build the rheology master curves applying time-temperature-superposition principle (TTS). In all cases a Haake Mars III rheometer (ThermoScientific) (parallel plate geometry, plate diameter = 8 mm) was used. The data obtained at different temperatures were shifted using the Rheowin software routine (ThermoScientific). On the basis of preliminary strain amplitude sweep measurements the shear strain amplitude was set to 0.1%. Temperature sweeps from 0 to 200 °C at a frequency of 1 Hz were performed to establish the shifting temperatures. Frequency sweep experiments from 10 to 0.1 Hz were performed with steps of $\Delta T = 5$ °C over the temperature range from 0 and 80 °C for all polyimides and C9PA, while steps of $\Delta T = 10$ °C were used for the Linear-PA in the range 95 and 220 °C.

The maximum of the loss component of the shear modulus G'' in the temperature sweep tests was used as the internal reference to set the shifting temperature as it

Table 3.1: **Selected polymer properties.** Molecular weight distribution (M_w and D), apparent molecular weight between entanglements ($M_{e,app}$) as calculated using rubber elasticity ($M_{e,app} = \rho RT_0/G_N$, where ρ is the material density, R is the universal gas constant, T is the shifting temperature and G_N is the plateau modulus as obtained from the van Gurp-Palmen plot), T_g as obtained by DSC analysis. Linear-PA molecular weight distribution is not available since this polymer is not soluble in the available GPC solvents.

Polymer	M_w (kDa)	D	$M_{e,app}$ (kDa)	DSC- T_g (°C)
ODPA-p1.0	32	2.0	2.9	13
ODPA-p0.9	32	2.0	2.1	17
BPADA-p1.0	29	1.6	3.3	24
6FDA-p1.0	41	2.0	3.3	25
C9PA	17	1.9	4.6	25
Linear-PA	n.a.	n.a.	0.9	120

is at the midpoint of the dynamic phase transition. The reference shifting temperatures were T_0 (ODPA-p0.9) = + 20 °C, T_0 (ODPA-p1.0) = + 15 °C, T_0 (BPADA-p) = + 25 °C, T_0 (6FDA-p) = +30 °C. C9PA and Linear-PA rheological master curves were built at the reference temperature of T_0 (C9PA) = + 35 °C and T_0 (Linear-PA) = + 120 °C.

Macroscopic healing was evaluated using tensile mechanical testing with dog-bone specimens according to the ASTM D1708 standard and applying a cross-head speed of 80 mm/min. To quantify the healing behaviour, pristine samples were cut with a sharp razor blade and directly put back in contact applying gentle pressure at ambient controlled temperature (21°C). After placing the sample halves in contact in closely fitting moulds the samples were subjected to healing treatments at specific healing temperatures for 11 days, without any additional load applied. The healing temperature was set at the temperature corresponding to the maximum of $\tan \delta = G''/G'$ extrapolated from preliminary temperature sweeps analyses. All polymers exhibited intrinsic self-healing behaviour with the exception of the Linear-PA. The lack of healing in the Linear-PA is attributed to the high degree of main chain crystallisation induced by unperturbed hydrogen bonds among amide linkages as a result of the absence of aliphatic dangling chains (which are present in all other investigated systems).

3.2.3. Fitting protocol

The developed protocol is schematized in **Figure 3.2** and was set, validated and applied to the master curves of the five polymers shown in Figure 3.1 . The construction of the rheology master curves is indicated as Step 0 in Figure 3.2.

Step 1 consists of the determination of the best estimate for the continuous relaxation spectrum function $H(\tau)_{exp}$. The spectrum $H(\tau)_{exp}$ is derived from the experimental data of storage and loss moduli through the mathematical resolution of a well-known ill-posed problem [13]. The solution is attained by applying the non-

linear regression method developed by Honerkamp and Weese [31], as this method is both reliable and simple to use [32]. The source code of the algorithm can be found in the CPC Program library [33]. In this protocol, the minimum and maximum relaxation times are user-defined. In our case we simply set $\tau_{\min} = 1/\omega_{\max}$ and $\tau_{\max} = 1/\omega_{\min}$ where ω_{\max} and ω_{\min} are the highest and the lowest angular frequency in the modulus data, as suggested in the library user manual. The construction of $H(\tau) \text{ exp.}$ facilitates the application of mechanical analogous modelling and sets up a multi-optimization problem as shown in Steps 2 and 3. Step 2 consists of the selection of the analogous mechanical model and the fit of the continuous relaxation spectrum $H(\tau) \text{ exp.}$ obtained in Step 1. Here we selected the infinite Maxwell model (or Maxwell-Weichert model) as the analogous mechanical model.

$$H_{Model}(\ln \tau) = \sum_{i=1}^n A_i \exp\left(-\frac{((\ln(\tau) - \ln(\tilde{\tau}_i))^2)}{2\sigma_i^2}\right) \quad (3.1)$$

The model entails an infinite number of Maxwell elements (a compliance and a dashpot in series) connected in parallel. The choice of this model allows us to approach the problem in the most general and unbiased way.

In Equation 3.1 $H_{Model}(\tau)$ is the model relaxation spectrum, τ is the vector of time containing the experimental time extrapolated from $H(\tau)$ acquired in Step 1. $\tilde{\tau}$, A , σ are fitting parameters. In particular $(\tilde{\tau}_i)$ regulates the position on the time axis of a specific Maxwell element i , A_i controls the maximum magnitude, σ_i controls the half height width. The function H_{Model} must be validated with respect to two variables: the number of Maxwell elements $i \rightarrow i_{optimum}$ (a number that is a priori in principle unknown and which will determine the number of dominant relaxation mechanisms) and the set of fitting parameters $(\tilde{\tau}, A, \sigma)$. The experimental $H(\tau) \text{ exp.}$ is fitted with a user-defined initial number of relaxation elements i , generating the fit function $H(\tau) \text{ Maxwell}$. $H(\tau) \text{ Maxwell}$ curve is represented by the red crosses in Step 2. Other markers in Step 2 represent the corresponding individual dominant relaxation mechanisms. Then, the optimal number of Maxwell elements and the set of best fitting parameter values is identified based on the minimization of the coefficient of determination (r^2) obtained by comparing the model storage and loss moduli ($G' \text{ Maxwell model}$ and $G'' \text{ Maxwell model}$, reconstructed from $H(\tau) \text{ Maxwell}$) with the experimental moduli ($G' \text{ exp.}$ and $G'' \text{ exp.}$) curve as shown in Step 3 and indicated with the arrows between Steps 2 and 3 as an iterative optimization process. $G' \text{ Maxwell model}$ and $G'' \text{ Maxwell model}$ are calculated using known relations [13] reported in Equation 3.1 and 3.2.

The optimization algorithm was set in Matlab R2017b using `lsqnonlin` function to solve the nonlinear data fitting (MathWorks Inc.).

$$G'(\omega) = \int_{-\infty}^{\infty} \frac{H \ln(\tau) \omega^2 \tau^2}{1 + \omega^2 \tau^2} d \ln \tau \quad (3.2)$$

$$G''(\omega) = \int_{-\infty}^{\infty} \frac{H \ln(\tau) \omega \tau}{1 + \omega^2 \tau^2} d \ln \tau \quad (3.3)$$

Baumgaertel and Winter [34] developed a conceptually similar procedure to infer the minimum number of Maxwell modes directly from $G^*(\omega)$ which is implemented in the commercially available IRIS software package.

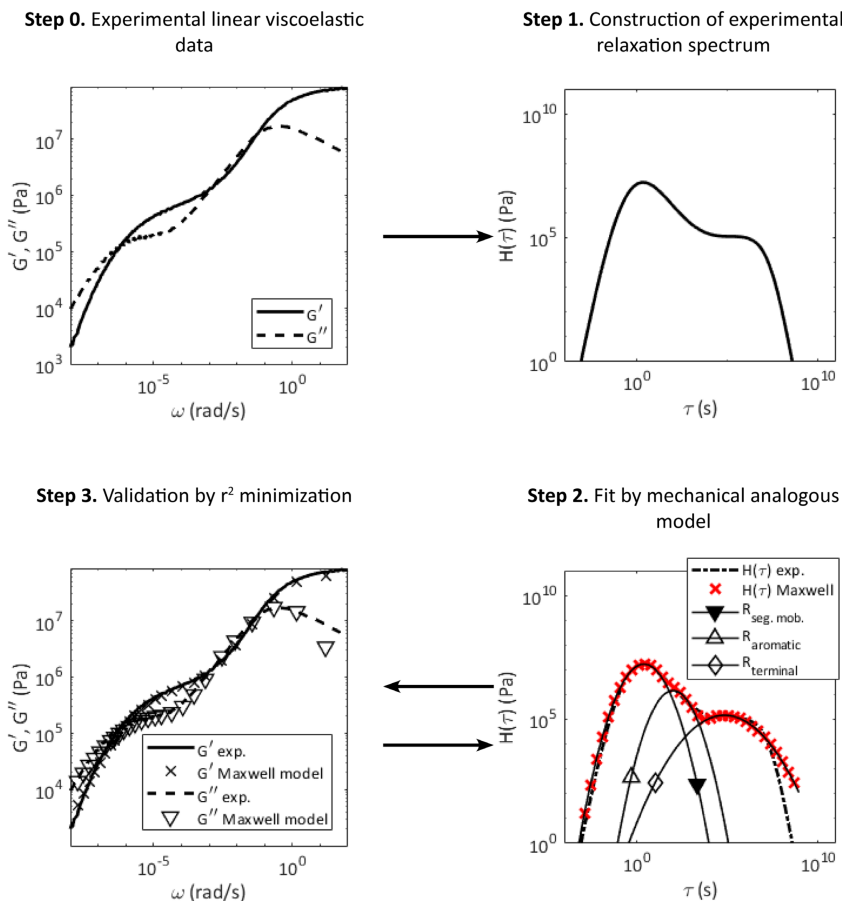


Figure 3.2: **Fitting protocol to determine the number of dominant relaxations as applied to ODPA-p1.0.** (i) Experimental rheological master curve build up (Step 0); (ii) derivation of the relaxation spectrum $H(\tau)_{exp}$. (Step 1); (iii) construction of the fit function $H(\tau)_{Maxwell}$ by using analogous mechanical models (Step 2); and (iv) validation and optimization of the mechanical model by reconstruction of $G'_{Maxwell}$ model and $G''_{Maxwell}$ model master curves (Steps 2 and 3).

3.3. Results

The experimental frequency master curves of ODPA-p0.9, ODPA-p1.0, 6FDA-p1.0, BPADA-p1.0 and C9PA are presented in **Figure 3.4G-K**. All polymers present the typical dynamical mechanical features of dynamic supramolecular networks [3]. For such systems the molecular weight between effective interaction points (M_e) is lower than the minimum possible molecular weight for entanglements (Table 3.1

Table 3.2: **Coefficient of determination (r^2) obtained when comparing the experimental master curve with the reconstructed master curve after the fitting process.** i indicates the number of Maxwell elements used in the fitting protocol. The optimum number of relaxation mechanisms for each polymer (i.e. Maxwell elements in series) is highlighted in bold.

	$i = 1$	$i = 2$	$i = 3$	$i = 4$	$i = 5$
ODPA-p0.9					
$r^2[G'(\omega)]$	0.3421	0.8406	0.8496	0.8430	0.6297
$r^2[G''(\omega)]$	-	-	-	-	-
ODPA-p1.0					
$r^2[G'(\omega)]$	0.9355	0.9479	0.9566	0.9549	0.9541
$r^2[G''(\omega)]$	0.9162	0.9134	0.9176	0.9129	0.9118
6FDA-p1.0					
$r^2[G'(\omega)]$	0.9060	0.9220	0.9350	0.9322	0.9339
$r^2[G''(\omega)]$	0.6311	0.6449	0.6498	0.6474	0.6441
BPADA-p1.0					
$r^2[G'(\omega)]$	0.9531	0.9722	0.9860	0.9853	0.9852
$r^2[G''(\omega)]$	0.8901	0.8963	0.8975	0.8957	0.9119
	$i = 2$	$i = 3$	$i = 4$	$i = 5$	$i = 6$
C9PA					
$r^2[G'(\omega)]$	0.9095	0.9100	0.9124	0.9110	0.8876
$r^2[G''(\omega)]$	0.8139	0.8041	0.8142	0.8091	0.3648

and references [18, 20]), so the apparent elastic plateau presence at intermediate frequency is attributed to the presence of supramolecular stickers, in accordance with sticky reptation theory by Rubinstein and Colby [23]. Such an apparent elastic plateau was also shown to exist in our previous work on self-healing polyimides similar to the ones used in this work [20]. None of these master curves do show any clear separation between the relaxation phenomena associated to the main chain segmental mobility and those to the supramolecular bonds.

The fitting protocol shown in Section 3.2.3 was applied to all rheological data sets for the six polymers explored.

Table 3.2 shows the r^2 values obtained during the fitting process to establish the optimal number of relaxation mechanisms i . Three relaxation phenomena ($i_{optimum} = 3$) were identified for the SH-PIs (ODPA-p0.9, ODPA-p1.0, 6FDA-p1.0, BPADA-p1.0), four in the case of the self-healing polyamide C9PA with aromatics and H-bonds ($i_{optimum} = 4$) and three for the non-healing Linear-PA ($i_{optimum} = 3$).

Figures 3.3A-F show for each polymer the optimal fit function with its corresponding reconstructed $H(\tau)$ Maxwell in red crosses, while **Figures 3.4G-L** show the val-

idation curves comparing the experimental and the reconstructed master curves. It should be noted that all inferred relaxation peaks (both experimental and model) fall in the range of validity proposed by Davies and Anderseen [35] and extensively verified by McDougall et al. [32] for the method developed by Weese and Honerkamp to construct the continuous relaxation spectrum using the mathematical operations described above. According to the Davies and Anderseen sampling localisation [35] the reliable interval for truly valid relaxation times τ is $\tau_{\min} = \frac{e^{\pi/2}}{\omega_{\max}}$;

$\tau_{\max} = \frac{e^{-\pi/2}}{\omega_{\min}}$ which is marked by sets of two dashed vertical lines in Figures 3.3A-F.

The validation results in Figures 3.4G-K show that the protocol captured the entire relaxation of the frequency set for the self-healing polymers. The sets of fitting parameters regulating time position ($\tilde{\tau}$), magnitude (A) and width (σ) of the individual relaxations for each polymer are reported in **Table 3.3**. Two overlapping phenomena at intermediate relaxation times were found for the set of SH-PIs (ODPA-p0.9, ODPA-p1.0, 6FDA-p1.0, BPADA-p1.0) while three overlapping relaxation mechanisms were identified for the SH-PA (C9PA). In the case of the high T_g non-healing system (Linear-PA) the protocol identified two overlapping relaxations at intermediate times, as for the SH-PIs. As will be shown in the Discussion section, each of the identified individual relaxation phenomena can be attributed to a specific polymer architectural feature having a specific effect on the viscoelastic relaxation profile, namely segmental mobility, aromatic interactions, H-bonds and terminal relaxation.

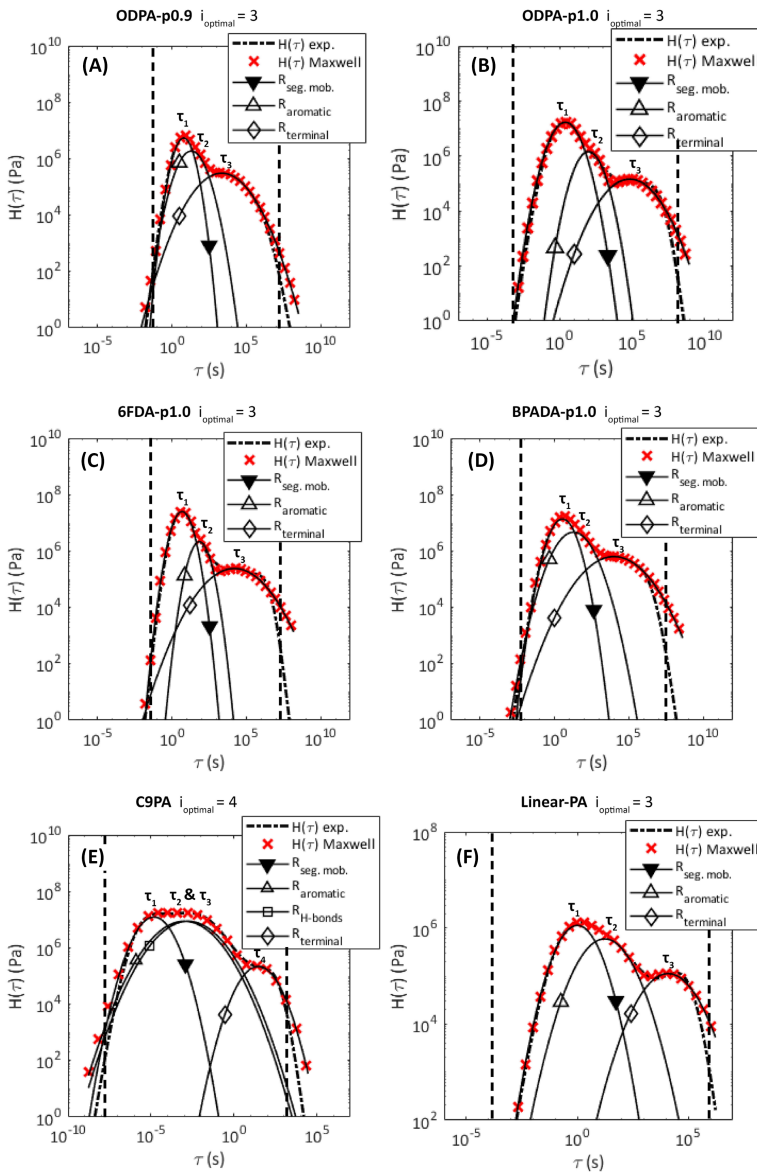


Figure 3.3: **Fitting results and validation after protocol implementation (relaxation spectrum).** (A-F) Optimal fit function $H(\tau)$ Maxwell (red cross markers) and dominant relaxation mechanisms (continuous lines with marker) on top of experimentally calculated relaxation spectrum $H(\tau) \text{ exp.}$ (dashed line). The individual relaxations can be related to the presence of certain polymer features as discussed in the Discussion section and shown here with different markers (segmental relaxation $R_{\text{seg. mob.}}$ as filled triangle marker, aromatic interactions R_{aromatic} as empty triangle marker, hydrogen bonds interaction $R_{\text{H-bonds}}$ as squared marker, terminal relaxation R_{terminal} as diamond marker). The vertical dash lines show the lower and upper limits of validity of the relaxation time for the continuous relaxation spectrum as inferred by Davies et al. [35]

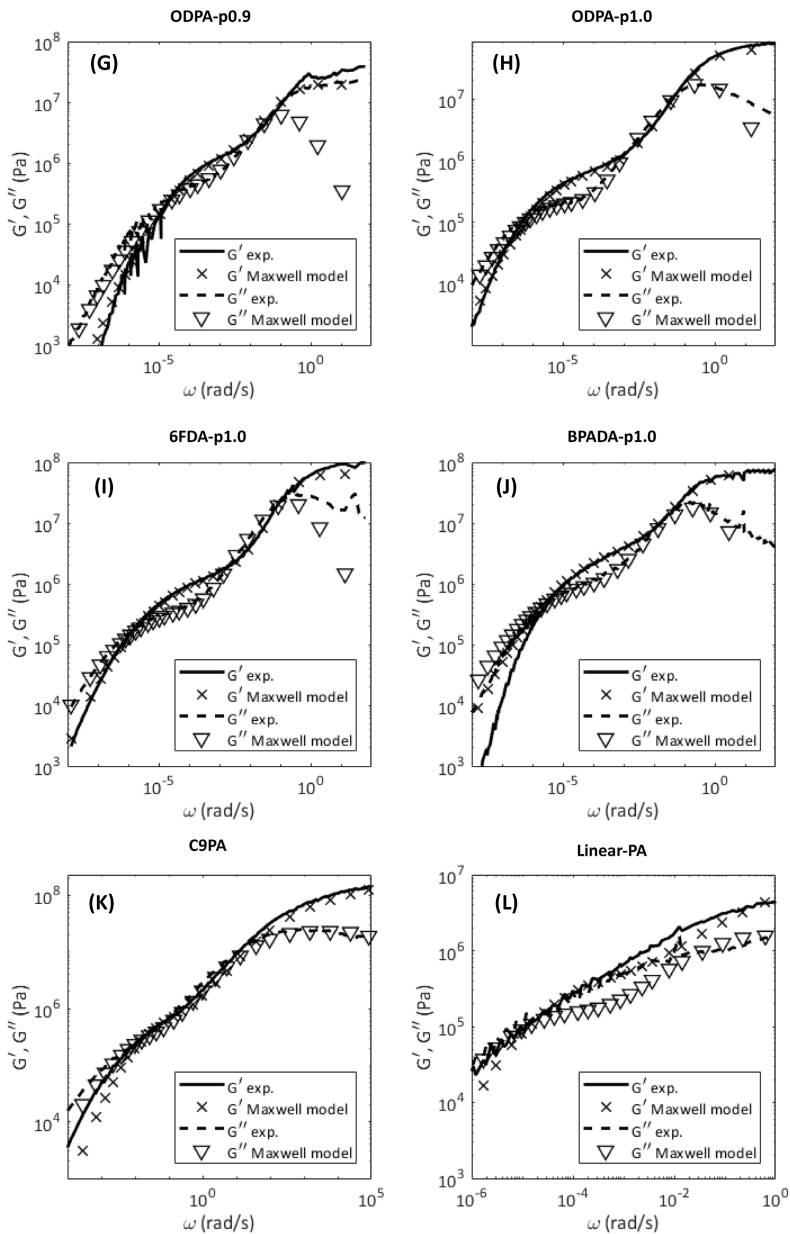


Figure 3.4: **Fitting results and validation after protocol implementation (shear moduli).** (G-L) Comparison of the experimental moduli G' exp. and G'' exp. (continuous and dashed lines) and the moduli derived from the fitting procedure G' Maxwell model and G'' Maxwell model (cross and triangle markers), showing good correlation.

Table 3.3: **Fitting parameters as output by protocol application to the set of SH-PIs, the self-healing polyamide (C9PA) and non-healing polyamide (Linear-PA).**

Polymer	$\tilde{\tau}_1$ (s)	$\tilde{\tau}_2$ (s)	$\tilde{\tau}_3$ (s)	$\tilde{\tau}_4$ (s)	A_1 (MPa)	A_2 (MPa)	A_3 (MPa)	A_4 (MPa)
ODPA-p.09	6.1	19.8	2.2 e3	-	5.5	1.9	0.31	-
ODPA-p1.0	2.5	100	7.1 e4	-	17.2	1.5	0.15	-
6FDA-p.10	4.7	70.0	1.6 e4	-	25.5	2.2	0.24	-
BPADA-p.10	3.4	18.9	1.0 e4	-	14.0	4.7	0.69	-
C9PA	1.5 e-5	1.0 e-3	1.7 e-3	31.2	12.6	8.9	8.9	0.23
Linear-PA	1.0	16.8	1.2 e3	-	1.14	0.60	0.11	-

Polymer	σ_1 (-)	σ_2 (-)	σ_3 (-)	σ_4 (-)
ODPA-p0.9	1.06	0.747	0.403	-
ODPA-p1.0	0.699	0.758	0.401	-
6FDA-p1.0 p1.0	1.02	1.03	0.350	-
BPADA-p1.0	0.796	0.562	0.343	-
C9PA	0.639	0.379	0.379	0.675
Linear-PA	0.676	0.543	0.505	-

3.4. Discussion

3.4.1. Type and distribution of relaxation events

The fitting protocol applied to the experimental relaxation spectrum clearly reveals the existence of different relaxation mechanisms (**Figure 3.3A-F**) as it shows the presence of overlapping relaxations not identifiable in simple experimental frequency master curves. The identification of all the relaxations taking place allows discussing the contribution of different polymer features to a given macroscopic phenomenon, e.g. self-healing, in a relatively simple approach in case the polymer architecture is known.

ODPA-p1.0 is a polyimide showing complete macroscopic healing in a three stage process consisting of fast-tack followed by time dependent long range interactions (self-diffusion) at the temperature of interest used in this work [18]. For this polymer the fitting protocol shows three relaxation mechanisms (Figure 3.3B). Two of these phenomena strongly overlap at short-intermediate timescales ($\tilde{\tau}_1, \tilde{\tau}_2$) in the so-called transition region. A third relaxation mechanism is identified for long timescales ($\tilde{\tau}_3$) in the so-called terminal region. This branched unentangled low molecular weight polymer owes its high mechanical properties below T_g to the presence of non-covalent n-n interactions in the hard blocks and, to a lesser extent, to side branch interactions in the soft blocks (see molecular architecture in Figure 3.1 and reference [19]) as has been demonstrated by combining rheology and NMR [20]. In a near- T_g healing polymer as ODPA-p1.0, with a known and relatively simple polymer architecture, it is possible to allocate the transition region relaxations ($\tilde{\tau}_1, \tilde{\tau}_2$) to short range main chain segmental mobility and to the opening of a transient network constituted by physical reversible interactions among dianhydride aromatic units. Here, $\tilde{\tau}_1$ is attributed to the main chain segmental mobility as these relaxation phenomena at such short time scales require low energetic main chain conformation rearrangements incompatible with physical crosslinks. It follows that $\tilde{\tau}_2$ can be associated to aromatic interactions disjunction. Ultimately, ODPA-p1.0 being a non-crosslinked polymer, the terminal relaxation ($\tilde{\tau}_3$) is associated to sticky chain reptation, when the chain is able to escape its 'tube' [20]. In analogy to our analysis of ODPA-p1.0 the three relaxation events observed in the other polymers with comparable architecture, namely ODPA-p0.9 (Figure 3.3A), 6FDA-p1.0 (Figure 3.3C), BPADA-p1.0 (Figure 3.3D), can be associated to main chain segmental mobility ($\tilde{\tau}_1$), physical network dissociation given by aromatics interactions ($\tilde{\tau}_2$), and chain reptation ($\tilde{\tau}_3$).

The results and analysis is somewhat different for the case of the polymer including an extra polymer feature (H-bonding), namely C9PA. In this case the optimum number of relaxation events is four ($i_{optimum} = 4$) as shown in Figure 3.3E and confirmed by the values of r^2 as presented in Table 3.2. For this polymer, a broad transition region with a higher relaxation strength (absolute value of $H(\tau)$) at short-intermediate timescales can be observed. The optimized fitting reveals three deconvoluted relaxation events ($\tilde{\tau}_1, \tilde{\tau}_2, \tilde{\tau}_3$) in the broad transition region present at short-intermediate timescales, although it should be noted that two of these strongly overlap in the time domain ($\tilde{\tau}_2, \tilde{\tau}_3$), possibly suggesting that these relaxation mechanisms are cooperatively contributing to one dominant dynamic process.

Based on the molecular design and on the optimisation of the dominant relaxation mechanisms through the protocol ($i_{optimum} = 4$), the relaxations can be attributed to the overlap of main chain segmental mobility ($\tilde{\tau}_1$) and the disengagement of a double transient network constituted by hydrogen bonds between the amide units and those between the aromatics ($\tilde{\tau}_2, \tilde{\tau}_3$). The strong overlap of these two suggests these phenomena are strongly bound to each other, which is not surprising considering the proximity of the two responsible segments in the polymer architecture (Figure 3.1). $\tilde{\tau}_4$ at long timescales is attributed to terminal relaxation.

3.4.2. Physical meaning of the fitting parameters

The relaxation spectrum $H(\tau)$ has the nature of a distribution function, even though it has the dimension of a modulus rather than the dimensionless character of a common distribution function. Strictly speaking h is defined as: $h = H / G_g$ where G_g is the stress/strain ratio for an instantaneous deformation [13]. Considering τ^* as a generic relaxation time, the absolute value of the relaxation spectrum $|H(\tau^*)|$ is proportional to the energy dissipation at that time location. For this reason, the area under the distribution curve $H(\tau)$ is proportional to the energy stored during the relaxation process and therefore to the plateau of G' obtained by macro-rheology. Hence a physical meaning can be bestowed onto the fitting parameters obtained. In particular, for a certain relaxation mechanism i , $\tilde{\tau}_i$ defines the relaxation time corresponding to the maximum of dissipation so it regulates the kinetics of the relaxation transition. The ratio A_i/σ_i is the area under the curve of the individual relaxation event and is therefore related to the energy stored in the system related to the relaxation transition i and is proportional to G_g (stress/strain ratio for an instantaneous deformation). We will refer to the ratio A_i/σ_i as "energy distribution shape" parameter. In this manner we can correlate the macroscopic healing behaviour to quantifiable data extracted from the fitting protocol.

In self-healing polymers, a precise indication of supramolecular bond lifetime (τ_b) is fundamental to understand the timescale of the interfacial wetting step of the healing process [11]. For the set of SH-PIs, $\tilde{\tau}_2$ was associated to the opening of a transient network consisting of aromatics interactions. The $\tilde{\tau}_2$ results obtained with the protocol implementation (Table 3.3) are consistent with the intermediate range of bond lifetime ($1 < \tau_b < 100$ s) previously reported for functional (and self-healing) supramolecular polymers [11, 36]. This confirms the hypothesis of the existence of a short-term healing step consisting of interfacial wetting, followed by a long-term chain interdiffusion and randomization related to terminal flow originally proposed by Wool and co-workers [37].

The broadening of the transition region in C9PA when compared to the analysed SH-PIs can be evaluated quantitatively by analysing the difference in the ratio of the fitting parameters A_2/σ_2 shown in the summary table, **Table 3.4**. The increase in the value of A_2/σ_2 can be attributed to the additional amount of dissipated energy necessary to open up the double transient network (or stronger physical crosslinks due to the presence of two supramolecular features).

Similarly, the ratio A_1/σ_1 can be related to the main chain rigidity. This transition is attributed to the main chain segmental mobility. So, for polymers with a higher

Table 3.4: **Ratio of the fitting parameters A_i/σ_i for the SH-PIs and SH-PA as obtained by the application of the deconvolution protocol.** The ratio A_i/σ_i is proportional to G_g and so it is related to the energy stored by the system to accomplish each relaxation transition.

Relaxation mechanisms	$i_{optimal}$	Polymer	A_1/σ_1 (MPa)	A_2/σ_2 (MPa)	A_3/σ_3 (MPa)	A_4/σ_4 (MPa)
1) Segmental mobility	3	ODPA-p0.9	5.16	2.53	0.76	-
2) Aromatics		ODPA-p0.9	24.6	1.94	0.36	-
3) Terminal relaxation		6FDA-p1.0	25.0	2.09	0.69	-
		BPADA-p1.0	17.6	8.41	1.86	-
1) Segmental mobility	4	C9PA	19.72	23.48	23.48	0.34
2) Aromatics						
3) H-bonds						
4) Terminal relaxation						

main chain flexibility we reasonably expect a lower amount of energy stored by the system to accomplish the relaxation. Considering the series of SH-PIs, Control group 2, the highest chain flexibility of BPADA-p1.0 (DRF = 2) is linked to the lowest stored energy A_1/σ_1 (Table 3.4 and **Figure 3.5**). Analogously the higher chain flexibility of ODPA-p1.0 (DRF = 1) when compared to 6FDA-p1.0 (DRF = 0) results in a relative lower A_1/σ_1 (Table 3.4 and Figure 3.5). So, fundamental arguments along with experimental evidence seems to confirm the physical meaning assigned to the optimized fitting parameters.

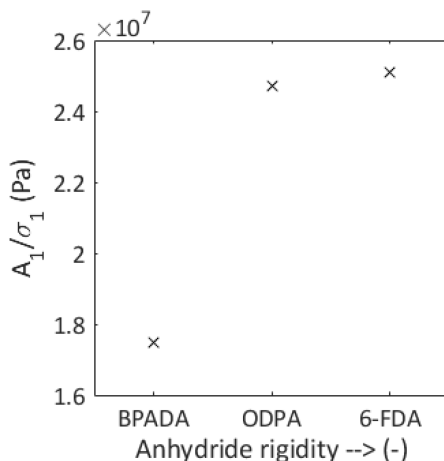


Figure 3.5: **Maxwell-Weichert model best fit of energy distribution shape related to main chain segmental mobility (A_1/σ_1) for SH-PIs Control group 2 with increasing main chain rigidity.** Higher energy stored by the system to accomplish the relaxation transition corresponds to higher main chain rigidity.

3.4.3. Relating fitting protocol outcome to self-healing efficiency

Theoretical studies by Wool and co-authors [37, 38] demonstrate that in non-crosslinked polymers crack-healing consists of five steps: segmental surface rearrangements, surface approach, wetting, diffusion, and randomization. The reptation model theory semi-quantifies such healing events and shows that the recovery of the fracture stress is related to molecular weight M and time t via $\sigma \propto (t/M)^{1/4}$. While this dependence on time and molecular weight was experimentally shown for crack healing poly(methylmethacrylate) (PMMA) and supramolecular elastomers [39], it is not reflected in the series of SH-PIs as has been reported elsewhere [19, 20]. Using healing efficiency (HE) as $HE = \frac{\varepsilon_{b,healed}}{\varepsilon_{b,pristine}}$ with ε_b being strain at break, as an indicator for healing efficiency there is no real correlation between the number molecular weight (M_n) shown in Table 3.1 ($M_{n,ODPA-p} < M_{n,BPADA-p} < M_{n,6FDA-p}$) and the experimental long term healing data extrapolated by tensile mechanical data shown in **Figure 3.6** ($HE_{BPADA-p} < HE_{6FDA-p} < HE_{ODPA-p}$) nor with the terminal relaxation values from the macro-rheology tests where shorter timescales are obtained for BPADA-p1.0 compared to 6FDA-p1.0 and ODPA-p1.0 [19].

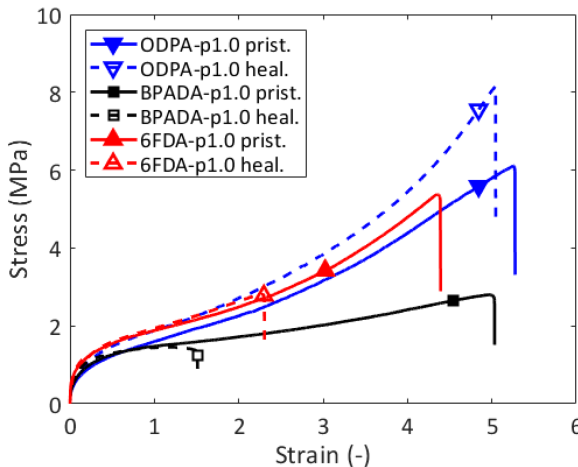


Figure 3.6: **Mechanical tensile testing of pristine and healed PI Control Group 2 after 11 days at $T_{healing} = T_g$.**

Interestingly, the analysis of the fitting protocol relaxation times ($\tilde{\tau}_i$) from Table 3.3 gives similarly contradicting results. As shown in **Figure 3.7A-B** (empty markers), low values of healing efficiency corresponds to the shorter timescales of BPADA-p1.0 polymer (low values of τ_2 and τ_3), while high healing efficiency corresponds to the longer timescales of 6FDA-p1.0 and ODPA-p1.0.

The weak agreement between theory, macro-rheology and long term healing experiments can be accounted for by the fact that the reptation model proposed by Wool does not consider bond cleavage and intermolecular interactions. We ar-

gue that this information can be inferred by the analysis of the energy distribution shape parameter (A / σ). As discussed in Section 3.4.2, the energy distribution shape parameter (A / σ) reflects the energy that the system stores during the relaxation transition. Therefore in our analysis the ratio A_2 / σ_2 is attributed to the energy needed to break the reversible interactions among aromatics and A_3 / σ_3 is attributed to the energy needed for chain interdiffusion. If bonds cleavage and intermolecular interactions play a major role in the determining high healing efficiency, then low A / σ values should yield high healing efficiency. In other words, less energy must be stored by the system to relax and self-heal. Effectively, as shown in Figure 3.7B (filled markers), we indeed found this correspondence: lower A_2 / σ_2 and A_3 / σ_3 values belong to high healing efficiency polymers.

An independent estimation of the energy stored by the system in the overall relaxation process can be obtained using the William-Landel-Ferry fit to the experimental rheological shift factors [13]. The results of the calculation are shown in **Figure 3.9A-B**. For the spectrum of shifted temperatures, $\Delta H_{\text{apparent}}$ follows the trend of the energy values obtained from the fitting as shown in Figure 3.7 and healing efficiency.

Similar considerations can be made when comparing two PIs with different branched monomer/aromatic dianhydride (Priamine/ODPA) ratios. In these polymers there is also no agreement between macroscopic healing efficiency, macrorheology and fitting protocol relaxation time ($\tilde{\tau}_i$ trend represented in **Figure 3.8B**). However the trend of A_3/σ_3 (Figure 3.8C) and $\Delta H_{\text{apparent}}$ of the overall relaxation process computed through WLF fit of the shifted data (Figure 3.9C-D) are in mutual agreement and in accordance with the macroscopic healing data reported in Figure 3.8A.

In conclusion, while high chain flexibility and fast relaxation time constants seem to govern the first stage of self-healing (interfacial healing) [40], we show for the first time in a quantitative manner for a number of polymers that the energy stored by the system during the healing process is crucial when considering the design of efficient self-healing polymers because it regulates reversible bond cleavage and chain interdiffusion. The fitting protocol developed offers a simple way of identifying individual relaxation contributions and estimating the energetic contribution to the involved relaxation processes.

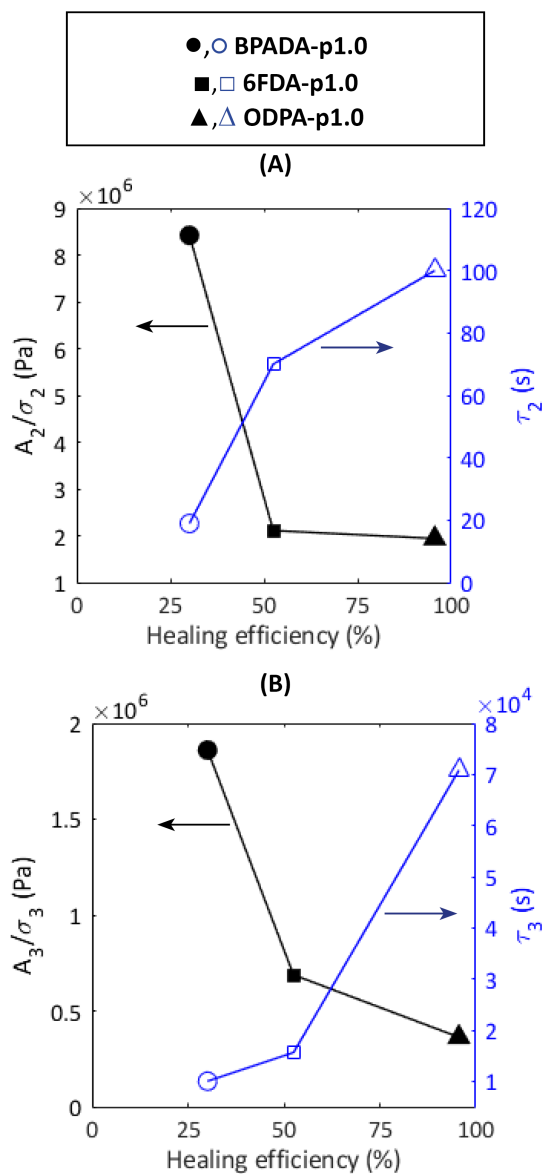


Figure 3.7: **Energy distribution shape (A/σ) and relaxation time constants (τ) as obtained for SH-PIs Control group 2 and related long term (11 days) healing efficiency. (A) Parameters related to reversible interactions among aromatics ($A_2/\sigma_2, \tau_2$). (B) Parameters related to the chain interdiffusion transition ($A_3/\sigma_3, \tau_3$).**

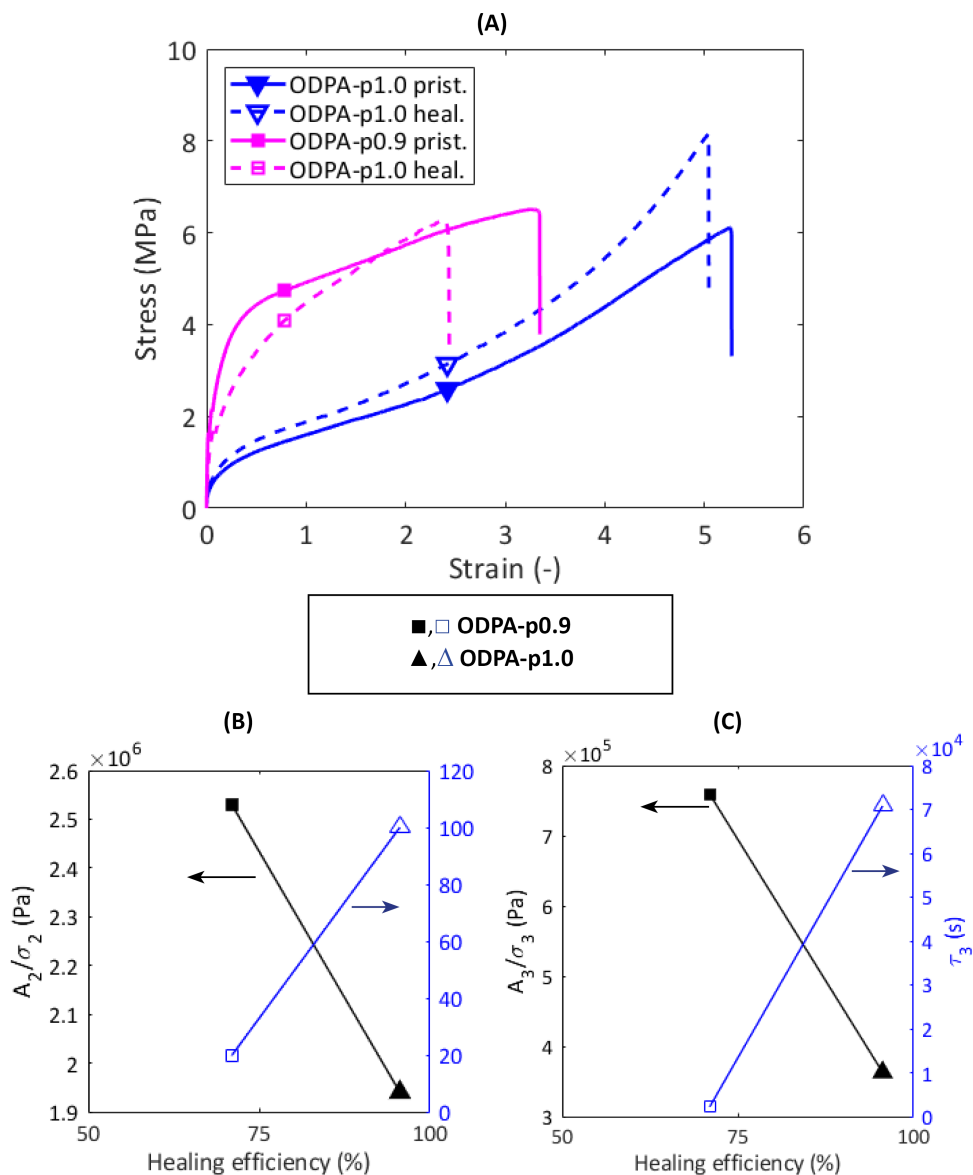


Figure 3.8: **Mechanical properties and energy distribution parameters for SH-PIs Control group 1.** (A) Mechanical tensile testing of pristine and healed SH-PIs Control group 1 after 11 days at $T_{healing} = T_g$. (B-C) Energy distribution shape and relaxation time constants as obtained for Control group 1. (B) Parameters related to reversible interactions among aromatics (A_2 / σ_2 , τ_2). (C) Parameters related to the chain interdiffusion transition (A_3 / σ_3 , τ_3).

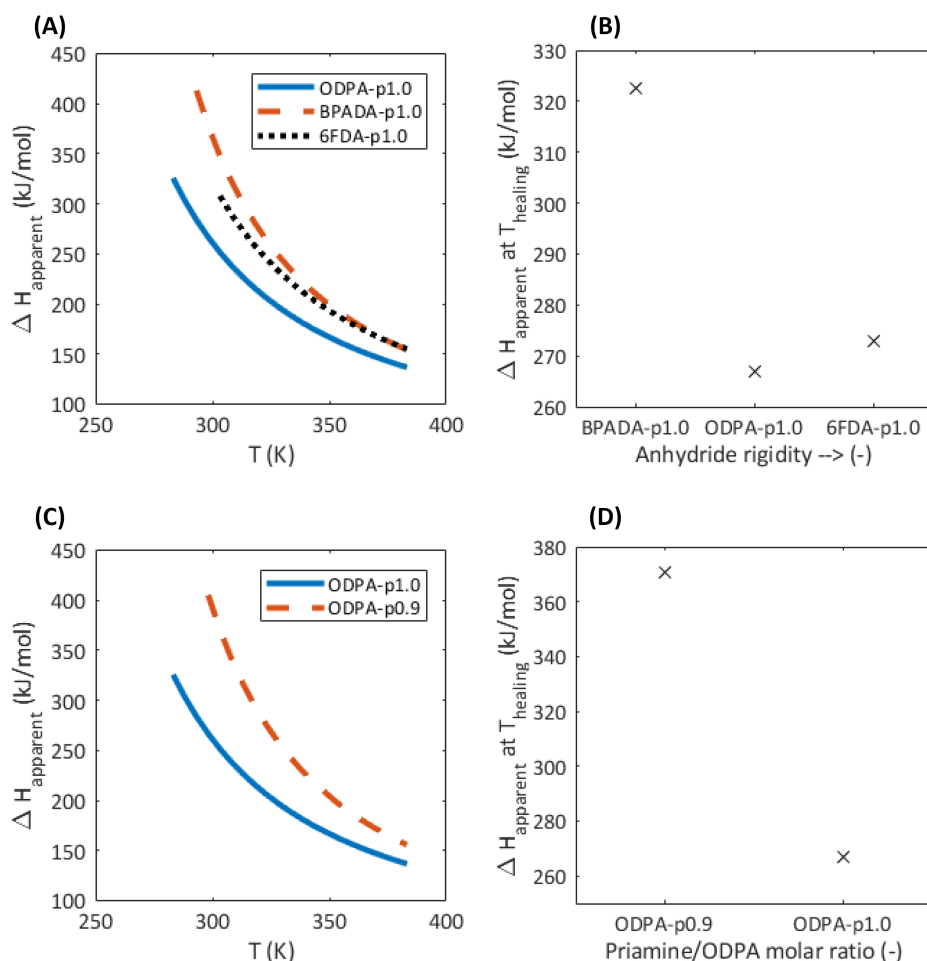


Figure 3.9: **Apparent enthalpy of relaxation transition computed through the WLF fit of experimental rheology frequency master curves. (A-B) Effect of the dianhydride type. (C-D) Effect of the ODP/Priamine molar ratio.** The enthalpy barrier increases with higher degrees of rotational freedom and with lower amount of branched diamine, acting as limiting factor on the long term healing behaviour of the SH-PIs.

3.5. Conclusions

We successfully developed and implemented a deconvolution protocol of the conventional macro-rheology master curve. This approach enables the determination of the number of individual relaxations related to different polymer features contributing to the overall relaxation spectrum, showing for the first time a clear separation between the relaxation timescales associated to main-chain segmental mobility and reversible lateral interactions in near- T_g polymers. The concept was proven for a set of self-healing polyimides (SH-PIs), a self-healing polyamide (C9PA) and

a non-healing reference polyamide (Linear-PA). For these polymers the protocol accurately identified the overlapping relaxation dynamics attributed to main chain segmental mobility and a number of supramolecular interactions as well as the terminal relaxation. The continuous relaxation spectrum unveiled some features that could not have been inferred from classical representations of linear viscoelastic data.

The approach bridges an existent gap between the macro-rheological analysis based on relaxation timescales and the macroscopic healing data and opens the way to predicting the long term macroscopic healing behaviour as a function of the polymer architecture. With the method presented here we can identify the effect of the implementation of a number of reversible chemistries on the rheological relaxation mechanics and therefore on the healing behaviour. This should allow a more meaningful and more effective design of self-healing polymers.

References

- [1] M. D. Hager, P. Greil, C. Leyens, S. van der Zwaag, and U. S. Schubert, *Self-healing materials*, *Advanced Materials* **22**, 5424 (2010).
- [2] P. Cordier, F. Tournilhac, C. Soulié-Ziakovic, and L. Leibler, *Self-healing and thermoreversible rubber from supramolecular assembly*, *Nature* **451**, 977 (2008).
- [3] F. Herbst, S. Seiffert, and W. H. Binder, *Dynamic supramolecular poly (isobutylene)s for self-healing materials*, *Polymer Chemistry* **3**, 3084 (2012).
- [4] S. D. Bergman and F. Wudl, *Mendable polymers*, *Journal of Materials Chemistry* **18**, 41 (2008).
- [5] W. Post, A. Cohades, V. Michaud, S. van der Zwaag, and S. J. Garcia, *Healing of a glass fibre reinforced composite with a disulphide containing organic-inorganic epoxy matrix*, *Composites Science and Technology* **152**, 85 (2017).
- [6] S. Bode, L. Zedler, F. H. Schacher, B. Dietzek, M. Schmitt, J. Popp, M. D. Hager, and U. S. Schubert, *Self-healing polymer coatings based on crosslinked metallosupramolecular copolymers*, *Advanced Materials* **25**, 1634 (2013).
- [7] S. J. Benight, C. Wang, J. B. Tok, and Z. Bao, *Stretchable and self-healing polymers and devices for electronic skin*, *Progress in Polymer Science* **38**, 1961 (2013).
- [8] D. Y. Wu, S. Meure, and D. Solomon, *Self-healing polymeric materials: a review of recent developments*, *Progress in polymer science* **33**, 479 (2008).
- [9] T. McLeish, *Tube theory of entangled polymer dynamics*, *Advances in physics* **51**, 1379 (2002).
- [10] M. Van Gorp and J. Palmen, *Time-temperature superposition for polymeric blends*, *Rheol. Bull* **67**, 5 (1998).

- [11] R. K. Bose, N. Hohlbein, S. J. Garcia, A. M. Schmidt, and S. van der Zwaag, *Connecting supramolecular bond lifetime and network mobility for scratch healing in poly (butyl acrylate) ionomers containing sodium, zinc and cobalt*, *Physical Chemistry Chemical Physics* **17**, 1697 (2015).
- [12] R. K. Bose, N. Hohlbein, S. J. Garcia, A. M. Schmidt, and S. van der Zwaag, *Relationship between the network dynamics, supramolecular relaxation time and healing kinetics of cobalt poly (butyl acrylate) ionomers*, *Polymer* **69**, 228 (2015).
- [13] J. D. Ferry, *Viscoelastic properties of polymers* (John Wiley & Sons, 1980).
- [14] J. M. Dealy, D. J. Read, and R. G. Larson, *Structure and rheology of molten polymers: from structure to flow behavior and back again* (Carl Hanser Verlag GmbH Co KG, 2018).
- [15] K. M. Kirkwood, L. G. Leal, D. Vlassopoulos, P. Driva, and N. Hadjichristidis, *Stress relaxation of comb polymers with short branches*, *Macromolecules* **42**, 9592 (2009).
- [16] M. Kapnistos, D. Vlassopoulos, J. Roovers, and L. Leal, *Linear rheology of architecturally complex macromolecules: Comb polymers with linear backbones*, *Macromolecules* **38**, 7852 (2005).
- [17] S. Bode, M. Enke, R. Bose, F. Schacher, S. J. Garcia, S. van der Zwaag, M. Hager, and U. Schubert, *Correlation between scratch healing and rheological behavior for terpyridine complex based metallopolymers*, *Journal of Materials Chemistry A* **3**, 22145 (2015).
- [18] A. Susa, R. Bose, A. M. Grande, S. van der Zwaag, and S. J. Garcia, *Effect of the dianhydride/branched diamine ratio on the architecture and room temperature healing behavior of polyetherimides*, *ACS applied materials & interfaces* **8**, 34068 (2016).
- [19] A. Susa, J. Bijleveld, M. Hernandez Santana, and S. J. Garcia, *Understanding the effect of the dianhydride structure on the properties of semiaromatic polyimides containing a biobased fatty diamine*, *ACS sustainable chemistry & engineering* **6**, 668 (2018).
- [20] A. Susa, A. Mordvinkin, K. Saalwächter, S. van der Zwaag, and S. J. Garcia, *Identifying the role of primary and secondary interactions on the mechanical properties and healing of densely branched polyimides*, *Macromolecules* **51**, 8333 (2018).
- [21] J. Wu, L.-H. Cai, and D. A. Weitz, *Tough self-healing elastomers by molecular enforced integration of covalent and reversible networks*, *Advanced materials* **29**, 1702616 (2017).

- [22] B. Gold, C. Hövelmann, N. Lühmann, N. Székely, W. Pyckhout-Hintzen, A. Wischniewski, and D. Richter, *Importance of compact random walks for the rheology of transient networks*, ACS Macro Letters **6**, 73 (2017).
- [23] L. Leibler, M. Rubinstein, and R. H. Colby, *Dynamics of reversible networks*, Macromolecules **24**, 4701 (1991).
- [24] F. Herbst, D. Döhler, P. Michael, and W. H. Binder, *Self-healing polymers via supramolecular forces*, Macromolecular rapid communications **34**, 203 (2013).
- [25] M. Ahmadi, L. G. Hawke, H. Goldansaz, and E. Van Ruymbeke, *Dynamics of entangled linear supramolecular chains with sticky side groups: Influence of hindered fluctuations*, Macromolecules **48**, 7300 (2015).
- [26] Q. Chen, Z. Zhang, and R. H. Colby, *Viscoelasticity of entangled random polystyrene ionomers*, Journal of Rheology **60**, 1031 (2016).
- [27] M. J. Mateyisi, J.-U. Sommer, K. K. Müller-Nedebock, and G. Heinrich, *Influence of weak reversible cross-linkers on entangled polymer melt dynamics*, The Journal of Chemical Physics **148**, 244901 (2018).
- [28] S. Ankiewicz, N. Orbey, H. Watanabe, H. Lentzakis, and J. Dealy, *On the use of continuous relaxation spectra to characterize model polymers*, Journal of Rheology **60**, 1115 (2016).
- [29] V. Yesilyurt, A. M. Ayoob, E. A. Appel, J. T. Borenstein, R. Langer, and D. G. Anderson, *Mixed reversible covalent crosslink kinetics enable precise, hierarchical mechanical tuning of hydrogel networks*, Advanced Materials **29**, 1605947 (2017).
- [30] B. Reck and H. Ringsdorf, *Combined liquid-crystalline polymers: Rigid rod and semiflexible main chain polyesters with lateral mesogenic groups*, Die Makromolekulare Chemie, Rapid Communications **7**, 389 (1986).
- [31] J. Honerkamp and J. Weese, *A nonlinear regularization method for the calculation of relaxation spectra*, Rheologica acta **32**, 65 (1993).
- [32] I. McDougall, N. Orbey, and J. M. Dealy, *Inferring meaningful relaxation spectra from experimental data*, Journal of Rheology **58**, 779 (2014).
- [33] T. Roths, M. Marth, J. Weese, and J. Honerkamp, *A generalized regularization method for nonlinear ill-posed problems enhanced for nonlinear regularization terms*, Computer physics communications **139**, 279 (2001).
- [34] M. Baumgaertel and H. Winter, *Determination of discrete relaxation and retardation time spectra from dynamic mechanical data*, Rheologica Acta **28**, 511 (1989).
- [35] A. Davies and R. S. Anderssen, *Sampling localization in determining the relaxation spectrum*, Journal of Non-Newtonian Fluid Mechanics **73**, 163 (1997).

- [36] T. Aida, E. Meijer, and S. Stupp, *Functional supramolecular polymers*, *Science* **335**, 813 (2012).
- [37] R. Wool and K. O'Connor, *A theory crack healing in polymers*, *Journal of applied physics* **52**, 5953 (1981).
- [38] Y. H. Kim and R. P. Wool, *A theory of healing at a polymer-polymer interface*, *Macromolecules* **16**, 1115 (1983).
- [39] A. M. Grande, S. J. Garcia, and S. van der Zwaag, *On the interfacial healing of a supramolecular elastomer*, *Polymer* **56**, 435 (2015).
- [40] Y. Yang and M. W. Urban, *Self-healing polymeric materials*, *Chemical Society Reviews* **42**, 7446 (2013).

4

Linking interfacial work of deformation from deconvoluted macro-rheological spectrum to early stage healing in selected polyurethanes

*In questa terra oscura, senza peccato e senza redenzione,
dove il male non è morale, ma è un dolore terrestre,
che sta per sempre nelle cose,
Cristo non è disceso.
Cristo si è fermato a Eboli.*

Carlo Levi

Abstract

The use of rheology and terminal flow relaxation times to predict healing behavior at long healing times is by now quite well accepted. In this work we go one step further and explore the use of macro-rheology (in particular the stored work of deformation) to predict the early stage interfacial healing properties (fracture resistance) of a set of self-healing polyurethanes. The interfacial healing is measured by single edge notch fracture experiments, using short healing times and a low healing temperature to exclude the effect of long range molecular motion on mechanical properties restoration. The systems based on aromatic diisocyanates show high fracture resistance after healing, while very limited restoration of the mechanical properties is observed for aliphatic and cycloaliphatic based polyurethanes. Linear sweep rheology and time-temperature-superposition allow obtaining the macro-rheological master curve and the mechanical relaxation spectra $H(t)$. The application of a recently established deconvolution protocol to the $H(t)$ gives the characteristic relaxation times and stored works of deformation associated to individual dynamic processes such as segmental motion, reversible bonds, and terminal flow. It is found that the calculated stored works of deformation related to the reversible bond relaxation reproduce the trend observed by fracture resistance at healed interfaces and reveal a qualitative correspondence between reversible bonds work of deformation and interfacial healing fracture resistance. Moreover, the method seems to point to the existence of a threshold interfacial work of deformation below which no efficient load transfer can be observed.

4.1. Introduction

The field of self-healing polymers has rapidly grown in recent times driven by increasing environmental concerns related to plastic overconsumption that boost the scientific research towards the development of alternatives to current commodities polymers, including functional and self-healing systems.

Many proofs of concepts have been presented exploiting the intrinsic healing approach. Intrinsic healing is addressed by the molecular design of the network in opposition to extrinsic systems which rely on the present of discretely dispersed carriers containing the healing agent [1, 2]. In order to exploit the intrinsic self-healing ability two requirements have to be fulfilled: (i) high density of reversible bonds to deconstruct and reconstruct the broken interface and (ii) sufficient chain mobility to facilitate local flow at the damage site. A number of reviews summarize how the incorporation of different reversible chemical and physical bonds can successfully lead to the production of self-healing polymers [3–6]. A careful analysis of these works evidences that the use of van der Waals [7, 8], π - π stacking [9] and/or microphase separation [10] could be used to turn commodity-like systems into self-healing variants without the introduction of severe chemical modifications. The healing action in intrinsic systems occurs in two successive stages: initial interface restoration by reversible bonds swapping and subsequent interphase healing by macromolecular diffusion [11]. In this work we aim to clarify the contribution of non-covalent reversible bonds to the initial recovery of interfacial strength. In a previous study we showed evidences that the incorporation of multiple reversible moieties (namely hydrogen bonding and disulphide exchange) with different association/dissociation kinetics strongly influence the early steps of healing, in which fast hydrogen bonding relaxation dynamics determines initial tack, and affect long term healing, when the opening of sulphur-sulphur bonds allows long range motion [12]. This issue is critical because it defines the design boundaries between systems with a very high density of reversible bonds but a sluggish terminal relaxation and polymers with fast terminal relaxation but a sparse physical network. Macro-rheology has been used to estimate the timescale of interphase diffusion and macroscopic crack closure by comparing the kinetics of these processes to the supramolecular bond lifetime ($\tau_b = 2\pi / \omega_{cr}$) of embedded reversible interactions [7, 13]. However, this method does not offer insights on the processes that govern the initial interface strength restoration. In this work we try to bridge this gap and explore how to extract more information from the rheological tests that can be used to predict early stage macroscopic healing strength. To do this we extend our deconvolution protocol of the mechanical relaxation spectrum constructed by rheology that allow to isolate the dynamics of individual molecular features [14], including the calculation of the stored work of deformation.

We explore the use of this approach to predict early stage interfacial healing properties of a set of polyurethanes, for which the recombination of reversible bonds at the deconstructed interface defines the initial tack. To this purpose, we use four diisocyanates (diphenylmethane 4,4' diisocyanate MDI, 1,4-phenylene diisocyanate PPDI, hexamethylene diisocyanate HDI, 4,4'-methylenebis(cyclohexyl) isocyanate HMDI) with different symmetry and aromaticity to selectively incorporate multiple reversible

interactions in the network (hydrogen bonding from the urethane linkage and aromatic interactions from the isocyanates) and to study the effect of the monomer symmetry on the fracture resistance restoration using the single edge notch tensile (SENT) protocol [15–17].

4.2. Experimental Section

4.2.1. Materials

2-Ethyl-1,3-hexanediol (EHD, 99%), diphenylmethane 4,4' diisocyanate (MDI, 98%), 1,4-phenylene diisocyanate (PPDI), hexamethylene diisocyanate (HDI, >98%), 4,4'-methylenebis(cyclohexyl isocyanate) (HMDI, mixture of isomers 90%), dibutyltin dilaurate (DBTDL, 95%) were purchased from Sigma-Aldrich. CroHeal 2000™ (equivalent molecular weight 2000 g/mol) was kindly provided from Croda Nederland B.V.

4.2.2. Synthesis of segmented polyurethanes

Four polyurethanes were synthesized by single shot technique reacting CroHeal 2000, EHD and different diisocyanates (MDI, PPDI, HDI, HMDI). The diisocyanates were selected considering increasing level of aromaticity $\text{HMDI} = \text{HDI} < \text{PPDI} < \text{MDI}$, and symmetry $\text{HMDI} \cong \text{MDI} < \text{PPDI} \cong \text{HDI}$. For all the polymers the molar ratio of the hydroxyl chemical functionalities OH (CroHeal 2000) : OH (EHD) was kept fixed at 1 : 0.6. 10% molar excess of NCO was used to carry the reaction to full completion. Samples are coded by the name of the isocyanate used followed by the addition '-p' to distinguish the polymer from the monomer (e.g. MDI based polymer is coded as MDI-p). Below we report the synthesis of polymer MDI-p. Analogous procedures were followed for the other polymers in this study. Details on their syntheses are reported in the Supplementary Material. The molecular structure of the segmented polyurethanes is schematically represented in **Figure 4.1**.

CroHeal 2000 was heated for 1 hour at 90 °C to reduce the intrinsic viscosity of the monomer (melting the ordered domains). Subsequently 90.0 grams (45.0 mmol) were transferred to a 300 mL polypropylene cup. 3.95 g of EHD (27.0 mmol) were then added to the cup. 31.64 g (79.20 mmol) of MDI were weighted in a separate 25 mL polypropylene cup, purged under nitrogen inert environment and heated 1 hour at 60 °C to reduce its intrinsic viscosity (melting crystalline domains). The MDI was rapidly poured into the main reaction cup (containing CroHeal 2000 and EHD). The mixture was sheared under vacuum at 2300 rpm for 135 seconds using a vacuum assisted high speed mixer (SpeedMixer™ DAC 400.2 VAC-P). The application of high vacuum (pressure below 100 mbar) turned out to be critical for the formation of bubble-free polymers. The mixture was then transferred to a 20x20x0.2 cm PTFE mold, equilibrated for 30 minutes at ambient conditions and subsequently cured overnight at 60 °C. The obtained bulk polymers were then equilibrated for 1 week at ambient conditions before testing.

The degree of completion of the polyurethane synthesis was monitored by Attenuated Total Reflectance Fourier transform Infrared (ATR-FTIR) analysis by monitoring the appearance of the characteristic carbonyl stretching absorption peak at

$\approx 1700 \text{ cm}^{-1}$ and the disappearance of isocyanate absorption peak at about $\approx 2270 \text{ cm}^{-1}$. ATR-FTIR spectra of all synthesized polymers are shown in Figure S1.

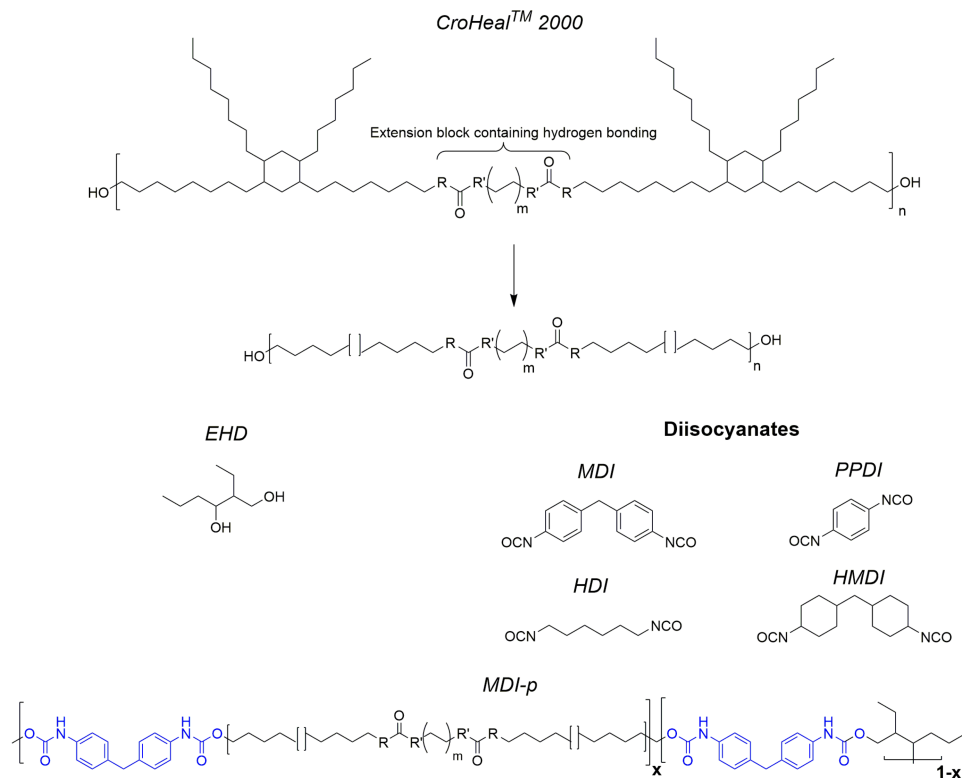


Figure 4.1: **Monomers used and molecular structure of synthesized segmented polyurethanes.** (MDI-p is shown as mode of example).

4.2.3. Characterisation Methods

Rheology and mechanical relaxation spectrum deconvolution protocol

Temperature sweep and frequency sweep tests were performed to build the rheological master curves, applying the time-temperature superposition principle (TTS). A Haake Mars III rheometer (ThermoScientific) was used, employing a parallel plate geometry (plate diameter = 8 mm). The data obtained at different temperatures were shifted using Reptate software (University of Leeds, gplv3 license). On the basis of preliminary strain amplitude sweep measurements the shear strain amplitude was set to 0.1%. Frequency sweep experiments from 10 to 0.1 Hz were performed with steps of $\Delta T = 10^\circ \text{C}$ over the temperature range from -20 to 200°C for MDI-p and PPDI-p, steps of $\Delta T = 10^\circ \text{C}$ were used for HDI-p in the range -20 to 170°C and steps of $\Delta T = 10^\circ \text{C}$ were used for HMDI-p in the range -20 to 70°C . The isotherms were shifted to the reference temperature $T_R = 30^\circ \text{C}$, corresponding to the temperature at which interfacial healing was observed and tested for all systems. The mechanical relaxation spectrum $H(t)$ was constructed applying the non-linear

regression method developed by Honerkamp and Weese [18, 19]. The source code of the algorithm can be found in the CPC Program library [20]. In this protocol, the minimum and maximum relaxation times are pre-selected by the user. In our case we simply set $\tau_{\min} = \frac{1}{\omega_{\max}}$ and $\tau_{\max} = \frac{1}{\omega_{\min}}$ where ω_{\max} and ω_{\min} are the highest and the lowest angular frequency in the modulus data, as suggested in the library user manual. The deconvolution protocol was performed following the procedure reported in *Chapter 3* (and ref. [14]). For all the deconvoluted spectra the coefficients of determination of the reconstructed mastercurve ($|r_G^2|$ and $|r_G'^2|$) exceed 0.9 confirming the high quality of the fit. Details of the protocol, including the calculation of stored work of deformation (W) are reported in the Supplementary Material.

4

Extension Dynamic mechanical analyses (DMA)

Dynamical mechanical experiments were carried out on a strain-controlled Q800 (TA Instruments) in tension mode. The gauge length used was ≈ 10 mm. The sample thickness was uniform per sample but varied between polymer grades between 0.45 to 1.0 mm. Temperature sweep analyses were carried out over the temperature range from -50 °C to 80 and 120 °C (depending on the thermal stability of the polymer) using a heating rate of 2.0 °C/min. All the tests were run at the fixed amplitude of 10 μm , which falls within the linear viscoelastic regime as established by the preliminary strain amplitude analyses.

Single edge notch tensile (SENT) fracture test

SENT fracture experiments were performed using an Instron Universal Tensile Testing machine equipped with a 1 kN load cell. Rectangular samples (70 x 20 mm) were cut with a die from 2 mm thick polymer sheets. A sharp pre-notch with length of 10 mm was made from the middle of the longest edge, perpendicularly to it, using a razor blade. The polymers were cooled for 1 hour at 2 °C prior to the damaging procedure, in order to produce sharp cut surfaces.

The mechanical tests were performed at a cross-head speed of 0.5 mm/s, allowing detailed observation of crack tip opening. The testing temperature was controlled using an environmental chamber (Instron) with a glass window using evaporating liquid nitrogen and was set at 10 °C. Optical snapshots at a frequency of 10 Hz were taken during testing using an Optomotive Velociraptor camera in order to observe crack opening and propagation. The camera was placed on a vibration damping tripod at ≈ 50 cm of distance from the sample.

The fracture properties were determined using the J-integral analysis method, as described elsewhere [12, 15, 21]. Critical fracture resistance values, J_c were calculated as:

$$J_c \left[\frac{\text{kJ}}{\text{m}^2} \right] = \frac{\eta U_c}{b(w-a)} \Big|_{u_c} \quad (4.1)$$

where U_c is the energy calculated as the area under the Load-Displacement curves at the terminal displacement u_c when the samples fail, η is the proportionality factor (a value of 0.9 was selected according to literature [21]); b , w , a are the sample thickness, sample width and pre-crack length respectively.

Preparation of healed specimens

Specimens for healing experiments were taken from pre-notched 70 x 20 mm samples used for SENT testing. The samples were completely fractured following a trajectory extending the pre-notch path, perpendicularly to the longest edge of the rectangular specimen. The fractured samples were immediately positioned in a PTFE mold and healed using a recirculating furnace for $\approx 3.6 \times 10^3$ s (1 hour), 8.64×10^4 s (1 day) and 1.2×10^6 (2 weeks) at 30 °C. During the healing procedure the actual pre-notch area was prevented to heal by placing a thin PTFE foil in between the broken surfaces, to avoid cross interface contact being re-established.

The healed samples were mechanically tested following the SENT procedure described in the experimental section to obtain a value for the critical fracture resistance after healing $J_C^{interfacial}$.

Thermal Analyses

Thermal properties were determined by thermogravimetric analysis (TGA) and differential scanning calorimetry (DSC). TGA analyses were performed from room temperature to 600 °C, under dry nitrogen atmosphere at 10 °C/min heating rate using a Perkin Elmer TGA 4000. DSC measurements were performed under dry nitrogen atmosphere at 10 °C/min heating and cooling rates over the range from -40 °C to 200 °C using a Perkin Elmer Pyris Sapphire DSC. The glass transition temperature (T_g) was determined using the inflection point method.

Table 4.1 reports the results of TGA analyses and the DSC- T_g (glass transition). All polymers reported a high thermal stability (5% weight loss at $T > 350$ °C).

All systems showed a single endothermic transition in the DSC curve located between -5 and 10 °C which is attributed to the main chain segmental mobility. The relatively low content of EHD monomer feed is responsible for the absence of a high temperature first order thermal transition, generally attributed to the melting of the hard segment (chain extender + isocyanate) [22, 23].

Attenuated total reflectance infrared spectroscopy (ATR-FTIR)

Attenuated total reflectance Fourier transform infrared spectroscopy was used to follow synthesis completion and to study the state of hydrogen bonding in the proposed segmented polyurethanes. Each reported ATR-FTIR spectrum is the average of 32 scans over the wavenumber region 4000 – 500 cm^{-1} with resolution of 1 cm^{-1} . All the spectra are available in Figure S1.

Micro-attenuated total reflectance FTIR (μ ATR-FTIR)

μ ATR-FTIR spectra were recorded using a Perkin Elmer Spotlight 200i FTIR microscope system. A diamond ATR crystal was utilized. The spectra were collected with a 4 cm^{-1} spectral resolution and 16 accumulations, scanning an area of 300 to 500 μm^2 , in the wavenumber region 4000 – 750 cm^{-1} . The analysis was performed at a constant contact pressure between the ATR crystal and the sample. The spectral density was set at 1.56 μm allowing the imaging of μ -size network heterogeneities. Principal component analysis (PCA) was applied to identify spectral heterogeneities. The PCA is based on the generation of 8 principal spectral scores. The analysis was

Table 4.1: **Thermal analyses results.** The increase in the aromatic character of the diisocyanate monomer provokes an increase in thermal stability and retards main chain segmental mobility.

Polymer	TGA-5% weigh loss	DSC- T_g
MDI-p	353	5.2
PPDI-p	361	10.0
HMDI-p	353	-5.5
HDI-p	344	0.4

performed using the built-in function of the ImageSpectra software (Perkin Elmer).

4

4.3. Results and Discussion

4.3.1. Deconvolution protocol to unveil individual relaxations and related work of deformation

The first step to establish the relationship between the dynamics and energy storage of individual relaxation processes and the interfacial healing fracture resistance is the application of the deconvolution protocol to the mechanical relaxation spectrum following previous reports [14].

The resulting deconvoluted $H(t)$ with identified individual time constants are shown in **Figure 4.2** for the aromatic-based polyurethanes (MDI-p and PPDI-P) and in **Figure 4.3** for the aliphatic-based polyurethanes (HMDI-p, HDI-p). Starting from a known polymer architecture the method allows to assign a physical meaning to the relaxation mechanisms identified through the deconvolution. Figure 4.2A shows that five dominant relaxation mechanisms are obtained for MDI-p. Polyurethanes synthesized from a mixture of a high molecular weight diol (polyol), a low molecular weight diol (chain extender) and a diisocyanate may present a segmented structure. The segmented structure is physically described as hard phase regions, enriched with chain extender + diisocyanate segments, intercalated in a soft matrix, enriched of polyol + diisocyanate segments [24, 25]. The phase separated architecture is responsible for the elastomeric properties of this class of material, where the hard phase works as stable physical crosslinks of the polymer network (this systems are known as thermoplastic polyurethanes TPUs). These preliminary considerations are essential to infer the physical meaning of the five relaxation mechanisms deconvoluted for MDI-p. The first dynamic event (R_1) is associated to main chain segmental motion occurring in the soft matrix of the segmented polyurethane microstructure. As inferred from the molecular structure of this system, reversible bonds (hydrogen bonding and aromatic π - π stacking) are present in the soft phase. They are responsible of the second relaxation event (R_2). The transition part of the spectrum ($103 \text{ s} < \tau < 105 \text{ s}$) is dominated by relaxation of the hard blocks dispersed in the segmented microstructure. Hard blocks segmental motion (R_3) is followed by hydrogen bonds and aromatic π - π stacking relaxations (R_4). Thermoplastic elastomers present a strong but transient crosslinked network, therefore terminal relaxation can be observed but is very sluggish (R_5). The elastomeric

nature of MDI-p is confirmed by its mechanical behaviour, tested by SENT in the pristine state and shown as auxiliary data in Figure 4.2A. Analogous arguments follow the deconvolution of PPDI-p (Figure 4.2B) which shows five dominant relaxation mechanisms and mechanical features typical of a thermoplastic elastomer.

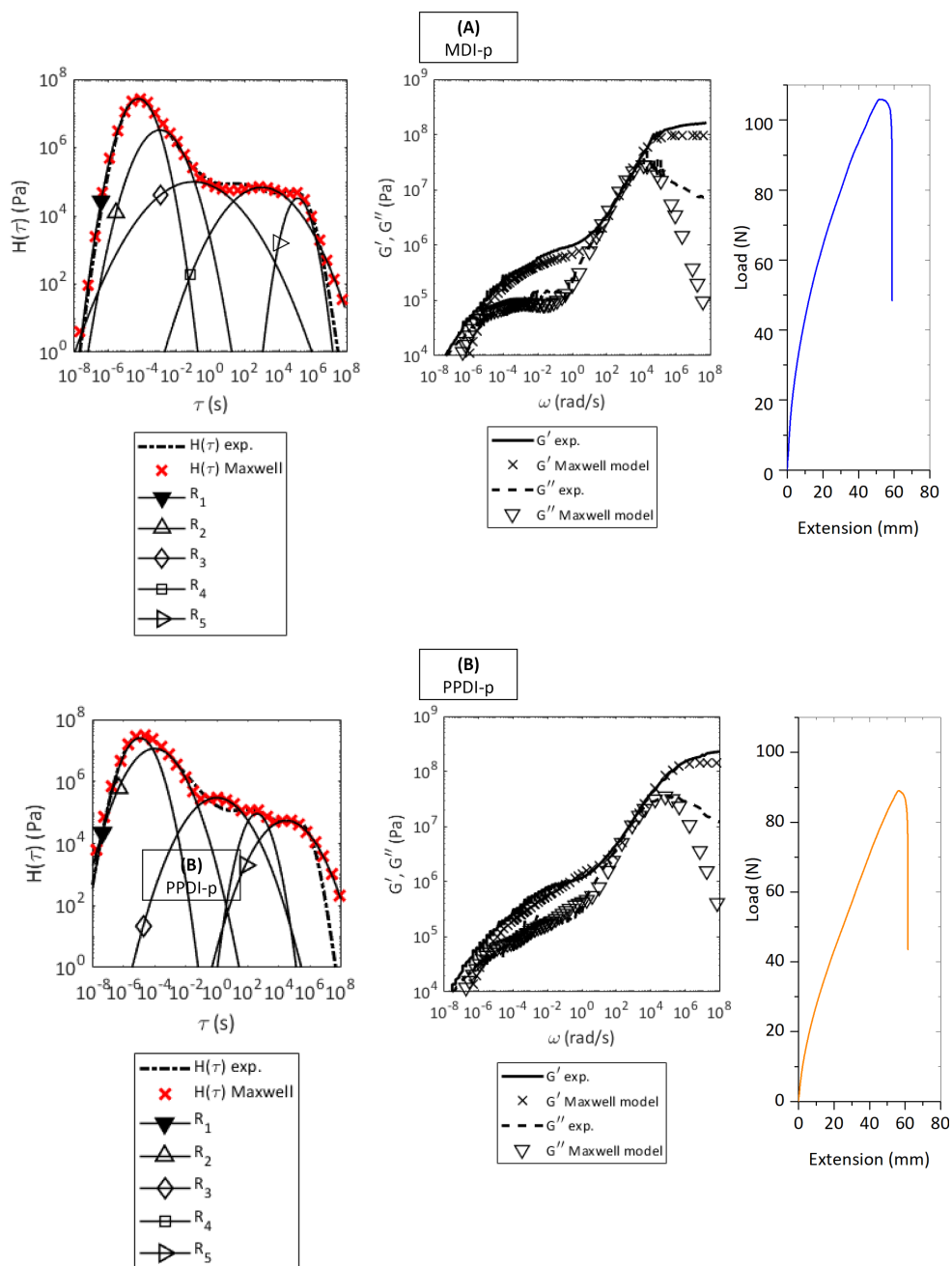


Figure 4.2: **Deconvoluted relaxation spectra, mastercurve reconstruction and SENT load-displacement data of MDI-p and PPDI-p.** (A) MDI-p. (B) PPDI-p. For both polymers the method identifies five dominant relaxation mechanisms. R_1 = soft phase segmental mobility. R_2 = soft phase reversible bonds disjunction. R_3 = hard phase segmental mobility. R_4 = hard phase reversible bonds disjunction. R_5 = terminal relaxation. Mechanical properties are typical of thermoplastic elastomers. The mastercurves are shifted at the reference temperature $T_R = 30$.

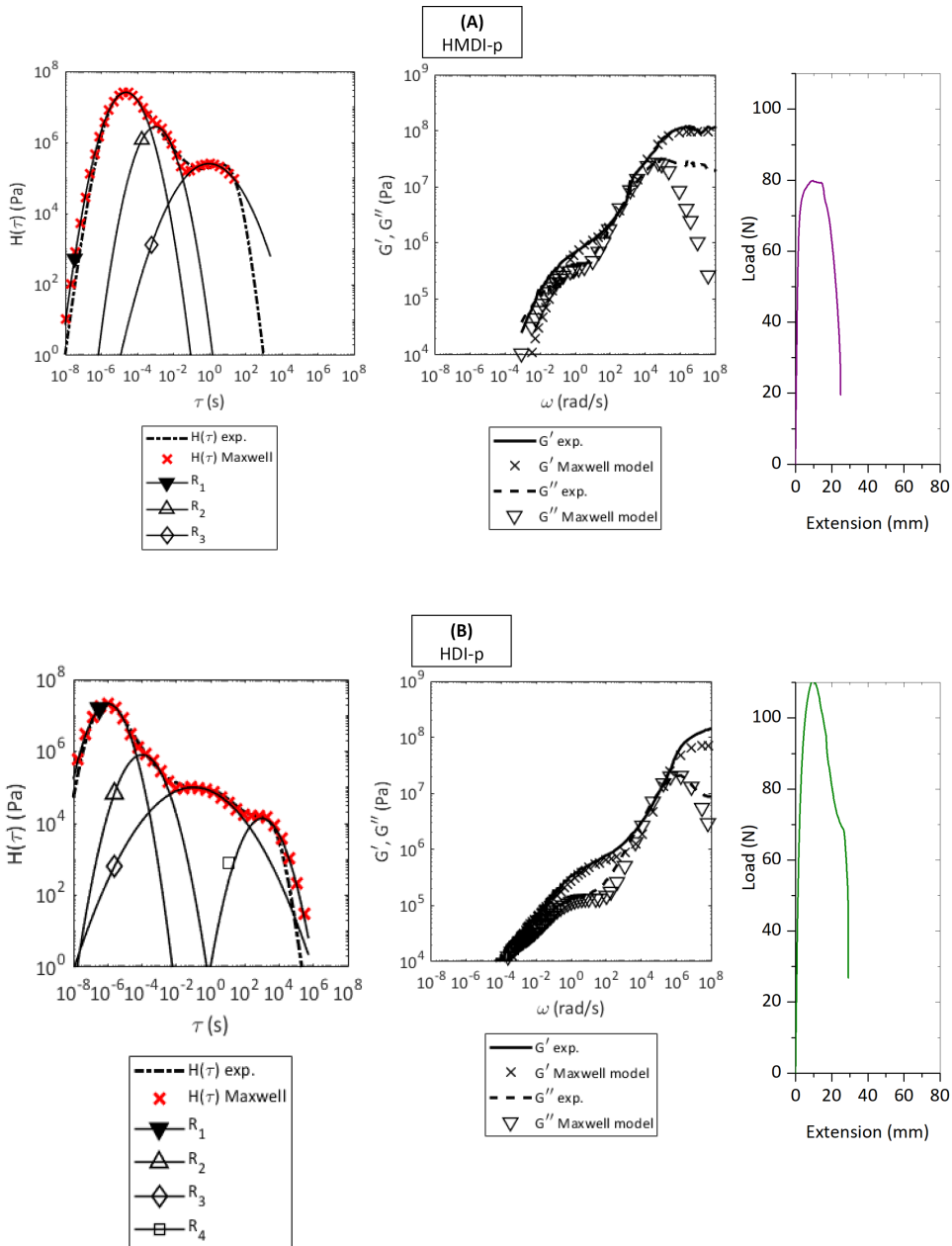


Figure 4.3: **Deconvoluted relaxation spectra, mastercurve reconstruction and SENT results of HMDI-p and HDI-p.** (A) HMDI-p. The deconvolution method identifies three dominant relaxation mechanisms. R_1 = main chain segmental mobility. R_2 = reversible bonds disjunction. R_3 = terminal relaxation. (B) HDI-p. The deconvolution method identifies three dominant relaxation mechanisms. R_1 = main chain segmental mobility. R_2 and R_3 = reversible bonds disjunction and quasi-crystalline melting. R_4 = terminal relaxation. The mechanical properties are typical of thermoplastic polymers.

The deconvolution procedure applied to HMDI-p results in a radically different outcome (Figure 4.3A). In this case only three main relaxation mechanisms can be identified with a complete disappearance of the wide transient region previously observed for MDI-p and PPDI-p. The deconvolution spectrum resembles the one of lightly crosslinked systems reported elsewhere [14]. The first dynamic process is attributed to main chain segmental motion (R_1), followed by a temporary restriction of mobility associated to entanglements and/or physical interactions (R_2) (e.g. hydrogen bonds) and rapid terminal relaxation (R_3). The absence of segmented structure and rubbery elasticity for HMDI-p is confirmed from static mechanical properties (auxiliary data in Figure 4.3A). Moreover, extensional DMA data for HMDI-p (Figure S4) show a complete absence of the rubbery plateau and terminal flow occurring at ≈ 60 °C, a typical feature of linear unentangled/lightly entangled networks [9, 26]. A similar description applies to the deconvolution of HDI-p, for which an optimal fit is found when assuming four relaxation mechanisms (Figure 4.3B). The additional relaxation mechanism located in the transient regime is related to the stacking of highly linear and symmetric HDI segments that determines crystalline-like ordered structures [27]. Nevertheless in analogy with HMDI-p, because of no aromatic entities being present there is no segmented microstructure. In parallel with HMDI-p, the mechanical SENT data of the pristine HDI-p sample shows the typical behaviour of linear networks and appearance of terminal flow in DMA analysis at about ≈ 100 °C (Figure S5).

Table 4.2 shows the quantitative data extracted from the deconvolution protocol in terms of kinetics of the relaxation transition (τ) and stored work of deformation (W). The information regarding the physical nature of the individual relaxation mechanisms is conveyed through the parameters subscript and superscript: W_{sp}^{seg} (soft phase segmental mobility) W_{sp}^{rev} (soft phase reversible bonds) W_{hp}^{seg} (hard phase segmental mobility) W_{hp}^{rev} (hard phase reversible bonds) W_t (terminal relaxation). $W_{interfacial}$ corresponds to the sum of all the works of deformation associated to reversible ligands relaxation ($W_{interfacial} = W_{sp}^{rev} + W_{hp}^{rev}$). This choice is based on the assumption that segmental motion/short range conformational re-arrangements do not contribute to the reconstruction of the broken interface. MDI-p and PPDI-p present comparable soft and hard segmental relaxation timescales. The slightly lower values for the kinetic parameters of PPDI-p are attributed to the higher rigidity and symmetry of the PPDI diisocyanate monomer when compared to MDI. The work of deformation related to reversible bonds in the soft phase (W_{sp}^{rev}) is higher for PPDI-p. Such an increase can be explained considering the rigid segment design and in particular to the reduced periodic distance among reversible bonding moieties (aromatic units and urethane linkages).

Beyond the reduced number of relaxation mechanisms obtained by the deconvolution process, HMDI-p deviates from MDI-p and PPDI-p in its rapid terminal relaxation kinetics ($\tau_t \cong 1$ s) and the reduced interfacial work of deformation ($W_{interfacial}$), an expected result when considering the absence of π - π stacking interactions among aromatics and therefore the formation of a weaker transient network. For the second aliphatic polyurethane (HDI-p), as qualitatively discussed in the previous paragraph, the slower terminal relaxation ($\tau_t \cong 103$ s) when compared to HMDI-p is

Table 4.2: Time constants and work of deformations associated to individual relaxation mechanisms.

Polymer	τ_{sp}^{seg} (s)	τ_{sp}^{rev} (s)	τ_{hp}^{seg} (s)	τ_{hp}^{rev} (s)	τ_t (s)
MDI-p	6.2 e-05	1.1 e-05	0.1	1.0 e+03	1.3 e+05
PPDI-p	1.1 e-05	1.0 e-04	1.0	0.3 e+03	3.1 e+04
HMDI-p	2.3 e-05	1.0 e-03	-	-	0.92
HDI-p	1.0 e-06	1.0 e-04	-	0.10	1.0 e+03

Polymer	W_{sp}^{seg} (kJ/m ³) x 10 ⁻¹	W_{sp}^{rev} (kJ/m ³) x 10 ⁻¹	W_{hp}^{seg} (kJ/m ³) x 10 ⁻¹	W_{hp}^{rev} (kJ/m ³) x 10 ⁻¹	W_t (kJ/m ³) x 10 ⁻¹	$W_{interfacial}$ (kJ/m ³) x 10 ⁻¹
MDI-p	579	120	6.9	12.9	3.4	132.9
PPDI-p	481	407	25.1	6.5	11.8	413.5
HMDI-p	512	73.1	-	-	19.5	73.1
HDI-p	356	23.6	-	12.2	15	35.8

attributed to HDI monomer stacking and the strong chemical compatibility between HDI monomer and the CroHeal 2000 segment, which yields a denser transient network (higher chain packing and friction). Nevertheless, the two aliphatic systems maintain comparable levels of $W_{interfacial}$ indicating that the physically crosslinked networks constituted by fully aliphatic chains are able to store similar amount of energy related to reversible interactions.

The effect of the diisocyanate chemistry on the macromolecular segmentation in turn responsible for microphase separation in polyurethanes was further investigated by dedicated μ ATR-FTIR analysis. **Figure 4.4** reports the infrared spectra maps obtained upon application of principal component analysis of the four polyurethanes. The aromatic-based polyurethanes (MDI-p and PPDI-p) show a continuous phase (reported in grey color) intercalated by a micron-sized dispersed phase (yellow color). The aliphatic and linear polyurethane (HDI-p) presents a homogeneous microstructure (no dispersed phase is probed), while HMDI-p shows some phase separation, yet to a lower extent and smaller dimension than in the case of MDI-p and PPDI-p. The analysis of the infrared spectra traces corresponding to the continuous (points numbered as '1' in Figure 4.4) and the dispersed phases (points numbered as '2' in Figure 4.4) gives insights into the molecular differences between the two probed regions. All shifts and intensity variations point towards a microstructure composed of a soft continuous phase (enriched in CroHeal 2000 + MDI segments) and hard and urea-rich heterogeneities (enriched in EHD + MDI

segments). For MDI-p the carbonyl band (C=O) probed for the continuous phase at 1695 cm^{-1} shifts to 1643 cm^{-1} due to increase in bidentate urea ligands and aromatic conjugation [28]. The N-H band located at 3324 cm^{-1} broadens and shifts to 3274 cm^{-1} indicating a stronger hydrogen bonding state. The aliphatic C-H bands at 2852 and 2919 cm^{-1} undergo a strong decrease in intensity due to the scarcity of highly aliphatic branch in the hard heterogeneities. The C-O-C stretch peak loses intensity and shifts from 1220 cm^{-1} to 1234 cm^{-1} as result of loss of urethane linkages in favor of formation of urea units. The C-H stretch in the aromatic rings clearly visible for the soft phase at 1600 cm^{-1} , only appears as a shoulder of the intense and broader main carbonyl peak in the hard phase spectrum. For HDI-p no substantial shift is observed when scanning through the probed infrared map. Only a slight shoulder of the carbonyl C=O peak located at 1680 cm^{-1} appears at about 1630 cm^{-1} as a sign of a possible increase in the hydrogen bonding strength in the small (size $< 2\text{ }\mu\text{m}$) yellow-grey regions. HMDI-p presents similar spectral feature when compared to MDI-p and PPDI-p, yet the band associated to the C-O-C stretch at 1253 cm^{-1} does not undergo any shift nor decrease in intensity suggesting a minimal difference in the urethane linkages content. The higher content in bidentate urea and the stronger hydrogen bonded state of the segregated phase might be responsible for a slower molecular reorganization which, in turn, determines a local higher T_g [29].

4.3.2. Interfacial work of deformation relation to early-stage healing fracture resistance

The deconvolution results were not only used to obtain information on the physical state of the network. Starting from the hypothesis that interfacial healing is governed by the reconstruction of reversible bonds at the broken interface and using SENT data collected for all the polymers in the early stage of healing, we explore the existence of a relationship between the interfacial work of deformation (obtained by melt rheology) and fracture resistance (a mechanical measure of interfacial healing obtained by SENT analysis). All the mechanical raw data and optical snapshots used for fracture resistance calculation are reported in the Supplementary Material (Figure S6 MDI-p, Figure S7 PPDI-p, Figure S8 HMDI-p, Figure S9 HDI-p). **Figure 4.5** displays the relation between the calculated interfacial work of deformation ($W_{interfacial}$) from rheology and $J_C^{interfacial}$ from the SENT tests of the polymers healed for $3.6 \times 10^3\text{ s}$ (1 hour) at $30\text{ }^\circ\text{C}$. A closer look to the data (Table 4.2) reveals that higher $W_{interfacial}$ of the PPDI-p and MDI-p samples is mainly related to the higher work of deformation assigned to the relaxation of the reversible ligands (concurrent relaxation of hydrogen bonds and aromatics) in the soft phase (W_{sp}^{rev}). Since the soft phase undergoes fast conformational re-arrangements, its reversible bonds reshuffling are expected to be the main contributors to the reconstruction of the broken interface at short healing times [10, 11, 30]. In this framework the use of the deconvolution protocol offers a critical advance to the understanding and optimization of interfacial healing, since its results are successfully sensitive to the incorporation of multiple reversible ligands, their symmetry and their energetic contribution to the reconstruction of the broken interface.

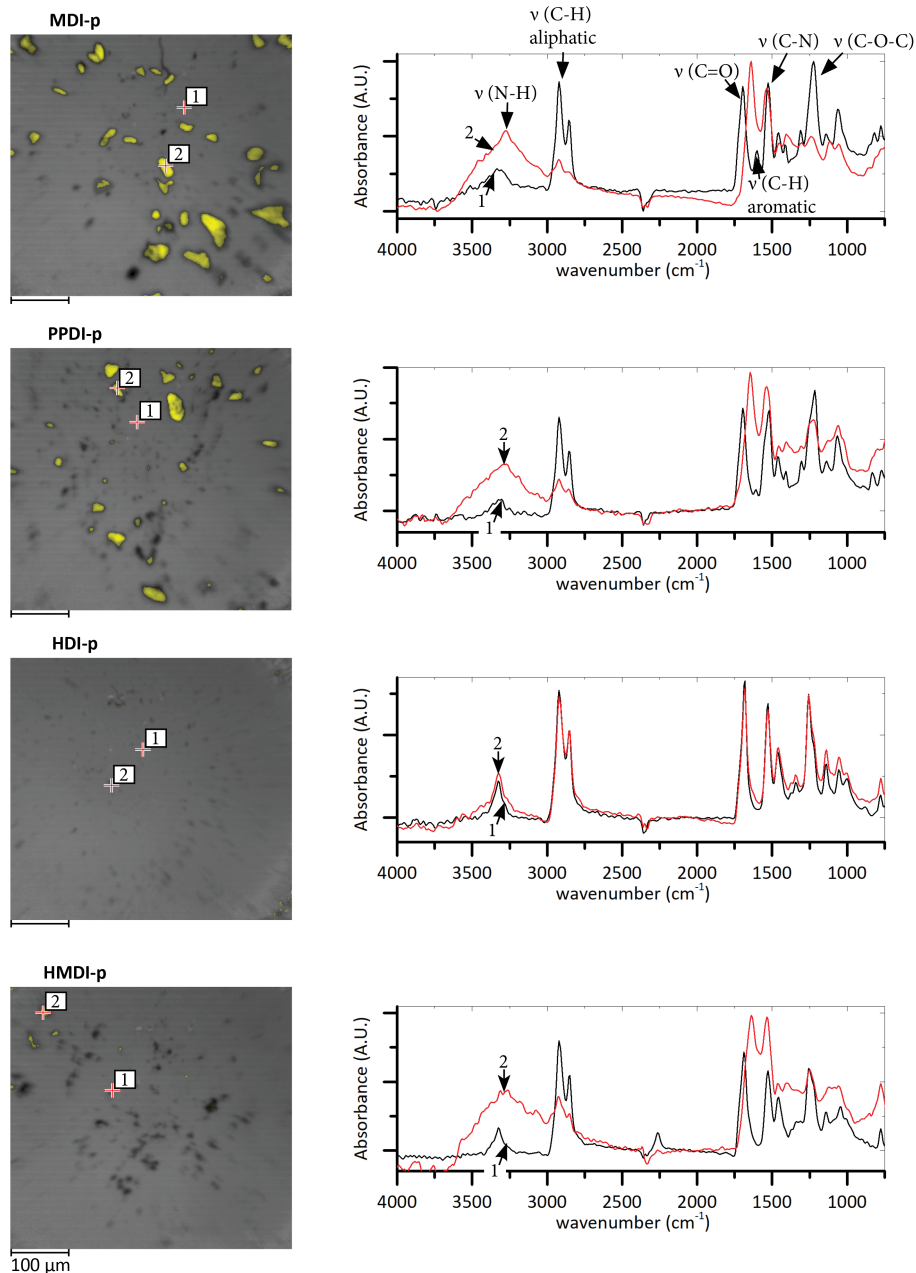


Figure 4.4: $\mu\text{ATR-FTIR}$ mapping of self-healing polyurethane elastomers. Principal component analysis reveals a phase separated microstructure consisting in a continuous matrix (grey color) intercalated by heterogeneities (yellow color). Right figures show the local IR spectra of locations 1 (continuous phase) and 2 (heterogeneities).

Quantitatively, for short healing times (3600 seconds at 30 °C), both the aliphatic systems (HMDI-p and HDI-p) show a virtual absence of tensile fracture resistance ($J_C^{interfacial}$ HMDI-p = 0.18 kJ/m², $J_C^{interfacial}$ HDI-p = 0.03 kJ/m²), as can be easily inferred from optical snapshots acquired during SENT testing (Figure S8 and Figure S9). In this sense the data provided by macro-rheology seems to point to the existence of a limiting $W_{interfacial}$ that must be surpassed to get sufficient recovery of fracture resistance upon interfacial healing. However, more systems, ideally incorporating different types and numbers of reversible ligands, should be tested in a wide range of $W_{interfacial}$ to confirm and locate the presence of such threshold.

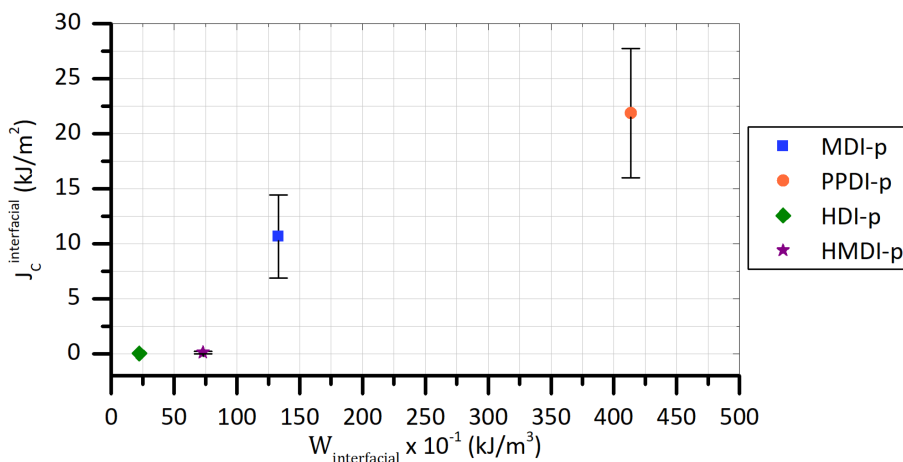


Figure 4.5: **Comparison between interfacial healing fracture resistance and interfacial work of deformation as obtained by macro-rheology.** While qualitatively an increase in $W_{interfacial}$ corresponds to higher $J_C^{interfacial}$, from a quantitative point of view the work of deformation does not capture the dramatic drop of fracture resistance for the aliphatic polyurethanes (HDI-p, HMDI-p). HDI-p point data does not include error bars due to immediate breakage of the samples tested upon application of the minimal sample alignment load of 3N.

Another possible explanation to absence of fracture resistance for HMDI-p and HDI-p at the early stage of healing can be found in the characteristics of the different polyurethanes microstructures. The aromatic polymers present a segmented microstructure and, as probed by μ FTIR-ATR, show some high T_g segregated heterogeneities at the microscale (Figure 4.4 and Table S1). The high T_g of these segregates implies, locally, a much slower reorganization and an improved directionality of the reversible ligands. This effect, when occurring at a damage site, leads to a more efficient interfacial re-bonding/healing. The lack of such structures in the aliphatic polymers causes a dramatic drop of $J_C^{interfacial}$. In a recent work Yang et al. [31] show similar beneficial effects of micro-segregated structures on scratch-healing behavior of PU coatings, attributing the healing enhancement to a more efficient entropic energy storage during local deformation. Furthermore, Chen et al. [10] have shown that a multiphase microstructure in self-healing thermoplastic elastomers is crucial to the re-arrangement of the polymer soft phase

leading to high healing.

Long range dynamics is expected to determine interphase randomisation and to lead the system to higher degree of property restoration at longer healing times. The deconvolution procedure provides kinetics of terminal relaxation in the range $\tau_t = 100$ to 10^3 s for HDI-p and HMDI-p and very sluggish terminal flow for MDI-p and PPDI-p ($\tau_t > 10^5$ s). Figure 4.6 shows a quantitative impression of the effect of long term healing on the polyurethane systems used for this study. The aliphatic polymers show a significant recovery of fracture resistance going from being virtually absent for short healing times (3.6×10^3 seconds) to a moderate mechanical stability at longer healing times (after 10^6 seconds J_C HMDI-p = 11.4 kJ/m², J_C HDI-p = 1.8 kJ/m²). An immediate feedback regarding the increase in fracture properties when going from short to longer healing times can be obtained when looking at the optical snapshots acquired during SENT testing and used for J_C calculation (Figure S8 and Figure S9), in which a higher deformation can be seen before fracture at the healed interface. Moreover, in accordance with kinetics predictions obtained by rheology deconvolution, MDI-p and PPDI-p do not show any significant improvement in the fracture resistance which remains virtually constant over long holding times at the healing temperature of 30 °C.

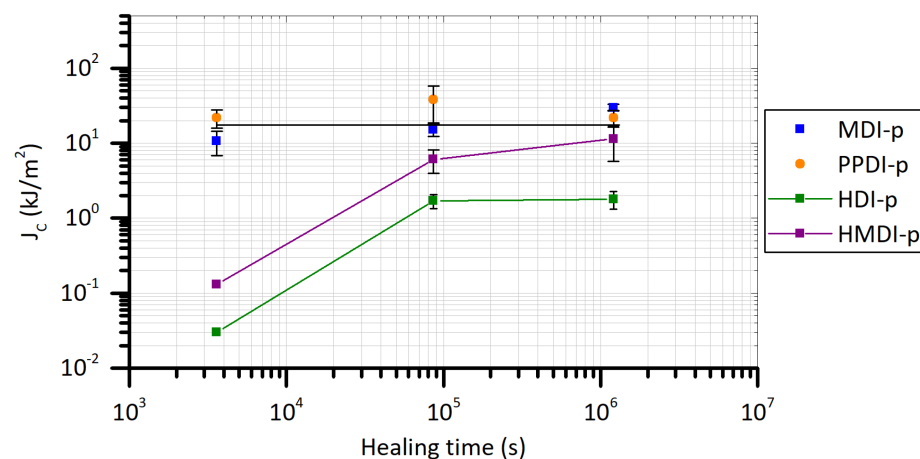


Figure 4.6: **Long range dynamics effect on fracture resistance recovery.** In accordance with time constants obtained from deconvolution, the beneficial effect of long range dynamics is only observed for aliphatic polyurethanes (HDI-p, HMDI-p). Healing temperature is 30 °C.

4.4. Conclusions

In this work we demonstrate that the intelligent use of macro-rheology data can provide semi-quantitative information on the degree of interfacial healing in polymers. In this framework, we apply a deconvolution protocol of the mechanical relaxation spectrum derived from macro-rheology to a set of self-healing polyurethanes and explore the relation between the derived stored work of deformation and the de-

gree of mechanical restoration in the early stage of polymer healing.

The deconvolution protocol is found to be sensitive to the variations in the polymer architecture and in particular to the addition of multiple reversible ligands, to the symmetry of the rigid backbone segments and to their individual energetic contribution to the relaxation process.

The work of deformation associated to the disjunction of reversible moieties reflects in a semi-quantitative way the recovery of fracture resistance in the early stage of healing. It results higher for polymers endowed of multiple reversible ligands that coherently show a higher degree of mechanical restoration. The results points at the existence of a so far unidentified threshold of interfacial work of deformation marking the transition between healing (i.e. sufficient reversible bonds at interface to transfer load along the fracture plane) and no healing. Furthermore, the time constants capture the kinetics of the entire healing process, predicting the access to long range motion for less physically crosslinked systems.

These insights on the relation between polymer structure, rheology and interfacial healing benefit the design of novel systems showing high mechanical restoration in the early stage of healing.

4.5. Supporting Information

Synthesis of self-healing segmented polyurethanes

PPDI-p. CroHeal 2000 was heated for 1 hour at 90 °C to reduce the intrinsic viscosity of the monomer, melting crystalline domains. Subsequently 90.0 grams (45.0 mmol) were transferred to a 300 mL polypropylene cup. 3.19 g of EHD (27.0 mmol) were then added to the cup. 12.68 g (79.20 mmol) of PPDI were weighted in a separate 25 mL polypropylene cup, purged under nitrogen inert environment and heated 1 hour at 120°C to reduce its intrinsic viscosity, melting crystalline domain. The PPDI was rapidly poured into the main reaction cup (containing CroHeal 2000 and EHD). The mixture was sheared under vacuum at 2300 rpm for 130 seconds using a vacuum assisted speed mixer (SpeedMixer™ DAC 400.2 VAC-P). The application of high vacuum (pressure below 100 mbar) turned out to be critical for the formation of bubble-free polymers. The mixture was then transferred to a 20x20 cm PTFE mold, equilibrated for 30 minutes at ambient conditions and subsequently cured overnight at 60 °C. The bulk polymers were equilibrated for 1 week at ambient condition before testing.

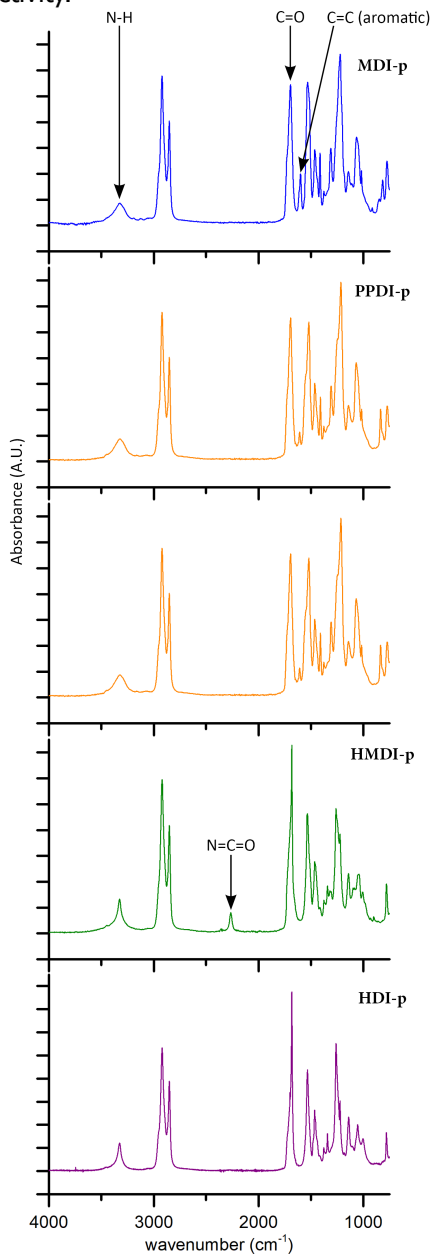
HMDI-p. CroHeal 2000 was heated for 1 hour at 90 °C to reduce the intrinsic viscosity of the monomer, melting crystalline domains. Subsequently 90.0 grams (45.0 mmol) were transferred to a 300 mL polypropylene cup. 3.95 g of EHD (27.0 mmol) were then added to the cup. 20.78 g (79.20 mmol) of HMDI were weighted in a separate 25 mL polypropylene cup and purged under nitrogen inert environment. The HMDI was injected into the main reaction cup (containing CroHeal 2000 and EHD) using a syringe. The mixture was sheared under vacuum at 2300 rpm for 180 seconds using a vacuum assisted speed mixer (SpeedMixer™ DAC 400.2 VAC-P). The application of high vacuum (pressure below 100 mbar) turned out to be critical for the formation of bubble-free polymers. The mixture was then transferred

to a 20x20 cm PTFE mold, equilibrated for 30 minutes at ambient conditions and subsequently cured overnight at 50 °C. The bulk polymers were equilibrated for 1 week at ambient condition before testing.

HDI-p. CroHeal 2000 was heated for 1 hour at 90 °C to reduce the intrinsic viscosity of the monomer, melting crystalline domains. Subsequently 90.0 grams (45.0 mmol) were transferred to a 300 mL polypropylene cup. 3.95 g of EHD (27.0 mmol) were then added to the cup. 13.32 g (79.20 mmol) of HDI were weighted in a separate 25 mL polypropylene cup and purged under nitrogen inert environment. The HDI was injected into the main reaction cup (containing CroHeal 2000 and EHD) using a syringe. The mixture was sheared under vacuum at 2300 rpm for 180 seconds using a vacuum assisted speed mixer (SpeedMixer™ DAC 400.2 VAC-P). The application of high vacuum (pressure below 100 mbar) turned out to be critical for the formation of bubble-free polymers. The mixture was then transferred to a 20x20 cm PTFE mold, equilibrated for 30 minutes at ambient conditions and subsequently cured overnight at 60 °C. The bulk polymers were equilibrated for 1 week at ambient condition before testing.

ATR-FTIR

Figure S1. ATR-FTIR spectra of the synthesized PU. Synthesis completion was followed through disappearance of N=C=O stretching band at 2270 cm^{-1} and appearance of absorption peaks at 1170 cm^{-1} (C=O bond) and 2270 cm^{-1} (N-H bond). A small peak of unreacted isocyanate is observed for HMDI-p attributed to the monomer low reactivity.



Macro-rheology deconvolution protocol

The mechanical relaxation spectrum was deconvoluted following the procedure introduced elsewhere [14]. Herein we reports some principal highlights and the procedure to compute the average stored work of deformation associated to individual relaxation process.

To fit the relaxation spectrum the infinite Maxwell-Weichert model was chosen:

$$H_{Model}(\ln \tau) = \sum_{i=1}^n A_i \exp\left(-\frac{((\ln(\tau) - \ln(\tilde{\tau}_i))^2)}{2\sigma_i^2}\right)$$

The model entails an infinite number of Maxwell elements (a compliance and a dashpot in series) connected in parallel. The choice of this model allows us to approach the problem in the most general and unbiased way.

The experimental $H(\tau)_{exp}$ is fitted with a user-defined initial number of relaxation elements i . the optimal number of Maxwell elements and the set of best fitting parameter values is identified based on the minimization of the coefficient of determination (r^2) obtained by comparing the model storage and loss moduli with experimental moduli. The model storage and loss moduli are calculated as:

$$G'(\omega) = \int_{-\infty}^{\infty} \frac{H \ln(\tau) \omega^2 \tau^2}{1 + \omega^2 \tau^2} d \ln \tau$$

$$G''(\omega) = \int_{-\infty}^{\infty} \frac{H \ln(\tau) \omega \tau}{1 + \omega^2 \tau^2} d \ln \tau$$

The average stored work of deformation is defined as in ref. [32]:

$$W_s(\omega)_{average} = \left(\frac{\omega}{2\pi}\right) \int_{\frac{2\pi(n-1)}{\omega}}^{\frac{2\pi n}{\omega}} W_s(t) dt = (\epsilon_0^2/4) G'(\omega)$$

Substituting the expression of $G'(\omega)$

$$W_s(\omega)_{average} = (\epsilon_0^2/4) \int_{-\infty}^{\infty} \frac{H \ln(\tau) \omega^2 \tau^2}{1 + \omega^2 \tau^2} d \ln \tau$$

The individual stored work of deformation are then obtained substituting in this relation the single components of the deconvoluted relaxation spectrum.

Extensional DMA data

Figure S2. MDI-p Temperature Sweep.

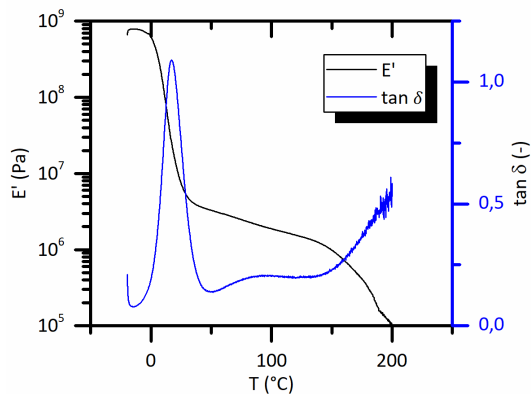


Figure S3. PPDI-p Temperature Sweep.

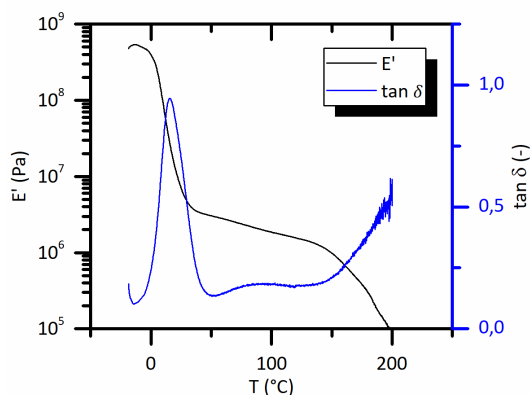


Figure S4. HMDI-p Temperature Sweep.

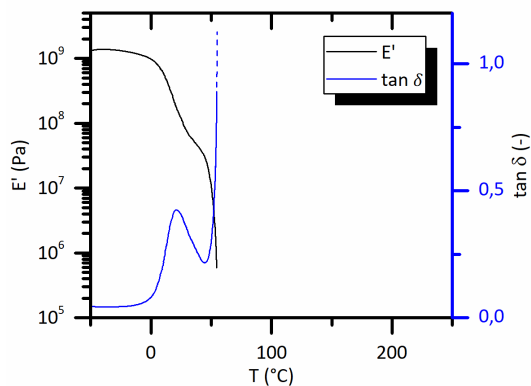
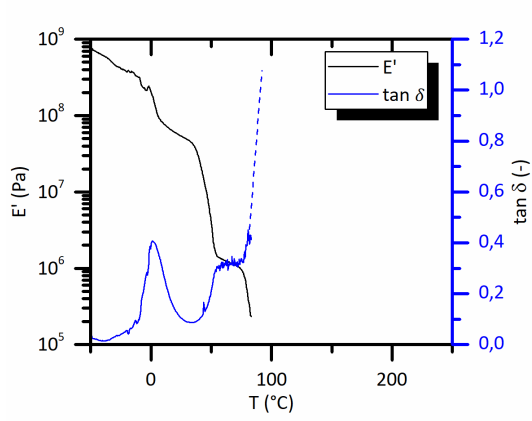


Figure S5. HDI-p Temperature Sweep.



SENT raw data

Figure S6. MDI-p SENT raw data. The figure shows the initial and final frames of the mechanical test and the load-displacement curve. From up to down: Pristine, Healing 3.6×10^3 s (1 hour) at 30 °C, Healing 8.64×10^4 s (1 day) at 30 °C, Healing 1.2×10^6 (2 weeks) at 30 °C.

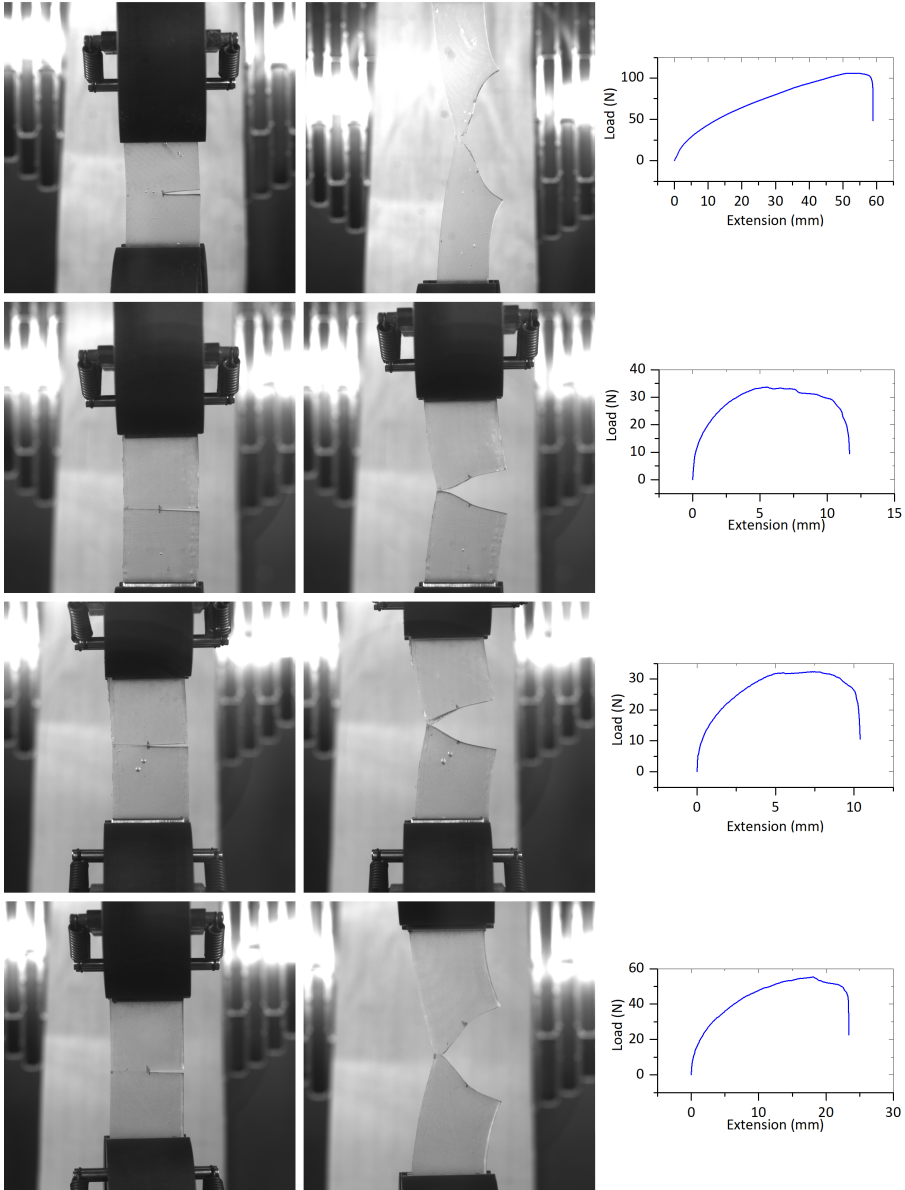


Figure S7. PPDI-p SENT raw data. The figure shows the initial and final frames of the mechanical test and the load-displacement curve. From up to down: Pristine, Healing 3.6×10^3 s (1 hour) at 30 °C, Healing 8.64×10^4 s (1 day) at 30 °C, Healing 1.2×10^6 (2 weeks) at 30 °C.

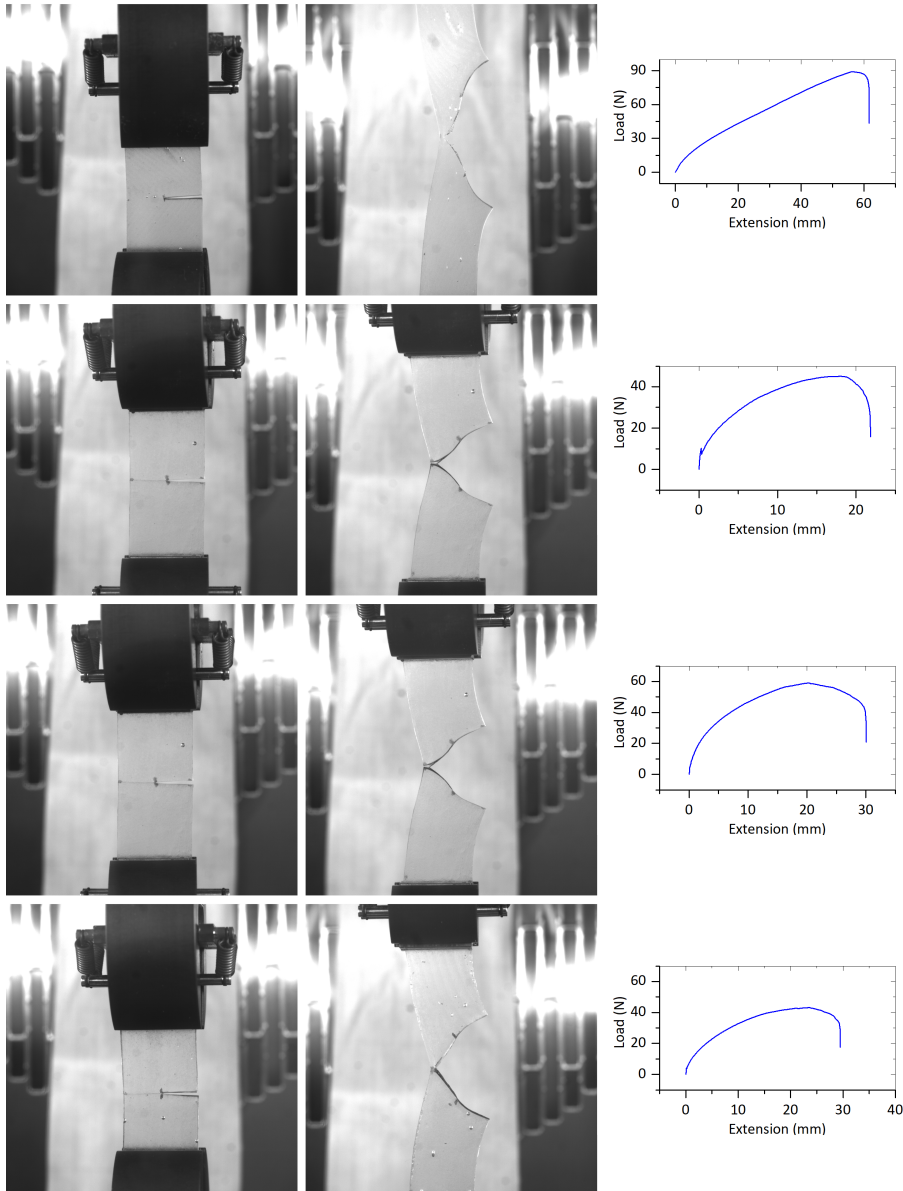


Figure S8. HMDI-p SENT raw data. The figure shows the initial and final frames of the mechanical test and the load-displacement curve. From up to down: Pristine, Healing 3.6×10^3 s (1 hour) at 30 °C, Healing 8.64×10^4 s (1 day) at 30 °C, Healing 1.2×10^6 s (2 weeks) at 30 °C.

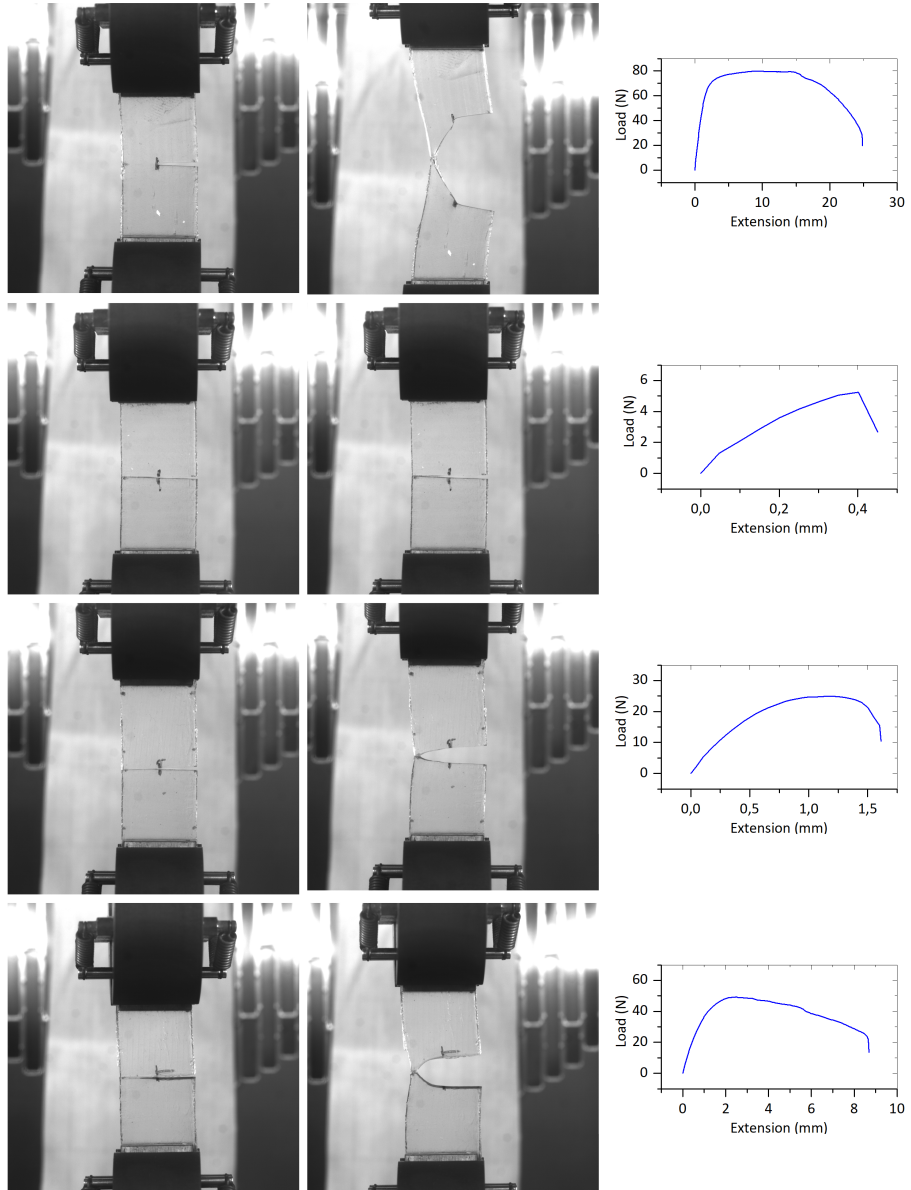


Figure S9. HDI-p SENT raw data. The figure shows the initial and final frames of the mechanical test and the load-displacement curve. From up to down: Pristine, Healing 3.6×10^3 s (1 hour) at 30 °C, Healing 8.64×10^4 s (1 day) at 30 °C, Healing 1.2×10^6 (2 weeks) at 30 °C.

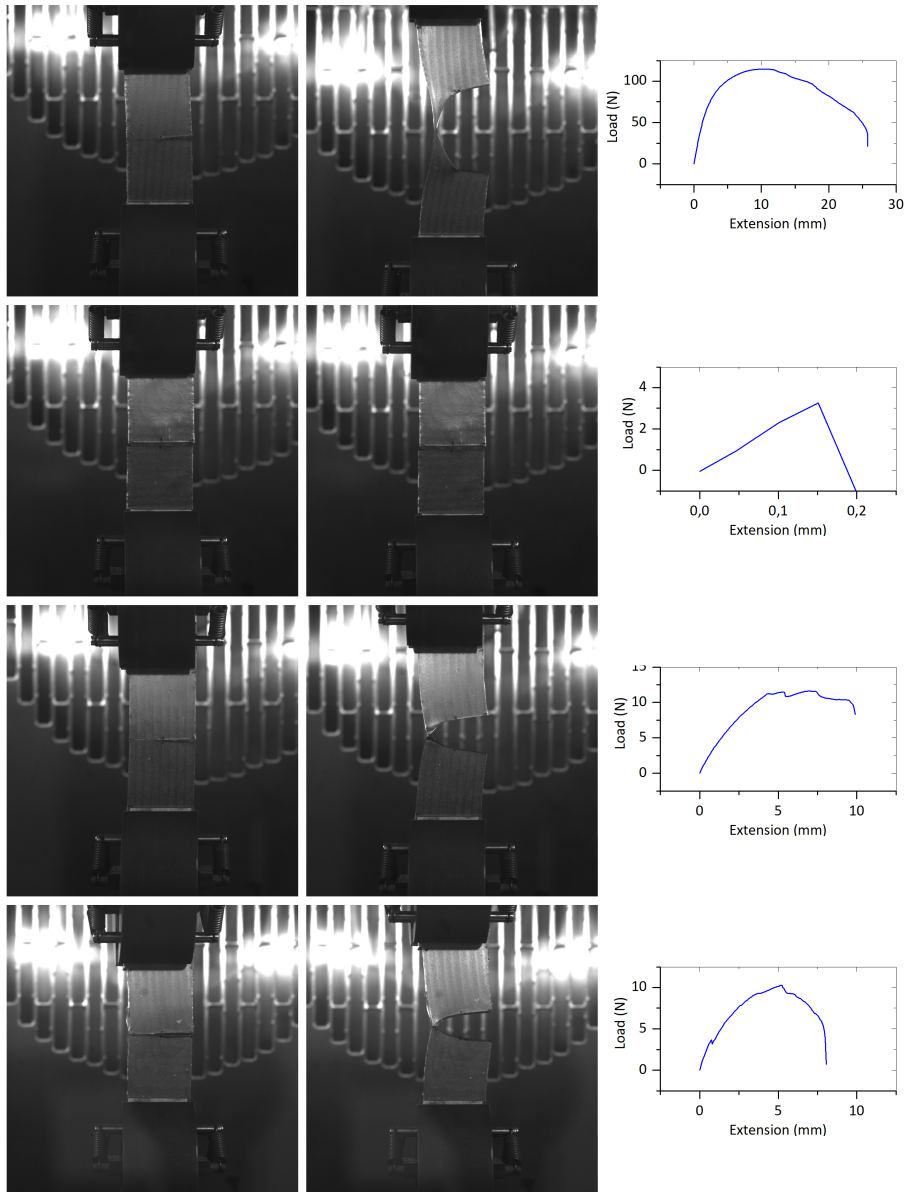


Table S1. Amount of microscopic segregated phase for PU systems. The segregated phase content is quantified by μ FTIR-ATR via principal component analysis.

Polymer	Segregated Phase (PCA%)
MDI-p	10.1 \pm 1.6
PPDI-p	6.1 \pm 1.3
HMDI-p	<1
HDI-p	<1

References

- [1] D. Y. Zhu, M. Z. Rong, and M. Q. Zhang, *Self-healing polymeric materials based on microencapsulated healing agents: From design to preparation*, Progress in Polymer Science **49**, 175 (2015).
- [2] S. J. Garcia, *Effect of polymer architecture on the intrinsic self-healing character of polymers*, European Polymer Journal **53**, 118 (2014).
- [3] M. D. Hager, P. Greil, C. Leyens, S. van der Zwaag, and U. S. Schubert, *Self-healing materials*, Advanced Materials **22**, 5424 (2010).
- [4] S. J. García, H. Fischer, and S. van der Zwaag, *A critical appraisal of the potential of self healing polymeric coatings*, Progress in Organic Coatings **72**, 211 (2011).
- [5] Y. Yang, X. Ding, and M. W. Urban, *Chemical and physical aspects of self-healing materials*, Progress in Polymer Science **49**, 34 (2015).
- [6] A. Campanella, D. Döhler, and W. H. Binder, *Self-healing in supramolecular polymers*, Macromolecular Rapid Communications **39**, 1700739 (2018).
- [7] A. Susa, R. Bose, A. M. Grande, S. van der Zwaag, and S. J. Garcia, *Effect of the dianhydride/branched diamine ratio on the architecture and room temperature healing behavior of polyetherimides*, ACS applied materials & interfaces **8**, 34068 (2016).
- [8] V. Montano, M. M. Wempe, S. M. Does, J. C. Bijleveld, S. van der Zwaag, and S. J. Garcia, *Controlling healing and toughness in polyurethanes by branch-mediated tube dilation*, Macromolecules **52**, 8067 (2019).
- [9] A. Susa, J. Bijleveld, M. Hernandez Santana, and S. J. Garcia, *Understanding the effect of the dianhydride structure on the properties of semiaromatic polyimides containing a biobased fatty diamine*, ACS sustainable chemistry & engineering **6**, 668 (2018).
- [10] Y. Chen, A. M. Kushner, G. A. Williams, and Z. Guan, *Multiphase design of autonomic self-healing thermoplastic elastomers*, Nature chemistry **4**, 467 (2012).

- [11] Y. H. Kim and R. P. Wool, *A theory of healing at a polymer-polymer interface*, *Macromolecules* **16**, 1115 (1983).
- [12] A. M. Grande, R. Martin, I. Odriozola, S. van der Zwaag, and S. J. Garcia, *Effect of the polymer structure on the viscoelastic and interfacial healing behaviour of poly (urea-urethane) networks containing aromatic disulphides*, *European Polymer Journal* **97**, 120 (2017).
- [13] R. K. Bose, N. Hohlbein, S. J. Garcia, A. M. Schmidt, and S. van der Zwaag, *Connecting supramolecular bond lifetime and network mobility for scratch healing in poly (butyl acrylate) ionomers containing sodium, zinc and cobalt*, *Physical Chemistry Chemical Physics* **17**, 1697 (2015).
- [14] V. Montano, S. J. Picken, S. van der Zwaag, and S. J. Garcia, *A deconvolution protocol of the mechanical relaxation spectrum to identify and quantify individual polymer feature contributions to self-healing*, *Physical Chemistry Chemical Physics* **21**, 10171 (2019).
- [15] A. M. Grande, S. J. Garcia, and S. van der Zwaag, *On the interfacial healing of a supramolecular elastomer*, *Polymer* **56**, 435 (2015).
- [16] F. Maes, D. Montarnal, S. Cantournet, F. Tournilhac, L. Corté, and L. Leibler, *Activation and deactivation of self-healing in supramolecular rubbers*, *Soft Matter* **8**, 1681 (2012).
- [17] A. M. Grande, J. Bijleveld, S. J. Garcia, and S. van der Zwaag, *A combined fracture mechanical-rheological study to separate the contributions of hydrogen bonds and disulphide linkages to the healing of poly (urea-urethane) networks*, *Polymer* **96**, 26 (2016).
- [18] J. Honerkamp and J. Weese, *A nonlinear regularization method for the calculation of relaxation spectra*, *Rheologica acta* **32**, 65 (1993).
- [19] I. McDougall, N. Orbey, and J. M. Dealy, *Inferring meaningful relaxation spectra from experimental data*, *Journal of Rheology* **58**, 779 (2014).
- [20] T. Roths, M. Marth, J. Weese, and J. Honerkamp, *A generalized regularization method for nonlinear ill-posed problems enhanced for nonlinear regularization terms*, *Computer physics communications* **139**, 279 (2001).
- [21] G. Ramorino, S. Agnelli, R. De Santis, and T. Riccò, *Investigation of fracture resistance of natural rubber/clay nanocomposites by J-testing*, *Engineering Fracture Mechanics* **77**, 1527 (2010).
- [22] A. Eceiza, M. Martin, K. De La Caba, G. Kortaberria, N. Gabilondo, M. Corcuera, and I. Mondragon, *Thermoplastic polyurethane elastomers based on polycarbonate diols with different soft segment molecular weight and chemical structure: mechanical and thermal properties*, *Polymer Engineering & Science* **48**, 297 (2008).

- [23] Z. Yang, H. Peng, W. Wang, and T. Liu, *Crystallization behavior of poly (ϵ -caprolactone)/layered double hydroxide nanocomposites*, *Journal of applied polymer science* **116**, 2658 (2010).
- [24] I. Yilgör, E. Yilgör, and G. L. Wilkes, *Critical parameters in designing segmented polyurethanes and their effect on morphology and properties: A comprehensive review*, *Polymer* **58**, A1 (2015).
- [25] J. P. Sheth, D. B. Klinedinst, G. L. Wilkes, I. Yilgor, and E. Yilgor, *Role of chain symmetry and hydrogen bonding in segmented copolymers with monodisperse hard segments*, *Polymer* **46**, 7317 (2005).
- [26] T. Aida, E. Meijer, and S. Stupp, *Functional supramolecular polymers*, *Science* **335**, 813 (2012).
- [27] R. L. McKiernan, S. P. Gido, and J. Penelle, *Synthesis and characterization of polyethylene-like polyurethanes derived from long-chain, aliphatic α, ω -diols*, *Polymer* **43**, 3007 (2002).
- [28] P. J. Woodward, D. Hermida Merino, B. W. Greenland, I. W. Hamley, Z. Light, A. T. Slark, and W. Hayes, *Hydrogen bonded supramolecular elastomers: correlating hydrogen bonding strength with morphology and rheology*, *Macromolecules* **43**, 2512 (2010).
- [29] L. Ning, W. De-Ning, and Y. Sheng-Kang, *Hydrogen-bonding properties of segmented polyether poly (urethane urea) copolymer*, *Macromolecules* **30**, 4405 (1997).
- [30] R. Wool and K. O'Connor, *A theory crack healing in polymers*, *Journal of applied physics* **52**, 5953 (1981).
- [31] Y. Yang, D. Davydovich, C. C. Hornat, X. Liu, and M. W. Urban, *Leaf-inspired self-healing polymers*, *Chem* **4**, 1928 (2018).
- [32] N. W. Tschoegl, *The phenomenological theory of linear viscoelastic behavior: an introduction* (Springer Science & Business Media, 2012).

5

Scratch closure in thermoplastic polyurethanes: an energetic analysis

*Odio gli indifferenti.
Credo che vivere voglia dire partecipare.
Chi vive veramente non può non essere cittadino partecipe.
L'indifferenza è abulia, è parassitismo, è vigliaccheria, non è vita.
Perciò odio gli indifferenti.*

Antonio Gramsci

Abstract

Scratch closure in polymers requires an internally stored energy field acting as the driving force to closure. In this work we apply the rubber elasticity theory to quantify the stored and released entropic energy density during damage-repair cycles and relate these quantities to the scratch closure observed with microscopy.

To this aim we developed a set of five thermoplastic polyurethanes, with equivalent backbones but different soft phase fraction contents. The storage and release of energy is controlled by varying the scratch deformation and healing temperatures in relation to the specific viscoelastic length of transition. The closure increases linearly with release entropy and can be related to two characteristic design parameters of the network (junction density and damping factor). In case a scratch is made such that it does not result in storage of internal mechanical energy healing does not occur.

5.1. Introduction

Environmental concerns related to material overconsumption and the ineffective life cycle of commodity polymers are valuable drivers for the development of alternative and sustainable solutions to current materials and design rules. Polymer scientists are facing the issues in creative manners [1–3]. Among the various approaches, the development of so-called self-healing polymers might be a promising route to extend the life-time of polymers [4–8]. Self-healing polymers rely on the incorporation of a fraction of reversible bonds that allow the de-construction of a broken interface, while permanent crosslinks, main chain entanglements or microphase separation ensure mechanical robustness and network integrity [9]. In recent years the inclusion of multiple yet low energetic physical interactions (mainly Van der Waals interactions and hydrogen bonds) has appeared as a clear direction for the synthesis of self-healing commodity polymers requiring only minimal chemical modifications, i.e. retaining their commodity character [10–13].

Recent studies have shown that self-healing polymer systems exhibit viscoelastic length transitions (VLTs) near the glass transition (T_g) [11, 14, 15] when deforming and temperature cycling in dynamical mechanical analysis (DMA) tests. The testing protocol macroscopically consists of imposing a set directional extension and to monitor the fractional retraction, a feature typical of shape memory polymers (SMPs). Mechanistically, the viscous component of the network is responsible for the length extension while the retraction is an entropy-driven process provoked by the storage and release of free conformational states. By quantifying the entropic storage (ΔS_S) and entropic release (ΔS_R) at VLT a relative measurement of the shape memory effect (SME) can be obtained. Previous studies have shown that, for a given set of DMA testing condition (e.g. deformation amplitude, oscillation frequency and heating rate) ΔS_S increases linearly with the junction density (ν_j) and the peak value of the damping factor ($\tan \delta_{max}$) [14].

The combination of self-healing and shape memory effects is exploited in the so-called shape memory assisted self-healing (SMASH) method to ease scratch closure. In these systems the release of the conformational entropic energy stored during the damage event is used to facilitate scratch closure while the dynamic nature of reversible molecular moieties contributes to the interfacial re-bonding. Since many systems satisfy these requirements several studies focused on this phenomenon [16–19]. However, the quantitative aspects of entropy release and scratch closure displacement still remain unaddressed. This is critical for the future design and optimisation of self-healing polymers with market potential. The current study tests the hypothesis that different level of released entropy can be accessed by controlling the damage and healing temperatures, which can be quantitatively assessed in terms of the released entropy that contributes to the scratch closure. Using this approach empirical relations between released entropy, junction density and scratch closure displacement for thermoplastic polyurethanes with known and variable healing kinetics can be developed. Since the closure mechanism is based solely on the viscoelastic nature of the material, this concept can be extended to other self-healing and/or shape memory polymers.

5.2. Experimental Section

5.2.1. Materials

Butyl acetate (BuAc, >99.7%), 1,4-butanediol (BDO, 99%), isophorone diisocyanate (IPDI, 98%), dibutyltin dilaurate (DBTDL, 95%) were purchased from Sigma-Aldrich. Polyether siloxane copolymer wetting additive TEGO Wet 270 was purchased from Evonik Industries. Polyol CroHeal™ 1000 (equivalent molecular weight 1200 g/mol) was kindly provided from Croda Nederland B.V. Sodium chloride was purchased from VWR International. All the reagents were used as received without further purification.

5.2.2. Synthesis of the TPUs and coating preparation

Five thermoplastic polyurethanes (TPUs) were synthesized by single shot technique reacting CroHeal™ 1000, IPDI and BDO. The compositions cover a broad range theoretical soft phase molar fraction (χ_{SF}) defined as:

$$\chi_{SF} = \frac{n(\text{CroHeal1000})}{n(\text{CroHeal1000}) + n(\text{BDO})}$$

Below the synthesis of the PU with $\chi_{SF}=0.42$ is reported in details. Analogous procedures were followed for the other polymers in this study. Details on their synthesis are reported in the Supporting Information at Table S1.

CroHeal™ 1000 was heated for 1 hour at 60 °C to reduce the intrinsic viscosity of the monomer. Subsequently 6.0 grams (5.00 mmol) of CroHeal 1000 were transferred to a 20 ml polypropylene cup. Butyl acetate solvent (BuAc, 0.6 g, 6.66 mmol) was quickly added to further reduce the intrinsic viscosity. 0.6 g of 1,4-butanediol were then transferred to the cup (BDO, 0.6 g, 6.66 mmol). Subsequently TEGO 270 (0.024 g) and dibutyltin dilaurate (DBTDL, 0.063 g, 0.1 mmol) were added dropwise. Immediately thereafter, isophorone diisocyanates (IPDI, 2.82 g, 12.68 mmol) was injected. The system was stirred vigorously using a mechanical agitator and the reaction proceeded for 15 seconds at room temperature. The mixture was then applied on a acetone cleaned carbon automotive steel plate (Q-panel) using a coating bar with a wet thickness of 150 μm . The coated panel was dried for 30 minutes at ambient laboratory conditions and subsequently cured for 30 minutes at 60 °C in an air recirculating furnace. The polyurethane coatings were then equilibrated for 1 week at ambient laboratory conditions prior to scratch and corrosion resistance testing. For bulk characterization of the at the end of the synthesis the polymer was transferred to a 4x4 PTFE mold, then equilibrated for 30 minutes in ambient condition and subsequently cured 30 minutes at 60 °C. The bulk polymers were equilibrated for 1 week at ambient condition before testing using TGA, DSC and DMA analysis. All the TPUs were synthesized following an analogous procedure but varying the monomer feed ratio. Details are reported in Table S1.

5.2.3. Characterisation methods

Dynamical mechanical analysis

DMA analysis was performed on a Q800 DMA (TA Instrument) in strain control mode. The initial gauge length was set to 10.0 ± 0.1 mm, strain amplitude = 10 μm , force track = 125% and frequency set a 1 Hz, with heating rate = 2 $^{\circ}\text{C}/\text{min}$ and frequency = 10 Hz. The samples have rectangular geometry, with average width = 2.0 ± 0.05 mm and average thickness = 0.5 ± 0.1 mm. The test chamber was cooled to the starting temperature (-50 $^{\circ}\text{C}$) without applying any force on the polymer specimen (floating condition) to ensure that any pre-deformation was applied before the start of the experiment. DMA VLT values were calculated as described by Hornat et al. [14], and are explained in details in the main text. Every composition was tested three times. The VLT values used in this study are obtained as the algebraic mean of the set of DMA tests.

Damage and healing conditions

In order to obtain comparable initial scratch damage and exclude any effect related to the network dissipations on damage mechanics, the TPUs were damaged at the temperature corresponding to a fixed strain of $\varepsilon = 0.1\%$ (T_i of Figure 5.1B), well within the glassy regime. The temperature was controlled by using a Peltier TEC Heating/Cooling Module, in cooling mode, varying the input voltage between 0.1 and 4 V. The damages of 5 mm in length were produced by using a razor blade tip (width ≈ 100 μm) and a fixed axial force ($F_N = 1.8$ N), causing the blade tip to reach the metal substrate. The damages were subsequently subjected to isothermal healing at the temperature corresponding to the midpoint and the end point of the strain-temperature VLT retraction (T_{mid} and $T_{end-point}$ of Figure 5.1B) using a Peltier TEC Heating/Cooling Module, in heating mode, varying the input voltage between 0.5 and 4 V. The damages were healed for 60 seconds in accordance with typical kinetics of the SME in polymers [17, 20]. The use of such a short healing time excluded any effect of long-range polymer dynamics on scratch closure displacement. The damage/healing protocol is linked to the DMA VLT protocol to access a wide range of theoretical ΔS_R which was calculated for every damage/healing condition by using Equation 5.6. All scratching (T_i) and healing temperatures (T_{mid} and $T_{end-point}$) used and the corresponding ΔS_R values are reported in Table S3. The formulations $\chi_{SF} = 0.71$ and $\chi_{SF} = 0.51$ were additionally tested at the temperature reported in Table S4.

Engrave damages of 5 millimeters in length were produced using a mechanical engraver equipped with AC125-BAL-PRO-.002 Carbide Profiler for Engraving with a 15 degrees tip (tip width size of 0.002 inches ≈ 50 μm).

Optical microscopy

High resolution optical micrographs of damaged and healing coatings were acquired using a Keyence VHX-2000 digital microscope with optical magnification in the range 20X to 1000X.

Calculation of scratch closure displacement

The scratch closure displacement ($\delta_{CLOSURE}$) was estimated as:

$$\delta_{CLOSURE} = W_i - W_f$$

where W_i and W_f are the damage width measured at the polymer-air interface respectively before (W_i) and after (W_f) the isothermal healing treatment. Every closure experiment was repeated three times to ensure data statistics. W_i and W_f were estimated from high resolution optical micrographs, using the ImageJ software.

5.3. Results and Discussion

5.3.1. Network architecture influence on shape memory VLTs

To set the stage, we illustrate the network morphology of the thermoplastic polyurethanes (TPU) used for this study in **Figure 5.1A** and analyse the classical dependence of the measured strain (ϵ) on temperature during an extensional dynamical mechanical analysis (Figure 5.1B). Soft segments segmental mobility is responsible for the increase of dissipation at low temperature (vitrification T_g) while the hard blocks act as semi-permanent netpoints guaranteeing network integrity upon large strain deformation. As result, shape memory viscoelastic length transitions (VLTs) are observed near T_g . The initial length extension is attributed to decoiling of the soft segments (Step I). The subsequent length retraction is an effect of the release of entropic energy density (ΔS_R) which is accumulated due to the mobility restrictions imposed by soft segment H-bonding and soft segment chain entanglements (Step II). The following slow extension is attributed to delayed decoiling of hard blocks (Step III). Starting from extensional dynamical mechanical analysis, a similar description of network dynamics was attributed to shape memory TPU having an amorphous soft phase [21].

As derived from thermodynamics and rubber elasticity theory [22, 23] the decrease in conformational entropy occurring at VLTs[14] can be estimated as

$$\Delta S = -\frac{\nu_j R}{2} \left[\alpha^2 + \frac{2}{\alpha} - 3 \right] \quad (5.1)$$

where α is the extension ratio ($\alpha = \frac{L}{L_0}$, an observable of the DMA measurements), ν_j is the junction density ($\nu_j = \frac{\rho}{M_j}$, where M_j is the apparent molecular weight between entanglements and is the characteristic design parameter of the network), and R is the universal gas constant. The entropic energy storage generates a retractive force (F_R) expressed as

$$\frac{F_R}{A} = \sigma_R = \nu_j RT \left[\alpha - \frac{1}{\alpha^2} \right] \quad (5.2)$$

where T is temperature, A is the cross-section area and σ_R is the corresponding retractive stress. Following the analytical relationships derived through the rubbery elasticity theory, an experimental protocol [14, 15] that consists in the performance of a single DMA experiment, was used to quantify the stored (ΔS_S) and released (ΔS_R) entropy density at the viscoelastic length of transition. The entropy is stored during the length extension observed during the DMA analysis (Step I of Figure

5.1B). As derived from classical thermodynamics:

$$\Delta S_S = -T_{\varepsilon I} S_{\varepsilon I} + T_i S_i \quad (5.3)$$

By coupling Equation 5.3 and Equation 5.1 it follows that:

$$\Delta S_S = \frac{Rv_j T_{\varepsilon I}}{2} \left(\alpha_I^2 + \frac{2}{\alpha_I} - 3 \right) - \frac{Rv_j T_i}{2} \left(\alpha_i^2 + \frac{2}{\alpha_i} - 3 \right) \quad (5.4)$$

where $\alpha_I = \frac{L_I}{L_{glass}}$ is the ratio between the length of the DMA tested sample at any point during extension (L_I) and its length well within the glassy regime (L_{glass}). $\alpha_i = \frac{L_{glass}}{L_{glass}} = 1$. The stored entropy reaches a maximum when $L_I = L_{max}$, in correspondence of the maximum elongation (ε_{max} of Figure 5.1B):

$$\Delta S_S^{max} = \frac{Rv_j T_{\varepsilon_{max}}}{2} \left(\alpha_{max}^2 + \frac{2}{\alpha_{max}} - 3 \right) - \frac{Rv_j T_i}{2} \left(\alpha_i^2 + \frac{2}{\alpha_i} - 3 \right) \quad (5.5)$$

The entropy is released during the length retraction (Step II of Figure 5.1B):

$$\Delta S_R = -T_{\varepsilon_{min}} S_{\varepsilon_{min}} + T_{\varepsilon_{max}} S_{\varepsilon_{max}} \quad (5.6)$$

By coupling Equation 5.6 to Equation 5.1 it is derived:

$$\Delta S_R = \frac{Rv_j T_{\varepsilon_{II}}}{2} \left(\alpha_{II}^2 + \frac{2}{\alpha_{II}} - 3 \right) - \frac{Rv_j T_{\varepsilon_{max}}}{2} \left(\alpha_{\varepsilon_{max}}^2 + \frac{2}{\alpha_{\varepsilon_{max}}} - 3 \right) \quad (5.7)$$

where $\alpha_{II} = \frac{L_{II}}{L_{glass}}$ is the ratio between the length of the DMA tested sample at any point during retraction (L_{II}) and L_{glass} . The released entropy reaches a maximum when $L_{II} = L_{min}$, in correspondence of the minimum in elongation (ε_{min} of Figure 5.1B):

$$\Delta S_R^{max} = \frac{Rv_j T_{\varepsilon_{min}}}{2} \left(\alpha_{min}^2 + \frac{2}{\alpha_{min}} - 3 \right) - \frac{Rv_j T_{\varepsilon_{max}}}{2} \left(\alpha_{\varepsilon_{max}}^2 + \frac{2}{\alpha_{\varepsilon_{max}}} - 3 \right) \quad (5.8)$$

L_{glass} , L_{max} , L_{min} are observables of the DMA test. Then, assuming that the retractive stress $\frac{F_R}{A} = \sigma_R = \sigma_{SF}$ at ε_{max} (the stress measured from the DMA loading cell at the maximum of the elongation) we can estimate the junction density v_j through Equation 5.2 as:

$$v_j = \frac{\sigma_{SF} \text{ at } \varepsilon_{max}}{RT_{\varepsilon_{max}}} * \left(\frac{1}{\alpha_{max} - \frac{1}{\alpha_{\varepsilon_{max}}^2}} \right) \quad (5.9)$$

Having v_j and α , ΔS_S and ΔS_R are calculated using Equation 5.4 and Equation 5.7. A set of TPUs were synthesized by varying the nominal soft phase fraction (χ_{SF}) and tested by DMA to quantify all VLTs-related parameters (ΔS , v_j , σ_R). Figure 5.1C-D show the temperature dependence of sample length and normal

force for a specific TPU ($\chi_{SF} = 0.41$) as obtained in DMA analysis. L_{glass} is selected in correspondence of a deformation of 0.1%. L_{max} and L_{min} are respectively the length at the maximum of extension and retraction. F_R corresponds to the normal (static) force measured from the DMA loading cell at the moment of the maximum extension, when sample retraction starts. Using these observables, ΔS_R is calculated at different temperatures inside the retraction step by using Equation 5.7 and plotted in Figure 5.1E.

Hornat et al. [14], using the careful analysis of the relation between the DMA observables (ε_{max} and σ_{SF} at ε_{max}) and two characteristic network parameters ($\tan \delta_{max}$ which is indicative of network viscoelasticity and v_j that represents network connectivity) have shown that ΔS can be correlated to $\tan \delta_{max}$ and v_j . In particular $\Delta S \propto \sigma_{SF}$ at $\varepsilon_{max} = (\tan \delta_{max} \times v_j^{0.6613}) \times (\tan \delta_{max} \times \ln v_j)$. $\tan \delta_{max}$ and v_j can be extrapolated from the DMA analysis and are controlled through the network chemical modifications. Figure 5.1F-G show the effect that an increase in polyurethane soft phase fraction determines on $\tan \delta_{max}$ and v_j . The first polymer extension was attributed to the decoiling of the polyurethane soft phase, polymers designed with higher soft phase fraction (χ_{SF}) show higher viscous dissipation (higher $\tan \delta_{max}$) at the VLTs (Figure 5.1F) because a larger network fraction is able to dissipate the mechanical load. Moreover, hydrogen bonds and main chain entanglements in the soft phase act as molecular switches for the shape memory viscoelastic transition (the VLT transition). Therefore it is not surprising that an increase in soft phase molar fraction (χ_{SF}) coincides with an increase of junction density v_j (Figure 5.1G). The junction density tends to plateau for $\chi_{SF} > 0.5$, suggesting that a saturation level in hydrogen bonding and entanglements is reached in the soft phase. As illustrated in Figure 5.1H, when connecting ΔS_R^{max} to the network characteristic parameters a linear relationship is obtained:

$$\Delta S_R^{max} = 0.295 \frac{(\tan \delta_{max})^2 * v_j^{0.6613}}{\ln v_j} \quad (5.10)$$

TPUs with high $\tan \delta_{max}$ and v_j undergo a more effective limitation of conformational states during VLTs, determining an increase of maximum released entropy ΔS_R^{max} . This equation can be used to directly obtain the values of ΔS_R^{max} from δ_{max} and v_j .

Details regarding synthesis, characterisation and analysis methods are provided in the Supplementary Materials. All the VLT parameters (ΔS_S^{max} , ΔS_R^{max} , v_j , σ_{SF} at ε_{max} , ε_{max}) are listed in Table S2.

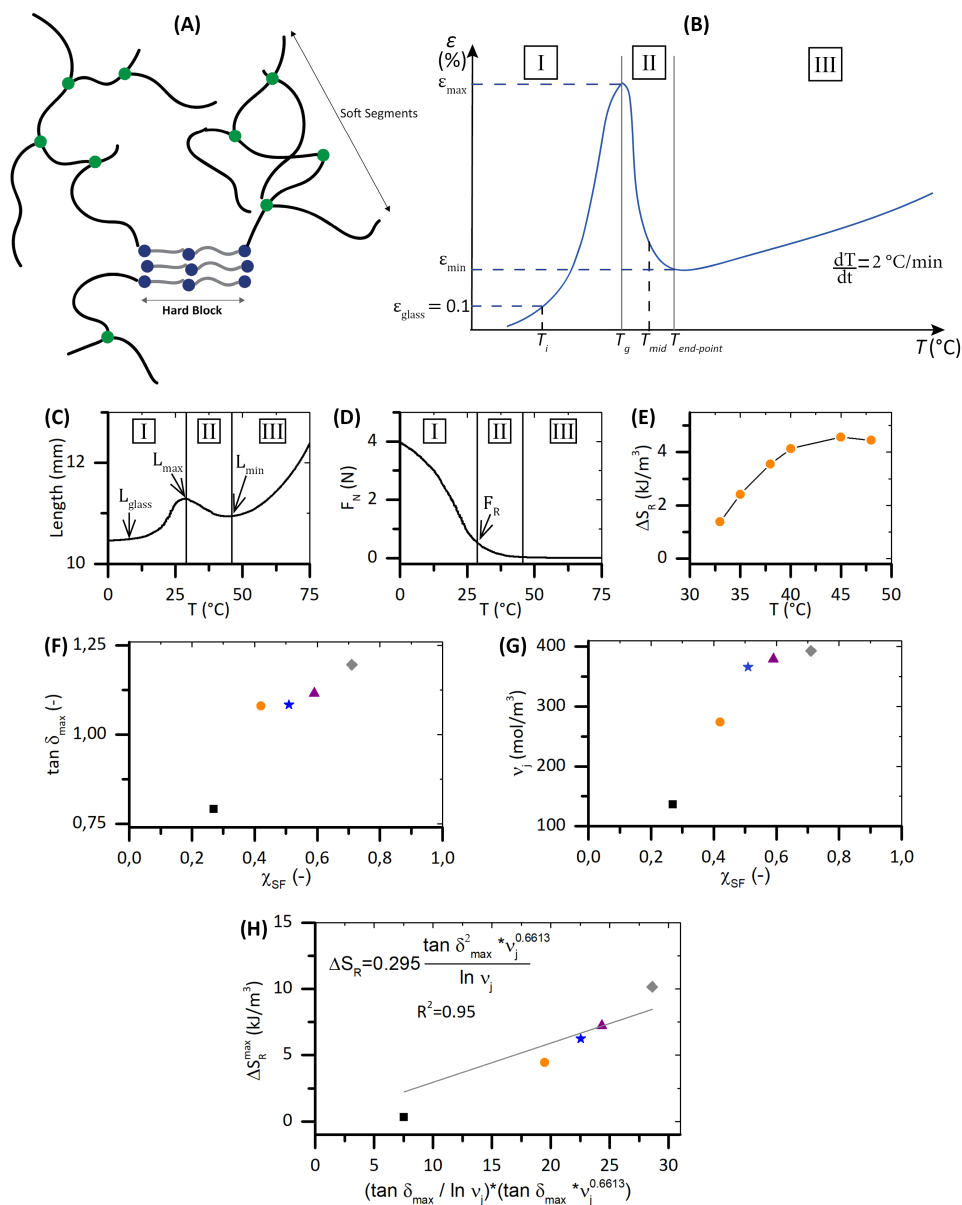


Figure 5.1: **Network morphology and shape memory VLTs results.** **(A)** Schematic representation of TPU phase separated morphology. **(B)** Schematics of the classical dependence of strain on temperature during VLT transition. Step I: extension due to soft segments decoiling. Step II: Retraction due to release of stored conformational entropy. Step III: extension due to hard blocks delayed decoiling. **(C-D)** Experimental temperature dependence of sample length (Sample Length) and normal static force (F_N) for $\chi_{SF} = 0.42$ as obtained by DMA analysis. **(E)** ΔS_R temperature dependence as calculated by applying Equation 5.6. Note that $\Delta S_R > 0$ only during stage 2 of the VLT transition, in the retraction phase. **(F-G)** Polymer viscoelasticity ($\tan \delta_{max}$) and junction density (v_j) dependence on soft phase molar fraction.

5.3.2. Relation between macroscopic scratch closure and released entropy

To examine the relationship between the released entropy calculated through the VLTs analyses and the macroscopic scratch closure behaviour we introduce a testing protocol based on controlled temperature scratching/healing combined with optical microscopy analysis of 100 μm thick TPU polymers. The damage and healing temperatures were established analysing the strain-temperature relationship during DMA measurements and the testing protocol is fully provided in Supplementary Information.

Figure 5.2A-B-C summarises selected scratch closure optical micrographs, the theoretical values of ΔS_R and the specific healing temperatures of three TPUs designed with different soft phase molar fraction (χ_{SF}). For all specimens, the damage recovery stems from an effective entropic release ($\Delta\Delta S_R$). In fact, all the polymers undergo entropy driven closure upon isothermal heating (healing) for 1 minute. Interestingly the severe temperature required to trigger the closure of $\chi_{SF} = 0.27$ ($T_{healing} = 80$ °C, snapshots AI and AII) does not correspond to a larger closure displacement when compared to the closure occurring for $\chi_{SF} = 0.71$ which takes place at a considerably lower temperature ($T_{healing} = 35.0$ °C, snapshots CI and CII). The closure looks solely to dependent on the exploited $\Delta\Delta S_R$, showing good qualitative agreement between scratch closure displacement and released entropy. In order to quantitatively relate closure to released entropy and shape memory polymer design, the scratch closure displacement ($\delta_{CLOSURE}$) was estimated as

$$\delta_{CLOSURE} = W_i - W_f \quad (5.11)$$

where W_i and W_f are the damage width measured at the polymer-air interface respectively before (W_i) and after (W_f) the isothermal healing treatment. As illustrated in Figure 5.2D the $\delta_{CLOSURE}$ increases monotonically with $\Delta\Delta S_R$. The data points are well fitted by common linear dependence:

$$\delta_{CLOSURE} = 15.79 + 10.68(\Delta\Delta S_R) \quad (5.12)$$

Interestingly, both experimental data and empirical predictions indicate $\delta_{CLOSURE} \neq 0$ at a virtual $\Delta\Delta S_R = 0$. The result is not surprising since our observations are based on the fundamental assumptions that all the energy stored during the mechanical deformation is used to limit the polymer conformational states ($\Delta S_S = \Delta\Delta S_S$ and $\Delta S_R = \Delta\Delta S_R$). In reality, since during damaging the deformation exceeds the characteristic linear regime, while the majority of the energy is stored as entropic energy density, part will cause chain scission and part will be elastically stored by the network (chemical bonds bending and contraction). The latter will cause partial (marginal) macroscopic closure upon release at VLT onset.

It is relevant to access a prediction of the scratch closure displacement in relation to the network characteristic design parameter (junction density ν_j) and its intrinsic dissipative behaviour (maximum of the damping factor $\tan \delta_{max}$). The plot of $\delta_{CLOSURE}$ against $(\tan \delta_{max} \times \nu_j^{0.6613}) \times (\tan \delta_{max} \times \ln \nu_j)$ is shown in Figure 5.2E.

An empirical linear relationship is obtained as

$$\delta_{CLOSURE} = 4.04 \frac{(\tan \delta_{max})^2 * v_j^{0.6616}}{\ln v_j} \tag{5.13}$$

The linear trend was expected, considering the linearity between ΔS_R and $\frac{(\tan \delta_{max})^2 * v_j^{0.6613}}{\ln v_j}$ (Equation 5.10). This relationship can be used to predict the value of closure starting from a known polymer design parameter (v_j) and δ_{max} measured through a single DMA temperature sweep analysis. Inversely, it can be employed to optimize polymer design (v_j), based on an objective desired closure ($\delta_{CLOSURE}$) (e.g. dictated from a specific application).

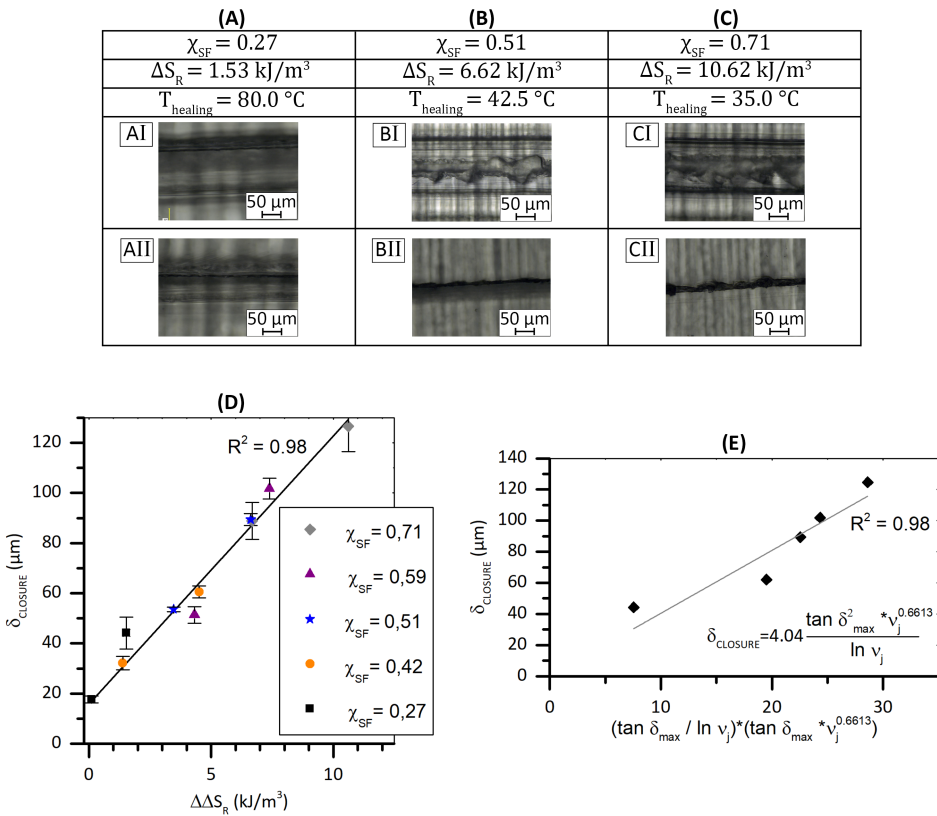


Figure 5.2: **Closure displacement relation to released entropy and polymer design. (A-B-C)** Optical micrographs of damage TPU polymers. $\chi_{SF} = 0.27$ ($\Delta S_R = 1.53 \text{ kJ/m}^3$) was heated at $80 \text{ }^\circ\text{C}$ (AI-AII). $\chi_{SF} = 0.51$ ($\Delta S_R = 6.62 \text{ kJ/m}^3$) was heated at $42.5 \text{ }^\circ\text{C}$ (BI-BII). $\chi_{SF} = 0.71$ ($\Delta S_R = 10.62 \text{ kJ/m}^3$) was heated at $35 \text{ }^\circ\text{C}$ (CI-CII). **(D)** $\delta_{CLOSURE}$ dependence on $\Delta \Delta S_R$. Note that data points are well fitted by a linear spline. **(E)** $\delta_{CLOSURE}$ dependence on $\tan \delta_{max} \times v_j^{0.6613} \times (\tan \delta_{max} \times \ln v_j)$ equivalent to the product $\sigma_{SF} \text{ at } \epsilon_{max} \times \epsilon_{max}$. Note that data points are well fit by a linear spline.

The five TPU polymers used to obtain the data points showed in Figure 5.2D were

examined by healing every polymer at two temperatures corresponding to the to the midpoint and the end point of the strain-temperature VLT. This approach allowed us to assess a spectrum of released entropy ($0.1 < \Delta\Delta S_R < 11 \text{ kJ/m}^3$). An equally broad range can be accessed by exploiting the different temperatures of VLT retraction ($T_{retraction}$) of a specific system. In particular, by analysing the relation between ΔS_R at $T_{retraction}$ for $\chi_{SF} = 0.71$ and 0.51 , the broad spectrum of released entropy was reconstructed by testing these two systems under six healing conditions marked as data-points in **Figure 5.3A**. The additional healing temperatures and the calculated ΔS_R are provided at Table S4. The scratch-healing results are presented in Figure 5.3B and show linear dependence of $\delta_{CLOSURE}$ on $\Delta\Delta S_R$ (continuous grey line in Figure 5.3B). The spline is in good agreement with the linear relationship derived by testing all the polymer compositions ($\chi_{SF} = 0.71, 0.59, 0.51, 0.42, 0.27$) at the T_{mid} and $T_{end-point}$ and reported as dashed black line in Figure 5.3B. The two fittings diverge at high $\Delta\Delta S_R$ values where the error bars on the measurement become wider. This analysis confirms that a quantitative prediction of $\delta_{CLOSURE}$ based on the entropic storage estimated by DMA analysis (ΔS_R) is possible [14, 15].

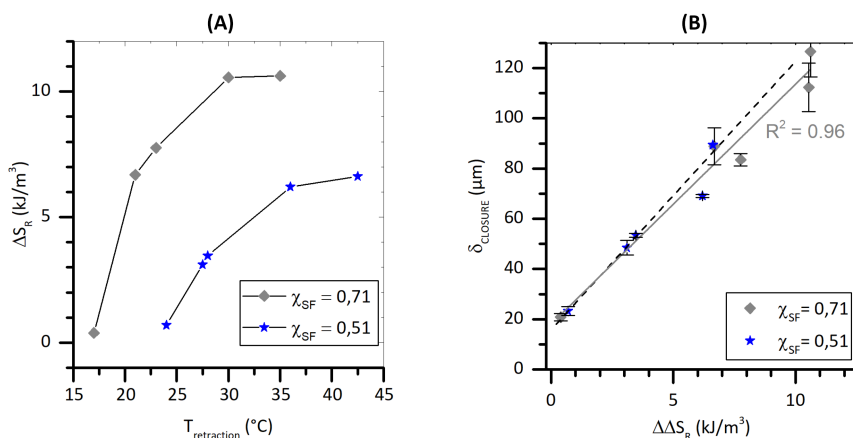


Figure 5.3: **Closure displacement relation to released entropy in wide range of healing temperature for two specific systems ($\chi_{SF} = 0.71$ and 0.51).** (A) ΔS_R dependence on $T_{retraction}$. (B) $\delta_{CLOSURE}$ dependence on $\Delta\Delta S_R$.

5.3.3. Entropy storage as a strain-induced phenomenon

Now we investigate the role of the damage mode and geometry in generating the internal energy storage in proximity of the scratch. The linear relationship linking the $\delta_{CLOSURE}$ to ΔS_R was derived for a specific damage condition that consists of the use of a sharp $100 \mu\text{m}$ wide razor blade tip. Therefore, during damaging the material is subjected to the deformation state represented qualitatively in **Figure 5.4A**. Upon scratching a large polymer displacement occurs in damage zone, setting a damage-induced strain region. Figure 5.4AI-II propose again the optical

micrographs of before and after healing. This event determines the local entropic storage responsible of the polymer delayed elasticity upon healing that causes the closure. Minimal or no material removal is caused in this case.

An analogous experiment was performed on the same TPU by producing a damage using a rotating carbide tip by means of a mechanical engraver. The high torque of the metal tip shatters the polymer provoking the material removal and a substantially different deformation state when compared to the scratching, as imaged in Figure 5.4B. The material is only minimally displaced, therefore only a small damage-induced strain region is set, in correspondence of the damage lateral walls. Upon healing, the closure displacement is limited to the lateral walls and the scratch is still fully open. The drop in closure is visible from the optical micrographs of the scratch provided in Figure 5.4BI-BII and it is quantitatively reported in Figure 5.4C as red ball marker.

This experiment indicates that despite the theoretical entropy storage of the systems used calculated between damage and healing temperature, is unchanged, the effective entropy storage that determines the entropy driven closure have to be exploited through a damage mode that privileges material displacement over material removal. Entropy storage is a strain-induced phenomenon.

Since the entropy storage is dependent on the presence of a strain profile in proximity of the damage zone, we argue that the use of a blunter or narrower tip will lead respectively to a higher and lower entropy storage/release, even if the polymer used and the damage/healing temperature conditions are unaltered. A blunter tip induces a broader strain field, while a narrower one yields to a shrinking of the strain field. To confirm the hypothesis the controlled temperature scratching/healing tests were repeated using a conical Rockwell diamond tip (width $\approx 100 \mu\text{m}$, curvature radius $r \approx 200 \mu\text{m}$) and a razor blade tip, equal to the previous one used but thinned to $70 \mu\text{m}$. Schematic overviews of the additional scratching tips used is shown in Figure 5.4D-E. The use of the blunt Rockwell results in a higher initial damage width ($W_i^{\text{Rockwell}} \approx 200 \mu\text{m}$) compared to that for the razor blade damage ($W_i^{\text{RzB}} \approx 130 \mu\text{m}$). Upon isothermal healing, driven by the conformational SME the damages displace to the final width of $W_f \approx 20 \mu\text{m}$ ($\delta_{\text{CLOSURE}} \approx 110 \mu\text{m}$) as shown from the optical micrographs acquired after damage and healing (Figure 5.4DI-DII). The use of a blunter tip sets a larger strain-induced region that determines a higher entropy storage/release resulting in a higher closure. A qualitative estimation of the $\Delta\Delta S_R$ exploited when using the Rockwell tip is realized by inverting the derived linear relationship linking δ_{CLOSURE} to $\Delta\Delta S_R$ (Equation 5.11, reported as grey spline in Figure 5.4C). As shown in Figure 5.4C (cyan square marker) a value of $\Delta\Delta S_R \approx 9.0 \text{ kJ/m}^3$ corresponds to the observed closure displacement of $110 \mu\text{m}$.

A strong decrease in closure is obtained when comparing indenters with equivalent shape (razor blades) but different tip width ($100 \mu\text{m}$ and $70 \mu\text{m}$). In case the $70 \mu\text{m}$ razor blade is used, a smaller initial scratch width is set ($W_i \approx 90 \mu\text{m}$), and lower closure is observed ($\delta_{\text{CLOSURE}} \approx 80 \mu\text{m}$), confirming the hypothesized shrinking of the damage-induced strain region (Figure 5.4EI-EII). However, despite the absolute reduction of δ_{CLOSURE} , the scratch is only barely visible. In fact, much lower

levels of released entropy are sufficient to fully heal the damage, setting a system specific level of damage closure saturation. By inverting Equation 5.10 we argue that values of $\Delta\Delta S_R$ no higher than $\approx 5.2 \text{ kJ/m}^3$ will be sufficient to fully close up an $90 \text{ }\mu\text{m}$ wide damage (red square marker in Figure 5.4C). The approach is universal provided that the material shows length extension and successive retraction at the VLT.

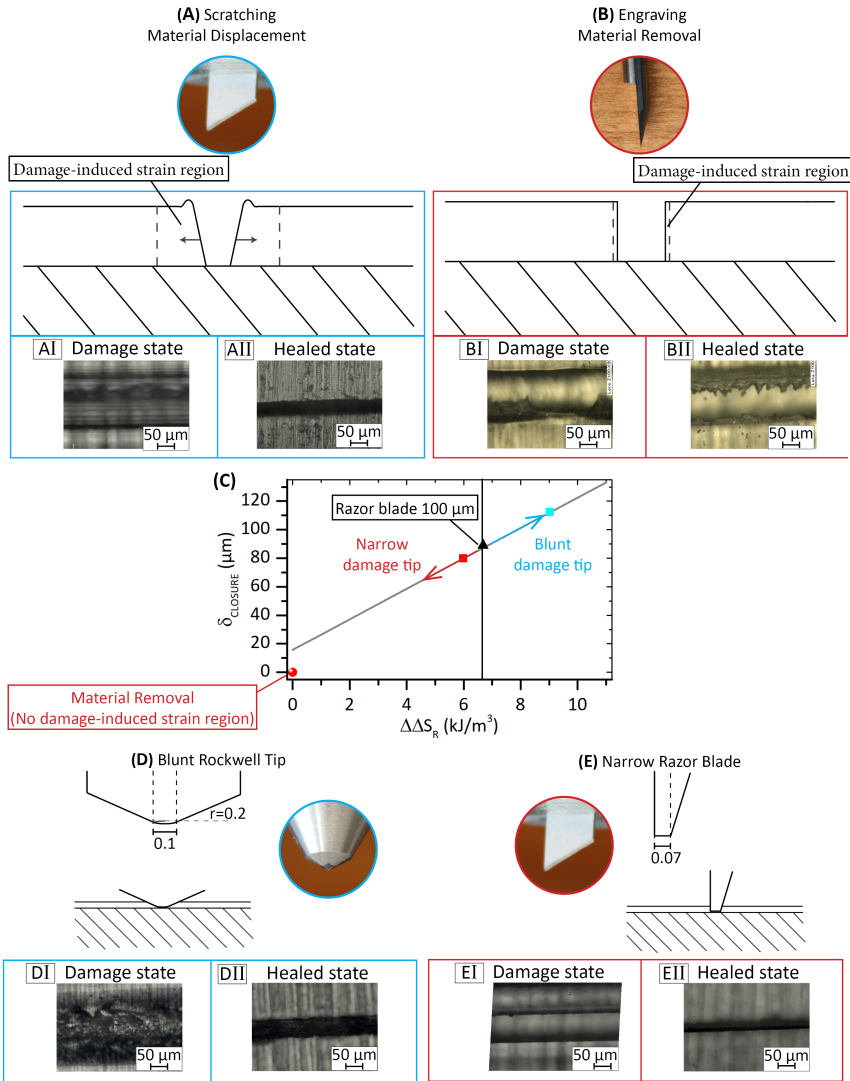


Figure 5.4: **Effect of damage mode on closure displacement.** (A) Scratching causes material displacement at the damage zone. A damage-induced strain region is set, enabling efficient entropy storage. Good closure is observed upon healing. (B) Engraving determines material removal. Since the material is removed but not displaced, only a minimal entropic storage is possible at the damage lateral walls. Poor closure is observed upon healing. (C) Quantitative evaluation of the effect of damage mode and the use of a blunt and a narrow indenter. (D) Schematic overviews and photographs of the damaging tips used. All the quotes are given in millimetres. (DI, DII, EI, EII) Optical micrographs acquired before and after healing treatment of samples damaged with Rockwell tip (DI-DII) and narrow razor blade (EI-EII).

5.4. Conclusions

We observed a linear relation between the amount of released locally stored energy in a scratched thermoplastic polymer coating and the closure of the scratch. In general terms, a higher closure will be obtained for polymers with a high junction density and combinations of deformation and healing temperatures which lead to an optimal release of the stored energy. Specific polymer design could be used to target unique applications. This work proposes a critical advance in the design of the next generation shape memory and self-healing polymer commodities.

5.5. Supporting Information

Experimental conditions

Table S1. Synthesis of segmented polyurethanes: Stoichiometry and molar content.

OH (CroHeal 1000) / OH(CroHeal 1000)+OH(BDO) (mol/mol)	Soft phase fraction (χ_{SF})	NCO / OH (total)
0.71	0.71	1.1
0.59	0.59	1.1
0.51	0.51	1.1
0.42	0.42	1.1
0.27	0.27	1.1

$$\chi_{SF} = 0.71$$

Monomer	Mass (g)	Molar content (mmol)
CroHeal 1000	6.0	5.00
BuAc	0.790	6.79
BDO	0.18	1.997
TEGO270	0.028	n.a.
DBTDL	0.063	0.1
IPDI	1.711	7.697

$$\chi_{SF} = 0.59$$

Monomer	Mass (g)	Molar content (mmol)
CroHeal 1000	6.0	5.00
BuAc	0.83	7.18
BDO	0.30	3.329
TEGO270	0.028	n.a.
DBTDL	0.063	0.1
IPDI	2.04	9.16

$$\chi_{SF} = 0.51$$

Monomer	Mass (g)	Molar content (mmol)
CroHeal 1000	6.0	5.00
BuAc	0.88	7.56
BDO	0.42	4.66
TEGO270	0.028	n.a.
DBTDL	0.063	0.1
IPDI	2.36	10.63

$$\chi_{SF} = 0.27$$

Monomer	Mass (g)	Molar content (mmol)
CroHeal 1000	6.0	5.00
BuAc	1.17	10.05
BDO	1.20	13.31
TEGO270	0.028	n.a.
DBTDL	0.063	0.1
IPDI	4.48	20.15

VLT parameters and damaging temperatures

Table S2. Stress from static force at ε_{\max} (σ_{SF} at ε_{\max}), maximum strain (ε_{\max}), junction density (ν_j) maximum released entropy density (ΔS_R^{\max}), maximum stored entropy density (ΔS_S^{\max}) for the different polyurethane formulations obtained via DMA analysis. The data reported are the average value and standard deviation calculated on a set of three DMA experiments.

χ_{SF}	σ_{SF} at ε_{\max} (MPa)	ε_{\max} (%)	ν_j (mol/m ³)	ΔS_R^{\max} (kJ/m ³)	ΔS_S^{\max} (kJ/m ³)
0.71	0.243±0.018	9.4±0.30	393±30	10.16±0.90	11.75±0.94
0.59	0.202±0.014	7.9±0.45	379±11	7.23±0.66	8.20±1.02
0.51	0.190±0.013	7.5±0.22	366±24	6.23±0.62	7.35±0.64
0.42	0.159±0.007	8.3±0.19	274±16	4.45±0.45	6.80±0.19
0.27	0.0514±0.001	4.8±0.85	136±11	0.71±0.58	1.31±0.52

5

Table S3. Temperatures corresponding to the mid and end-point of VLT transition and corresponding ΔS_R as calculated by VLT DMA study. These points were used as healing temperatures of the PU coatings.

χ_{SF}	T_i (°C)	T_{mid} (°C)	$T_{end-point}$ (°C)	ΔS_R^{mid} (kJ/m ³)	$\Delta S_R^{end-point}$ (kJ/m ³)
0.71	3±0.2	21±0.3	35±0.3	6.68±1.44	10.62±0.89
0.59	4±0.2	23.5±0.3	38.5±0.3	4.32±1.61	7.39±0.66
0.51	9±0.2	27.5±0.3	42.5±0.3	3.46±1.05	6.62±0.62
0.42	12.5±0.3	33±0.3	48±0.5	1.39±0.41	4.51±0.57
0.27	18±0.3	55±0.5	80±1.1	0.112±0.08	0.71±0.20

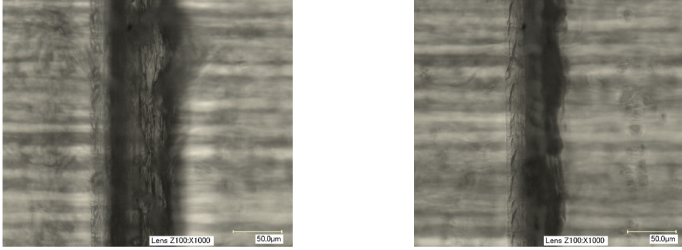
Table S4. Additional healing temperatures tested for $\chi_{SF} = 0.71$ and $\chi_{SF} = 0.51$ and corresponding ΔS_R as calculated by VLT DMA study.

χ_{SF}	T_i (°C)	$T_{retraction}$ (°C)	ΔS_R (kJ/m ³)
0.71	3±0.2	17±0.3	0.39±0.09
		23±0.3	7.76±1.15
		30±0.3	10.55±0.92
0.51	9±0.2	24±0.3	0.69±0.18
		28±0.3	3.10±0.93
		36±0.3	6.20±0.69

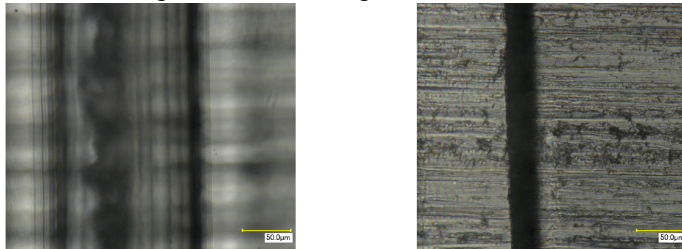
Optical micrographs of damaged and healed coatings

In this section we show exemplary optical micrographs of the damaged and healed coatings. Optical micrographs of the coating in the damage state are reported on the left end side, while the optical micrographs of the coating in the healed state (60 seconds of healing treatment) are reported on the right end side. The scale bar measures a length of 50 μm .

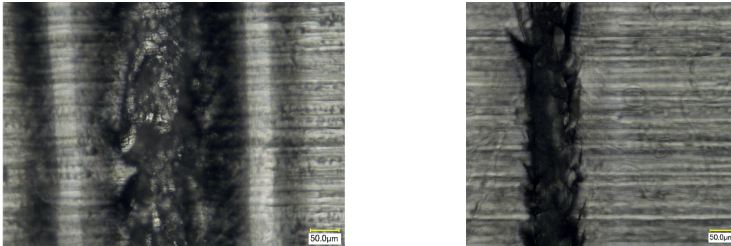
$$\chi_{SF} = 0.71, T_{damage} = 3^\circ\text{C}, T_{healing} = 17^\circ\text{C}$$



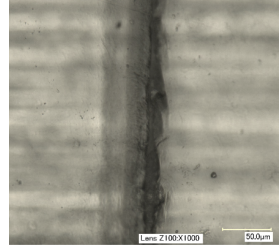
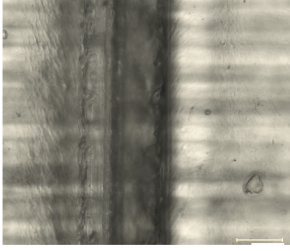
$$\chi_{SF} = 0.71, T_{damage} = 3^\circ\text{C}, T_{healing} = 21^\circ\text{C}$$



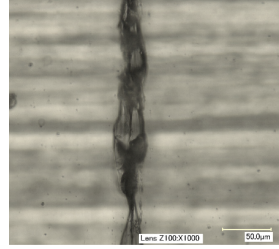
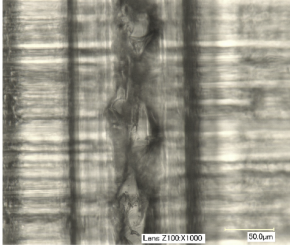
$$\chi_{SF} = 0.71, T_{damage} = 3^\circ\text{C}, T_{healing} = 21^\circ\text{C}, \text{Rockwell Tip}$$



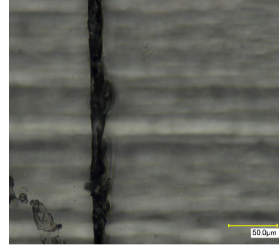
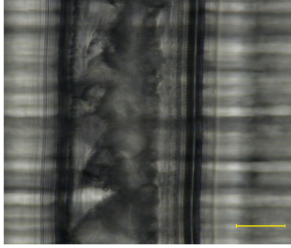
$$\chi_{SF} = 0.71, T_{damage} = 3\text{ }^{\circ}\text{C}, T_{heating} = 23\text{ }^{\circ}\text{C}$$



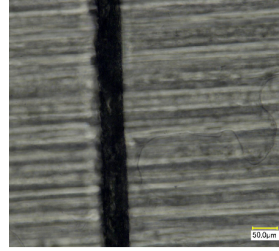
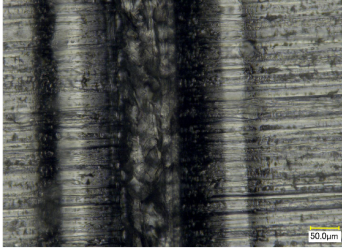
$$\chi_{SF} = 0.71, T_{damage} = 3\text{ }^{\circ}\text{C}, T_{heating} = 30\text{ }^{\circ}\text{C}$$



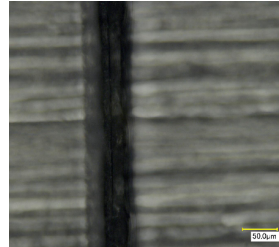
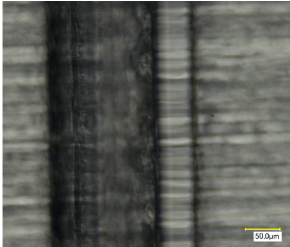
$$\chi_{SF} = 0.71, T_{damage} = 3\text{ }^{\circ}\text{C}, T_{heating} = 35\text{ }^{\circ}\text{C}$$



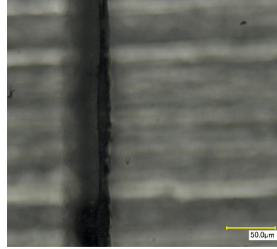
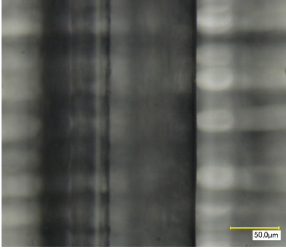
$$\chi_{SF} = 0.71, T_{damage} = 3\text{ }^{\circ}\text{C}, T_{heating} = 35\text{ }^{\circ}\text{C}, \text{Rockwell Tip}$$



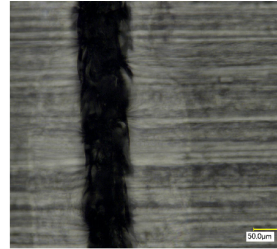
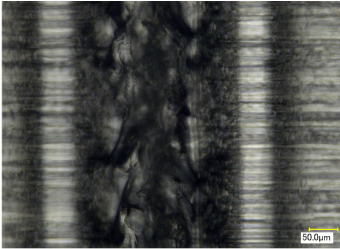
$$\chi_{SF} = 0.59, T_{damage} = 4\text{ }^{\circ}\text{C}, T_{heating} = 23.5\text{ }^{\circ}\text{C}$$



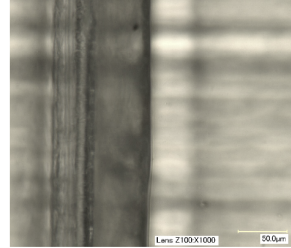
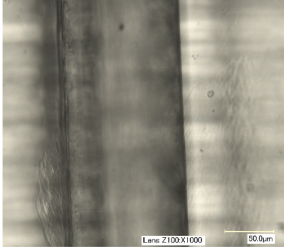
$$\chi_{SF} = 0.59, T_{damage} = 4\text{ }^{\circ}\text{C}, T_{healing} = 38.5\text{ }^{\circ}\text{C}$$



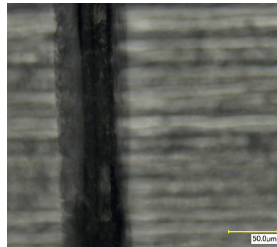
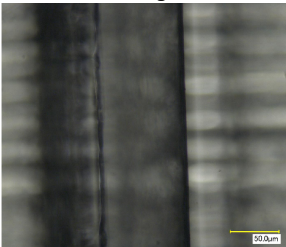
$$\chi_{SF} = 0.59, T_{damage} = 4\text{ }^{\circ}\text{C}, T_{healing} = 38.5\text{ }^{\circ}\text{C}, \text{Rockwell Tip}$$



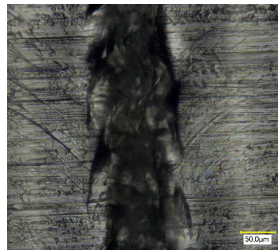
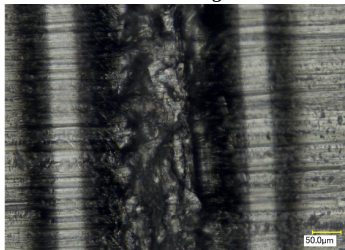
$$\chi_{SF} = 0.51, T_{damage} = 9\text{ }^{\circ}\text{C}, T_{healing} = 24\text{ }^{\circ}\text{C}$$



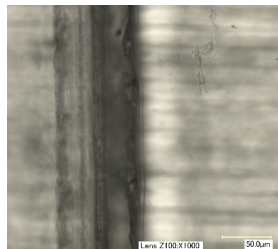
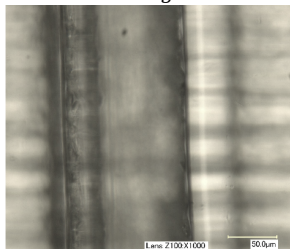
$$\chi_{SF} = 0.51, T_{damage} = 9\text{ }^{\circ}\text{C}, T_{healing} = 27.5\text{ }^{\circ}\text{C}$$



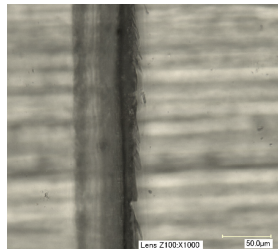
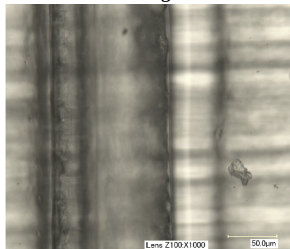
$\chi_{SF} = 0.51, T_{damage} = 9\text{ }^{\circ}\text{C}, T_{heating} = 27.5, \text{Rokwell Tip } ^{\circ}\text{C}$



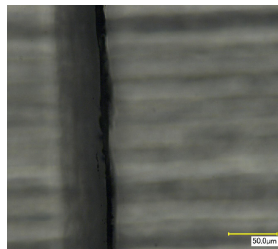
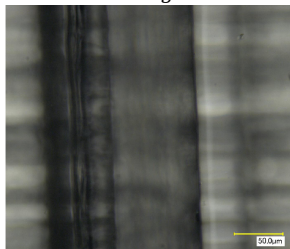
$\chi_{SF} = 0.51, T_{damage} = 9\text{ }^{\circ}\text{C}, T_{heating} = 28\text{ }^{\circ}\text{C}$



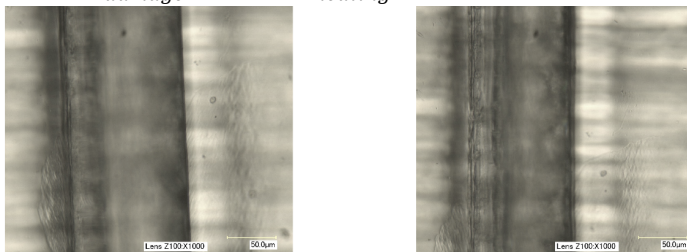
$\chi_{SF} = 0.51, T_{damage} = 9\text{ }^{\circ}\text{C}, T_{heating} = 36\text{ }^{\circ}\text{C}$



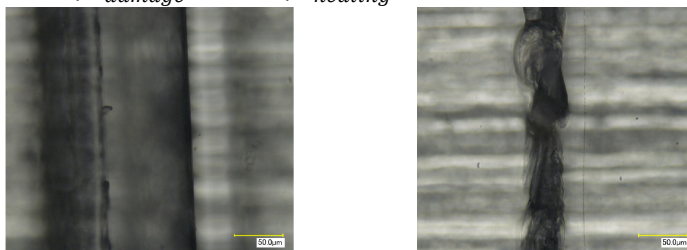
$\chi_{SF} = 0.51, T_{damage} = 9\text{ }^{\circ}\text{C}, T_{heating} = 42.5\text{ }^{\circ}\text{C}$



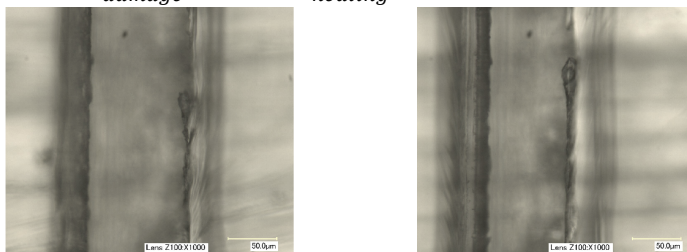
$$\chi_{SF} = 0.42, T_{damage} = 12\text{ }^{\circ}\text{C}, T_{healing} = 33\text{ }^{\circ}\text{C}$$



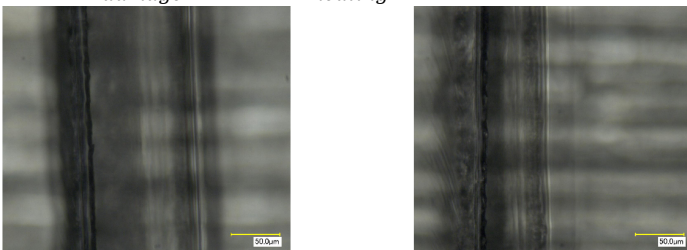
$$\chi_{SF} = 0.42, T_{damage} = 12\text{ }^{\circ}\text{C}, T_{healing} = 48\text{ }^{\circ}\text{C}$$



$$\chi_{SF} = 0.27, T_{damage} = 18\text{ }^{\circ}\text{C}, T_{healing} = 55\text{ }^{\circ}\text{C}$$



$$\chi_{SF} = 0.27, T_{damage} = 18\text{ }^{\circ}\text{C}, T_{healing} = 80\text{ }^{\circ}\text{C}$$



References

- [1] X. Zhang, M. Fevre, G. O. Jones, and R. M. Waymouth, *Catalysis as an enabling science for sustainable polymers*, *Chemical reviews* **118**, 839 (2018).
- [2] M. A. Meier, J. O. Metzger, and U. S. Schubert, *Plant oil renewable resources as green alternatives in polymer science*, *Chemical Society Reviews* **36**, 1788 (2007).

- [3] B. S. Sumerlin, *Next-generation self-healing materials*, *Science* **362**, 150 (2018).
- [4] M. Hager, P. Greil, L. C. S. van der Zwaag, and U. S. Schubert, *Self-healing materials*, *Advanced Materials* **22**, 5424 (2010).
- [5] S. J. García, H. R. Fischer, and S. van der Zwaag, *A critical appraisal of the potential of self healing polymeric coatings*, *Progress in Organic Coatings* **72**, 211 (2011).
- [6] Y. Yang, X. Ding, and M. W. Urban, *Chemical and physical aspects of self-healing materials*, *Progress in Polymer Science* **49**, 34 (2015).
- [7] M.-M. Song, Y.-M. Wang, X.-Y. Liang, X.-Q. Zhang, S. Zhang, and B.-J. Li, *Functional materials with self-healing properties: a review*, *Soft Matter* **15**, 6615 (2019).
- [8] A. Stoddart, *Holding the key to healing*, *Nature Reviews Materials* **3**, 416 (2018).
- [9] J. A. Neal, D. Mozhdghi, and Z. Guan, *Enhancing mechanical performance of a covalent self-healing material by sacrificial noncovalent bonds*, *Journal of the American Chemical Society* **137**, 4846 (2015).
- [10] A. Susa, R. Bose, A. M. Grande, S. van der Zwaag, and S. J. Garcia, *Effect of the dianhydride/branched diamine ratio on the architecture and room temperature healing behavior of polyetherimides*, *ACS applied materials & interfaces* **8**, 34068 (2016).
- [11] M. W. Urban, D. Davydovich, Y. Yang, T. Demir, Y. Zhang, and L. Casabianca, *Key-and-lock commodity self-healing copolymers*, *Science* **362**, 220 (2018).
- [12] V. Montano, M. M. Wempe, S. M. Does, J. C. Bijleveld, S. van der Zwaag, and S. J. Garcia, *Controlling healing and toughness in polyurethanes by branch-mediated tube dilation*, *Macromolecules* **52**, 8067 (2019).
- [13] Y. Yanagisawa, Y. Nan, K. Okuro, and T. Aida, *Mechanically robust, readily repairable polymers via tailored noncovalent cross-linking*, *Science* **359**, 72 (2018).
- [14] C. C. Hornat, Y. Yang, and M. W. Urban, *Quantitative predictions of shape-memory effects in polymers*, *Advanced Materials* **29**, 1603334 (2017).
- [15] C. C. Hornat and M. W. Urban, *Entropy and interfacial energy driven self-healable polymers*, *Nature communications* **11**, 1 (2020).
- [16] E. D. Rodriguez, X. Luo, and P. T. Mather, *Linear/network poly(ϵ -caprolactone) blends exhibiting shape memory assisted self-healing (smash)*, *ACS applied materials & interfaces* **3**, 152 (2011).

- [17] X. Luo and P. T. Mather, *Shape memory assisted self-healing coating*, *ACS Macro Letters* **2**, 152 (2013).
- [18] Q. Zhao, W. Zou, Y. Luo, and T. Xie, *Shape memory polymer network with thermally distinct elasticity and plasticity*, *Science advances* **2**, e1501297 (2016).
- [19] Y. Heo and H. A. Sodano, *Self-healing polyurethanes with shape recovery*, *Advanced Functional Materials* **24**, 5261 (2014).
- [20] M. Heuchel, J. Cui, K. Kratz, H. Kosmella, and A. Lendlein, *Relaxation based modeling of tunable shape recovery kinetics observed under isothermal conditions for amorphous shape-memory polymers*, *Polymer* **51**, 6212 (2010).
- [21] B. K. Kim, Y. J. Shin, S. M. Cho, and H. M. Jeong, *Shape-memory behavior of segmented polyurethanes with an amorphous reversible phase: The effect of block length and content*, *Journal of Polymer Science Part B: Polymer Physics* **38**, 2652 (2000).
- [22] H. M. James and E. Guth, *Theory of the elastic properties of rubber*, *The Journal of Chemical Physics* **11**, 455 (1943).
- [23] L. R. G. Treloar, *The physics of rubber elasticity* (Oxford University Press, USA, 1975).

6

From damage closure to electrolyte barrier restoration in self-healing polyurethane coatings: a function of the soft-to-hard ratio and hydrogen bond state

*I thought up an ending for my book.
'And he lives happily ever after, till the end of his days'.*

John R. R. Tolkien, in *The Lord of the Rings*

Abstract

The use of self-healing polymeric coatings has long been proposed as a way to make coated metals less sensitive to scratch damage and to extend their lifetime under corrosive conditions. Nevertheless, the requirements for the polymer structure to lead to desirable scratch closure and sealing are not clear yet. In this work we control the soft phase fraction in thermoplastic polyurethanes to study its influence on the two steps of the healing process of organic coatings, namely the scratch closure and the restoration of the barrier against electrolyte ingress. To this aim, comparable polyurethanes with different segmentation states are applied as organic coatings on plain carbon steel plates, scratched under very well controlled conditions, and the damage closure and sealing kinetics are studied in details. The scratch closure is measured optically while the barrier restoration is probed by the accelerated cyclic electrochemical technique (ACET). Scratch closure due to entropic elastic recovery followed by sealing induced by local viscous flow and interfacial hydrogen bonding shows a strong and positive dependence on the soft phase fraction content and the state of the H-bond (urea/urethane ratio). Polyurethanes with a lower soft phase fraction lead to a higher urea/urethane ratio and interestingly show less efficient crack closure but a more efficient barrier restoration. The present work highlights the critical role of soft/hard block and urea/urethane content on crack closure and barrier restoration of anticorrosive organic coatings.

6.1. Introduction

The use of self-healing polymeric coatings has been proposed already for many years as a promising method to extend the lifetime of coated structures exposed to aqueous corrosion conditions [1–4]. The principal challenge remains to develop self-healing coatings with mechanical properties acceptable by industry such that, when damaged, they not only are able to close cracks but also to fully recover the original barrier function of the coating such that no preferential corrosion will take place at the former damage site.

Intrinsic healing polymers offer the potential of healing large damages in corrosion protective coatings. Such polymers owe the healing ability to the molecular design of the polymer network through the use of reversible chemical moieties that allow on-demand local temporary mobility of the network. In order to effectively exploit this characteristic in the field of coatings with the least human intervention possible, a proper balance between elastic recovery after damage, required to bring the two crack planes in contact, and local viscous flow, required to allow for interface diffusion and reaction to restore barrier, seems to be required. The pressure-free scratch closure may be achieved by viscous flow or by using so called shape memory principles to allow the mechanical closure of cracks by releasing the (elastic) energy stored during the damage [5]. This last concept is used in several intrinsic self-healing polymer coatings. In particular, from a polymer design point of view, the energy storage during damage leading to shape memory effect has been shown through the use of main chain entanglements, permanent crosslinking [6, 7], polymer blending [8, 9], and micro-phase separation [10, 11].

While the mechanical closure of cracks, which is relatively easy to monitor with conventional optical or SEM microscopy, is a pre-requisite, the formation of entanglements and physical and chemical bonds at the polymer-polymer and polymer-metal interfaces are equally important from a corrosion protection perspective. These interfacial properties can be monitored using electrochemical techniques such as electrochemical impedance spectroscopy (EIS) [4, 12–15]. Quasi autonomous crack closure in combination with interfacial healing may be hard to realise in a one-phase polymer system due to the intrinsic dichotomy between fast chain interdiffusion (which guarantee rapid damage disappearance) and high binding energy of reversible moieties (which ensures high interfacial healing). In order to maximize the potential of the healing concept in protective coatings it is necessary to control the polymer architecture and identify the polymer features that help maximizing both damage closure and interfacial sealing. In earlier works we initiated this task and showed that it is possible to control the mechanical properties of healed interfaces in branched polyurethanes by tuning the length of the dangling side chains [16]. We also introduced a quasi-quantitative method to relate the content of reversible dynamic bonds to early-stage healing fracture resistance through the use of deconvolution protocols and work of deformation [17]. Work by others on self-healing polyurethane coatings showed how their characteristic phase separation at the nanoscale induces delayed elasticity upon damage driving the scratch closure process [18–20]. Nevertheless, there are no reported systematic works trying to unveil the role of the soft to hard block ratio on the different stages of the healing

process in polyurethane coatings.

The effect of hydrogen bonding on the interfacial healing of free standing polymers has been for long reported. For comparable polymer networks, an increase in the content of dynamic hydrogen bonds and the use of hydrogen-bonding reversible moieties with higher binding energies (e.g. multidentate ligands) lead to stronger healed interfaces when broken parts are manually brought in contact. The hydrogen bonding functionality can be interred from the reported dimerization constants calculated for several hydrogen bonding groups ranging from monodentate to quadruple bonding groups [21]. This idea has recently been intentionally exploited with well selected monomers to increase the mechanical properties of intrinsic self-healing polymers [22], but the positive effect of an increase in hydrogen bonding binding energy on interfacial healing of polymers and coatings remains to be demonstrated.

In the present work we investigate the effect of both soft/hard block ratio and urea/urethane content on the healing process and efficiency of a set of self-healing polyurethanes with comparable chemistry and properties. By varying the ratio between the polyol (which contains short dangling chain regularly distributed on the main chain, see Figure 6.1), chain extender and isocyanate we control the degree of segmentation and soft phase fraction and investigated its impact on the balance between scratch closure and barrier restoration responsible for the passive corrosion protection functionality. The resulting polyurethane formulations are applied on carbon steel panels. As a result of the monomers used, the implemented strategy leads to a change in the relative ratio between urea (bidentate) and urethane (monodentate) reversible ligands. This allows to get insights into the effect of an increase in binding energy of the reversible group on both crack closure and crack sealing. FTIR was employed to quantify the urea/urethane content as function of the soft fraction. Light optical microscopy and scanning electron microscopy allowed the monitoring and quantification of the crack closure process and kinetics. Accelerated cyclic electrochemical technique (ACET) is used to monitor the effect of the soft fraction and urea/urethane ratio on the barrier properties and the sealing restoration after damage.

6.2. Experimental Section

6.2.1. Materials

Butyl acetate (BuAc, >99.7%), 1,4-butanediol (BDO, 99%), isophorone diisocyanate (IPDI, 98%), dibutyltin dilaurate (DBTDL, 95%) were purchased from Sigma-Aldrich. Polyether siloxane copolymer wetting additive TEGO Wet 270 was purchased from Evonik Industries. Polyol CroHeal 1000 (equivalent molecular weight 1200 g/mol) was kindly provided from Croda Nederland B.V. Sodium chloride was purchased from VWR International. All the reagents were used as received without further purification.

6.2.2. Synthesis segmented polyurethanes and coating preparation

Six segmented polyurethanes were synthesized by single-shot technique reacting IPDI (diisocyanate), BDO (chain extender) and CroHeal™ 1000 (polyol). The molecular structure of the segmented polyurethanes is shown schematically in **Figure 6.1**. The short hard segments (IPDI + BDO) are connected by long and highly aliphatic soft segments (IPDI + CroHeal™ 1000). The nominal molar soft phase fraction was estimated as:

$$\chi_{SF} = \frac{n(\text{CroHeal1000})}{n(\text{CroHeal1000}) + n(\text{BDO})}$$

where n stands for number of moles.

The nominal soft phase fraction was controlled by varying the molar ratio $\text{CroHeal}/\text{BDO}$ in the monomer feed yet maintaining the same isocyanate/hydroxyl functional groups ratio ($\text{NCO}/\text{OH}=1.1$). By this approach χ_{SF} was set to the following levels $\chi_{SF} = 0.71, 0.59, 0.51, 0.42$ and 0.27 . Here, the synthesis of polymer $\chi_{SF} = 0.42$ is reported in some more detail as it is representative of the synthesis process used for all polymer systems.

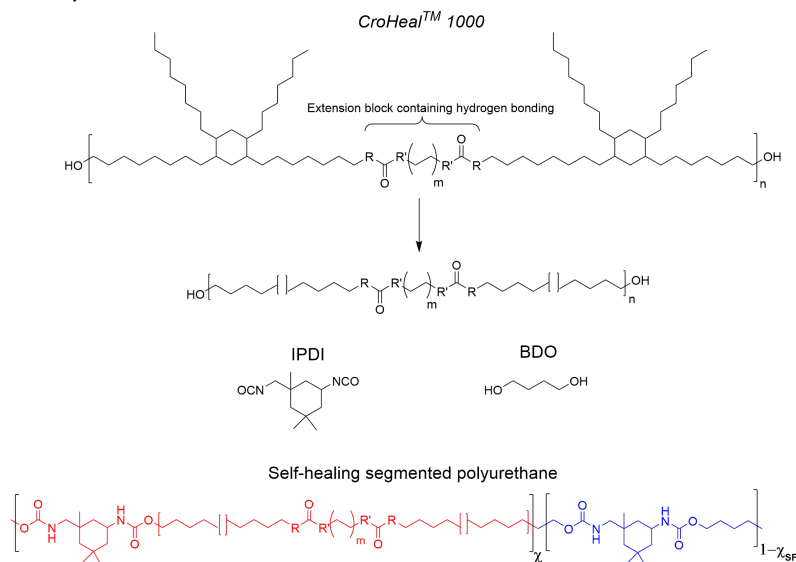


Figure 6.1: **Monomers used and segmented molecular structure of the synthesized polyurethanes. Red structure represents the nominal soft blocks and blue the hard blocks.**

CroHeal™ 1000 was heated for 1 hour at 60 °C to reduce the intrinsic viscosity of the monomer and facilitate mixing. Subsequently 6.0 grams (5.00 mmol) of CroHeal™ 1000 were transferred to a 20 ml polypropylene cup. Butyl acetate solvent (BuAc, 0.94 g, 8.13 mmol) was quickly added to further reduce the intrinsic viscosity. 0.6 grams of 1,4-butanediol were then transferred to the cup (BDO, 0.6 g, 6.66 mmol). Subsequently TEGO 270 (0.024 grams) and dibutyltin dilaurate (DBDTL, 0.063 grams, 0.1 mmol) were added dropwise. Immediately thereafter,

isophorone diisocyanate (IPDI, 2.85 grams, 12.82 mmol) was dosed from a syringe. The system was stirred vigorously using a mechanical agitator and the reaction left to proceed for 15 seconds at room temperature. The mixture was then applied on an acetone-cleaned carbon automotive steel plate (Q-panel) using a coating bar with a wet thickness of 150 μm leading to coatings with a dry thickness of $100 \pm 5.0 \mu\text{m}$. For bulk polymer characterization, part of the polymer mixture was poured into a 4x4 cm PTFE molds to obtain free-standing films of $1 \pm 0.2 \text{ mm}$ thick. Analogous procedures were followed for the other polymers as detailed in the Supporting Information at Table S1.

Both the coated panels and the PTFE molds with the polymer mixtures were dried for 30 minutes at ambient laboratory conditions and subsequently cured for 30 minutes at 60 °C in an air recirculating furnace. The polyurethane coatings and free standing films were then equilibrated for at least 1 week at ambient laboratory conditions prior to testing.

6.2.3. Characterization Methods

Attenuated total reflectance infrared spectroscopy (ATR-FTIR)

Attenuated total reflectance Fourier transform infrared spectroscopy was used to monitor synthesis completion and to study the state of hydrogen bonding in the proposed segmented polyurethanes. Each analyzed ATR-FTIR spectrum, obtained with a PerkinElmer Spectrum 100, was the average of 32 scans over the wavenumber region $4000 - 500 \text{ cm}^{-1}$ with resolution of 1 cm^{-1} .

The infrared spectra were deconvoluted over the wavenumber range $1800 - 1600 \text{ cm}^{-1}$ in order to identify hidden sub-peaks that give physical information on the state of hydrogen bond of the carbonyl group (i.e. monodentate and bidentate hydrogen bonds related to urea and urethane groups respectively). The sub-peaks were identified by the analysis of the second order derivatives of the infrared spectrum function. A fitting procedure was subsequently applied using Gaussian functions centered at the wavenumber corresponding to the local minima of the second order derivative. The fitting procedures were performed using the software Origin-Pro 2015 (OriginLab). For all polymers the coefficients of determination (r^2) were higher than 0.99, indicating a high fitting reliability.

Accelerated cyclic electrochemical technique (ACET)

The ACET measurements were performed at room temperature following well-established procedures [23, 24]. The tests were performed with an Autolab PGSTAT 302N potentiostat/galvanostat, using a conventional three-electrode cell configuration consisting of a saturated Ag/AgCl reference electrode, a carbon black rod with diameter of 50 mm as the counter electrode, and the coated carbon steel substrate as the working electrode. 50mL of stagnant 0.5 M NaCl aqueous solution in equilibrium with air was used as electrolyte. The samples were placed vertically in the electrochemical cell with an exposed area of around 0.8 cm^2 . This geometry allowed monitoring the sample under immersion during the whole duration of the test with a CCD camera as performed elsewhere [25]. A Faraday cage was

employed to avoid the interference of external electromagnetic fields. The intact and healed coating systems were electrochemically characterized in duplo showing good reproducibility.

Prior to the test, the open circuit potential (OCP) of the samples was measured and used for the first electrochemical impedance spectroscopy (EIS) test. As this moment, the testing procedure consists of the repetition of three consecutive steps: (i) a non-destructive EIS at 10 mV (rms) sinusoidal perturbation with respect to the OCP in the frequency range $10^{-1} - 10^4$ Hz. Ten data points per frequency decade were acquired; (ii) a cathodic polarization at a constant potential of -4 V for 20 min; and (iii) a potential relaxation for 3 hours to record the open circuit potential (OCP) evolution with time. The test sequence was repeated for 5 times.

Calculation of coating capacitance

The coating capacitance was calculated directly from the EIS data as using equation (1):

$$C_c = \frac{1}{2\pi f_i Z''} \quad (6.1)$$

where f_i the excitation frequency and Z'' is the imaginary part of the impedance at the f_i excitation frequency. f_i was set at 230 Hz, where the total impedance of all systems is entirely dominated by the polymer capacitance and without external interferences [26–28]. C_c is a direct estimation of the water uptake considering the relation:

$$C_c = \epsilon \epsilon_0 \frac{A}{d} \quad (6.2)$$

where ϵ is the dielectric constant of the coating, ϵ_0 the vacuum permittivity, A the area of the coating exposed to the electrolyte and d is the coating thickness. As the coating absorbs water the dielectric constant of the coating increases and with it the coating capacitance.

Creation of scratch damage

Scratches of 5 millimeters in length and 100 μm width were produced at $T = 21^\circ\text{C}$ by a computerized scratch machine CSM Instrument Scratch Tester, using a fresh razor blade with a 100 μm wide tip until the razor blade tip reached the steel substrate. To do so, the axial force was varied between a minimum of 1 N ($\chi_{SF} = 0.71$) and a maximum of 1.8 N ($\chi_{SF} = 0.27$), depending on the hardness of the coating. The sliding speed was set to 1 mm/min and the tip-to-metal contact monitored with an LED.

Scanning electron microscopy

A high resolution JOEL SEM (JSM-75000F) operating at 5 kV was employed to visualize the degree of damage closure at the end of the healing process. To do this the polymer coatings were subjected to a high vacuum, gold sputtering treatment before observation. Since gold sputtering was required for samples to be observed, every data-points shown in the closure kinetics study (Figure 6.7) corresponds to a different coating specimen.

Thermal Analyses

Thermal properties were determined by thermogravimetric analysis (TGA) and differential scanning calorimetry (DSC). TGA analyses were performed from room temperature to 600 °C, under a dry nitrogen atmosphere at 10 °C/min heating rate using a Perkin Elmer TGA 4000. DSC measurements were performed under a dry nitrogen atmosphere and 10 °C/min heating and cooling rates over the temperature range -40 °C to 200 °C using a Perkin Elmer Pyris Sapphire DSC. The glass transition temperature (T_g) was determined using the inflection point method.

Melt rheology

Oscillatory shear experiments were carried out on a strain-controlled Physica MCR 102 (Anton Paar GmbH) rheometer using a parallel plate geometry. The diameter of the plate was 8 mm and the sample thickness was set to 1.0 ± 0.2 mm. Temperature sweep analyses were carried out over the temperature range -20 °C to 180 °C using a heating rate of 2.8 °C/min. All the tests were run at fixed strain of $\gamma = 0.1\%$, which is always within the linear viscoelastic regime as established by preliminary strain amplitude analyses.

X-Ray diffraction analysis

Room temperature X-ray diffraction (XRD) spectra of the polymers deposited on aluminum holders were recorded using a Rigaku MiniFlex 600 diffractometer. The angle ranged from $2\theta = 1^\circ$ to 60° with 0.1° increments. The samples were rotated during the measurement in an evacuated vacuum chamber.

6.3. Results and Discussion

6.3.1. Effect of soft phase fraction on polymer structure and dynamics

Segmented polyurethanes (TPUs) are well-known for their characteristic nano-phase separated morphology which determines rubber-like properties (e.g. rubbery elasticity). The phase separation at the nanoscale is attributed to the presence in the main chain of short hydrophilic blocks (the hard block) connected by long hydrophobic segments (the soft block). The block-like molecular structure of the segmented polyurethanes presented in this manuscript is shown in **Figure 6.1**. Short blocks with strong hydrogen bonds (IPDI and BDO) are connected by long hydrophobic segments (IPDI + CroHeal 1000). As a result, when less CroHeal 1000 is used (less χ_{SF}) the polymer becomes more segmented and with longer hard blocks within the random character of the polymers.

All polymers are partially hazy, with a glass transition (T_g) located between 4 °C ($\chi_{SF} = 0.71$) and 27 °C ($\chi_{SF} = 0.27$) as determined by DSC (Figure S2 and Table S2). Independently of the χ_{SF} all polymers show an equally high temperature stability with 5% weight loss at temperatures higher than 300 °C (Table S2).

Given the monomers used and the resulting bonds, the polymers used in this work are expected to have both monodentate (urethane) and bidentate (urea) groups

in the polymer network. The formation of urea linkages is determined by a simple chemical process: in poly(urea)urethanes the urea linkages can be formed due to reaction with moisture. In this particular case part of the isocyanate groups of IPDI can react with water molecules to give carbamic acid groups that decompose in amines and CO_2 , the amines will subsequently react with another isocyanate groups to form a urea bond. Due to the large steric hindrance of the CroHeal™ 1000 polyol, the free IPDI preferentially reacts with BDO to form urethane bonds. Some of these subsequently react with the amines resulting from side reaction between IPDI and moisture to form urea bonds.

In view of the difference in binding energy between the two ligands and its potential impact on interfacial healing, we quantified the relative ratio between urea and urethane ligands with an FTIR deconvolution protocol [29, 30]. As a first step we calculated the second derivative of the IR spectrum for the Amide I carbonyl stretching vibration region of interest ($1800\text{--}1640\text{ cm}^{-1}$) and identified all the sub-bands (**Figure 6.2A** shows the example for three compositions). This process revealed the presence of four peaks hidden in the carbonyl region. Based on previous reports on segmented polyurethanes [31] and theory on the bond vibration strength (higher strength leads to lower wavenumbers) we identified the peaks as: free carbonyl groups (1727 cm^{-1}), disordered hydrogen bonded urethane carbonyl (1711 cm^{-1}), ordered hydrogen bonded urethane carbonyl (1694 cm^{-1}) and hydrogen bonded urea groups (1671 cm^{-1}). The same principal sub-bands were found for all the polyurethanes studied here (see Support Information Figure S8).

With the peaks identified we proceeded with the deconvolution of the IR spectrum by running a mean square minimization fitting procedure to optimize the fit for the Amide I experimental IR curve using four time constants. The results of the fitting procedure for $\chi_{SF} = 0.27$ are shown in Figure 6.2B. For all polymers the correlation coefficient was higher than 0.99, which confirms the very good agreement between fitness and experimental functions. With the fit complete we integrated the area under each single Gaussian sub-peak to obtain quantitative information about the distribution of the hydrogen bond state. For $\chi_{SF} = 0.27$ a very low fraction of free carbonyl groups (non-hydrogen bonded) was obtained as it can be inferred from the small area under the free carbonyl sub-band (1727 cm^{-1}). Urethane (1711 and 1691 cm^{-1} sub-bands) and urea hydrogen bonded carbonyls (1674 cm^{-1}) appear as equally concentrated. The fitting procedure was applied to all coating formulations with comparable conclusions as shown in Table S3 and Figure S8.

Figure 6.2C shows the *Urea fraction* dependency with the χ_{SF} (blue squared data-points). The *Urea fraction* was calculated by using the quantitative data obtained by the FTIR deconvolution fitting as:

$$\text{Urea fraction} = \frac{A\text{Intg}(\text{Urea})}{A\text{Intg}(\text{Urea}) + A\text{Intg}(\text{Ord.Urethane}) + A\text{Intg}(\text{Dis.Urethane})} \quad (6.3)$$

where *AIntg* stands for the integrated area under the specific deconvoluted IR peak. As can be seen, the *Urea fraction* decreases linearly with the increase of soft block fraction χ_{SF} from values > 0.3 for the most segmented polyurethane ($\chi_{SF} = 0.27$) to about 0.19 for the least segmented polyurethane ($\chi_{SF} = 0.71$). The

increase in *Urea fraction* with the decrease of χ_{SF} is simply explained looking at the monomer feed for the different formulations. Since BDO has a much lower molecular weight compared to CroHeal 1000, in order to keep the ratio OH/NCO constant (OH/NCO = 1.1), a higher IPDI molar content is fed for the polymer designed with low χ_{SF} . As explained, the reaction between IPDI and moisture originates amines in the mixture which then lead to the formation of urea linkages. Therefore the higher IPDI molar content justifies the higher fraction of urea units in the final network. This confirms the influence of soft/hard phase ratio on the presence of high energetic bidentate reversible groups.

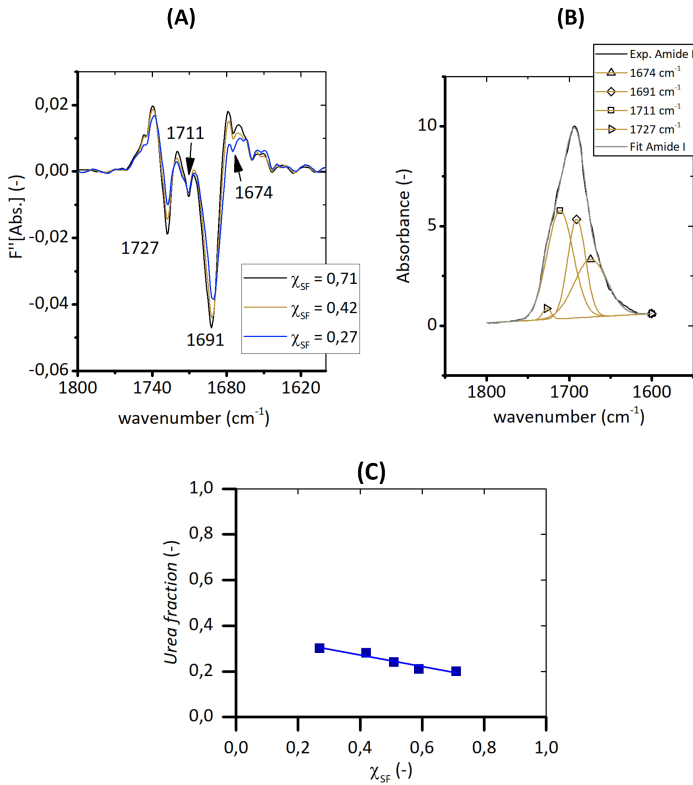


Figure 6.2: **Quantification of urea and urethane groups from FTIR deconvolution.** (A) Second derivative plots of ATR-FTIR spectra of $\chi_{SF} = 0.71$, 0.42 , 0.27 showing the presence of four local minima in the Amide I band. (B) $\chi_{SF} = 0.27$ Amide I deconvolution. (C) Evolution of the *Urea fraction* as function of the χ_{SF} .

The differences in polymer architecture due to the variation of the soft phase fraction can be found back in the macromolecular dynamics of the networks. **Figure 6.3** presents the small amplitude, temperature sweep shear tests for all the synthesized polymers. The elastic data are presented as elastic shear modulus (G') as a function of temperature. The viscoelastic data are reported in the form of the tangent of the phase angle (damping factor, $\tan \delta = G'' / G'$) to quantify the ratio

between energy lost and the energy stored [32], particularly relevant during a relaxation transition. Following the temperature dependence of $\tan \delta$ we infer that the viscoelastic behavior indeed resembles that of segmented polyurethanes. In this framework, the first dynamic transition at $T_{\max \tan \delta}$ is attributed to the relaxation of the continuous soft matrix while the next transition is associated to the presence of segregated hard segments which are able to store mechanical energy for a broad range of temperature until terminal relaxation occurs ($T > T_{\text{terminal}}$). By decreasing the soft phase fraction χ_{SF} three effects are apparent: (i) in analogy with results on T_g obtained via calorimetry, the $T_{\max \tan \delta}$ (which is used as alternative mechanical definition of the glass transition) shifts upwards from 9 °C (for $\chi_{SF} = 0.71$) to 31 °C (for $\chi_{SF} = 0.27$); (ii) more segmented (low χ_{SF}) polymers show delayed access to terminal relaxation (T_{terminal}) as well as a decrease of the absolute value of $\tan \delta$ in the plateau region ($T_{\max \tan \delta} < T < T_{\text{terminal}}$) indicating a more efficient energy storage which can be attributed to the higher hard block fraction and nanophase segregation; and (iii) as expected for lower amount of energy-dissipating blocks, lower χ_{SF} leads to a decrease in damping at $T_{\max \tan \delta}$ (lower $\tan \delta$) because a lower fraction of the material is relaxing at the glass transition temperature. Similar effects were observed in earlier studies on segmented polyurethanes by Ferguson et al. [33] in which the polymer structure was systematically controlled by changing the amount of chain extender used.

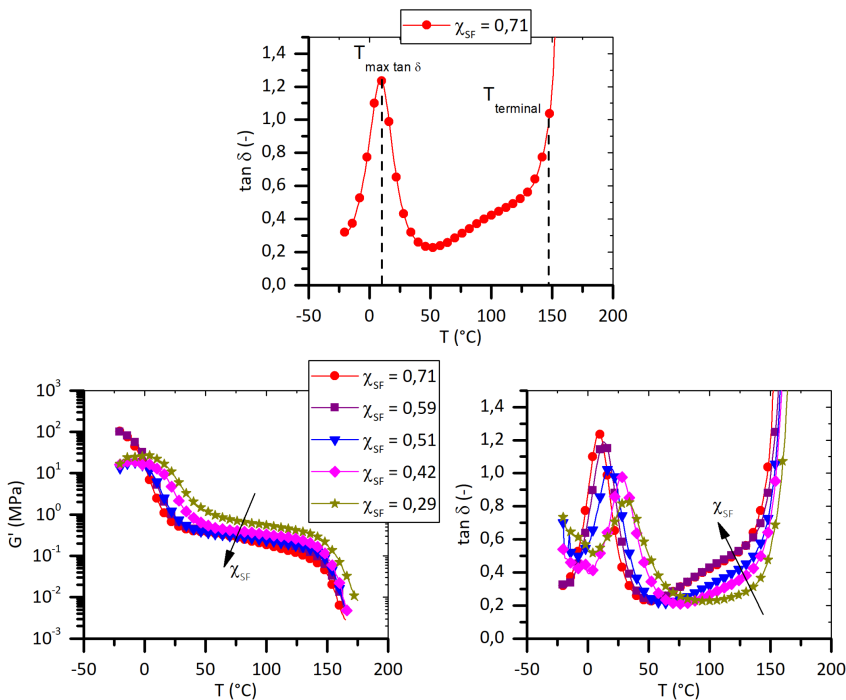


Figure 6.3: **Oscillatory shear analysis results.** The viscoelastic behaviour resembles the typical one of segmented polyurethanes. The increase of χ_{SF} determines a faster access to terminal relaxation, a increased of dissipation in the apparent-plateau region and a higher damping at glass transition.

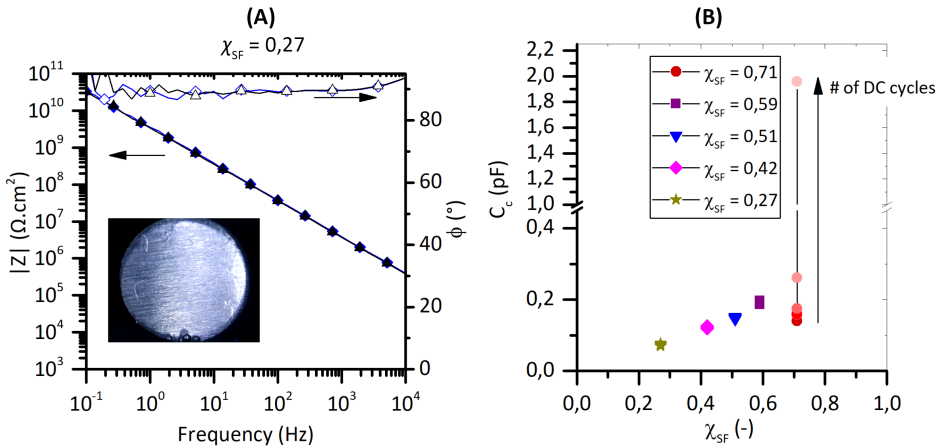


Figure 6.4: **Barrier properties of the intact coatings. (A)** Bode plot showing the EIS results as function of the ACET cycles for the sample $\chi_{SF} = 0.27$. The blue diamond markers show the initial EIS results (prior to any direct polarisation). The black triangle markers show the final EIS (upon the fifth polarisation cycle). Filled markers refer to the total impedance $|Z|$, open markers refer to the phase Φ . The inset shows a photograph of the coating under immersion during the last ACET cycle. **(B)** Coating capacitance evolution with the polymer soft phase fraction χ_{SF} and the polarization cycles. Note that the coating capacitance increases with the polymer soft phase fraction χ_{SF} .

6

6.3.2. Effect of soft phase fraction on barrier properties of intact coatings

Figure 6.4A shows a Bode plot with the EIS results obtained from the ACET test for an intact sample $\chi_{SF} = 0.27$ as a function of the number of ACET cycles. The inset shows an optical snapshot of the sample obtained after the last ACET cycle to demonstrate the absence of defects. The Bode plot resembles that of a perfect capacitor (frequency independent phase $\Phi \approx 90^\circ$) characteristic of intact barrier coatings. The high impedance and phase angle, and the absence of defects is maintained during the whole duration of the ACET test, i.e. there is no substantial difference between the first (blue diamond markers) and the last (black triangle markers) cycle. In agreement with previous works using this technique for intact coatings, the high stability of the EIS signal and absence of blisters with the cycles despite the strong polarization (-4 Volts) is an indication of the system being a coating with low permeability, no manufacturing defects and a strong adhesion. In order to obtain a relation of the water uptake as function of the polarization cycles and the soft block fraction, the coating capacitance (C_c) was extrapolated using Equation 1. Figure 6.4B shows the capacitance results for all the coating formulations and cycles. As can be seen, the coating capacitance C_c , and therefore water uptake increases with the soft fraction (χ_{SF}) content which in its turn corresponds to a lower urea/urethane fraction. A similar trend was observed in a previous study [34] using segmented hybrid poly(urea)urethanes in which a higher urea/urethane content led to a lower water uptake. Figure 6.4B also shows how the coatings maintain a similar coating capacitance throughout the ACET cycles. The

highest soft fraction ($\chi_{SF} = 0.71$) represents an exception to these trends, as this sample shows an initially lower coating capacitance than expected and an increase in the coating capacitance between the 3rd and 5th DC cycle. This suggests that when the fraction of soft phase is clearly higher than that of the hard block the hydrophobic character of the polyol monomer dictates the initial degree of water permeability. The effect is nevertheless lost with the polarization cycles as, once the water ingresses, the resistance to absorb water decreases due to the lower amount of physical crosslinks (hard blocks) to refrain the polymer from adapting to more water ingress. The trend of the coating capacitance with the cycles for each sample can be seen in Figure S3 of the Supplementary Information.

6.3.3. Effect of soft phase fraction on scratch closure kinetics

The scratch-healing mechanism of the polyurethane coatings can be visualized by considering the thermodynamic response of the polymer to the mechanical damaging and healing events. **Figure 6.5** schematizes the evolution of the local entropy density near the crack with time during a classical coating damage/healing process. When scratched by a razor blade at temperature below the glass transition temperature ($T_{damage} < T_g$), the actual cutting not only produces a scratch extending to the metallic substrate but also displaces the polymer in a lateral direction perpendicular to the scratch. This induced deformation produces an abrupt decrease in the system entropy near the damage. This change in local entropy is quasi-permanent due to the stable segregated phase that provides stable physical crosslink points which prevent the rapid network relaxation. This leads to entropy-driven energy storage at the damage location. Highly elastic polymer networks with high amount of physical crosslink points are in theory able to store more entropy-driven energy. Upon heating at $T_{healing} > T_g$, the entropic energy stored during mechanical damage is released in a process known as entropy driven elastic recovery (EER). This allows the displacement of the two sides of the damage towards the crack center. If this EER is sufficient, the two sides of the scratch will re-establish physical contact, and a healing interface will be formed to allow for the re-shuffling of built-in reversible moieties. In case the polymer is scratched at a temperature above the glass transition temperature ($T_{damage} > T_g$) no significant storage of entropic energy is expected since the polymer relaxes right after the creation of damage. The scratch front displacement and the kinetics of the process are functions of the characteristic network. After the EER, longer times at $T_{healing} > T_g$ lead to no significant variation in entropy, while the system is energetically driven to viscous flow which ultimately can lead to complete scar disappearance. The mechanism, here explained in thermodynamic terms, is known in literature as shape memory assisted self-healing (SMASH) [8].

In the current work, all the polymers were damaged at room temperature ($T_{damage} = 21\text{ }^\circ\text{C}$), which is well above the T_g for systems with $\chi_{SF} = 0.71$, 0.59 and 0.51. In agreement with the theory exposed above, in these systems no entropy driven damage closure could be captured during the post-scratching optical observations as crack closure happened almost immediately after scratching. The other two samples, $\chi_{SF} = 0.42$ and 0.27, were damaged at $T_{damage} < T_g$ and did show EER at

the healing temperature. **Figure 6.6** shows the process for $\chi_{SF} = 0.42$ at $T_{healing} = 65\text{ }^{\circ}\text{C}$ with photo snapshots: start at 0 minutes, end of the EER process at ≈ 1 minute and viscous flow leading to scar disappearance at ≈ 5 minutes.

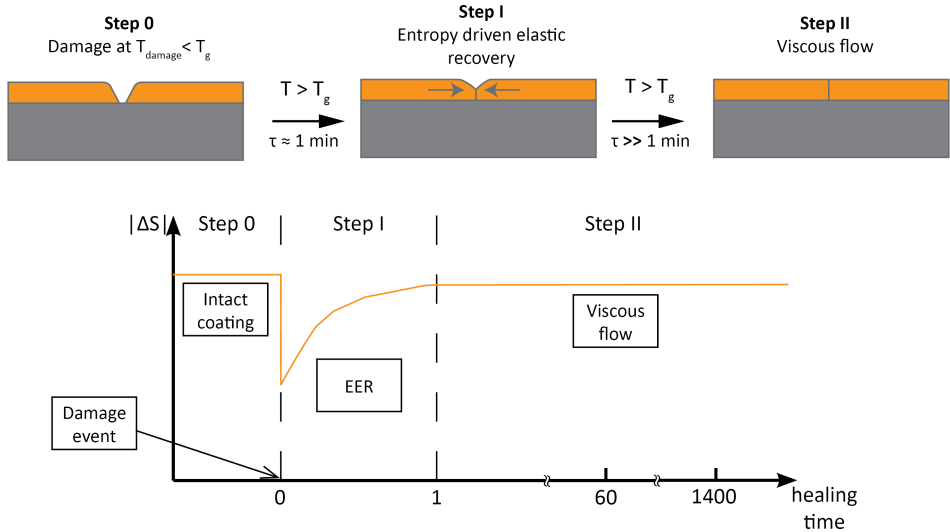


Figure 6.5: **Schematic representation of entropy storage evolution in time in a damage and healing process at $T_{damage} < T_g$ and $T_{healing} > T_g$.**

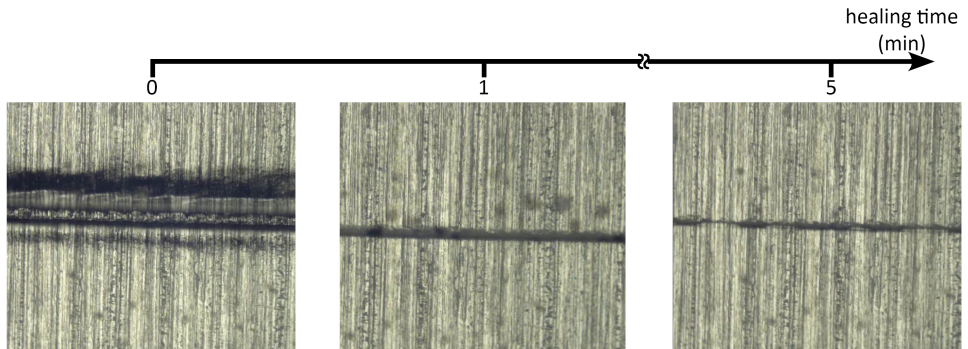


Figure 6.6: **Time evolution of the healing process of $\chi_{SF} = 0.42$ using snapshots of the video footage shown in the Support Information.** At healing time = 0 the scratch is fully open and the metal substrate is clearly visible in between the two scratch fronts. At healing time = 1 minute, the EER process is fully exploited and it brings the scratch fronts back to contact. At healing = 5 minutes viscous flow largely takes place as evidenced by bridging and (partial) scar disappearance.

The quantification of the crack closure at the end of the healing process was performed using scanning electron microscopy (SEM). The micrographs for all compositions are shown in Figure S6. In **Figure 6.7** we report the quantified evolution of the crack width at the top surface of the coating as function of the healing time

at $T_{healing} = 65\text{ }^{\circ}\text{C}$. It should be noted that there was a delay of 8 minutes at $21\text{ }^{\circ}\text{C}$ between the damage event and the first datapoint at $65\text{ }^{\circ}\text{C}$ (heal time = 0.1 min) due to SEM sample preparation time. From Figure 6 we infer that at the moment of the start of the healing process at $T = 65\text{ }^{\circ}\text{C}$ (heal time = 0.1 minutes) the polyurethane coatings with dominant soft phase fractions ($\chi_{SF} = 0.71, 0.59$ and 0.51) showed comparably low scratch widths, one order of magnitude lower than the width of the razor blade. For these polymers $T_{damage} \geq T_g$, and therefore the entropy driven elastic recovery occurred right after damage and before the moment of the actual optical observation. Since $\chi_{SF} = 0.27$ was damaged at a $T_{damage} \ll T_g$ the stored entropy is high and the scratch width at the start of the healing process is very close to the width of the razor blade ($\approx 100\text{ }\mu\text{m}$). As expected $\chi_{SF} = 0.42$, being damaged near its T_g temperature, shows an intermediate behavior. As it can be seen, healing at $65\text{ }^{\circ}\text{C}$ induced a progressive scratch closure in all the polymers. At the end of the test (1400 minutes) all polymers show full crack closure (the scratches become invisible by SEM), with the exception of $\chi_{SF} = 0.27$, which showed full closure at 2800 minutes (not shown here). It is evident that the kinetics of scratch closure increase with the increase of the soft phase fraction. This result is in agreement with our observations on melt dynamics (Figure 6.3), which indicate a faster access to terminal relaxation when increasing χ_{SF} .

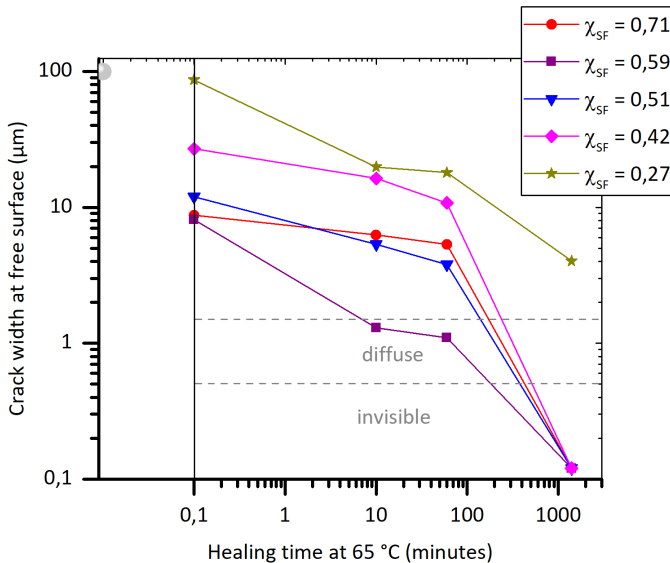


Figure 6.7: **Scanning electron microscopy monitoring of crack closure.** All the coatings were damaged with a razor blade tip ($\approx 100\text{ }\mu\text{m}$ width). As a result the initial damage width in all cases was $100\text{ }\mu\text{m}$ as indicated by the grey ball. As the SEM sample preparation process takes time, the first healing time (healing time 0.1) was obtained after 8 minutes at $T=21\text{ }^{\circ}\text{C}$. The grey lines named "invisible" and "diffuse" refer to the optical perception of the state of the damage closure.

6.3.4. Effect of soft phase fraction on barrier restoration

Besides scratch closure, the healing process of protective organic coatings must take into consideration the restoration of its original functionality as barrier layer against the ingress of electrochemical active species. For convenience we will refer to the restoration of barrier property as scratch sealing, while the physical disappearance of the scratch trace is referred to as scratch closure. We will show that for the present PU's the two processes are decoupled.

Figure 6.8 shows the results of the electrochemical analysis of $\chi_{SF} = 0.27$ when tested in two distinct conditions: (i) damaged (Figure 6.8A-I), and (ii) after 60 minutes healing at 65 °C (Figure 6.8A-II). As a result of the presence of the scratch the coating offers no barrier to the electrolyte as seen in the total impedance similar to that of bare steel and a phase angle much lower than that for a pure capacitor (Figure 6.8A-I, blue diamond markers). Right after the first polarization the coating fails even further showing processes compatible with cathodic de-bonding and gas evolution induced during the ACET test as clearly visible in the snapshots taken during the immersion with the CCD camera (insets of Figure 6.8A-I).

The ACET results for a sample with the same composition and damage but healed for 1 h at 65 °C are radically different as seen in Figure 6.8A-II. Despite the crack seemingly not being fully closed (Figure 6.7 points at a crack width at free surface of $\approx 20 \mu\text{m}$) the EIS signals suggest a complete recovery of the damage from an electrochemical perspective (full capacitive recovery) which is maintained with increasing number of polarization cycles. Similar results were obtained for most of the other polyurethane systems studied here.

In order to obtain a quantification of the degree of restoration of the barrier properties and to be able to compare the scratched-and-healed coatings with intact coatings of the same composition, the coating capacitances of the healed coatings were calculated from the EIS data in a similar way as for the intact coatings and are reported in Figure 6.8B. For coatings with high segmentation ($\chi_{SF} = 0.51, 0.42$ and 0.27) the barrier properties are completely restored to values comparable to the intact coatings ($C_c < 0.2 \text{ pF}$). Moreover, the in-situ imaging showed no degradation signals at the healed scar during the whole duration of the ACET test, from which we conclude that the scratches are fully sealed in the tested conditions.

On the other hand, the two polymers designed with the highest soft phase fraction ($\chi_{SF} = 0.59$ and 0.71) show a substantial decrease in barrier functionality when compared to the intact coatings. For $\chi_{SF} = 0.59$ a high capacitance is already probed at the first EIS measurement, even before any polarization is applied. This suggests the presence of an electrochemical path and therefore no full scratch sealing even though the crack width at the free surface is one order of magnitude smaller than that of the coatings with higher segmentation ($2 \mu\text{m}$ vs $20 \mu\text{m}$, Figure 6.7). After the first polarization the coating capacitance drops to values comparable to the intact coatings ($C_c < 1 \text{ pF}$) probably due to the water-induced closure of the damage through coating expansion, which can perfectly bridge $1 \mu\text{m}$. The high barrier functionality is kept intact for the subsequent cycles until, at cycle 5, the capacitance suddenly increases probably due to the reopening of the damage induced by the polarization events. Such a behaviour has also been observed in

other healing systems evaluated with this technique [24] and is in line with the delamination and significant oxide growth at the interface (insert in Figure 6.8B). Samples with $\chi_{SF} = 0.71$ show an analogous behavior, although in this case the failure of the healed damage occurred already after the first polarization cycle showing a continuous increase of the capacitance with subsequent polarization cycles. Figure S12 shows the impedance and photographs before polarization and after cycle 5. The presence of two bubbles at the scratch during the first EIS suggests the incompleteness of the damage closure while the photograph after 5 cycles shows the same locations with bigger bubbles and delamination around the damage location, thereby confirming the indicated continued loss of barrier functionality.

The present results show that visual scratch closure does not necessarily lead to sealing (barrier restoration) but both are influenced by the characteristic soft phase fraction. The physical explanation for this behavior is discussed in section 6.3.5. Moreover, we effectively show that an optimal restoration of barrier performances of polyurethane coatings can be obtained with targeted soft phase fraction.

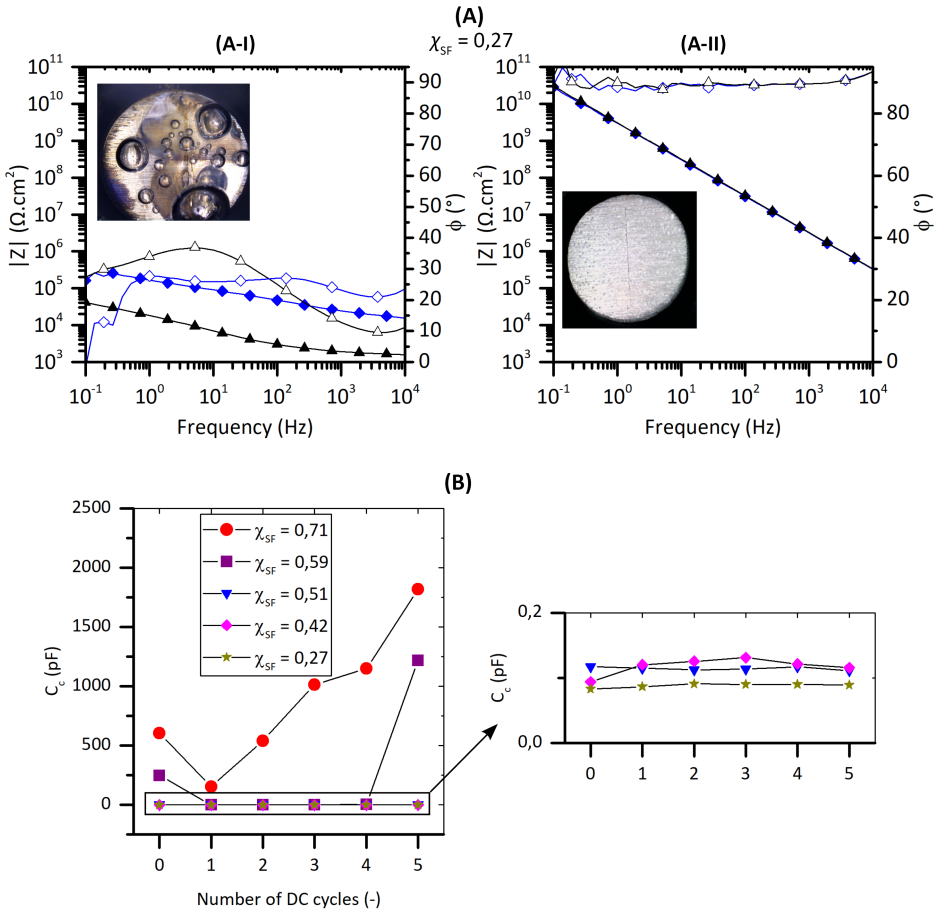


Figure 6.8: **ACET results of healed PU coatings.** (A-I) Bode plot of $\chi_{SF} = 0,27$ tested in damaged condition (no healing treatment). (A-II) Bode plot of $\chi_{SF} = 0,27$ tested after healing 60 minutes at 65 °C. (B) Coating capacitance evolution with number of polarization cycles during ACET test for all TPU compositions. The insets in 8A-I and 8A-II are snapshot acquired at the end of the ACET tests.

As the coatings with the highest soft block ratio ($\chi_{SF} = 0,71$ and $0,59$) showed full damage closure but incomplete barrier restoration, a detailed study of the effect of healing time on sealing was performed. Figure 6.9 shows the results as the difference between the coating capacitance at cycles 0 and 5 (i.e. $|\Delta C_c| = |C_{C \text{ Number Of DC cycle} = 0} - C_{C \text{ Number Of DC cycle} = 5}|$) as function of the healing time. The data points plotted at cycle = 0 correspond to the as-damaged coatings. The results show how the sample $\chi_{SF} = 0,59$ reaches high degrees of sealing after 1400 minutes of healing proving that chain interdiffusion and randomisation at the interface are time dependent processes, even if the capacitance remains lower than that of the other samples. The sample with the highest soft block fraction on the other hand did not show any significant improvement when healing from 60 to 1400 minutes at 65 °C despite the crack optically has disappeared completely (see Figure

6.7). A possible explanation may reside in the low content of highly energetic urea bonds as will be discussed in section 6.3.5.

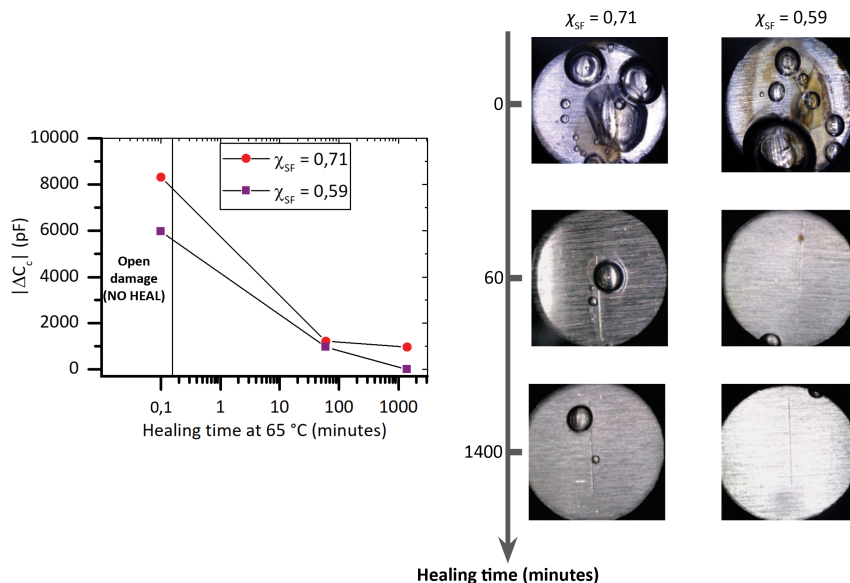


Figure 6.9: **Effect of healing time at 65 °C on the barrier property restoration for $\chi_{SF} = 0.71$ and 0.59.** Note that the data-points plotted at Healing Time = 0.1 minute correspond to an open damage (no healing) condition.

6.3.5. Physical insights to scratch closure and scratch sealing

As shown in section 6.3.4 a complete crack closure estimated by optical analysis does not necessarily lead to full recovery of the electrochemical barrier properties. This effect can be achieved when polymer diffusion and supramolecular reversible moieties reshuffling occur at the healed interface. The polymers used in this work contain two favorable features which promote interfacial healing. On the one hand the effect of branch mediated tube dilation to increase chain diffusion [16] and on the other hand the presence of dynamic hydrogen bonds (urethane and urea units) which assist the interfacial restoration. By combining all the results above presented it becomes clear that polymers with a higher content of monodentate urethane linkages show faster scratch closure and damage optical disappearance (**Figure 6.10A**). This comes as a result of the increase of mobility in the main chain induced by the decrease in reversible bond connectivity (lower energy is needed to break urethane units when compared to urea bonds). Moreover, the systems showing faster closure benefit from a higher main chain dilution effect due to the aliphatic side chains present in the soft segment. Nevertheless, the faster closure does not offset the beneficial effect that the reconstitution of highly energetic (bidentate) urea units have on the interfacial healing, as shown in Figure 6.10B. Figure 6.10C shows an schematic overview of the effect of polymer architecture

(χ_{SF}) and *Urea fraction* on the two phenomena investigated (damage closure and barrier restoration). The increase in soft phase fraction leads to a larger scratch closure. Nevertheless, this increase in scratch closure does not correspond to a higher level of barrier restoration. The results may be explained by the energetic bonding energy of the involved dynamic groups. Since the urethane group is a monodentate group and its free energy of hydrogen bond association is $\approx 25\%$ lower than the one calculated for urea units as obtained through quantum mechanical calculations [35], higher contents of urea groups will lead to a reduced segmental mobility at the healed interface. The restriction of interfacial mobility induced by the urea groups is responsible for the drop in electrolyte diffusivity (barrier increase). The strong interfacial healing for poly(urea)urethane containing high degrees of urea linkages [31, 36], has been already reported by others for free standing polymers after interfaces are manually brought together. The results shown here report for the first time a direct comparison in terms of damage closure and barrier restoration between polymeric coatings having a gradient of monodentate and multidentate reversible moieties.

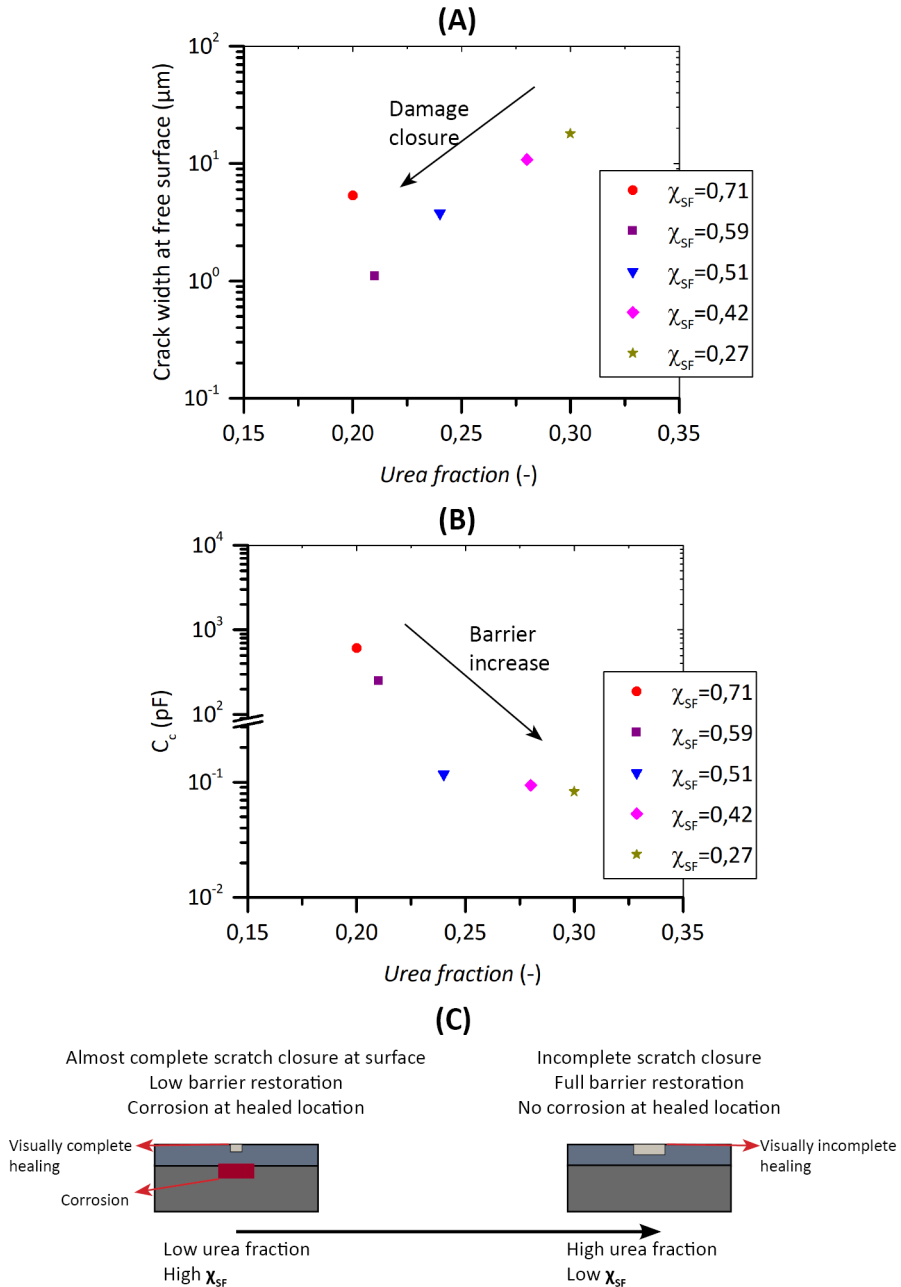


Figure 6.10: **Effect of Urea fraction on self-healing of protective PU coatings. (A)** Residual crack width at free surface after 60 minutes of healing at 65 °C as measured by SEM as function of the *Urea fraction*. **(B)** Coating capacitance as a measure of barrier against electrolyte permeation after 60 minutes of healing at 65 °C obtained after 5th polarisation cycle in ACET. Note that low coatings capacitance C_c indicates high barrier against electrolyte migration to the metal substrate. **(C)** Schematic representation of the effect of polymer architecture (χ_{SF}) and *Urea fraction* on scratch closure and barrier restoration after 60 min at 65 °C.

6.4. Conclusions

The control of the soft phase fraction (χ_{SF}) in segmented polyurethanes is investigated as a design strategy to conjugate efficient scratch closure to high barrier restoration in anticorrosive barrier organic coatings. The kinetics of scratch closure accelerates with increasing soft phase, χ_{SF} . This is in agreement with the observed faster terminal relaxation. However, high levels of scratch closure for high χ_{SF} systems do not necessarily correspond to higher levels of barrier restoration as shown with electrochemical tests. More segmented coatings (lower χ_{SF}) on the other hand show slower and sometimes even incomplete scratch closure at the coating surface, but a more efficient sealing with high degrees of barrier restoration. This result is unexpected but very relevant as it sets a new but crucial design criterion for corrosion protective and efficient self-healing organic coatings where optically detectable damage closure cannot be directly related to restoration of the barrier functionality. In the systems studied the reduced amount of high energetic bidentate urea linkages in polymers with high soft phase fraction cannot guarantee an efficient and stable healed interface despite the more efficient damage closure. High barrier restoration in the harder polymers may be attributed to higher content of urea linkages leading to stronger interfacial bonds with restricted segmental mobility. The results moreover confirm that softer polymers with lower T_g do not necessarily lead to higher degrees of healing in polyurethane coatings.

6

6.5. Supporting Information

Synthesis of segmented polyurethanes

The syntheses of the segmented polyurethanes were performed following the procedure described in the main manuscript for $\chi_{SF} = 0.42$. The stoichiometry was adapted to the variation of the weight content of BDO. In Table S1 we give details about molarity and stoichiometry used for the synthesis of every segmented polyurethane.

Table S1. Synthesis of segmented polyurethanes: Stoichiometry and molar content.

OH (CroHeal 1000) / OH(CroHeal 1000)+OH(BDO) (mol/mol)	Soft phase fraction (χ_{SF})	NCO / OH (total)
0.71	0.71	1.1
0.59	0.59	1.1
0.51	0.51	1.1
0.42	0.42	1.1
0.27	0.27	1.1

 $\chi_{SF} = 0.71$

Monomer	Mass (g)	Molar content (mmol)
CroHeal 1000	6.0	5.00
BuAc	0.790	6.79
BDO	0.18	1.997
TEGO270	0.028	n.a.
DBTDL	0.063	0.1
IPDI	1.711	7.697

 $\chi_{SF} = 0.59$

Monomer	Mass (g)	Molar content (mmol)
CroHeal 1000	6.0	5.00
BuAc	0.83	7.18
BDO	0.30	3.329
TEGO270	0.028	n.a.
DBTDL	0.063	0.1
IPDI	2.04	9.16

$\chi_{SF} = 0.51$

Monomer	Mass (g)	Molar content (mmol)
CroHeal 1000	6.0	5.00
BuAc	0.88	7.56
BDO	0.42	4.66
TEGO270	0.028	n.a.
DBTDL	0.063	0.1
IPDI	2.36	10.63

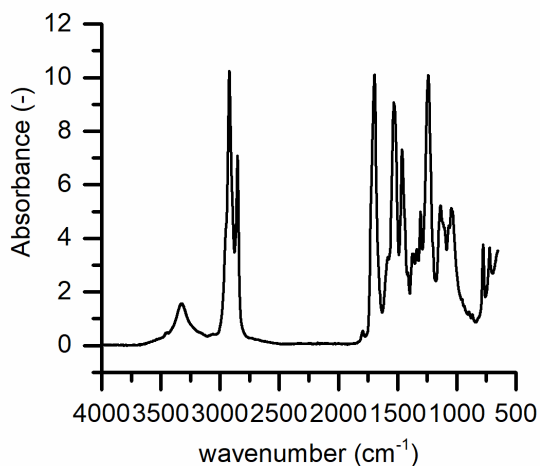
$\chi_{SF} = 0.27$

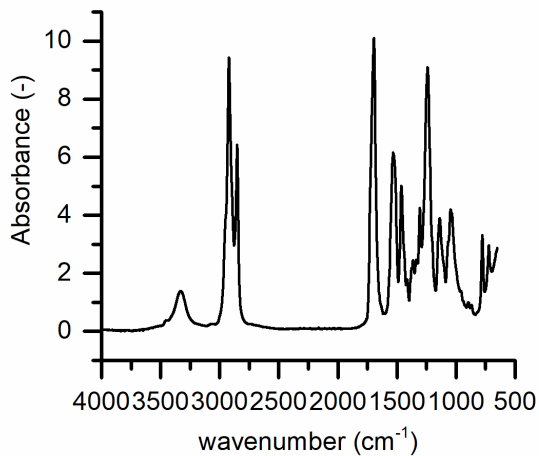
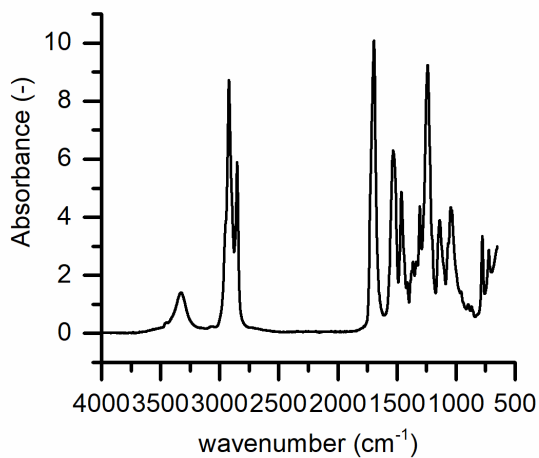
Monomer	Mass (g)	Molar content (mmol)
CroHeal 1000	6.0	5.00
BuAc	1.17	10.05
BDO	1.20	13.31
TEGO270	0.028	n.a.
DBTDL	0.063	0.1
IPDI	4.48	20.15

ATR-FTIR

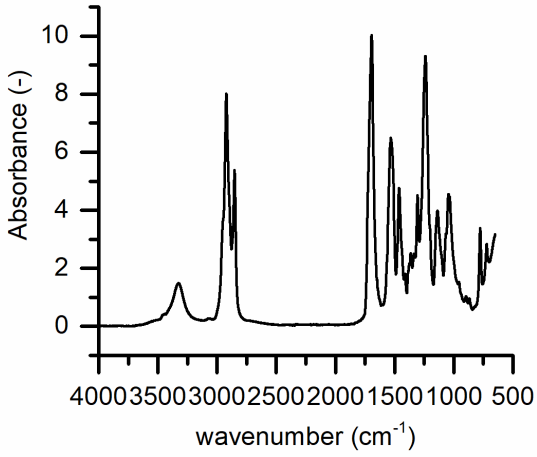
Figure S1. ATR-FTIR spectra.

$\chi_{SF} = 0.71$

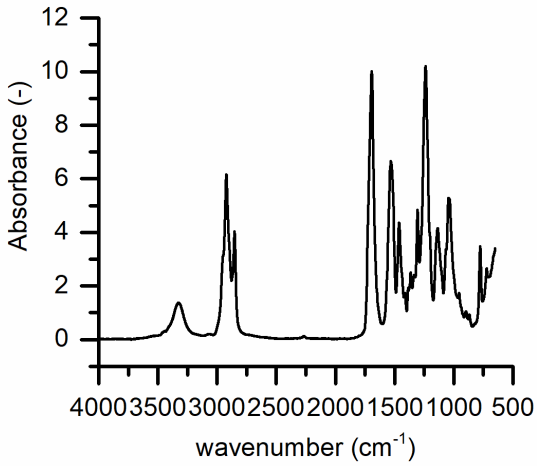


$\chi_{SF} = 0.59$  $\chi_{SF} = 0.51$ 

$\chi_{SF} = 0.42$



$\chi_{SF} = 0.27$



Thermal analyses

Figure S2. Exemplificative thermograms (DSC and TGA) of $\chi_{SF} = 0.42$.

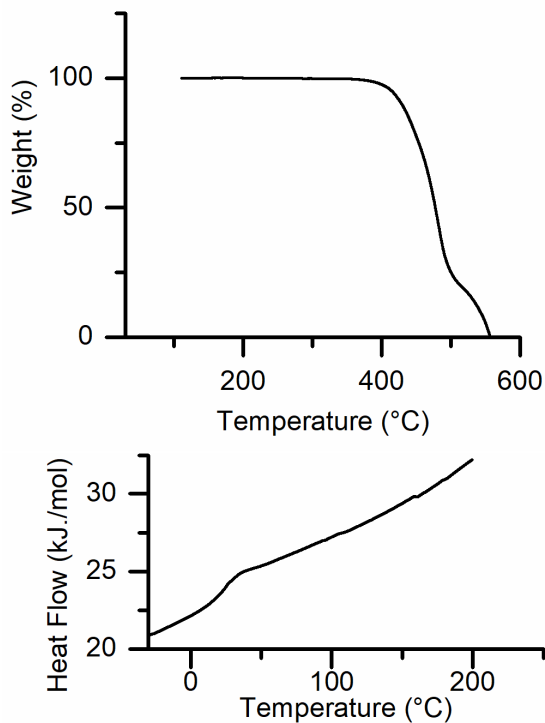
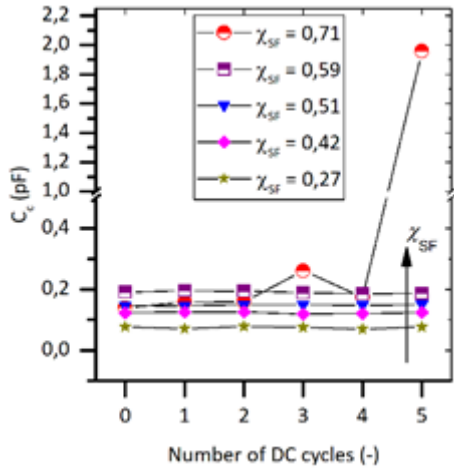


Table S2. Thermal properties of synthesized segmented polyurethanes.

χ_{SF}	TGA-5% weight loss (°C)	DSC- T_g at inflection point (°C)
0.71	316	4
0.59	317	7
0.51	314	14.6
0.42	305	25.5
0.27	288	27

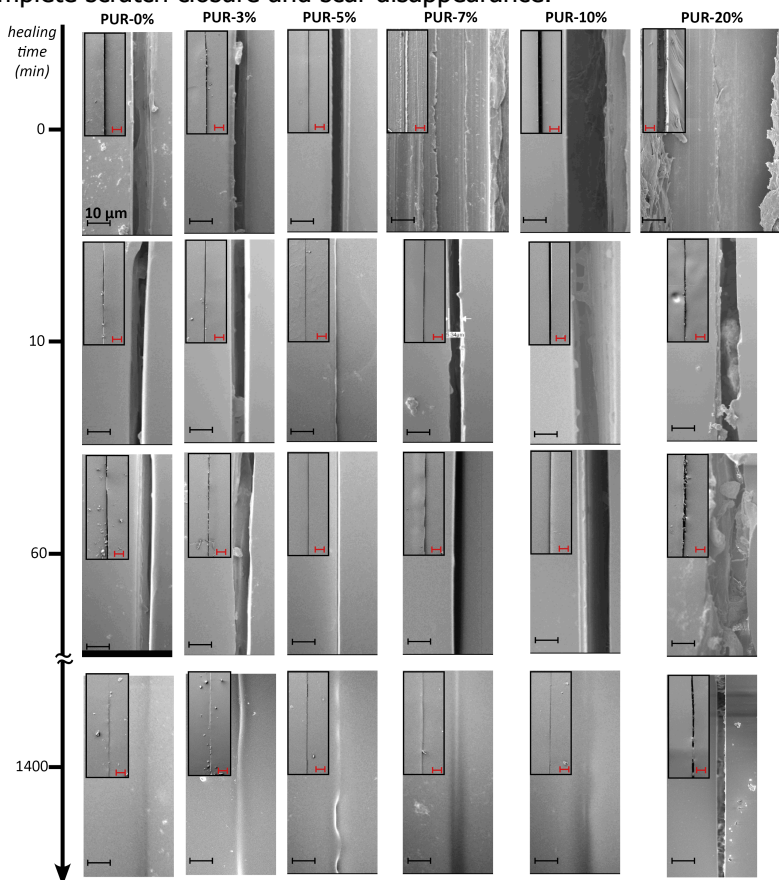
Intact coating capacitance as function of DC polarisation cycles
Figure S3. Intact coating capacitance as function of DC polarisation cycles.



Scratch closure SEM results

Figure S4. Time resolved scratch closure.

Crack closure monitored by SEM. The increase of phase separation determines larger scratch front displacement drive by EER and a slower viscous flow leading to complete scratch closure and scar disappearance.



FTIR deconvolution matrix

Table S3. FTIR fitting deconvolution results

In the tables below we report the results of the Amide I band Gaussian fitting performed using OriginPro 2015 software. Three fitting parameters were used: Xc (expressed in cm^{-1} , defines the wavenumber positioning of the maximum of the sub-band), A (defines the amplitude of the maximum of the sub-band), w (defines the full width at half maximum). For all the fitting the coefficient of determination $|r^2| > 0.99$.

$$\chi_{SF} = 0.71$$

Peak	X _C	A	w
1	1675	82.75	40.84
2	1692	162.43	24.02
4	1710	165.67	28.16
5	1728	57.12	22.10

$$\chi_{SF} = 0.59$$

Peak	X _C	A	w
1	1675	95.81	43.78
2	1692	125.32	23.75
4	1711	244.61	37.14
5	1728	9.59	10.72

6

$$\chi_{SF} = 0.51$$

Peak	X _C	A	w
1	1675	102.44	44.58
2	1692	169.06	24.70
4	1711	157.18	28.18
5	1728	46.85	21.30

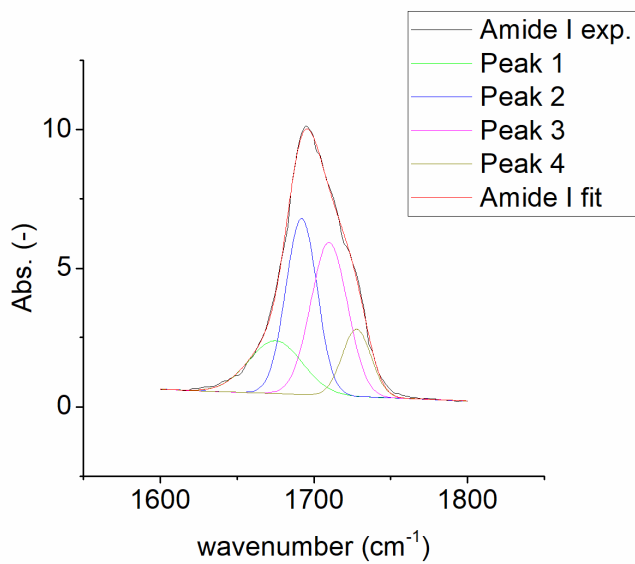
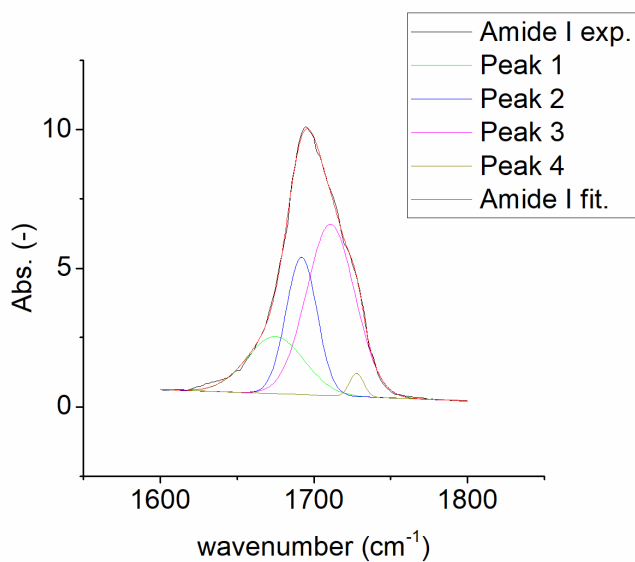
$$\chi_{SF} = 0.42$$

Peak	X _C	A	w
1	1675	121.37	47.15
2	1692	173.56	24.85
4	1711	134.13	25.79
5	1728	50.20	20.66

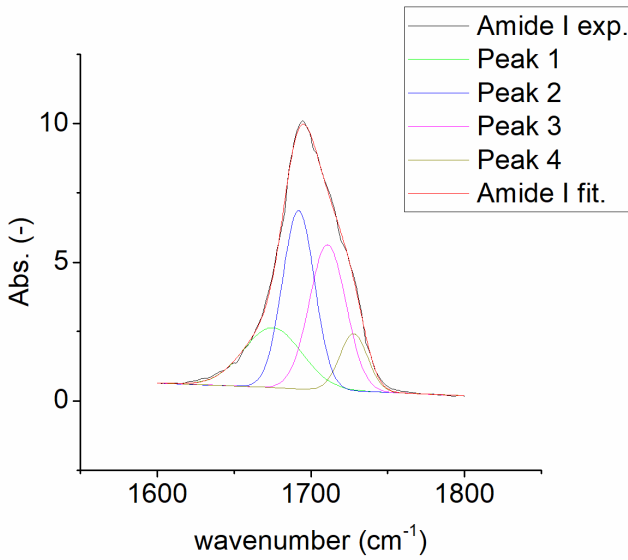
$$\chi_{SF} = 0.27$$

Peak	X _C	A	w
1	1674	144.73	46.85
2	1691	133.35	25.32
4	1711	214.64	37.19
5	1727	7.09	12.08

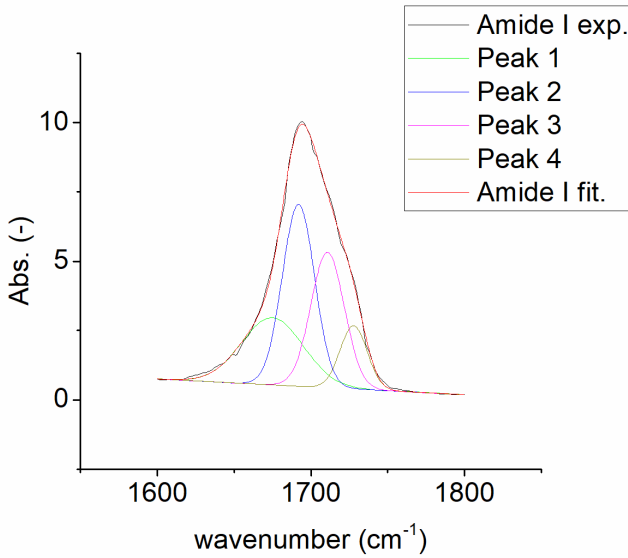
Figure S5. Amide I band deconvolution results.

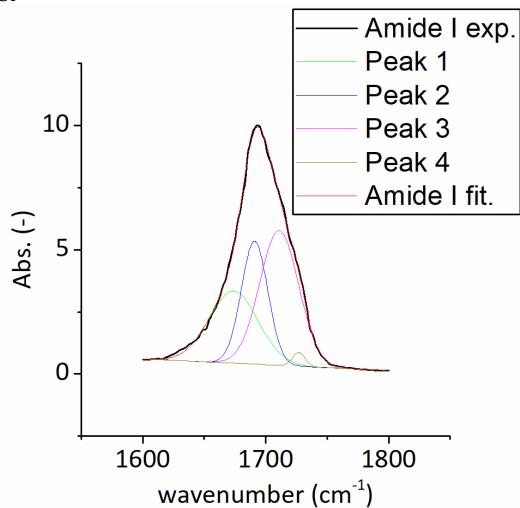
 $\chi_{SF} = 0.71$  $\chi_{SF} = 0.59$ 

$\chi_{SF} = 0.51$



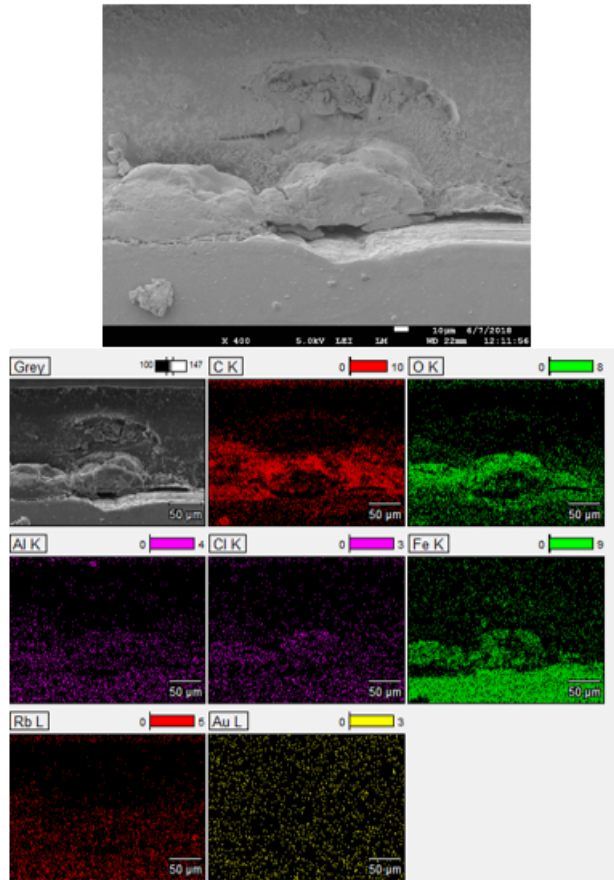
$\chi_{SF} = 0.42$



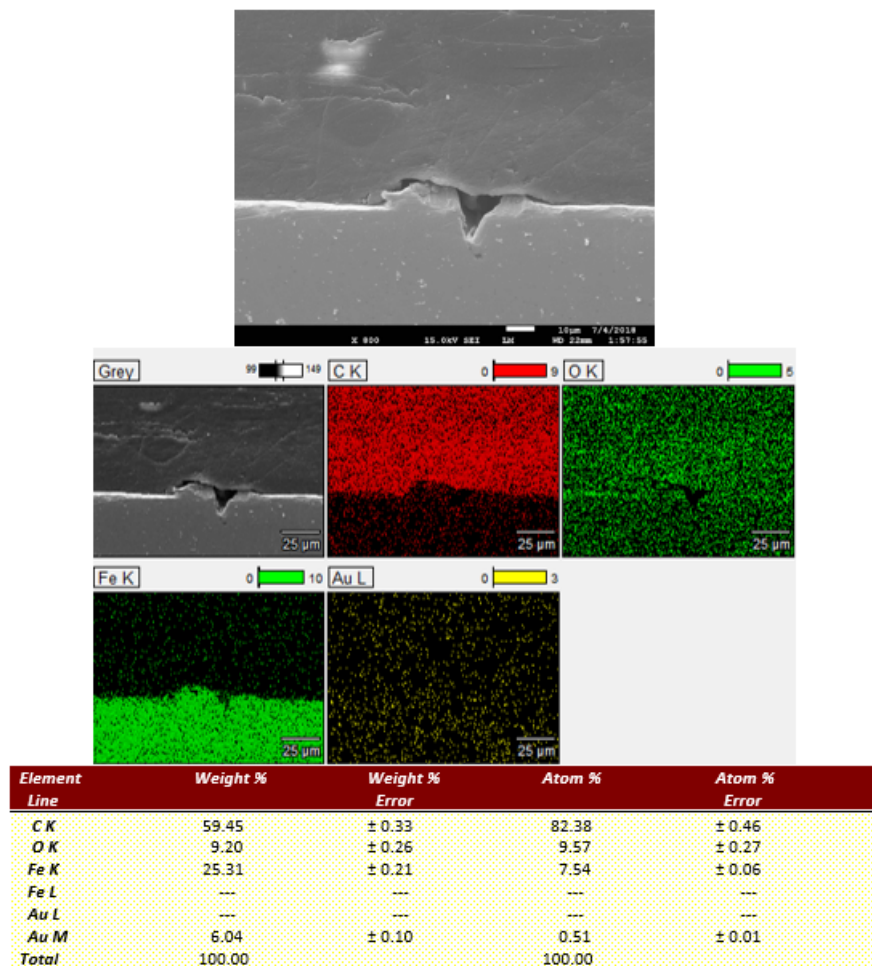
$\chi_{SF} = 0.27$ 

SEM and EDX investigation of damaged and healed cross-sections after ACET testing

Figure S6. SEM and EDX of damaged (non-healed) $\chi_{SF} = 0.42$ sample.



Element Line	Weight %	Weight % Error	Atom %	Atom % Error
C K	49.31	± 0.41	75.79	± 0.63
O K	12.37	± 0.18	14.27	± 0.21
Al K	0.16	± 0.02	0.11	± 0.01
Cl K	0.26	± 0.02	0.13	± 0.01
Cl L	---	---	---	---
Fe K	25.89	± 0.22	8.56	± 0.07
Fe L	---	---	---	---
Rb K	---	---	---	---
Rb L	0.04	± 0.03	0.01	± 0.01
Au L	---	---	---	---
Au M	11.98	± 0.16	1.12	± 0.02
Total	100.00		100.00	

Figure S7. SEM and EDX of healed (60 minutes at 65 °C) $\chi_{SF} = 0.42$ sample.

Additional ACET results for barrier restoration efficiency calculation

Figure S8. $\chi_{SF} = 0.71$ healed 60 minutes at 65 °C.

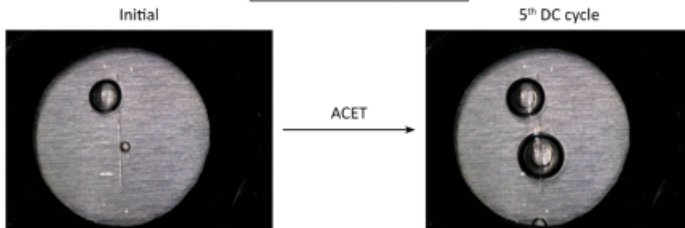
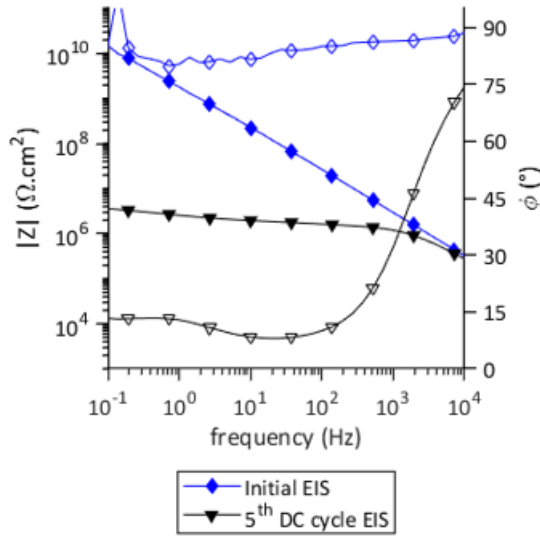


Figure S9. Open Circuit Potential (OCP) relaxation of $\chi_{SF} = 0.59$ after direct polarisation.

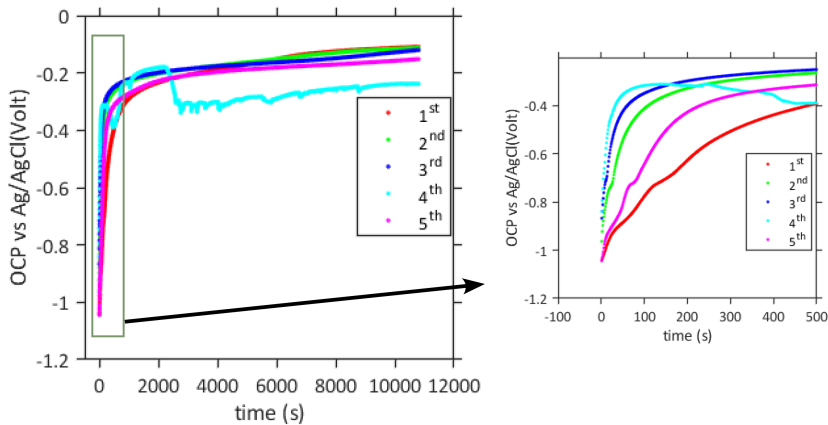
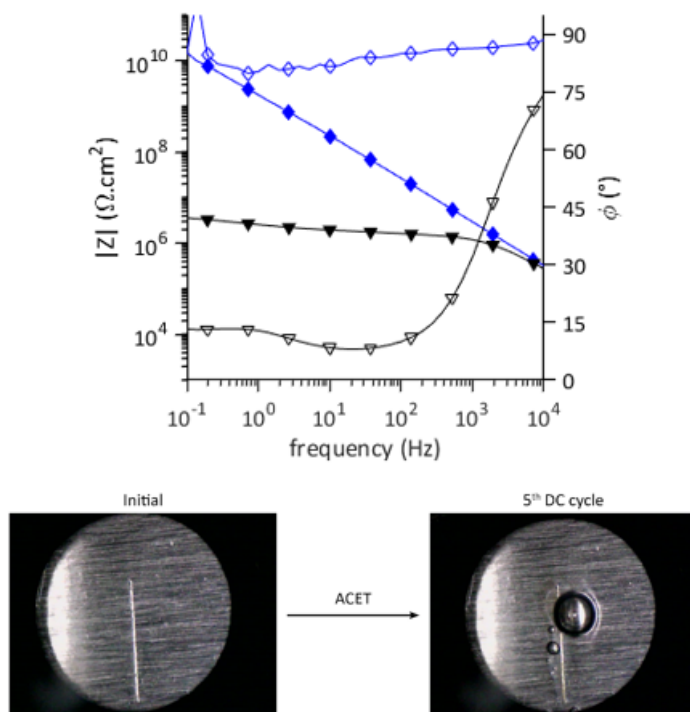
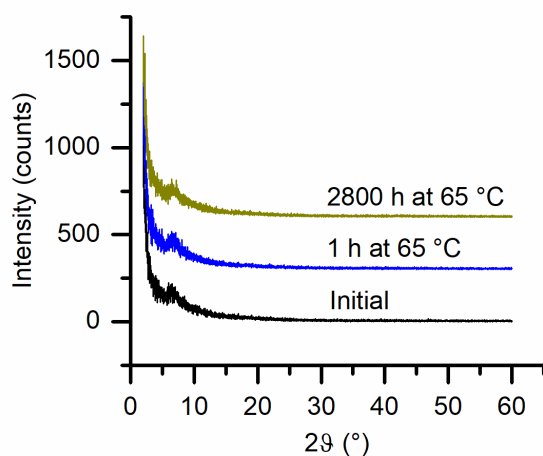


Figure S10. $\chi_{SF} = 0.71$ healed 1400 minutes at 65 °C



X-Ray diffraction

Figure S11. $\chi_{SF} = 0.27$ time resolved XRD results



References

- [1] S. J. García, H. R. Fischer, and S. van der Zwaag, *A critical appraisal of the potential of self healing polymeric coatings*, *Progress in Organic Coatings* **72**,

- 211 (2011).
- [2] A. Stankiewicz, I. Szczygieł, and B. Szczygieł, *Self-healing coatings in anti-corrosion applications*, Journal of Materials Science **48**, 8041 (2013).
- [3] X. Luo and P. T. Mather, *Shape memory assisted self-healing coating*, ACS Macro Letters **2**, 152 (2013).
- [4] A. Lutz, O. van den Berg, J. Van Damme, K. Verheyen, E. Bauters, I. De Graeve, F. E. Du Prez, and H. Terryn, *A shape-recovery polymer coating for the corrosion protection of metallic surfaces*, ACS applied materials & interfaces **7**, 175 (2015).
- [5] S. J. Garcia, *Effect of polymer architecture on the intrinsic self-healing character of polymers*, European Polymer Journal **53**, 118 (2014).
- [6] Z. Wang, H. Liang, H. Yang, L. Xiong, J. Zhou, S. Huang, C. Zhao, J. Zhong, and X. Fan, *Uv-curable self-healing polyurethane coating based on thiol-ene and diels-alder double click reactions*, Progress in Organic Coatings **137**, 105282 (2019).
- [7] F. Gao, J. Cao, Q. Wang, R. Liu, S. Zhang, J. Liu, and X. Liu, *Properties of uv-cured self-healing coatings prepared with PCDL-based polyurethane containing multiple H-bonds*, Progress in Organic Coatings **113**, 160 (2017).
- [8] E. D. Rodriguez, X. Luo, and P. T. Mather, *Linear/network poly (ϵ -caprolactone) blends exhibiting shape memory assisted self-healing (SMASH)*, ACS applied materials & interfaces **3**, 152 (2011).
- [9] T. Chen, L. Fang, X. Li, D. Gao, C. Lu, and Z. Xu, *Self-healing polymer coatings of polyurea-urethane/epoxy blends with reversible and dynamic bonds*, Progress in Organic Coatings **147**, 105876 (2020).
- [10] M. Yarmohammadi, M. Shahidzadeh, and B. Ramezanzadeh, *Designing an elastomeric polyurethane coating with enhanced mechanical and self-healing properties: the influence of disulfide chain extender*, Progress in Organic Coatings **121**, 45 (2018).
- [11] Z. Wang, J. Zhou, H. Liang, S. Ye, J. Zou, and H. Yang, *A novel polyurethane elastomer with super mechanical strength and excellent self-healing performance of wide scratches*, Progress in Organic Coatings **149**, 105943 (2020).
- [12] M. Samadzadeh, S. H. Boura, M. Peikari, A. Ashrafi, and M. Kasiriha, *Tung oil: An autonomous repairing agent for self-healing epoxy coatings*, Progress in Organic Coatings **70**, 383 (2011).
- [13] S. H. Cho, S. R. White, and P. V. Braun, *Self-healing polymer coatings*, Advanced Materials **21**, 645 (2009).

- [14] Y. González-García, S. García, A. Hughes, and J. Mol, *A combined redox-competition and negative-feedback secm study of self-healing anticorrosive coatings*, *Electrochemistry communications* **13**, 1094 (2011).
- [15] S. García, H. Fischer, P. White, J. Mardel, Y. González-García, J. Mol, and A. Hughes, *Self-healing anticorrosive organic coating based on an encapsulated water reactive silyl ester: synthesis and proof of concept*, *Progress in Organic Coatings* **70**, 142 (2011).
- [16] V. Montano, M. M. Wempe, S. M. Does, J. C. Bijleveld, S. van der Zwaag, and S. J. Garcia, *Controlling healing and toughness in polyurethanes by branch-mediated tube dilation*, *Macromolecules* **52**, 8067 (2019).
- [17] V. Montano, S. J. Picken, S. van der Zwaag, and S. J. Garcia, *A deconvolution protocol of the mechanical relaxation spectrum to identify and quantify individual polymer feature contributions to self-healing*, *Physical Chemistry Chemical Physics* **21**, 10171 (2019).
- [18] Y. González-García, J. Mol, T. Muselle, I. De Graeve, G. Van Assche, G. Scheltjens, B. Van Mele, and H. Terryn, *A combined mechanical, microscopic and local electrochemical evaluation of self-healing properties of shape-memory polyurethane coatings*, *Electrochimica acta* **56**, 9619 (2011).
- [19] J.-B. Jorcin, G. Scheltjens, Y. Van Ingelgem, E. Tourwé, G. Van Assche, I. De Graeve, B. Van Mele, H. Terryn, and A. Hubin, *Investigation of the self-healing properties of shape memory polyurethane coatings with the 'odd random phase multisine' electrochemical impedance spectroscopy*, *Electrochimica acta* **55**, 6195 (2010).
- [20] K. Chang, H. Jia, and S.-Y. Gu, *A transparent, highly stretchable, self-healing polyurethane based on disulfide bonds*, *European Polymer Journal* **112**, 822 (2019).
- [21] L. Brunsveld, B. Folmer, E. W. Meijer, and R. Sijbesma, *Supramolecular polymers*, *Chemical reviews* **101**, 4071 (2001).
- [22] Y. Yanagisawa, Y. Nan, K. Okuro, and T. Aida, *Mechanically robust, readily repairable polymers via tailored noncovalent cross-linking*, *Science* **359**, 72 (2018).
- [23] S. García, M. Rodríguez, R. Izquierdo, and J. Suay, *Evaluation of cure temperature effects in cataphoretic automotive primers by electrochemical techniques*, *Progress in organic coatings* **60**, 303 (2007).
- [24] M. A. Zadeh, S. van der Zwaag, and S. J. García, *Assessment of healed scratches in intrinsic healing coatings by ac/dc/ac accelerated electrochemical procedure*, *Surface and Coatings Technology* **303**, 396 (2016).

- [25] P. J. Denissen and S. J. Garcia, *Cerium-loaded algae exoskeletons for active corrosion protection of coated AA2024-T3*, *Corrosion Science* **128**, 164 (2017).
- [26] G. Walter, *The application of impedance spectroscopy to study the uptake of sodium chloride solution in painted metals*, *Corrosion science* **32**, 1041 (1991).
- [27] V. Barranco, J. Carpentier, and G. Grundmeier, *Correlation of morphology and barrier properties of thin microwave plasma polymer films on metal substrate*, *Electrochimica acta* **49**, 1999 (2004).
- [28] V. Barranco, P. Thiemann, H. Yasuda, M. Stratmann, and G. Grundmeier, *Spectroscopic and electrochemical characterisation of thin cathodic plasma polymer films on iron*, *Applied surface science* **229**, 87 (2004).
- [29] M. M. Coleman, K. H. Lee, D. J. Skrovanek, and P. C. Painter, *Hydrogen bonding in polymers. 4. infrared temperature studies of a simple polyurethane*, *Macromolecules* **19**, 2149 (1986).
- [30] J. Mattia and P. Painter, *A comparison of hydrogen bonding and order in a polyurethane and poly (urethane- urea) and their blends with poly (ethylene glycol)*, *Macromolecules* **40**, 1546 (2007).
- [31] A. Feula, A. Pethybridge, I. Giannakopoulos, X. Tang, A. Chippindale, C. R. Siviour, C. P. Buckley, I. W. Hamley, and W. Hayes, *A thermoreversible supramolecular polyurethane with excellent healing ability at 45 c*, *Macromolecules* **48**, 6132 (2015).
- [32] J. D. Ferry, *Viscoelastic properties of polymers* (John Wiley & Sons, 1980).
- [33] J. Ferguson, D. Hourston, R. Meredith, and D. Patsavoudis, *Mechanical relaxations in a series of polyurethanes with varying hard to soft segment ratio*, *European Polymer Journal* **8**, 369 (1972).
- [34] M. Oliveira, R. A. Antunes, and I. Costa, *Effect of the nco/oh molar ratio on the physical aging and on the electrochemical behavior of polyurethane-urea hybrid coatings*, *International Journal of Electrochemical Science* (2014).
- [35] E. Yilgör, I. Yilgör, and E. Yurtsever, *Hydrogen bonding and polyurethane morphology. i. quantum mechanical calculations of hydrogen bond energies and vibrational spectroscopy of model compounds*, *Polymer* **43**, 6551 (2002).
- [36] A. M. Grande, S. J. Garcia, and S. van der Zwaag, *On the interfacial healing of a supramolecular elastomer*, *Polymer* **56**, 435 (2015).

Summary

The work exposed in this thesis addresses two main scientific challenges in the field of intrinsic self-healing polymers that limit the translation of the academic research efforts into commercial products, namely: i) the implementation of the self-healing functionality in polymer commodities by minimal chemical modifications; and ii) the establishment of characterization protocols that allow a deeper understanding of the relation between polymer structure and efficient healing capability.

Chapter 1 is an introduction to the field of self-healing polymers. The models and theories describing the hierarchical processes regulating intrinsic healing are reviewed. The chapter ends by setting the specific goals for the thesis work.

Chapter 2 presents regular aliphatic branching of linear polyurethanes as a way to regulate chain dynamics and crystallisation, so that robust and healable polymers can be designed. The polyurethanes are synthesized by the polyaddition of aliphatically branched propane diol derivatives and hexamethylene diisocyanate. Following this route the polymers present regular alkyl branches ranging from butyl ($C = 4$) to octadecanyl ($C = 18$). The macro-rheological characterisation evidences that an amorphous regime appears when the branch length is in the intermediate range ($C = 4$ to $C = 8$). All amorphous systems show macroscopic healing of cut samples. However, in this branch length regime, the molecular dynamics is accelerated with the branch length due to the increase of the tube dilation. As a consequence faster macroscopic healing is observed for samples bearing longer aliphatic branches (i.e. $C = 8$).

No healing was observed for very short ($C < 4$) or very long ($C = 18$) brush lengths, due to crystallisation of the main chain and the side branches, respectively. In particular, hydrogen bonds clusters form in case very short brushes are used while side chain stacking is observed when long brushes are embodied.

Samples with medium to long length brushes ($C \geq 8$) lose their interfacial strength at the healed region after having been exposed for a long time to the healing temperature. These annealed samples, despite showing good initial tackiness, are unable to completely recover the macro-damage. A dedicated study attributes this behaviour to the annealing-induced interfacial crystallisation promoted by the aliphatic branches in the polymer bulk. Polyurethanes with branch length in the range between $C = 4$ to $C = 7$ do not show such a loss of healing property, indicating this as the optimal branch length healing regime. The work shows that polymer architecture modification via regular branching is an effective strategy to embody linear commodities of the self-healing functionalities.

Chapter 3 and *Chapter 4* deal with the development of a new rheology-based

analysis protocol that allows the deconvolution of overlapping relaxation mechanisms related to the polymer dynamics and healing. The protocol provides new quantitative insights into early stage and long term healing in polyurethane elastomers and the relation between healing and polymer structure.

Chapter 3 introduces the novel macro-rheology based fitting protocol. The classical rheological master curve is converted to a continuous relaxation spectrum $H(\tau)$ and fitted using a mechanical analogue model (the Maxwell-Weichert model) optimized with respect to the polymer shear moduli. By doing so we can successfully separate overlapping relaxation phenomena in the dissipative regime for a set of near- T_g intrinsic healing polymers. In particular, the protocol is able to deconvolute the overlapped relaxations attributed to segmental mobility and reversible interactions as shown for a set of polyimides and polyamides designed with none, one and two near- T_g reversible dynamic blocks (i.e. H-bonds and aromatic interactions).

The protocol provides physical and quantitative information about the relaxation timescales and the process enthalpy of every deconvoluted relaxation through the fitting parameters obtained. By comparing these data to the long term macroscopic healing results of the self-healing polymers analysed, a clear correspondence appears between the energy stored by the system to accomplish a reversible transition (e.g. H-bonds), the terminal relaxation transition and the mechanical long term healing efficiency of such polymers.

In **Chapter 4** we extend the rheology-based protocol introduced in Chapter 3 to a set of self-healing thermoplastic polyurethanes to use the quantitative information extracted (in particular the stored work of deformation) as a tool to predict the early stage interfacial healing properties (fracture resistance restoration). To exclude any effect of long range dynamics the polymers were healed for short time and at low temperature. Moreover, to obtain reliable mechanical data the samples were tested by single edge notch tensile testing, a procedure that magnifies the data resolution of the mechanical integrity of the healed interface by reducing bulk effects. After healing, the fracture resistance recovery of the polyurethanes based on aromatic diisocyanates is considerably higher than that of systems based on aliphatic and cycloaliphatic diisocyanates, which show very limited interfacial fracture strength. The deconvolution of the relaxation spectra $H(\tau)$ obtained by linear rheology gives the characteristic relaxation times (kinetics of relaxation) and the stored work of deformation associated to the single relaxation. The work of deformation related to the reversible bond relaxation shows a qualitative correspondence with the interfacial healing fracture resistance. Furthermore, data for the polymers showing efficient interfacial healing suggest that there is a threshold work of deformation below which the load transfer at the healed interface becomes very inefficient.

Chapter 5 and *Chapter 6* investigate the physical aspects of scratch closure and barrier restoration of self-healing coatings and the implication of damage closure-sealing in corrosion protection of coated metals.

Chapter 5 is devoted to the understanding of the entropy-driven damage closure

process and its relation to the polymer architecture in self-healing polyurethane coatings. The work addresses the existence of a quantitative relation between scratch closure and released entropy. Such a result is obtained by quantifying stored and released entropy density via a dynamical mechanical analysis and through a careful control of both damage and healing temperatures during the scratch healing experiments. It is shown that scratch closure displacement increases linearly with released entropy.

Chapter 6 investigates the relation between polymer structure and the two aspects of healing of organic protective coatings: the damage disappearance of visual damage (closure) and electrochemical barrier restoration (sealing). The polymer structure is controlled by varying the mobile phase fraction of a set of thermoplastic polyurethane coatings. The scratch closure is monitored and quantified using scanning electron microscopy while the barrier properties restoration (sealing) are probed by accelerated cyclic electrochemical technique. The research shows that the two properties are decoupled: the damage closure kinetics accelerates with the increase of soft phase fraction, but a higher optical closure does not necessarily correspond to a higher level of corrosion barrier restoration. The apparent discrepancy could be resolved by focusing on the balance between bidentate urea bonds and monodentate urethane linkages, in view of the difference in binding energy.

Samenvatting

Dit proefschrift beschrijft twee belangrijke wetenschappelijke uitdagingen op het gebied van intrinsiek self-healing polymeren die tot nu toe de transitie van academisch onderzoek naar commerciële toepassingen belemmeren: i) de implementatie van self-healing functionaliteit in standaard polymeren via kleinere chemische modificaties en ii) de formulering van testprotocollen die leiden tot een beter begrip van de relatie tussen de structuur van het polymeer en zijn self-healing gedrag.

Hoofdstuk I is een korte inleiding in het veld van self-healing polymeren. Het vat de bestaande modellen en theorieën rond de hiërarchie van self-healing polymeren samen. Het hoofdstuk eindigt met het formuleren van de doelstellingen voor dit onderzoek.

Hoofdstuk 2 presenteert het gebruik van vertakte alifatische monomeren in de creatie van lineaire polyurethanen om de keten-dynamiek en kristallisatie te reguleren met als doel om robuuste self-healing polymeren te ontwikkelen. De polyurethanen zijn gebaseerd op vertakte alifatische propaan-diol varianten en hexamethyleen di-isocyanaten. De ketenlengte van de zijtakken wordt gevarieerd van 4 tot 18. De macro-reologische karakterisering laat zien dat het beste self-healing gedrag verkregen wordt als de lengte van de zijgroep tussen de 4 en 18 ligt. De moleculaire kinetiek neemt toe als de lengte van de zijketens toeneemt. Geen healing werd waargenomen als de zijketenlengte kort ($C=4$) of lang is ($C=18$). Dit wordt respectievelijk toegeschreven aan voortijdige kristallisatie van de hoofdketen dan wel die van de zijketen. In het geval van korte zijketens spelen waterstofbindingen een belangrijke rol terwijl het stapelen van de zijketens een belangrijker rol speelt bij langere zijketens. Preparaten met een gemiddelde zijketenlengte groter dan 8 vertoonden een verlies aan sterkte na langdurige blootstelling aan de initieel optimale hersteltemperatuur. Verder onderzoek liet zien dat dit verlies aan sterkte-na-herstel het gevolg is van kristallisatie van de zijketens in de omgeving van het oorspronkelijke breukvlak. Polymeren met een zijketenlengte van 4-7 lieten dit ongewenste lange-duur gedrag niet zien en zijn daarom betere self-healing polymeren. Het onderzoek van dit hoofdstuk laat zien dat aanpassing van de ketenstructuur middels periodieke zijgroepen een geschikte route is om gewenst self-healing gedrag te verkrijgen.

Hoofdstukken 3 en 4 zijn gericht op de ontwikkeling van een nieuw op reologie gebaseerd protocol om het mechanisch relaxatie spectrum te ontleden in de diverse componenten die bijdragen aan polymeer-dynamica en self-healing gedrag. Het protocol verschaft nieuw inzicht in zowel het lange-termijn als het korte-termijn gedrag van self-healing polyurethaan elastomeren en leidt daarmee tot een beter

begrip van de relatie tussen ketenstructuur en het te verwachten self-healing gedrag.

Hoofdstuk 3 beschrijft het nieuwe protocol. De gebruikelijke reologische 'master curve' wordt omgezet in een continu relaxatiespectrum $H(\tau)$ dat vervolgens gefit wordt aan een verwant mechanisch model (het Maxwell-Weichert model) voor de afschuif-moduli van polymeren. Op deze manier slagen we er in om overlappende relaxatie fenomenen in intrinsiek self-healing polymeren rond hun glasovergangstemperatuur te scheiden. Dankzij dit protocol kunnen de relaxaties als gevolg van ketenmobiliteit en die van reversibele interacties gescheiden worden. De potentie van het protocol is aangetoond in onderzoek aan een collectie van polyimides en polyamides met één of twee reversibele dynamische entiteiten (waterstof-bruggen dan wel aromatische interacties).

Het protocol verschaft fysisch en kwantitatief inzicht in de tijdsconstanten en de enthalpie van de diverse relaxaties. Door de fit-parameters goed te analyseren kan een relatie gevonden worden tussen het energieniveau van een bepaalde overgang, de kinetiek van het herstelproces en het lange-duur mechanisch gedrag van dergelijke polymeren.

In **Hoofdstuk 4** gebruiken we het protocol zoals beschreven in Hoofdstuk 3 om het korte-termijn herstelgedrag, en in het bijzonder dat van de breuktaaiheid, van een aantal thermoplastische polyurethanen te analyseren op basis van de hoeveelheid opgeslagen energie. Hiertoe werden zogenaamde 'single edge' ingekeepte preparaten gebruikt omdat die een grotere gevoeligheid hebben voor de herstelreacties op het eerdere breukoppervlak. De experimenten lieten zien dat de polyurethanen op basis van aromatische di-isocyanaten een groter herstel van de breuktaaiheid vertoonden dan de systemen gebaseerd op alifatische of cycloalifatische di-isocyanaten. De deconvolutie van de relaxatiespectra gaf duidelijk aan waarom dat het geval was. Uit de analyse blijkt dat er een zekere hoeveelheid opgeslagen mechanische energie in de omgeving van het oorspronkelijke breukoppervlak nodig is om effectief herstelgedrag te laten plaatsvinden.

Hoofdstukken 5 en 6 richten zich op de fysische aspecten van het sluiten van oppervlaktescheuren en het herstel van de corrosie-werende werking van polymeer coatings op metallische substraten.

Hoofdstuk 5 is gericht op het begrijpen van de relatie tussen het sluiten van een oppervlaktescheur in polyurethaan coatings en de hoeveelheid entropie-verandering die daarmee gepaard gaat. Deze entropieverandering werd bepaald uit Dynamisch Mechanische metingen. De relatie met het self-healing vermogen werd geverifieerd door te kijken naar scheursluiting als functie van het verschil in de temperatuur van aanbrengen van de kras en die van het herstellen van de kras. De hoeveelheid opgeslagen mechanische energie rond de kras bleek de beperkende factor te zijn voor de mate van herstel.

Hoofdstuk 6 beschrijft het onderzoek naar de relatie tussen de ketenstructuur en twee belangrijke aspecten van het herstel van beschermende organische coa-

tings: het verdwijnen van visueel waarneembare schade (het sluiten van de kras) en het herstel van de corrosiewerende werking. Daartoe werd de ketenstructuur van een aantal thermoplastische polyurethaan coatings gevarieerd middels aanpassing van de mobiele fractie. Het sluiten van de scheur in de tijd werd gevolgd middels rasterelektronenmicroscopie. Het herstel van de corrosiewerende werking (het 'sealen') werd gevolgd middels een cyclische elektrochemische techniek voor het doen van versnelde corrosietesten. Het onderzoek liet zien dat de twee herstelprocessen niet gekoppeld zijn: het sluiten van de kras gaat sneller met toenemende fractie mobiele fase, maar een versnelde sluiting van de kras ging niet samen met een compleet herstel van de corrosiewerende werking. De ogenschijnlijke discrepantie kon verklaard worden door te kijken naar de balans tussen de bidentate urea bindingen en de monodentate urethaan bindingen, met het oog op het verschil in bindingsenergie.

Acknowledgements

A PhD thesis is never the work of a single. It is a path full of wonderful people. The acknowledgments are sincere and needful.

Thanks to my promotor Dr. Santiago Garcia. Your guidance and continuous support made possible to enrich this work of novel scientific ideas. We shared more than work: I will not forget our beautiful talks through the Japanese nights.

Thanks to my promotor prof. Sybrand van der Zwaag. Your scientific excellence have raised the value of the work and taught me the value of careful thinking.

A special thanks to Dr. Angela Smits, Dr. Wouter Vogel and Thomas Blundell for the tremendous support with samples synthesis and fruitful scientific discussions.

The work would have not been completed with experience, guidance and support during the long experimental session in the laboratories. Thanks to Dr. Johan Bijleveld, Dr. Atsushi Nagai and Dr. Marlies Nijemeisland for the support with research work and experiments design. My complete gratitude to the great bachelor and master students that contributed to the work: Max Wempe, Sam Does, Michele Senardi, Linda Ritzen, Ana Infante and Anniek Wiltink. In everyone of you I saw the same seed of passion for material science that I discovered in me a few years ago. I am sure you will all be successful in your personal and professional life.

Many thanks to prof. Marek Urban for the supervision and guidance during the time spent as guest researcher at Clemson University, and to Dr. Dmitriy Davydovich for helping me with experimental setups and for the nice time spent around the Clemson area.

This book would not exist without the continuous support that my family offered me through the past twenty years. You are my first sponsors and all my achievements belong to you first. Elí, my soon to be wife, every day you show me that life would be so empty without a person to love and share with. Mamma, Papá, Mary e Ale la distanza ci divide, ma la nostra forza resta immutata. Sofia, you are our joy. Remember that your family will love you forever and unconditionally.

NovAm is a special place to be. Thanks to all the bright people that I have met in the past four years in the group. The Friday afternoon at de Atmosfeer (and all the first places in the drinking standing) are history.

Paul, you are literally the first person I met here. Thank you for being the role model of the productive PhD student, for setting the bar sky high, and for your true friendship. Dimos, the Greek Freak. You are the real south hearth of group, passionate and smart. You are going to be great. Hugo (Ugo), I will bring your kindness and generosity around the world. You have been the best office and birthday-mate I could wish for.

Delft gifted me with a multitude of smart and beloved friends. Thank to all the guys of "After School" (Luis, Fabricio, Ilias, Jack, Davide, Antonio and my fratellino Luigi). We were probably the best customers in the history of the coffee machine, and that is just great. One day we will bring back the poker and Rotterdam nights. Thanks to Giulia, Ewoud, Antonio, Laura, Biagio, Lisa and Marco. Have some close friends is so important in a person life, and you are the best of this rare kind.

A special thanks to two of my dear friends from Milan: Federico and Akshay . Sometimes I have the impression you believe in me more than I do.

Un abbraccio ai miei fratelli di Acerra: Luca, Marcello, Renato, Vincenzo e Vicienzo. I nostri "momenti difficili" sono anche quelli ci uniscono e che non dimentichero mai.

Curriculum Vitæ

Vincenzo Montano was born in Acerra on 18th September 1992. In 2011 he obtained his 'Gymnasium' degree at Liceo Alfonso Maria de' Liguori in Acerra. In the same year he started his academic career at Università degli studi di Napoli Federico II enrolling in the Material Science and Engineering class. In 2014 he obtained his BSc. degree presenting a thesis titled "A semi-empirical method for the construction of the energy bands of common semiconductors". The work was conducted under the supervision of professor Domenico Ninno.

After finishing the bachelor degree, he moved to Politecnico di Milano for his master studies, enrolling in the Materials Engineering and Nanotechnology class. He graduated cum laude in 2016. His thesis work focused on the synthesis and characterisation of supramolecular self-healing polymers. The research was conducted under the supervision of professor Stefano Turri.

In January 2017 he started his doctoral studies at Technische Universiteit Delft on the development of novel self-healing polyurethanes within the Novel Aerospace Materials group under the supervision and promotion of Doctor Santiago Garcia and professor Sybrand van der Zwaag. During his Ph.D. studies he published several peer-reviewed papers on international journals. Moreover he received the Honorary Coating Science International Award at the European Coating Conference in 2018 and obtained the title of Accredited Polymer Scientist (RPK) from the National Dutch Graduate School of Polymer Science and Technology (PTN). During the last year of the Ph.D. he spent two months as visiting researcher at Clemson University in the U.S.A. within the Advanced Material Research Lab, where he conducted studies on the physics of scratch closure under the supervision of professor Marek Urban.

List of Publications

1. **V. Montano, A. Smits, S.J. García**, *The bio-touch: increasing coating functionalities via bio-mass derived components*, *Surface and Coatings Technology* **341**, 2-14 (2018).
2. **V. Montano, S.J. Picken, S. van der Zwaag, S.J. García**, *A deconvolution protocol of the mechanical relaxation spectrum to identify and quantify individual polymer feature contributions to self-healing*, *Physical Chemistry Chemical Physics* **21**, 19 (2019).
3. **V. Montano, M.M.B. Wempe, S.M.H. Does, J.B. Bijleveld, S. van der Zwaag, S.J. García**, *Controlling healing and toughness in polyurethanes by branch-mediated tube dilation*, *Macromolecules* **52**, 21 (2019).
4. **V. Montano, M. Senardi, S. van der Zwaag, S.J. García**, *Linking interfacial work of deformation from deconvoluted macro-rheological spectrum to early stage healing in selected polyurethanes*, *Physical Chemistry Chemical Physics* **22**, 38 (2020).
5. **V. Montano, W. Vogel, A. Smits, S. van der Zwaag, S.J. García**, *Role of the soft-to-hard ratio and hydrogen bond state on the crack closure and sealing behaviour of anti-corrosion self-healing polyurethane coatings*, submitted to *ACS Applied Polymer Materials*.
6. **V. Montano, M.W. Urban, S. van der Zwaag, S.J. García**, *Scratch closure in thermoplastic polyurethanes: an energetic analysis*, to be submitted to *Advanced Materials*.
7. **L. Ritzen, V. Montano, S.J. García**, *3D printing of a self-healing thermoplastic polyurethane through FDM: from polymer slab to mechanical assessment*, *Polymers* **13**, 305 (2021).

List of Conferences

1. **Poster Presentation** at *6th International Conference on Self-Healing Materials*, June 2017, Friedrichshafen, Germany.
Title: Self-healing through aliphatic interactions among branches: universality and extension of the concept.
2. **Oral Presentation** at *Dutch Polymer Days 2018*, April 2018, Lunteren, The Netherlands.
Title: Identifying the role of and contribution of T_g and reversible interactions on the macroscopic healing behaviour of near T_g healing polymers.
3. **Poster Presentation** at *European Technical Coatings Conference 2018*, June 2018, Amsterdam, The Netherlands.
Title: Identifying overlapping relaxation phenomena to optimize polymer design.
4. **Oral Presentation** at *AMI Self-healing Polymers 2018*, October 2018, London, UK.
Title: Extending materials and structures lifetime by using a holistic approach.
5. **Oral Presentation** at *6th International Symposium Frontier in Polymer Science*, May 2019, Budapest, Hungary.
Title: Effect of branch length on morphology and dynamics of densely branched self-healing polyurethanes.
6. **Oral Presentation** at *7th International Conference on Self-Healing Materials*, June 2019, Yokohama, Japan.
Title: A deconvolution protocol to identify and quantify individual polymer feature contributions to self-healing.
7. **Oral Presentation** at *Virtual EUROCORR 2020*, September 2020.
Title: On the relation between phase separation and barrier restoration of self-healing polyurethanes.